Impact de la microstructure des revêtements ZnAlMg sur les mécanismes de formation et la performance des couches de conversion sans Cr

Perrine Tanguy

To cite this version:

Perrine Tanguy. Impact de la microstructure des revêtements ZnAlMg sur les mécanismes de formation et la performance des couches de conversion sans Cr. Autre. Université Paris sciences et lettres, 2019. Français. ⟨NNT : 2019PSLEC007⟩. ⟨tel-02866111⟩

HAL Id: tel-02866111

https://pastel.hal.science/tel-02866111v1

Submitted on 12 Jun 2020

PSL
UNIVERSITÉ PARIS

THÈSE DE DOCTORAT
DE L'UNIVERSITÉ PSL

Préparée à L'École Nationale Supérieure de Chimie de Paris

Impact de la microstructure des revêtements ZnAlMg sur les mécanismes de formation et la performance des couches de conversion sans Cr^{VI}

(Impact of the microstructure of ZnAlMg coatings for steel on the formation mechanisms and performance of Cr^{VI}-free conversion coatings)

Soutenue par
Perrine TANGUY
Le 30 janvier 2019

Ecole doctorale n° 388
École doctorale de Chimie Physique et chimie Analytique de Paris

Spécialité
Chimie Physique

Composition du jury :

Dominique, THIERRY Directeur de recherche, Institut de la Corrosion	*Rapporteur*
Inger, ODNEVALL WALLINDER Professeur, KTH	*Rapporteur*
Herman, TERRYN Professeur, VUB	*Examinateur*
Kevin, OGLE Professeur, IRCP – I2E	*Président du jury*
Christian, ALLELY Expert, ArcelorMittal Maizières Research	*Examinateur*
Polina, VOLOVITCH Maître de Conférences, IRCP – I2E	*Directeur de thèse*

Chimie Paris
PSL
RESEARCH UNIVERSITY PARIS

Thèse de doctorat de
L'Université de recherche Paris Science & Lettres
PSL Research University

Ecole Nationale Supérieure de Chimie de Paris (ENSCP)

Impact of the microstructure of ZnAlMg coatings for steel on the formation mechanisms and performance of Cr-free conversion coatings

Présentée par

Perrine TANGUY

Pour obtenir le grade de

DOCTEUR DE L'UNIVERSITE DE RECHERCHE PARIS SCIENCE ET LETTRES

Spécialité Chimie physique

Soutenue le 30 janvier 2019

Devant le jury composé de :

Dominique THIERRY	Directeur de recherche, Institut de la Corrosion, Brest, France	Rapporteur
Inger ODNEVALL WALLINDER	Professeur, KTH, Stockholm, Suède	Rapporteur
Herman, TERRYN	Professeur, VUB, Bruxelles, Belgique	Examinateur
Kevin OGLE	Professeur, IRCP – I2E, Chimie ParisTech, Paris, France	Président du jury
Christian ALLELY	Expert, ArcelorMittal Research, Maizières-Les-Metz, France	Examinateur
Polina VOLOVITCH	Maître de Conférences, CNRS, IRCP, Chimie ParisTech, Paris, France	Directrice de thèse

TANGUY Perrine

4 rue du magasin aux vivres
57000 Metz
Birth: 19/10/1992 in Lannion (22)

p.emma.tanguy@gmail.com
06 58 75 54 17

EDUCATION

2016 - 2019 **Industrial PhD - Impact of the microstructure of ZnAlMg coatings for steel on the formation mechanisms and performance of Cr-free conversion coatings**, ArcelorMittal MaizièresResearch, Institut de Recherche de Chimie Paris (I2E), PSL

Sept. 2014 **Erasmus semester (6 months)** – Teaching focused on **Materials Science, Corrosion and Surfaces protection**, KTH, Stockholm, Sweden

2012 - 2015 **Chemical science and engineering graduate engineer,** Chimie ParisTech (ENSCP)

2010 - 2012 **DUT Mesures Physiques**, speciality « Matériaux et Contrôles Physico-chimiques », option « Chimie organique », IUT de Lannion

WORK EXPERIENCES

2016 – 2019 **Industrial PhD training - Comprehension of the conversion coatings mechanisms on multiphase ZnAlMg coated steel,** ArcelorMittal Maizières Research, IRCP (I2E), PSL

- Understand Ti-based and phosphate-based conversion coatings formation mechanisms on multiphase ZnAlMg materials
- Investigate an alternative conversion coating application process, improving corrosion resistance of painted ZnAlMg and suitable for industrial process
- Determination of the corrosion mechanisms of Ti-based conversion coatings on painted ZnAlMg coated steels

2015 (6 months) **Master thesis training – Applicability of SAF 2304 duplex stainless steel regarding its corrosion resistance in the GDI**, Sandvik Materials Technology, Sandviken, Sweden

- Evaluation of the pitting corrosion resistance of SAF 2304 in contact with ethanol-based biofuel
- Determination of the pitting corrosion resistance of SAF 2304-containing an intermetallic phase formed during brazing

2014 (5 months) **R&D training – Study of the twins created after tensile testing in a beta-metastable Ti-12Mo (%) alloy**, Université Catholique de Louvain, Louvain La Neuve, Belgium

- Determination of the connection between the grain size, twin size and the distance between two consecutive twins in a beta-metastable Ti-12Mo (%) alloy.
- Evaluation of the twins reversion kinetics in the alloy after tensile testing using thermal treatment

LANGUAGES

🇬🇧 : **Advanced level C1** 🇪🇸 : **Beginner level** 🇮🇹 : **Beginner level** 🇫🇷 : **Mother tongue**
(TOEIC: 990/990 - 2015)

SCIENTIFIC PRODUCTION

ArcelorMittal Project Reviews focused on "Knowledge Building" and "ZnAlMg for pre-painted applications" (2 reviews/year), 12 oral presentations (English), Maizières-Les-Metz (France) and Liège (Belgium).

Oral presentation at European Corrosion Congress 2018: P. Tanguy, C. Allély, D. Dragoe, P. Volovitch, "ZnAlMg microstructure effect on the composition and distribution of Ti-containing surface treatments", Krakow, Poland, September 2018.

Poster at European Corrosion Congress 2017: P. Tanguy, C. Allély, P. Volovitch, D. Dragoe, V. Sefl, J. Stoulil, "Phosphate-based conversion coating on Zn-based multiphase substrate: Impact of activator", Prague, Czech Republic, September 2017.

Poster at Doctoral school ED388 day (05/2016) and ArcelorMittal Learning week (06/2016): P. Tanguy, C. Allély, P. Volovitch **"**Formation and chemical stability of conversion coatings on ZnAlMg coated steels".

ArcelorMittal confidential internal reports

RELEVANT SKILLS

2016 – 2019: **Responsible of the chemicals storage** for the research group Surface and Coatings, ArcelorMittal Maizières Research – Chemicals storage (acids, bases, solvents, CMR products), inventory listing, discharge of chemicals based on constant interactions with the environmental, safety and health department

Techniques knowledge, user level: XRD, SEM-FEG, EDS, XPS, AES, GD-OES, Raman spectroscopy, electrochemistry, SKP

Acknowledgments

Maintenant que s'achève ma thèse, je voudrais en profiter pour remercier les personnes qui m'ont aidé et ont contribué à cette aventure. Plus je prends le temps de me remémorer ces 3 années et plus la liste des personnes à remercier s'allonge, c'est pourquoi je vais tâcher d'être aussi exhaustive que possible.

Tout d'abord, je voudrais remercier Polina Volovitch, ma directrice de thèse, pour m'avoir recommandée pour cette thèse, m'avoir fait confiance et s'être autant investie dans mon apprentissage, directement mais aussi par l'intermédiaire des nombreuses rencontres avec d'autres chercheurs dont elle a été à l'origine. Je voudrais aussi remercier Christian Allély, mon encadrant chez ArcelorMittal Maizières Research pour sa supervision tout au long de ces 3 années, ses conseils et tout le temps qu'il m'aura consacré. Grâce à eux, ces 3 années ont été enrichissantes à plus d'un niveau.

Je voudrais aussi profiter de ces quelques mots pour remercier Michel Babbit, directeur du Centre de recherche Maizières Products et Jacques Petitjean, responsable du département Surfaces and Coatings (SurCoat) du centre Maizières Products, de m'avoir accordé ma chance et de m'avoir permis d'intégrer le département.

Il me semble impossible de ne pas remercier comme il se doit Diana Dragoe pour les nombreuses analyses XPS qu'elle a réalisée ainsi que pour toute son implication, sa disponibilité et sa patience qui nous ont grandement aidé à avancer tout au long de la thèse.

J'adresse mes sincères remerciements à Mélanie Vaudescal et Michel Lahaye du Placamat à Bordeaux pour leur collaboration sur la réalisation d'analyses nano-auger et le temps qu'ils auront pris à me faire découvrir cette technique.

Je voudrais aussi en profiter pour remercier particulièrement Anna Krasnova pour son aide dans la réalisation de certaines manipulations LEIM et sa disponibilité pour répondre à mes questions.

Dans le cadre de cette thèse, certaines caractérisations de surface ont été réalisées en collaboration avec l'équipe d'Analyses de surface du département SurCoat gérée par Marie-José Cornu et Sébastien Crémel et je voudrais les remercier pour leur collaboration tout au long de ces 3 ans et les résultats qu'ils nous ont permis de mettre en évidence sur certains sujets.

De manière générale, je remercie tous les membres du département SurCoat pour l'aide qu'ils m'auront apporté pendant ces 3 ans. J'ai beaucoup appris à leur contact, plus que je ne l'aurais moi-même soupçonné. J'ai évidemment une pensée toute particulière pour l'équipe

d’électrochimistes que sont Astrid Grégoire, Charifa Riani et Aymeric Corbel. Ils ont été d’une bienveillance et d’un soutien sans faille à plus d’un niveau, qui me les feront regretter à l’avenir.

Comment ne pas remercier l’équipe I2E au grand complet pour tout leur soutien, leurs conseils et les nombreux services qu’ils m’auront rendus pendant cette thèse. Je voudrais en particulier remercier Thomas Sanchez, doctorant à l’I2E, Junsoo Han, post doc et Armelle Ringuedé, référente PSL de l’ED388 pour leur écoute, leur soutien sans faille et leurs précieux conseils, surtout pendant les derniers mois de la thèse. Une pensée spéciale pour Amandine Michot Mignucci pour les innombrables discussions que nous avons eues toutes les 2 et qui m’ont beaucoup fait grandir depuis que je l’ai rencontrée !

Je voudrais profiter de ces quelques lignes pour remercier Joël Marsal, directeur d’Allia-Tech. Les nombreuses discussions que j’ai eu avec lui ont toujours été très et il restera un très bon souvenir de mon expérience à Metz.

Quand je pense à tous les bons moments passés à Metz, ils sont quasi indissociables des personnes suivantes que je ne saurai remercier tant ils ont eu d’impact sur le souvenir que je garderai de ma vie à Metz : Cyril Nicard, Matthieu Siebentritt, Coralie Jung, Audrey Le Fichant, Vincent Feynerol, Benjamin Bauer, Aude Nadler, Céline Arrighi, Pauline Ronfart, Paula Vieira Salomao, Nicolas Tran et bien d’autres encore…merci pour tout ! 😊

Enfin, il y a des personnes qui m’ont soutenu d’aussi loin que je m’en souvienne et à qui je voudrais adresser mes remerciements les plus sincères et les plus profonds : mes parents Jean-Yves et Joëlle, ma sœur Aline, mon neveu Ronan ainsi que Nicolas Montesinos.

PhD thesis

Impact of the microstructure of ZnAlMg coatings for steel on the formation mechanisms and performance of Cr-free conversion coatings

Abstract

ZnAlMg multiphase sacrificial coatings on steel are regarded as a replacement of conventional hot dip galvanized steel in many applications including automotive and pre-painted market. Conversion coatings (CC) are applied to promote the paint adherence and improve the anticorrosion resistance of painted galvanized steels among which thick phosphate conversion coatings (PCC) and thin Ti-based coatings (TiCC) are used.

Preliminary outdoor corrosion testing has shown that, in presence of defects going down to the steel relevant for cosmetic corrosion evaluation, blisters can be developed on painted ZnAlMg coated steel with TiCC but not with PCC. Simultaneously, no blister was detected on painted monophase HDG sample treated with TiCC formulations.

One of the possible reasons for the blistering on ZnAlMg coated steel can be the presence of multiple phases (ZnAl-Zn_2Mg-Zn) resulting in a galvanic coupling between phases during the CC precipitation. CC are usually considered to precipitate according to a 2-step mechanism: (1) Dissolution of the underlying metal substrate in anodic areas associated with a pH increase from cathodic reaction in cathodic areas and (2) Precipitation of the conversion coating once a precipitation pH is reached. A multiphase substrate could, then, induce an inhomogeneous spatial distribution of cathodes and anodes and consequently modify the different rates of nucleation and growth of CC on these phases and the properties of the formed layer. The verification of the impact of the multiphase microstructure on the distribution of CC and is hence of great importance.

This PhD work had 2 main objectives:

- To identify the origins of the difference performance between PCC and TiCC-treated painted ZnAlMg materials during cosmetic corrosion testing, in particular, verify the impact of the ZnAlMg multiphase microstructure on the CCs composition, distribution and performance.
- To formulate a solution to overcome the impact of the multiphase ZnAlMg microstructure on the distribution of TiCC.

Model ZnAlMg coated steels and pure phases simulating ZnAlMg microstructure were characterized at different steps of the CC procedure. The similarity of Ti speciation in TiCC on all ZnAlMg phases was confirmed by XPS. Electron microscopy and nano-auger spectroscopy

and mapping however have shown that PCC grains form a homogeneous layer on all phases while the distribution of TiCC on ZnAlMg phases is heterogeneous, binary eutectic phases being better covered than monophase Zn dendrites. The heterogeneous CC distribution was consistent with the worsened blistering resistance of TiCC-treated ZnAlMg surfaces compared to PCC, verified by electrochemical measurements, LEIM and outdoor corrosion tests.

The origin of the homogeneous or heterogeneous distribution of CC on ZnAlMg was proposed to be related to the ratio between the ZnAlMg microstructure fineness and the conversion coating elements size. For PCC, the galvanic coupling inside the eutectic phases and between the micrometric-sized ZnAlMg phases has little influence on the distribution of micrometric phosphate grains. For nanometric TiCC, the galvanic coupling inside binary eutectic phases can be considered as the origin of different precipitation kinetics and CC distribution. This way, the galvanic coupling inside phases can be critical for CC-containing nanometric-sized elements.

The hypothesis was confirmed by electrochemical measurements on pure phases simulating ZnAlMg microstructure and by comparing conversion coating precipitation on ZnAlMg materials and pure phases.

A solution was proposed to overcome the microstructure/CC elements size ratio issue, using a Cu or Fe cementation pretreatment prior to TiCC procedure. SEM, AES and XPS confirmed the deposition of metallic Cu or Fe during pretreatment resulting in a finer distribution of local cathodes/anodes on ZnAlMg surface as well as a resulting homogeneous distribution of the TiCC on ZnAlMg. LEIM experiments demonstrated the improved blistering resistance of ZnAlMg coated steel with the Cu pretreatment while scab test outdoor exposure confirmed the blistering corrosion resistance gain after 1 year of testing.

List of figures

List of tables

Abbreviation list

ZnAlMg: ZM: Zinc-Aluminium-Magnesium coating for steel typically containing 1.5-11 wt. % of Al and 0.5-6 wt. % of Mg

HDG steel: Hot Deep Galvanized steel

CC: Conversion Coating

REACH: Registration, Evaluation, Authorization and Restriction of Chemicals

CrVI CC: Hexavalent chromium conversion coating (use restricted by REACH legislation)

TiCC: Ti-based conversion coating dedicated to the pre-painted market

PCC: Phosphate ZnNi-based conversion coating requiring a Ti-activation step prior to the conversion coating procedure

OC: Organic Coating

XPS: X-ray Photoelectron Spectroscopy

AES: Auger Electron Spectroscopy

TFA: Target Factor Analysis

PCA: Principal Component Analysis

FEG SEM: Field Emission Gun Scanning Electron Microscopy

EDS: Energy Dispersive Spectroscopy

GD-OES: Glow Discharge Optical Emission Spectroscopy

SKP-FM: Scanning Kelvin Probe Force Microscopy

OCP: Open Circuit Potential

SHE: Standard Hydrogen Electrode

SCE: Saturated Calomel Electrode

DiP: Differential Interferometry Profiles

EIS: Electrochemical Impedance Spectroscopy

LEIM: Local Electrochemical Impedance Spectroscopy

CPD: Contact Potential Difference

TEM: Transmission Electron Microscopy

wt. %: Weight Percent

at. %: Atomic Percent

BZS: Basic Zinc Salts

LDH: Layered Double Hydroxide

Summary

Introduction

ZnAlMg coatings are multiphase sacrificial coatings replacing monophase HDG Zn-0,2 Al wt. % in the automotive and pre-painted market. Thanks to the Al concentration increase and the addition of Mg, an improved corrosion resistance was allowed, reducing the sacrificial coating thickness as well as production costs of galvanic layers and increase of the lifetime of ZnAlMg coated steels.

To ensure the paint adherence on the ZnAlMg substrate, conversion coatings (CC) are applied prior to the different paint coatings. Due to the current European regulations, restrictions are in place about the use of phosphate and Cr^{VI}-based CC [1], [2]. Therefore, new alternative CC are being developed for the last decade to replace the toxic Cr^{VI}-based CC formulations. In the pre-painted market, Ti- based conversion coatings (TiCC) are regarded as a promising alternative.

However, in preliminary industrial tests made by ArcelorMittal Maizières Research on painted ZnAlMg coated steel dedicated to pre-painted market with TiCC, sometimes delamination and blisters were observed near the artificial scratches made down to the steel to simulate accidental defects that can occur in service life.

Unlike TiCC-treated ZnAlMg coated steel, ZnAlMg ones treated with phosphate-based CC (PCC) exhibit an enhanced blistering corrosion resistance. In addition, HDG coated steels treated with TiCC are not subject to blistering corrosion either. This way, the blistering issue results from a lack of adherence between the ZnAlMg coatings dedicated to the pre-painted market and the TiCC. One of the possible reasons of the latter can be an inhomogeneous TiCC distribution on the multiphase ZnAlMg substrate because of micro galvanic coupling between phases during the CC precipitation.

The identification of the origins of the different blistering resistance of painted TiCC and PCC-treated ZnAlMg, in particular, the impact of the microstructure on the CC distribution and performance and looking for a solution for improvement of TiCC performance were in the main scope of this PhD. The work was conducted in collaboration between ArcelorMittal Maizières Research and l'Institut de Recherche de Chimie Paris de l'Ecole Nationale Supérieure de Chimie de Paris. To achieve the objectives, several steps were necessary:

- The presence of preferential corrosion paths leading to the blistering on painted ZnAlMg coated steel treated with TiCC was confirmed.
- The reasons of formation of homogeneous PCC on multiphase ZnAlMg substrate were understood.
- The inhomogeneity of TiCC on multiphase ZnAlMg coating obtained by a standard treatment procedure was confirmed and the role of substrate phase composition and spatial distribution of these phases in the formation mechanism of TiCC was understood. The inhomogeneous distribution of cathodic zones was shown to be the main reason for the inhomogeneity of TiCC distribution.
- Based on the elucidated mechanisms, a pretreatment was proposed improving the TiCC distribution on ZnAlMg phases by means of noble metal cementation and the efficiency of the proposed solution was demonstrated.

The manuscript is organized in **four parts** and includes **seven chapters**.

The first part includes this **introduction** which develops the context and the scientific questions that were answered during the PhD and the **first chapter** which summarizes the state of the art relevant to the work. The composition, microstructure and corrosion resistance of ZnAlMg sacrificial coatings are reviewed as well as the existing knowledge of the conversion coatings formation mechanisms for TiCC and PCC on Zn-based substrates and the degradation mechanisms of painted Zn-based coated steel, described in the literature, leading to delamination and blistering. The literature review enabled the selection of the pure phases simulating the phases contained in the ZnAlMg microstructure.

The second part, **Materials and Methods**, covers the materials and the electrochemical setup used in this work and introduces the main techniques used throughout the PhD, namely surface analysis techniques used to characterize the CC distribution and chemical composition and local electrochemical techniques for the detection of under paint corrosion such as delamination or blistering.

The third part presents the most important results obtained during this PhD. This part consists of 4 chapters formatted as publications prepared for submission to different journals.

Chapter 3 (“**Comprehension of the degradation mechanisms TiCC-treated and painted ZnAlMg coated steels**”) approaches the impact of ZnAlMg microstructure in the development and propagation of delamination and blisters. Corrosion mechanisms of painted ZnAlMg coated steel are discussed.

Chapter 4 ("**On the effect of multiphase microstructure of ZnAlMg substrate on the Ti-based activation and phosphate conversion coating distribution**") focuses on the PCC distribution on ZnAlMg at different CC procedure steps and as a function of the activator freshness. The role of the Ti-based activator used prior to the phosphatation process in the formation of covering and crystalline grains on all ZnAlMg phases was exhibited. The inhomogeneity of the interaction of different ZnAlMg constituents with Ti-containing activator was shown and the importance of the micrometric grain size of PCC crystals for the formation of a homogeneous layer was demonstrated.

Chapter 5 ("**Impact of phases in ZnAlMg coatings on the distribution of Ti-based conversion coatings**") develops the origin of the heterogeneous distribution of TiCC on ZnAlMg substrates. The electrochemical behavior of pure phases contained in the ZnAlMg microstructure confirmed the existence of a galvanic coupling inside phases and inhomogeneous TiCC distribution assessed by surface analysis techniques correlated with the expected from galvanic coupling distribution of cathodic zones. A schematic mechanism of TiCC formation on multiphase ZnAlMg substrate was proposed and the role of the ratio between the microstructure inhomogeneity scale and the CC element size was highlighted.

Chapter 6 ("**Insight into the formation and degradation mechanisms of TiCC on multiphase ZnAlMg using Cu^{2+}-modified alkaline degreasing baths**") presents the solution selected to homogenize the TiCC distribution on ZnAlMg coatings, which is based on the cementation of metallic Cu during the degreasing step, allowing a finer cathodes/anodes distribution. The uniform chemical composition and the homogeneous thickness distribution of TiCC on ZnAlMg after the new pretreatment was confirmed by surface analysis techniques and better resistance in cosmetic corrosion test compared to a conventional procedure was confirmed by local electrochemical impedance mapping.

The last chapter ("**Conclusions and perspectives**") summarizes the general conclusions brought by the thesis, their importance regarding the corrosion resistance of painted ZnAlMg coated steels and the perspectives of the study.

Several appendices give some additional details like design of specific experiments or technics, parameters used for XPS peaks deconvolution etc.

[1] European Chemicals Agency, « Substances restricted under REACH », ECHA, 2006. [Online]. Available on: https://echa.europa.eu/substances-restricted-under-reach/-/dislist/details/0b0236e1807e2bc1. [Accessed on: 09/08/2018]

[2] European Chemicals Agency, “Nickel and its compounds”, ECHA, 2011. [Online]. Available on: https://echa.europa.eu/fr/substances-restricted-under-reach/-/dislist/details/0b0236e1807e266a. [Accessed on: 11/08/2018]

Chapter 1: State of the art

This chapter is a literature review about the structure and fabrication process of painted ZnAlMg coated steel. Additional research was carried out to compile the well-established degradation mechanisms leading to delamination and blistering on painted metallic substrate. This work was used as a basis for the methodology selected in the PhD. As the thesis will be presented in publication formatted chapters, it is worth noting that each chapter will include a short focused bibliographic introduction.

1. Basic knowledge about ZnAlMg sacrificial coatings for steel

1.1. Development of ZnAlMg sacrificial coatings

Historically, aluminium was the first alloying element to be incorporated to the galvanizing process at concentrations higher than the usual 0.2 wt. % Al used in continuous Hot Dip Galvanized steel (HDG). Notorious ZnAl sacrificial coatings in use nowadays are Galvalume ® (1972) and Galfan ® (1980) containing respectively 55 wt. % and 5 wt. % of Al [1]-[3].
It was later on noticed that adding up to 0.1 wt. % of Mg could significantly improve the corrosion resistance of Galfan ® in atmospheric and aqueous environments [4], leading to the commercialization of Super Zinc $ZnAl_{4.5}Mg_{0.1}$ (1985). This promising discovery opened the way to the development of ZAM ® (1998) by Nisshin Steel, exhibiting 6 wt. % Al and 3 wt. % Mg [5]. Not only the corrosion resistance of the sacrificial coating was improved but the cathodic protection induced by the magnesium was also significantly increased. It led European steel companies but also Nippon Steel Corporation to manufacture new compositions of ZnAlMg from the early 2000s with various Al and Mg proportions [1]-[7]:

Table 1: List of the ZnAlMg coatings compositions commercialized by the main European and Japanese steel companies [2]-[9]

Company	Commercial name	Commercialization year	wt.% Zn	wt.% Al	wt.% Mg
Nisshin Steel	ZAM	1998	91.0	6.0	3.0
Nippon Steel Corp.	Super Dyma	2002	86.0	11.0	3.0
Tata Steel	Magizinc	2007	97.0	1.5	1.5
Voestalpine	Corrender	2007	96.0	2.0	2.0
Thyssen Krupp	ZM Ecoprotect	2008	98.0	1.0	1.0
ArcelorMittal	Magnelis	2010	93.3	3.7	3.0

1.2. ZnAlMg microstructure

The microstructure of materials is strongly influenced by their production process. ZnAlMg coatings are produced by continuous hot dip galvanizing.

1.2.1. ZnAlMg production by Hot Dip Galvanizing

Whether the steel is galvanized with the classic zinc-based coating (Zn-0.2 wt. % Al) or with a ZnAlMg layer, a similar Hot Dip Galvanizing process is used (Appendix 1). In the case of ZnAlMg coatings, the immersion bath is constituted of liquid zinc, aluminium and magnesium elements in a concentration defined for each commercial composition. In the framework of this PhD, ZnAlMg compositions with Al ranging between 1 and 11 wt. % and Mg up to 3 wt. % were studied, whether dedicated to the automobile or pre-painted market.

In the Figure 1 is displayed a scheme of the coating process. Both faces are coated with the same ZnAlMg coating thickness. The line speed is typically in the order of 100 m/min.

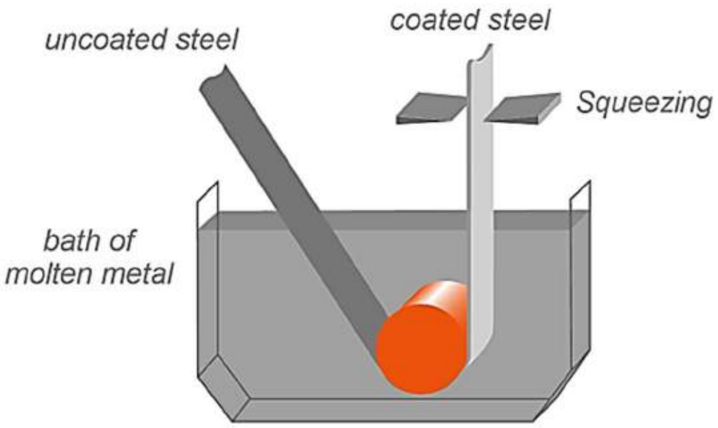

Figure 1: Scheme of the Hot Dip Galvanizing process [10]

First, the sheet surface must be free of contaminants and oxides to form a solid bonding between the zinc layer and the steel surface. To do so, an alkaline cleaning is performed to remove impurities and aluminium oxide. The steel sheet is heated in an annealing furnace to impart it the desired strength and formability. A protective atmosphere based on nitrogen and hydrogen (5 % H_2 and 95 % N_2) is used in the furnace to prevent the formation of an oxide layer on the steel surface.

In order to make sure that the correct ZnAlMg coating thickness is applied on the surface, “gas knives” are used as they inject air on both sides of the steel sheet to remove ZnAlMg excess [11].

Parameters such as the bath composition, bath temperature and dipping time have to be controlled to get the targeted microstructure.

1.2.2. ZnAlMg microstructure as a function of Al and Mg contents

In ZnAlMg coatings microstructures, four solid phases can be found, namely a Zn-rich phase, Al-rich phase, Zn_2Mg and $Zn_{11}Mg_2$. While $Zn_{11}Mg_2$ is rarely formed, other phases can form Zn dendrites, binary eutectics Zn-Zn_2Mg, binary eutectoid Zn-Al and/or the ternary eutectic Zn-Al-Zn_2Mg depending on the ZnAlMg coating composition (Figure 2). In the case of low magnesium-alloyed compositions, the ternary eutectic phase is considered as a binary Zn-Al phase due to the very low Mg concentration measured.

The variation of the chemical composition of the phases compared to the equilibrium values was attributed to the rapid solidification of the ZnAlMg coating [12]. It is also responsible for the fine and complex microstructure of the coating.

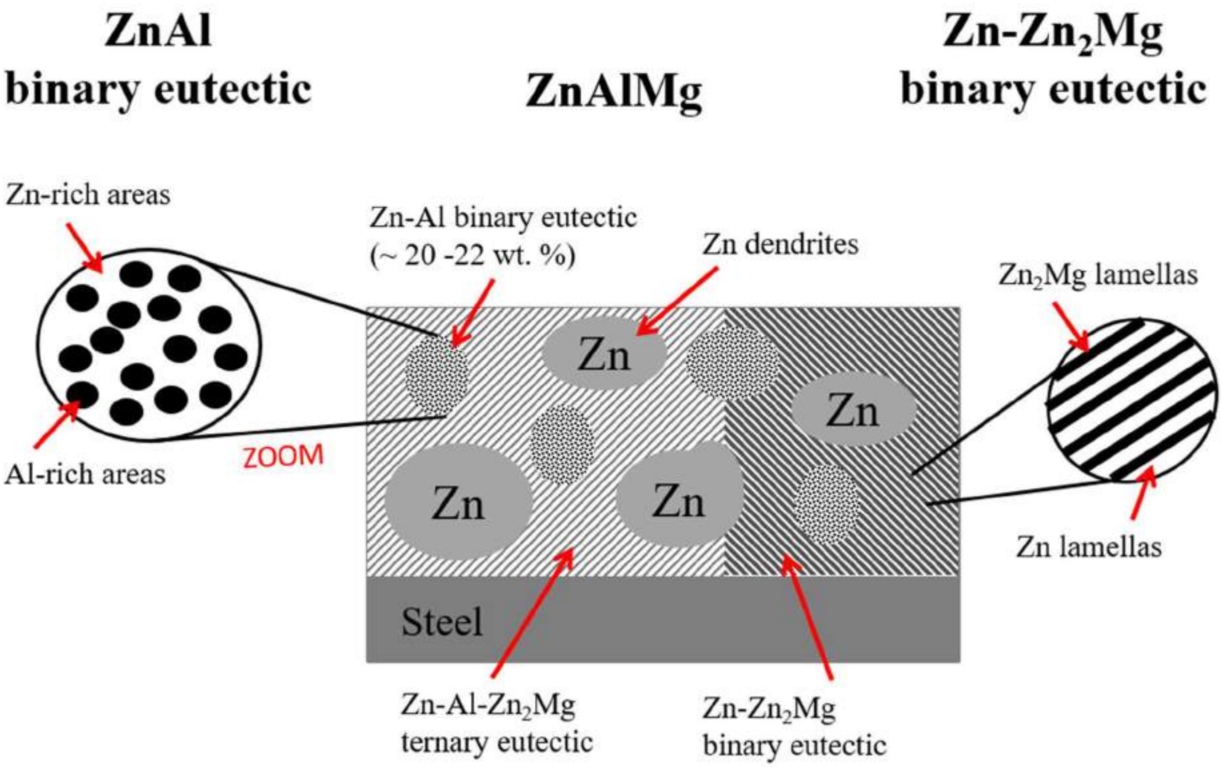

Figure 2: Scheme of the cross-section of ZnAlMg coated steel. Zn-Zn_2Mg binary phase is composed of bright Zn lamellas and dark Zn_2Mg ones while the ternary one includes Zn, Zn_2Mg and an Al mesh. Zn-Al binary phase is composed of bright Zn areas and dark Al-rich ones (inspired by [12])

Ratio of Al and Mg are usually adjusted depending on the desired mechanical, physico-chemical and other properties. In the pre-painted market, Al and Mg contents were selected to allow a high flexibility associated with a corrosion resistance twice better than HDG one [5], [9]. For low Mg-containing ZnAlMg compositions, the binary Zn-Zn_2Mg phase is mainly located at the surface of the coating, forming a continuous and surface located phase (first micron in depth), while Zn dendrites and the binary ZnAl phase form islands in the microstructure.

1.3. Corrosion resistance of bare ZnAlMg compared to HDG

It has been largely reported in the literature, through natural exposition and accelerated corrosion tests (VDA test, salt spray testing, scab test, Cl^- -free test etc), that ZnAlMg coated steels exhibit an enhanced corrosion resistance compared to Hot Dip Galvanized ones (HDG) in their un-painted state ([1], [3], [7], [8], [14]-[17] etc). However, different interpretations are proposed to explain this corrosion resistance gain.

The study of the corrosion resistance of ZnMg alloys compared to HDG coatings confirmed the beneficial effect of Mg alloying. It was explained that the formation of a dense layer of simonkolleite $Z_{n5}(OH)_8Cl_2 \cdot H_2O$, replacing poorly resistant ZnO on ZnMg surface, suppresses the O_2 reduction [18] which is the main reaction controlling the corrosion rate of the substrate in neutral and/or slightly alkaline environment [19]. A long-lasting cathodic protection was attributed to the newly formed simonkolleite. In addition, the formation of $Mg(OH)_2$ was reported by Hosking et al. to limit the O_2 reduction [20]. It was also proposed that the role of Mg^{2+} ions was to buffer the pH around 10 by the formation of $Mg(OH)_2$ as well as to react with carbonate ions, preventing CO_3^{2-} from reacting with simonkolleite or other Zn-based products, hence stabilizing them [14].

Considering the contribution of each alloying element in the improved corrosion resistance of ZnAlMg coatings compared to HDG ones, often the type of corrosion products formed on ZnAlMg was claimed to be at the origin of the corrosion resistance gain. Indeed, the formation of compact Layered Double Hydroxide (ZnAl-LDH) and simonkolleite corrosion products at the expense of poorly protective ZnO has been reported in many publications focusing on the characterization of the corrosion behavior of ZnAlMg compared to HDG coatings [1], [7], [8], [15], [17], [20]-[22].

Some other effects were also reported, for instance the released Mg^{2+} was proposed to induce the formation of Mg-containing corrosion products but also to react with CO_3^{2-} or SO_4^{2-} to stabilize corrosion products such as simonkolleite or zinc hydroxysulfate by preventing them from reacting with Zn to form soluble or low protective complexes [22]. The presence of Al was proposed to promote dense LDH formation at advanced stages of corrosion, as already reported in the literature [1], [7], [15], [21], while at initial stages of corrosion Al stays in insoluble form and selective dissolution of Zn and Mg occurs [22].

Thierry et al. studied the behavior of ZnAlMg coated steels in natural exposure and proposed that the dissolution of Al promotes the formation of different types of compact LDH corrosion products, lowering the corrosion rate of ZnAlMg [8]. The Mg was explained to induce a lower surface pH on cathodes and the formation of magnesium hydroxycarbonates and possibly magnesium hydroxychlorides on anodes.

Finally, Salgueiro et al. observed the formation of corrosion inhibiting Basic Zinc Salts (BZS) and LDH products on ZnAlMg surfaces under cathodic polarization in various electrolytes [16] which correlated with lower cathodic currents. The transformation of BZS into ZnO was delayed by the presence of Mg^{2+} ions while Al^{3+} ones promoted the formation of stable LDH even in very alkaline conditions. A non-oxidized Al skeleton was noted to keep corrosion products compactness.

The comparison of ZnAlMg coated and HDG coated steels has also demonstrated that the corrosion resistance gain is dependent on the exposure conditions and chloride content [8]. It was demonstrated that in environments involving a high time of wetness and high chloride load, the corrosion resistance gain of ZnAlMg over HDG was very relative.

In general terms, it has been commonly admitted that the formation of compact corrosion products acting as a barrier to the oxygen reduction on ZnAlMg surface is the source of the improved corrosion resistance of ZnAlMg coatings compared to HDG coatings.

Hence, it enabled reducing by a factor of two the ZnAlMg coating thickness/weight while keeping an equivalent corrosion resistance as HDG coatings [5], [9].

2. Painted ZnAlMg coated steels

2.1. Main layers present in painted ZnAlMg coated steel

A typical structure of painted ZnAlMg coated steels is illustrated in Figure 3 (layers thickness is not representative).

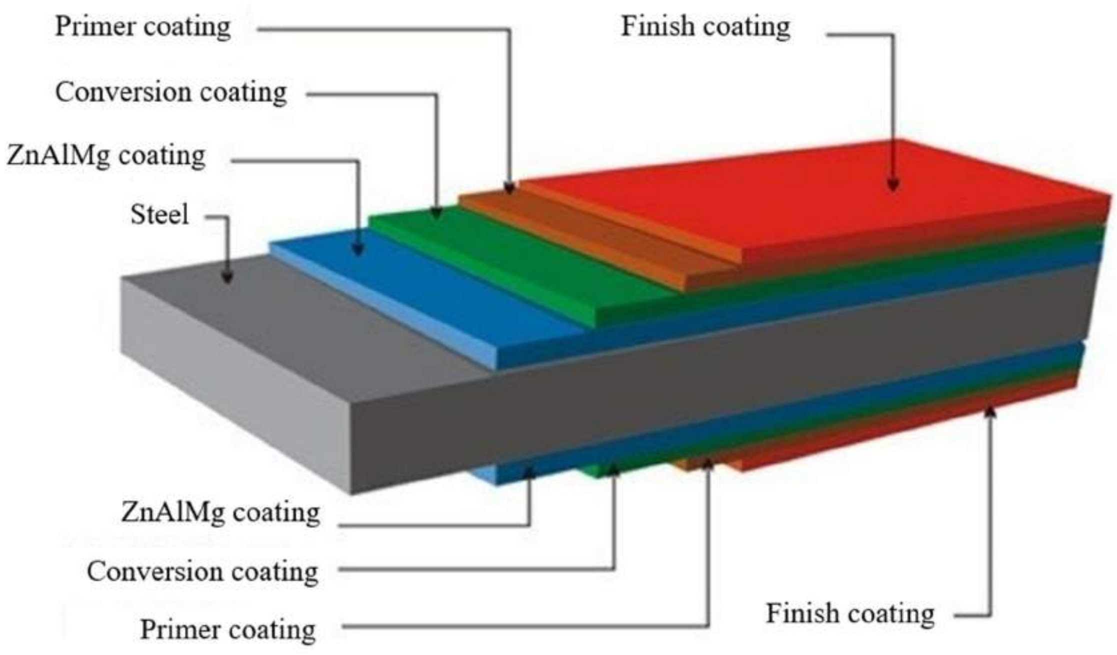

Figure 3: Structure of a painted ZnAlMg coated steel for the pre-painted market

As mentioned earlier (section 1.2.1.), the ZnAlMg, applied by hot dip galvanizing process, enables the formation of a sacrificial coating with a thickness of 10 µm [5], [9]. To ensure the paint adherence on the ZnAlMg coating and provide corrosion protection to the painted ZnAlMg coated steel, conversion coatings (CC) are applied prior to the paint. They are inorganic thin insoluble oxide layers with thicknesses ranging from 10 nm up to 1 µm depending on the type of conversion coating applied on the metal surface [24], [25]. Different layers of paint can be applied on the CC depending on the targeted physical, mechanical properties, corrosion resistance etc of the painted ZnAlMg coated steel among which a primer and a top coat. First, the primer, directly in contact with the CC, is applied to provide corrosion protection and ensure a good adhesion of the paint by wetting the surface. A top coat is commonly applied as the finish coating, promoting the cosmetic appearance and surface resistance required for the system. Depending on the exposure conditions, they might also exhibit UV, bacteria, condensation resistance properties etc. The paint thickness is comprised between 5 and 30 µm for the primer and 15 and 200 µm for the finishing coat.

Depending on the targeted application, both CC and paint layers can be deposited using different processes. Indeed, in the automotive sector, the immersion procedure is in use [25] while in the pre-painted market, coatings are applied by coil coating [10].

For painted Zn-based coated steel, the overall paint adherence and corrosion resistance is ensured by CC. They have been extensively studied in the literature and their formation mechanisms on metal substrates is of electrochemical nature. They act as a physical and insoluble barrier limiting the O_2 reduction on the metal surface, thus the corrosion rate [23], [24], [26]. Although various types of CC exist depending on the underlying metal substrate and application process, a common deposition mechanism pattern was observed for all of them.

2.2. Basics of conversion coatings procedure and formation mechanisms

Before the CC procedure, the galvanized steel surface is usually prepared by an alkaline degreasing to remove oil, grease and metallic oxides on the top of the sample. It is particularly efficient for aluminium and zinc oxides dissolution as they are very soluble in alkaline media [27]. The alkaline degreasing solution ($10 < pH < 13$) is composed of a base associated to surfactants and cleaning agents [28].

After the pretreatment, the conversion coating procedure is usually considered as a two-step mechanism. The first step is the establishment of cathodic and anodic sites on the surface, responsible for pH increase and Zn-ions release (Fig. 4). The metal dissolution corresponds to the anodic reaction while the reduction of hydrogen ions or the reduction of oxygen constitutes the cathodic reaction. The interaction between the conversion coating electrolyte and the substrate defines cathodic and anodic areas on the surface.

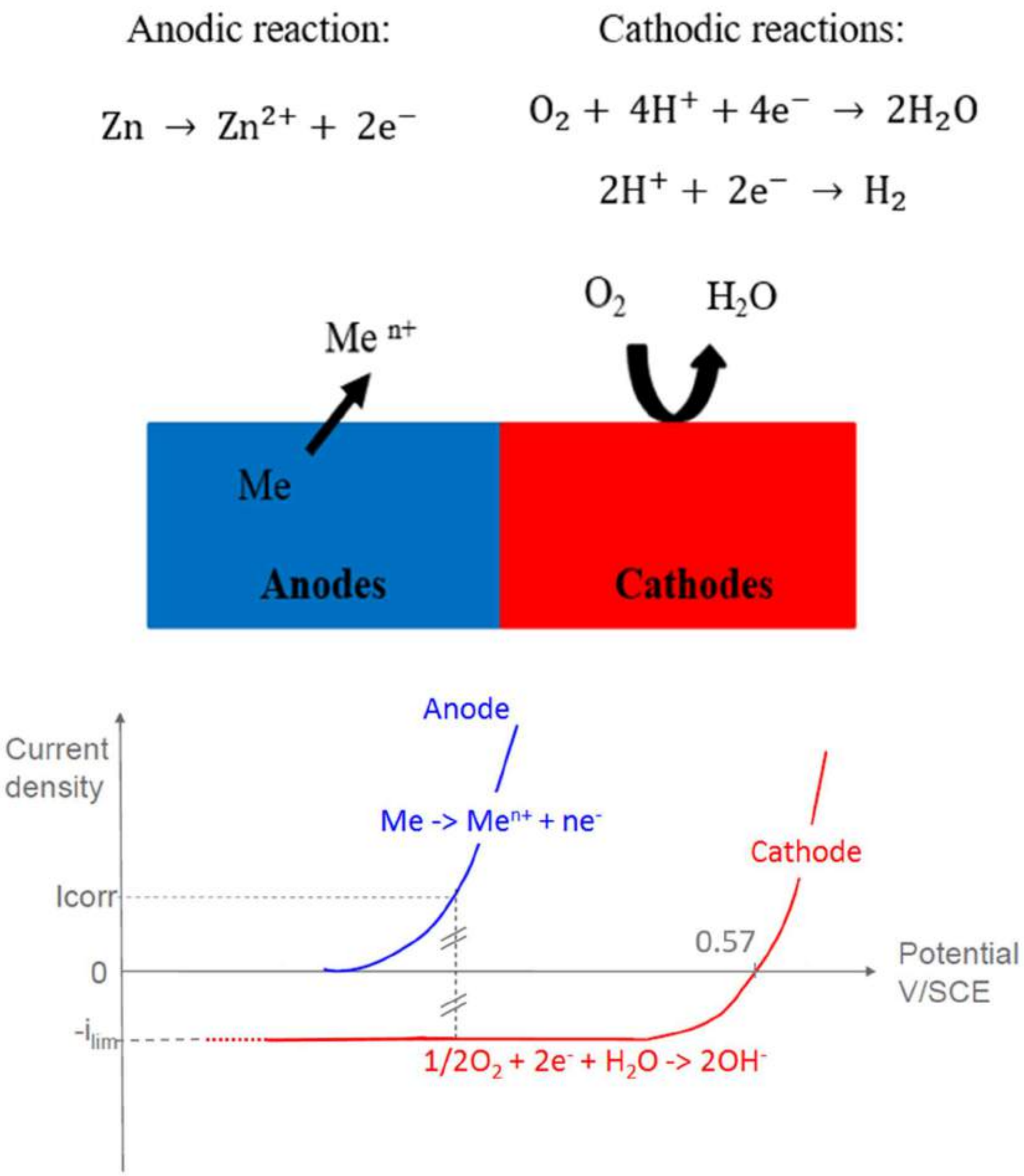

Figure 4: Schematic representation of anodic and cathodic reactions distribution during galvanic coupling

The pH increase acts as the trigger for the CC precipitation. Once a threshold pH is reached, the precipitation of the CC takes place, forming insoluble oxide layers of various thickness and isolating the underlying metal from the atmosphere. In function of the chemical composition of the bath and the formed layer, different types of conversion coatings are known for galvanized steels. They will be discussed in the following sections.

2.2.1. Chromiun (VI) CC

Historically, chromium (VI) CC has been the most widespread conversion coating as it provides excellent corrosion protection and adhesion for polymeric-based paint [23]. The CC versatility enables using it over a wide range of metal substrates such as steel [23], Zn-based [28], [29], Al-based [31]-[33], Mg-based [34] alloys etc. Their composition is considered as the simplest since the oxidant is strong enough to lead to the metal dissolution and the conversion coating formation. Cr^{VI} CC are aqueous solutions of chromic acid H_2CrO_4, chromium salts (sodium chromate Na_2CrO_4, potassium chromate K_2CrO_4 or dichromate), hydrofluoric acid HF and phosphoric acid H_3PO_4 [23]. The 2-step deposition mechanism of Cr^{VI} on HDG substrate can be described as follows:

- Anodic dissolution at anodes:

$$\mathrm{Zn} \rightarrow \mathrm{Zn}^{2+} + 2\mathrm{e}^{-} \qquad (1\text{-}1)$$

Cr^{VI} ions are very strong oxidants. Considering their concentration in the solution, the oxygen reduction and the hydrogen evolution are negligible. The reduction of Cr^{VI}, present either as CrO_4^{2-} or $Cr_2O_7^{2-}$ [27], [33], occurs from pH = 2 [23]:

- Oxidant reduction at cathodes from pH = 2:

$$\mathrm{CrO_4^{2-}} + 5\mathrm{H^+} + 3\mathrm{e^-} \rightarrow \mathrm{Cr(OH)_3} + \mathrm{H_2O} \qquad (1\text{-}2)$$

Or

$$\mathrm{Cr_2O_7^{2-}} + 8\mathrm{H^+} + 6\mathrm{e^-} \leftrightarrow \mathrm{Cr_2O_3.H_2O} + 3\mathrm{H_2O} \qquad (1\text{-}3)$$

The resulting CC thickness is about 100 nm [23]. In addition, Cr^{VI} CC are known for exhibiting a “self-healing” property in case the coating presents a defect down to the steel [23], [31], [32]. The self-healing ability of the conversion coating is built during the redox reaction occurring on the surface [32]. Indeed, as the CC is forming, Cr^{VI} ions get trapped inside the conversion layer. When a defect is created, the release of Cr^{VI} that diffuse to the defect and react with the metal substrate can form a new CC in the defect, hence provide corrosion protection.

Although Cr^{VI} CC proved their efficiency over the years, they represent a non-negligible carcinogenic, mutagenic and toxic threat [35], [36]. Legislations designed by the REACH organization (Registration, Evaluation, Authorization and Restriction of Chemicals) have required the development, and subsequent experimentation of various alternative Cr^{VI}-free CC formulations.

2.2.2. Phosphate CC

Phosphate CC (PCC) are among the most used CC for a wide range of substrates such as iron, steel, Zn, Al and Mg-based alloys [37]-[42]. The trication phosphating is the most common chemical conversion process in the automotive industry. PCC coatings exhibit thicknesses in the micrometric range. The PCC composition consists of a phosphate source, Zn cations and accelerators (NO_3^-, NO_2^- etc.) [37], [43]. Accelerators such as chlorates, nitrites or nitrates…also serve to prevent the reduction of H^+ into hydrogen gas which disturbs the phosphating process. Additional cations (Ni^{2+}, Mn^{2+} etc.) can be added to the basic formulation. While both, Mn^{2+} and Ni^{2+}, are considered to decrease the grain size of the precipitated phosphates, Ni^{2+} is expected to act as a cathode and accelerate the surface reaction during the phosphating process but seal the pores of the PCC, limiting the anodic undermining [44]-[47].

For HDG, the PCC formation mechanism is represented by the following reactions were proposed [37], [38], [48], [49]:

- Anodic dissolution:

$$Zn \rightarrow Zn^{2+} + 2e^- \tag{1-4}$$

- Cathodic reduction leading to pH increase:

$$NO_3^- + 2H^+ + 2e^- \rightarrow NO_2^- + H_2O \tag{1-5}$$

Or

$$NO_2^- + 8H^+ + 6e^- \rightarrow NH_4^+ + H_2O \tag{1-6}$$

- PCC precipitation in pH range from 4.7 to 8.5 [49]):

$$2PO_4^{3-} + 3Zn^{2+} + nH_2O \rightarrow Zn_3(PO_4)_2.nH_2O \text{ (Hopeite)} \tag{1-7}$$

In the case of a tri-cation phosphating, the reaction becomes:

$$\begin{gathered}(3-x-y)Zn^{2+} + xMn^{2+} + yNi^{2+} + 2PO_4^{3-} + zH_2O \\ \leftrightarrow Zn_{3-x-y}Mn_xNi_y(PO_4)_2.zH_2O\end{gathered} \tag{1-8}$$

A phosphate surface exhibit the presence of PCC grains as shown in the Figure 5

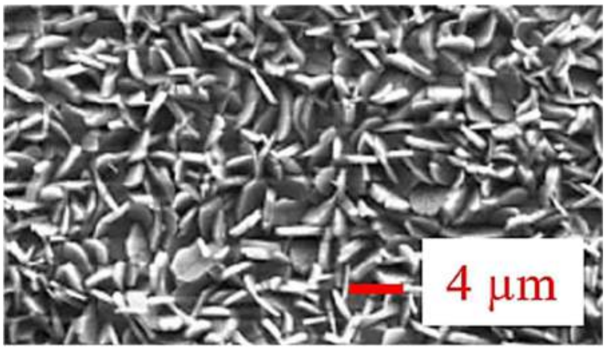

Figure 5: SEM photo of an electrogalvanized steel after 180 sec of phosphating in a ZnMnNi PCC bath [36]

To ensure a homogeneous distribution of the conversion coating on the surface, activators such as sodium titanium phosphates $Na_4TiO(PO_4)_2$ are commonly used as an activation step immediately before phosphating. The deposition mechanism of the activator on the surface is described as follows 1) particles of titanium phosphates adsorb on the surface of the metal substrate due to their low solubility and help the germination of the phosphate crystals. Then, 2) a cationic exchange between sodium and metal cations occurs that leads to the adsorption of the salt $Me_xTiO(PO_4)_2$ on the surface [50].

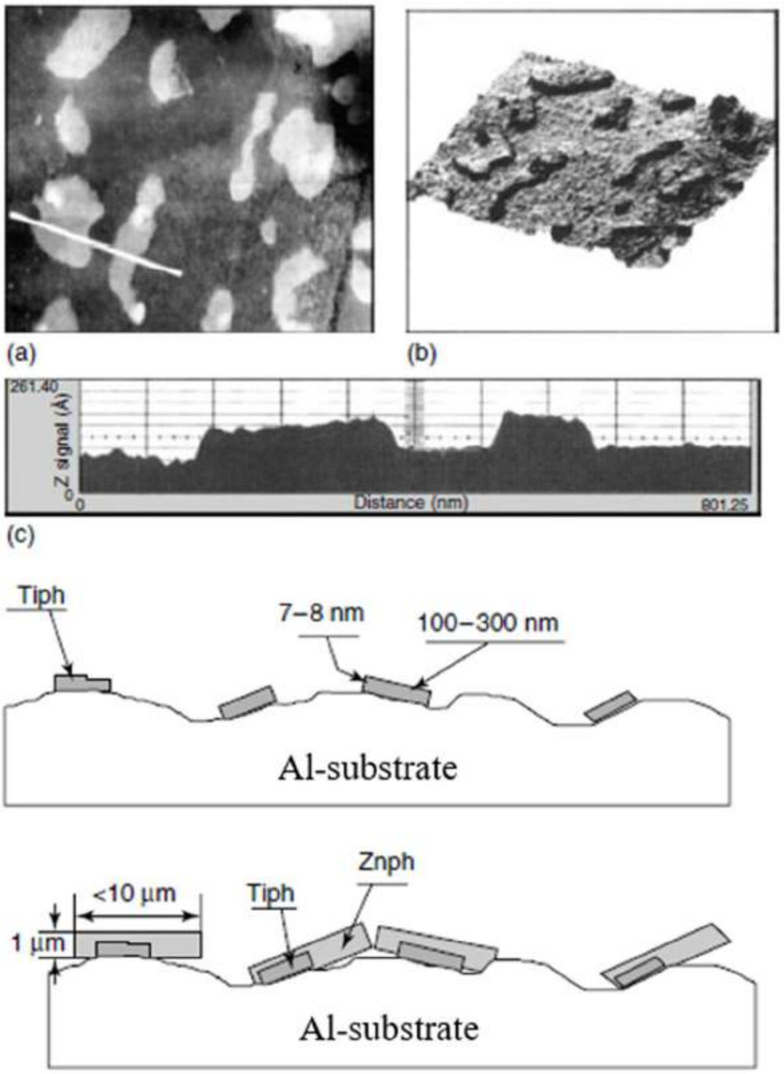

Figure 6: Germination of PCC crystals on sites with adsorbed activator [37]

The information gathered throughout the literature reported a similar behavior of the activator. Van Roy et al. demonstrated that zinc phosphate crystals preferentially nucleate on adsorbed activator particles during the PCC procedure [51]. According to Ogle et al., the activation step helps increasing the number of phosphate crystal per unit area while decreasing the crystal size, overall coating weight and minimize reaction time [37]. This interpretation was confirmed by Erbe et al. who compared the zinc phosphate distribution with and without activation step on an aluminium-silicon coated steel [52]. Indeed, they observed that the crystal size was reduced when an activation step was included in the process and that the size distribution of the crystals was more homogeneous.

Phosphating is a reliable conversion coating which does not rely on the use of Cr^{VI}. However, the trication phosphating involving the use of nickel also includes danger [53]. Indeed, nickel is also considered as a carcinogenic element but is not yet under the blow of a ban by the legislation. Alternatives are currently under development to be able to produce a conversion coating avoiding the use of Cr^{VI} and Ni.

2.2.3. Titanium and zirconium-(titanium) based conversion coatings

Titanium and zirconium-(titanium) based CC are now considered as one of the most promising alternatives to Cr^{VI} CC and PCC. These new formulations are not harmful for the health and the environment but are more complex than Cr^{VI} CC and PCC. Conversion coatings baths contain Ti and/or Zr as hexafluorotitanic acid (or hexafluorozirconic acid) H_2TiF_6/H_2ZrF_6, phosphoric acid H_3PO_4, manganese phosphate $Mn_3(PO_4)_2$, an organic phase and water [54]. It is generally assumed that thin Zr-based CC (ZrCC) and TiCC, follow a similar precipitation mechanism as they both exhibit a partial orbital-d filling (Ti: [Ar] $3d^2\ 4s^2$; Zr: [Kr] $4d^2\ 5s^2$). The coating thickness associated to TiCC and ZrCC is at nanometric scale [50]. Because of the low thickness of the TiCC/ZrCC, the chemistry of the formed CC is not fully understood yet. It has been largely admitted that the precipitation of TiCC and ZrCC leads to the formation of stable and insoluble oxides, TiO_2 and ZrO_2. However, Wilson et al. studied the formation mechanisms of TiCC on HDG coated steel and demonstrated the formation of a mixed manganese/titanium phosphate $Ti/Mn(PO_4)_x$, zinc phosphates $Zn_3(PO_4)_2$ and zinc hydroxides $Zn(OH)_2$ using FT-IRRAS and X-ray Photoelectron Spectroscopy (XPS) [55].

Similarly, as for Cr^{VI}-CC and PCC, the precipitation of TiCC on HDG is considered as a multi-step process consisting of 1) the metal substrate dissolution accompanied by local alkalization from cathodic reactions leading to 2) the CC precipitation as titanium oxide (1-9 and 1-10) at pH = 2.5 – 8.5 [24], [56].

- Anodic dissolution:

$$\mathrm{Zn} \rightarrow \mathrm{Zn}^{2+} + 2e^- \tag{1-9}$$

- Cathodic reduction leading to pH increase:

$$\mathrm{O_2} + 4\mathrm{H}^+ + 4e^- \rightarrow 2\mathrm{H_2O} \tag{1-10}$$

$$2\mathrm{H}^+ + 2e^- \rightarrow \mathrm{H_2} \tag{1-11}$$

- TiCC precipitation:

$$\mathrm{TiF_6}^{2-} + 4\mathrm{OH}^- \rightarrow \mathrm{TiO_2.H_2O} + 6\mathrm{F}^- \tag{1-12}$$

The conversion coating is reported to be composed of two different phases. The first one corresponds to the different phosphates, oxides and hydroxides while the second one refers to the organic coating flocculating with titanium oxide. The conversion of the second phase starts at pH=7 when the organic phase flocculates with titanium oxide before leading to a precipitation at pH=9 [50].

Globally, despite the various CC formulations, a common precipitation mechanism pattern exists between them. It is based on a 2-step mechanism: 1) the dissolution of the metal substrate at anodes accompanied by the oxidant reduction leading to a pH increase at cathodes and 2) the CC precipitation from a threshold pH. It makes the replacement of harmful CC such as Cr^{VI} and PCC easier. However, an evaluation of the corrosion resistance of CC is necessary to ensure their ability to replace Cr^{VI}-CC or PCC for the desired application.

3. Degradation mechanisms of painted ZnAlMg coated steels

3.1. Blistering corrosion of painted ZnAlMg coated steel with TiCC

Through natural exposure testing in an environment with a corrosivity index of C3 (for pure Zn) or C5 (for steel) according to the ISO 9223 standard, the corrosion resistance of painted ZnAlMg coated steel treated with TiCC was evaluated. After 22 months of natural exposure in a marine environment, blisters can be observed in case of a down to steel defect (Figure 7). In case of exposure in a semi-tropical environment, blisters can appear after 8 months of testing. In the framework of this PhD, blisters are associated with circled local paint decohesion which are distant from the down to steel defect and not directly with it, unlike delamination.

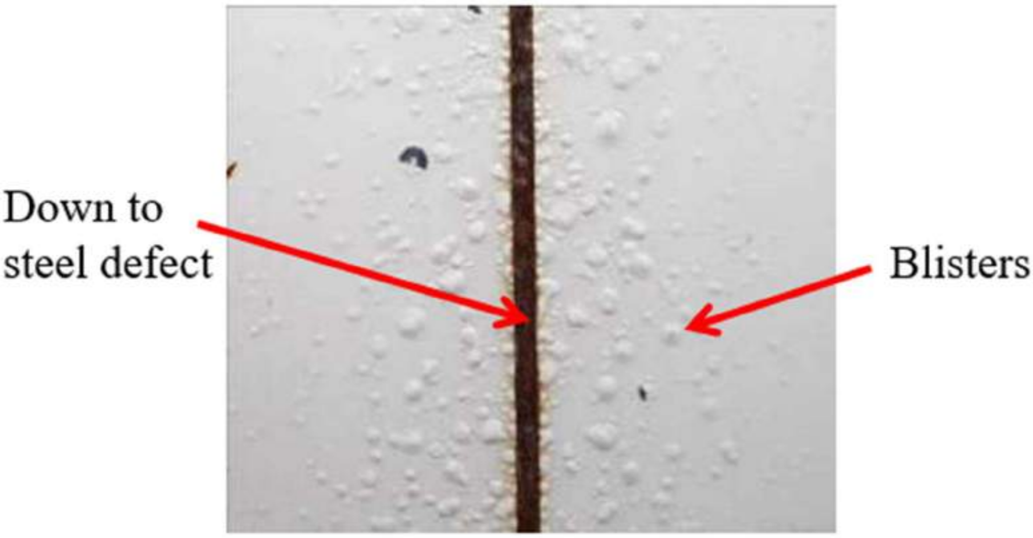

Figure 7 : Blistering around the down to steel defect after 22 months of natural exposure in a marine environment

The blistering corrosion has already been discussed in the literature [57]-[59] but no study reported the case of blistering occurring only if the defect goes down to the steel.

3.2. General blistering degradation mechanisms

Different mechanisms have been described in the literature to explain the coating disbondment on metallic substrate ([60]-[64]) Mechanisms taking place near the defect will participate in the delamination development while degradation mechanisms occurring away from the defect will enable blisters growth.

3.2.1. Anodic and cathodic delamination

Anodic delamination

Anodic delamination is observed when a ZnAlMg coated steel, painted or not, exhibits a down to steel scratch. Indeed, when an electrolyte gets in contact with ZnAlMg and the steel, a galvanic coupling is defined between the two metals. It will lead to the preferential dissolution of the zinc-based coating as its own galvanic potential is lower than the steel one:

Table 2: Standard electrochemical potential (V vs. SHE) in 1M NaCl, 25 °C, 1 atm [65]

	Electrochemical potential standard (V vs. SHE)
$Zn \leftrightarrow Zn^{2+} + 2e^-$	-0.76 ± 0.01
$Fe \leftrightarrow Fe^{2+} + 2e^-$	-0.44 ± 0.01

The contact between the two metals will induce an increase of the dissolution rate of zinc and a decrease of the iron one compared to the dissolution rate they have when they are not in contact with each other. This way, the zinc gets sacrificially consumed to protect the steel. The dissolution of the sacrificial coating creates paint delamination as shown in Figure 8.

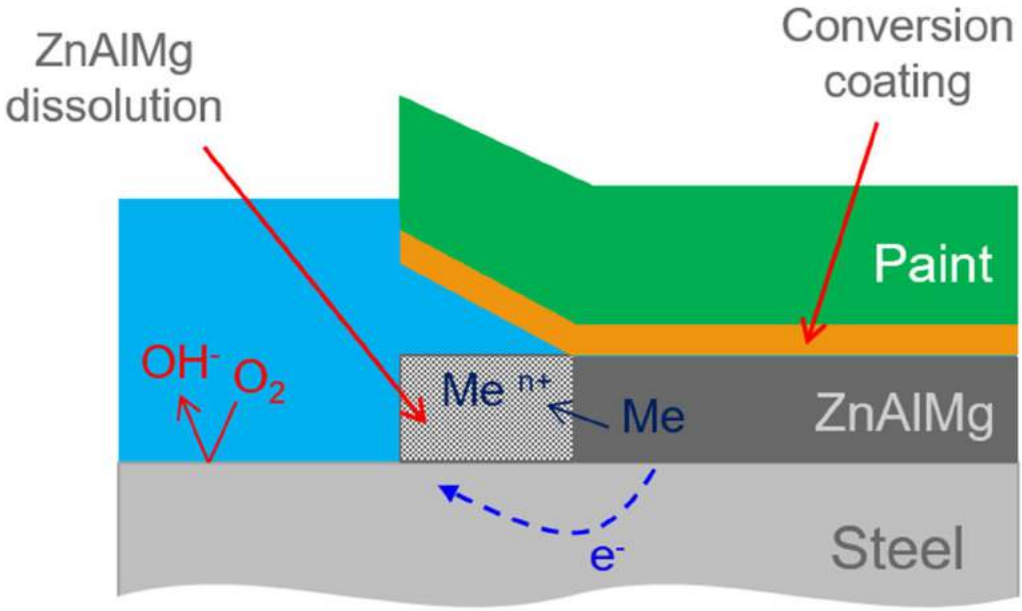

Figure 8: Anodic delamination mechanism

In a neutral environment, the corrosion rate is defined by the cathodic reaction which is the oxygen reduction. The corrosion mechanism is the following:

- Anodic dissolution of the metal:

$$\mathrm{Me} \rightarrow \mathrm{Me}^{n+} + n e^{-} \quad (1\text{-}13)$$

- Oxygen reduction at the cathode:

$$\frac{1}{2} O_2 + H_2O + 2e^{-} \rightarrow 2OH^{-} \quad (1\text{-}14)$$

The anodic delamination is also characteristic of a strong interface between the ZnAlMg and the paint. Indeed, the conversion coating is not affected by the dissolution and is adherent on the paint when delamination starts [60]-[61]. After paint removal, the coating is supposed to be located on the paint side.

For painted ZnAlMg steel with a down to steel defect, the anodic delamination takes place close to the defect, where the electrolyte is in contact with the steel and creates the galvanic coupling. Simultaneously, at the delamination front, the cathodic delamination is predominant.

Cathodic delamination:

The paint delamination results from a local alkalization of the media leading to the destruction of the interface between the polymer and the metal hence an electrolyte inflow. At the front delamination, the metal potential is more cathodic than closer to the defect. A galvanic coupling is created between the metal substrate located at the delamination front and the metal closer to the defect. In the confined zone, the oxygen concentration brought in by the electrolytic inflow is lower than near the scratch. In addition, corrosion products form a natural barrier that slows chlorides and hydroxyl ions from reaching the delamination front. At the delamination front, the pH evolution is governed by buffering reactions, diffusion rates of reactants to the front and hydroxyl ions, oxygen reduction rate and volume of liquid trapped under the paint [60]-[61]. The initiated oxydo-reduction reactions are described here after (Figure 9):

- Anodic dissolution close to the defect ("open area"):

$$\mathrm{Me} \rightarrow \mathrm{Me}^{n+} + \mathrm{ne}^{-} \tag{1-15}$$

- Oxygen reduction at the delamination front ("confined zone"):

$$\frac{1}{2}\mathrm{O}_2 + \mathrm{H}_2\mathrm{O} + 2\mathrm{e}^{-} \rightarrow 2\mathrm{OH}^{-} \tag{1-16}$$

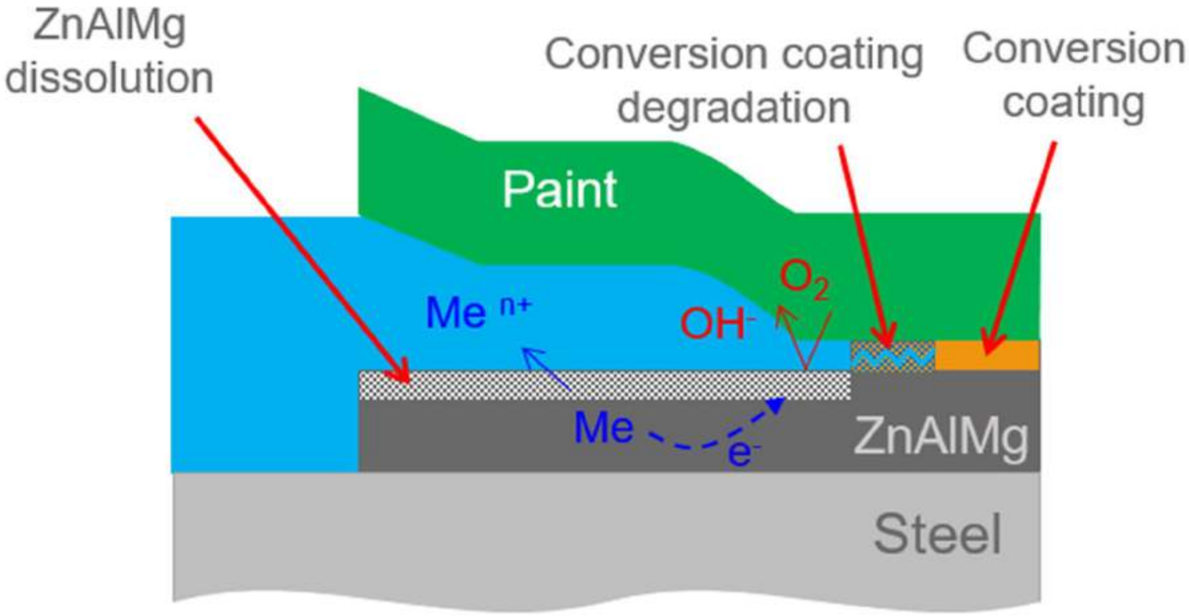

Figure 9: Cathodic delamination mechanism

Although a system exhibiting a scratch down to the steel will facilitate the incorporation of water through the scratch, water can also flow in through the paint which acts as a semi-permeable membrane [60]-[61] hence also leading to blistering.

3.2.2. Osmotic blistering

The driving force of the blistering formation is the concentration gradient of soluble products under the paint and the atmosphere [57], [66]. Indeed, polymers can be described as a semi-permeable membrane which allows water to flow in through the paint toward the coating and the substrate. If soluble products are present between the paint and the substrate, the penetration of water will lead to an under-paint solution with a high soluble products concentration. The dilution of the highly concentrated solution is the equilibrium the system will tend to reach. A water uptake through the paint will lead to the growth of blisters. Water soluble products can be of very different nature (inorganic salts, corrosion products, water soluble solvent traces etc) and be incorporated inside the structure in each step of the manufacturing of painted steels, but also during their period of use as corrosion products can form. It has been reported that the concentration of corrosion products is a more prevailing parameter in blister formation than the presence of these products themselves at the paint/substrate interface. It means that soluble products are very likely to be found one way or another under paint but the concentration they reach is a more important parameter to be considered [59].

One must also keep in mind that a lot of other parameters will influence the blistering ability of a painted material. Indeed, the CC and paint application modes and the internal stress induced from the paint application can be linked with the severity of blistering [62], [67], [68]. However, these other aspects will not be further detailed in this literature survey.

3.2.3. Cathodic blistering

The corrosion mechanism leading to cathodic blistering is similar to the cathodic delamination. The production of hydroxyl ions is responsible for the metal/polymer interface destruction. The blistering development can be described according to Figure 10.

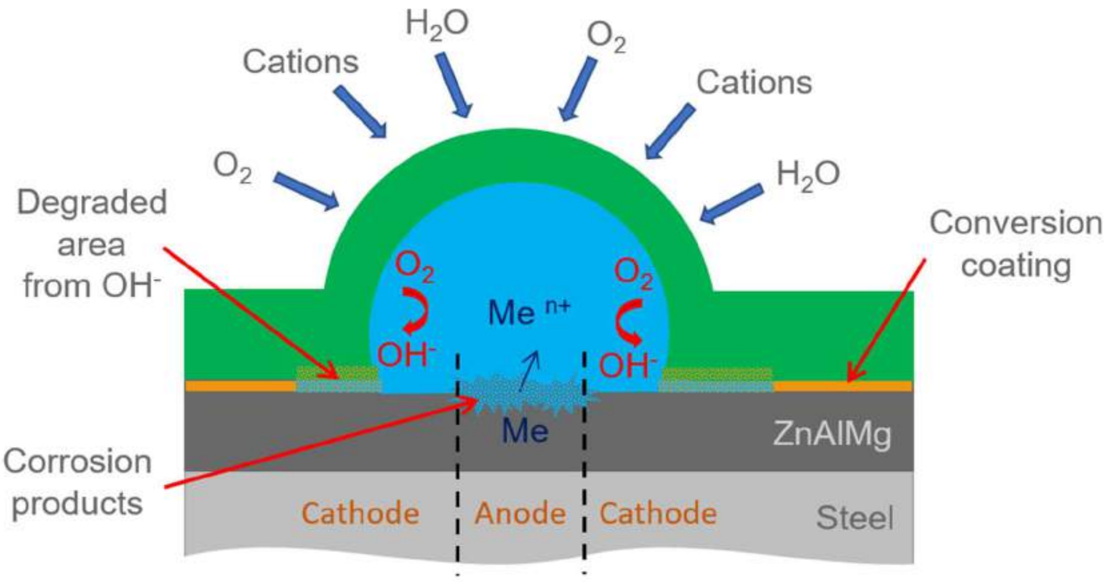

Figure 10: Scheme of the cathodic blistering mechanism

Water, oxygen and cations diffuse through the paint in absence of a defect. Under the blister, cathodic and anodic regions are well defined. The metal dissolution takes place at the center of the blister. The cathodic regions are located in the outer part of the blister where the oxygen is more easily renewed [60]-[61].

3.2.4. Mechanical blistering

The mechanical blistering is related to the production of corrosion products which will put pressure at the metal/polymer interface until the coating disbondment is initiated [60].

Publication focusing on the comprehension of the degradation mechanisms of painted metallic substrates showed that a weakness at the interface between the metal and the polymer is required for the corrosion to propagate [57], [58], [66].

4. Interface weakness of multiphase substrates treated with CC

The formation of blisters was not reported for painted HDG coated steels treated with TiCC. In addition, the blistering issue is not observed for painted ZnAlMg treated with PCC. The blistering evidences the lack of adherence and corrosion resistance of painted ZnAlMg coated steels treated with TiCC.

In addition, a ZnAlMg multiphase substrate can induce the galvanic coupling between phases hence impact the CC deposition mechanism.

Lostak et al. described the deposition mechanism of a ZrCC on a ZnAlMg substrate composed of a zinc rich-phase, aluminium rich-phase and a eutectic Zn-$MgZn_2$ with EDS, AFM and SKPFM [69]. They reported that a heterogeneous ZrCC precipitation was taking place on all phases. The zinc-rich phase was found to be the most noble and exhibited the highest surface coverage rate while alloyed Zn-Zn_2Mg and Al-rich phases were less covered in comparison. They proposed that the heterogeneous precipitation was linked to the ratio of Zn exposed during the CC procedure. The coverage of alloyed phases was initiated after the anodic dissolution of Mg-rich and Al-rich phases respectively leading to a sufficient enrichment of exposed Zn for the CC to start.

Similar observations were made on different substrates exhibiting a galvanic coupling inside the microstructure.

Andreatta et al. [70] studied the effect of the microstructure of AA6016 alloy on the formation of Zr-TiCC using SEM-EDS, SKPFM and electrochemical measurements. They observed that the CC was preferentially formed on cathodic Al(Fe, Mn)Si intermetallics contained in the alloy. Nordlien et al. and Lunder et al. [71], [72] draw a comparable observation when evaluating the Zr-TiCC distribution on AA6060 with SEM-EDS, GD-OES and TEM. They concluded that the precipitation of the Zr-TiCC was taking place on and around cathodic α-Al(Fe,Mn)Si intermetallics first.

Interesting solutions have been investigated to improve coating thickness and homogeneity. Lostak et al. tested the addition of $Cu^{2+/}Fe^{3+}$ ions to the CC bath to enable the precipitation of finely distributed Cu/Fe cathodes on HDG surface [73]. It led to a CC film thickness increase due to the enhanced precipitation kinetics.

Regarding PCC, we did not see any communication about the heterogeneous distribution of PCC on multiphase Zn or Al based substrates. It evidences the satisfying PCC distribution and corrosion resistance performance on these substrates. One work related to the impact of the microstructure of a die-cast AZ91D alloy on the Mn PCC distribution was carried out by Zhou et al [74]. They proposed that cathodic β phase of the alloy was first covered by flower-like phosphate nuclei at the expense of the anodic primary α phase. The resulting Mn PCC morphology was amorphous.

Conclusions of the State of the Art

As mentioned here above, different contributions and phenomena are simultaneously occurring on painted ZnAlMg coated steels during the corrosion process and several parameters are required for the blister formation.

In addition, the literature has evidenced the link between the blistering phenomenon and the interface metal/polymer weakness hence setting the focus on the CC. The impact of a multiphase substrate on the formation of TiCC or ZrCC has already been reported for various types of substrates. However, little information is available about the effect of multiphase substrates on the formation of PCC. It raises the following questions which will be addressed through this PhD thesis:

- **What are the origin and degradation mechanisms leading to blistering corrosion of painted ZnAlMg coated steels treated with TiCC?**
- **Is there an effect of the microstructure on PCC coating formation on ZnAlMg coated steel? Can it impact the coating performance?**
- **Is the TiCC distribution related to ZnAlMg microstructure on painted ZnAlMg coated steels?**
- **If so, how to overcome the impact of ZnAlMg microstructure to obtain a homogenized TiCC distribution with improved corrosion resistance performance?**

References

[1] S. Schuerz, M. Fleischanderl, G.H. Luckeneder, K. Preis, T. Haunschmied, G. Mori, A.C. Kneissl, Corrosion behaviour of Zn–Al–Mg coated steel sheet in sodium chloride-containing environment, Corros. Sci., 51 (2009) 2355-2363.

[2] M. Dutta, A. K. Halder, S. B. Singh, Morphology and properties of hot dip Zn–Mg and Zn–Mg–Al alloy coatings on steel sheet, Surf. Coat. Technol., 205 (2010) 2578-2584.

[3] R. P. Edavan, R. Kopinski, Corrosion resistance of painted zinc alloy coated steels, Corros. Sci., 51 (2009) 2429-2442.

[4] H.-K. Sohn, J-W. Lee, Y. Yoo, J. Min, K.Y. Kim, Corrosion behaviour of Zn-MgZn2 eutectic structure in Zn-Al-Mg coatings, Galvatech ’11, Genova, Italy

[5] Brochure of Nisshin steel, ‘Nisshin steel quality products ZAM’. [Online]. Available: http://www.nisshin-steel.co.jp/en/products/pdf/zam.pdf. [Accessed on 02/03/2018]

[6] Brochure of ThyssenKrupp Steel Europe AG, ZM EcoProtect® - The Innovative Coating, 2010. [Online]. Available: www.thyssenkrupp-steel-europe.com. [Accessed on 02/03/2018].

[7] N. Shimoda, Y. Kubo, K. Ueda, Corrosion resistance of several Zn-Al-Mg alloys coated steels, Nippon Steel & Sumitomo metal 108, 2015.

[8] D. Thierry, T. Prosek, N. Le Bozec, E. Diller, Corrosion protection and corrosion mechanisms of continuous galvanized steel sheet with focus on new coating alloys, Galvatech ‘11, Genova, Italy

[9] Tata Steel, MagiZinc® - The innovative metallic coating for pre-finished steel. 2012.

[10] User manual, Organic coated steel, ArcelorMittal Flat Carbon Europe 19, avenue de la Liberté L-2930 Luxembourg.

[11] User manual, Metallic coated steel, ArcelorMittal Flat Carbon Europe 19, avenue de la Liberté L-2930 Luxembourg.

[12] C. Commenda, J. Pühringer, Microstructural characterization and quantification of Zn–Al–Mg surface coatings, Mater. Charact., 61 (2010) 943-951.

[13] M. Salgueiro Azevedo, Mécanismes de corrosion de l’acier revêtu d’alliage à base de ZnAlMg en tests accélérés et en environnement naturel, PhD thesis, Université Pierre et Marie Curie, Paris, 2014.

[14] P. Volovitch, C. Allely, K. Ogle, Understanding corrosion via corrosion product characterization: I. Case study of the role of Mg alloying in Zn–Mg coating on steel, Corros. Sci., 51 (2009) 1251-1262.

[15] G. Luckeneder, M. Fleischanderl, T. Steck, K-H. Stellnberger, J. Faderl, Corrosion mechanisms and cosmetic corrosion aspects of zinc-aluminium-magnesium and zinc chromium alloy coated steel strip, Galvatech ’11, Genova, Italy

[16] M. Salgueiro Azevedo, C. Allély, K. Ogle, P. Volovitch, Corrosion mechanisms of Zn(Mg,Al) coated steel: 2. The effect of Mg and Al alloying on the formation and properties of corrosion products in different electrolytes, Corros. Sci., 90 (2015) 482-490.

[17] T. Tsujimura, A. Komatsu, A. Andoh, Influence of Mg content in coating layer and coating structure on corrosion resistance of hot-dip Zn–Al–Mg–Si alloy coated steel sheet, Proceedings of the Galvatech ’01, Brussels, Belgium

[18] J. Kawafuku, J. Katoh, M. Toyama, K. Ilkeda, H. Nishimoto, H. Sato, Properties of zinc alloy coated steel sheets obtained by continuous vapour deposition pilotline, Proceedings of the 5th Automotive Corr. & Prevention Conference, Michigan, United States, October 21–23, 1991.

[19] H. Dafydd, D. A. Worsley, H. N. McMurray, The kinetics and mechanism of cathodic oxygen reduction on zinc and zinc–aluminium alloy galvanized coatings, Corros. Sci., 47 (2005) 3006-3018.

[20] N.C. Hosking, M.A. Strom, P.H. Shipway, C.D. Rudd, Corrosion resistance of zinc–magnesium coated steel, Corros. Sci. 49 (2007) 3669–3695

[21] K. Ueda, A. Takahashi, Y. Kubo, Investigation of corrosion resistance of pre-painted Zn-11%Al-3%Mg-0,2%Si alloy coated steel sheet through outdoor exposure test in Okinawa, Galvatech ‘11, Genova, Italy

[22] P. Volovitch, T. N. Vu, C. Allély, A. Abdel Aal, K. Ogle, Understanding corrosion via corrosion product characterization: II. Role of alloying elements in improving the corrosion resistance of Zn–Al–Mg coatings on steel, Corros. Sci., 53 (2011) 2437-2445.

[23] P. L. Hagans, C. M. Haas, Chromate Conversion Coatings, 5 (1994) 405-411.

[24] I. Milosev, G. S. Frankel, Review—Conversion Coatings Based on Zirconium and/or Titanium, J. Electrochem. Soc., 165 (2018) C127-C144.

[25] N. K. Akafuah, S. Poozesh, A. Salaimeh, G. Patrick, K. Lawler, K. Saito, Evolution of the Automotive Body Coating Process—A Review, Coatings, 24 (2016) 1-22.

[26] T. S. N. Sankara Narayanan, Surface pretreatment by phosphate conversion coatings_ a review, Rev.Adv. Mater. Sci, 9 (2005) 130-177.

[27] Pourbaix, Atlas d'équilibres électrochimiques à 25°C, Gauthier-Villar. Paris, 1963.

[28] S. Mathieu, R. Hellouin, Techniques de l'ingénieur, tôles prélaquées, (2008) 1-13.

[29] A. A. O. Magalhães, B. Tribollet, O. R. Mattos, I. C. P. Margarit, O. E. Barcia, Chromate Conversion Coatings Formation on Zinc Studied by Electrochemical and Electrohydrodynamical Impedances, J. Electrochem. Soc., 150 (2003) B16–B25.

[30] X. Zhang, C. Van den Bos, W. G. Sloof, A. Hovestad, H. Terryn, J. H. W. de Wit, Comparison of the morphology and corrosion performance of Cr(VI)- and Cr(III)-based conversion coatings on zinc, Surf. Coat. Technol., 199 (2005) 92–104.

[31] P. Campestrini, E. P. M. van Westing, J. H. W. de Wit, Influence of surface preparation on performance of chromate conversion coatings on Alclad 2024 aluminium alloy: Part I: Nucleation and growth, Electrochim. Acta, 46 (2001) 2553–2571.

[32] S. A. Kulinich, A. S. Akhtar, D. Susac, P. C. Wong, K. C. Wong, K. A. R. Mitchell, On the growth of conversion chromate coatings on 2024-Al alloy, Appl. Surf. Sci., 253 (2007) 3144–3153.

[33] G. M. Brown, K. Shimizu, K. Kobayashi, G. E. Thompson, G. C. Wood, The morphology, structure and mechanism of growth of chemical conversion coatings on aluminium, Corros. Sci., 33 (1992) 1371-1385.

[34] S. Pommiers-Belin, J. Frayret, A. Uhart, J. Ledeuil, J.-C. Dupin, A. Castetbon, M. Potin-Gautier, Determination of the chemical mechanism of chromate conversion coating on magnesium alloys EV31A, Appl. Surf. Sci., 298 (2014) 199-207.

[35] Ocupational Safety and Health Administration, Occupational Safety and Health Standards - Toxic and Hazardous Substances, United States Department of Labor. [Online]. Available on: https://www.osha.gov/pls/oshaweb/owadisp.show_document?p_table=STANDARDS&p_id=13117. [Accessed on: 09/08/2018].

[36] European Chemicals Agency, Substances restricted under REACH, ECHA, 2006. [Online]. Available on: https://echa.europa.eu/substances-restricted-under-reach/-/dislist/details/0b0236e1807e2bc1. [Accessed on: 09/08/2018].

[37] K. Ogle, R. Buchheit, Conversion Coatings, in: A.J. Bard, M. Stratmann, J. Frankel (Eds.), Encyclopedia of Electrochemistry, 4, Corrosion and Oxide Films, Wiley-VCH, (2003), 460-495.

[38] K. Ogle, M. Wolpers, Phosphate conversion coatings, in: S.D. Cramer, B.S. Covino (Eds.), ASM Handbook, 13A, Corrosion: Fundamentals, Testing, and Protection, ASM International, (2003) 712-719.

[39] L. Jiang, P. Volovitch, M. Wolpers, K. Ogle, Activation and inhibition of Zn–Al and Zn–Al–Mg coatings on steel by nitrate in phosphoric acid solution, Corros. Sci., 60 (2012) 256–264.

[40] K. S. Fernandes, E. de A. Alvarenga, P. R. G. Brandão, V. de F. C. Lins, Análise por espectroscopia no infravermelho das camadas de fosfato de zinco e de zinco modificado com níquel e manganês em aço eletrogalvanizado, Rem Rev. Esc. Minas. 64 (2011) 45–49.

[41] W. Zhou, D. Shan, E.-H. Han, W. Ke, Structure and formation mechanism of phosphate conversion coating on die-cast AZ91D magnesium alloy, Corros. Sci., 50 (2008) 329–337.

[42] A. Losch, E. Klusmann, J. Schulze, Electrochemical investigations of phosphate layers by metal deposition and cataphoretic painting, Electrochim. Acta., 39 (1994) 1183–1187.

[43] J. Donofrio, Zinc phosphating, Met. Finish., 108 (2010) 40–56.

[44] A. S. Akhtar, K. C. Wong, K. A. R. Mitchell, The effect of pH and role of Ni^{2+} in zinc phosphating of 2024-Al alloy: Part I: Macroscopic studies with XPS and SEM, Appl. Surf. Sci. 253 (2006) 493–501.

[45] A. S. Akhtar, D. Susac, P. C. Wong, K. A. R. Mitchell, The effect of pH and role of Ni^{2+} in zinc phosphating of 2024-Al alloy: Part II: Microscopic studies with SEM and SAM, Appl. Surf. Sci. 253 (2006) 502-509.

[46] A. S. Akhtar, K. C. Wong, P. C. Wong, K. A. R. Mitchell, Effect of Mn^{2+} additive on the zinc phosphating of 2024-Al alloy, Thin Solid Films. 515 (2007) 7899-7905.

[47] D. Zimmermann, A. G. Muñoz, J. W. Schultze, Formation of Zn–Ni alloys in the phosphating of Zn layers, Surf. Coat. Technol. 197 (2005) 260–269.

[48] M. Wolpers, J. Angeli, Activation of galvanized steel surfaces before zinc phosphating - XPS and GD-OES investigations, Appl. Surf. Sci. 179 (2001) 281–291.

[49] L. Jiang, Application of atomic emission spectroelectrochemistry to the formation and degradation of conversion coatings on galvanized steel (Zn and Zn-Al-Mg)', PhD thesis, Université Pierre et Marie Curie, Paris, 2012.

[50] S. Le Manchet, Mécanismes de corrosion et de délamination d'un composite acier/polymère pour le marché automobile. Université de Technologie de Compiègne : PhD Thesis., Université de Technologie de Compiègne, Compiègne, 2010.

[51] I. Van Roy, H. Terryn, G. Goeminne, Study of the phosphating treatment of aluminium surfaces: role of the activating process, Colloids Surf. Physicochem. Eng. Asp., 136 (1998) 89-96.

[52] A. Erbe, P. Schneider, C. Gadiyar, F. U. Renner, Electrochemically triggered nucleation and growth of zinc phosphate on aluminium-silicon-coated steel, Electrochim. Acta, 182, (2015) 1132-1139.

[53] INRS, Nickel et ses oxydes - Fiche toxicologique N°68, 2009. [Online]. Available on: http://www.inrs.fr/publications/bdd/fichetox/fiche.html?refINRS=FICHETOX_68. [Accessed on: 16/05/2017].

[54] Henkel, Composition and process for treating metals, Patent 5427632. 1995.

[55] B. Wilson, N. Fink, G. Grundmeier, Formation of ultra-thin amorphous conversion films on zinc alloy coatings: Part 2: Nucleation, growth and properties of inorganic–organic ultra-thin hybrid films, Electrochim. Acta, 51 (2006) 3066-3075.

[56] L. Li, B. W. Whitman, G. M. Swain, Characterization and performance of a Zr/Ti pretreatment conversion coating on AA2024-T3, J. Electrochem. Soc., 162 (2015) C279-C284.

[57] E. Petrie, Osmotic blisters in coatings and adhesives, Met. Finish., (2011) 28–30.

[58] B. Liu, Y. Wei, W. Chen, L. Hou, C. Guo, Blistering failure analysis of organic coatings on AZ91D Mg-alloy components, Eng. Fail. Anal., 42 (2014) 231-239.

[59] M. Doherty, J. M. Sykes, A quantitative study of blister growth on lacquered food cans by scanning acoustic microscopy, Corros. Sci., 50 (2008) 2755-2772.

[60] A. Amirudin, D. Thierry, Corrosion mechanisms of phosphated zinc layers on steel as substrates for automotive coatings, Prog. Org. Coat., 28 (1996) 59-76.

[61] P. Marcus, Corrosion Mechanisms in Theory and Practice. CRC Press, 2011.

[62] T. Prosek, A. Nazarov, M.-G. Olivier, C. Vandermiers, D. Koberg, D. Thierry, The role of stress and topcoat properties in blistering of coil-coated materials, Prog. Org. Coat., 68 (2010) 328-333.

[63] W. Funke, Toward a unified view of the mechanism responsible for paint defects by metallic corrosion, Ind. Eng. Chem. Prod. Res. Dev., 24 (1985) 343-347.

[64] H. Leidheiser, Towards a Better Understanding of Corrosion beneath Organic Coatings, Corrosion, 39 (1983) 189-201.

[65] D. C. Harris, Quantitative chemical analysis, W.H. Freeman and Company. New-York, 2007.

[66] D. Greenfield, D. Scantlebury, The protective action of organic coatings on steel: A review, J. Corros. Sci. Eng., 3 (2000).

[67] D. Perera, Physical ageing of organic coating, Prog. Org. Coat., 47 (2003) 61–76.

[68] M. Piens, H De Deurwaerder, Effect of coating stress on adherence and corrosion prevention, Prog. Org. Coat., 43 (2001) 18–24.

[69] T. Lostak, A. Maljusch, B. Klink, S. Krebs, M. Kimpel, J. Flock, S. Schulz, W. Schuhmann, Zr-based conversion layer on Zn-Al-Mg alloy coated steel sheets: insights into the formation mechanism, Electrochim. Acta, 137 (2014) 65-74.

[70] F. Andreatta, A. Turco, I. de Graeve, H. Terryn, J. H. W. de Wit, L. Fedrizzi, SKPFM and SEM study of the deposition mechanism of Zr/Ti based pre-treatment on AA6016 aluminium alloy, Surf. Coat. Technol., 201 (2007) 7668-7685.

[71] J. H. Nordlien, J. C. Walmsley, H. Østerberg, K. Nisancioglu, Formation of a zirconium-titanium based conversion layer on AA 6060 aluminium, Surf. Coat. Technol., 153 (2002) 72-78.

[72] O. Lunder, C. Simensen, Y. Yu, K. Nisancioglu, Formation and characterisation of Ti–Zr based conversion layers on AA6060 aluminium, Surf. Coat. Technol., 184 (2004) 278-290.

[73] T. Lostak, S. Krebs, A. Maljusch, T. Gothe, M. Giza, M. Kimpel, J. Flock, S. Schulz, Formation and characterization of Fe^{3+}-/Cu^{2+}-modified zirconium oxide conversion layers on zinc alloy coated steel sheets, Electrochim. Acta, 112 (2013) 14-23.

[74] W. Zhou, D. Shan, E.-H. Han, W. Ke, Structure and formation mechanism of phosphate conversion coating on die-cast AZ91D magnesium alloy, Corros. Sci., 50 (2008) 329-337.

Chapter 2: Materials and Methods

From the literature review displayed in Chapter I – State of the art, different techniques were employed to understand the degradation mechanisms of painted ZnAlMg coated steels and the formation mechanisms of conversion coatings on ZnAlMg. On one hand, degradation mechanisms of conversion coatings were investigated using SKP, LEIM and current imposed dissolution. On the other hand, the comprehension of conversion coatings precipitation mechanisms was carried out through 2 complementary approaches. First, the distribution of conversion coating elements on ZnAlMg phases was determined using Scanning Electronic Microscopy (SEM) and Energy Dispersive Spectroscopy (EDS). The overall coating thickness on ZnAlMg was measured using GD-OES (Glow-Discharge Optical Emission Spectroscopy) while the conversion coating thickness on each ZnAlMg phases was measured with Auger Electron Spectroscopy (AES). The GD-OES technique was also used to evaluate the position of the TiCC elements as a function of depth. In complement, Open Circuit Potential (OCP) measurements and anodic/cathodic polarizations were performed on pure phases simulating ZnAlMg microstructure to confirm the TiCC precipitation mechanism on the ZnAlMg surface.

Second, The TiCC composition and concentration after immersion of the model ZnAlMg coating and pure phases in the TiCC bath were studied by X-ray Photoelectron Spectroscopy (XPS).

The objective of this chapter is to give an overview of materials and techniques used in this work. The reason of their use will be explained. Details and specific parameters of measurements are given in the experimental section of the respective result chapters.

1. Materials

HDG and ZnAlMg materials were provided by an ArcelorMittal industrial line whose production is dedicated to the pre-painted market. Various ZnAlMg modalities containing 0-5 wt. % of Al and 0-3 wt. % of Mg. Industrial hot dip galvanizing process (Appendix 1) was used to prepare ZnAlMg materials based on the process described in the WO 2013/160567 AI patent [1].

Phases identified in model coatings microstructure are listed in the Table 3. Further details about ZnAlMg coatings microstructure is available in Appendix 2.

Pure metals were supplied by Goodfellow and the other phases were synthesized in collaboration with the University of Chemistry and Technology of Prague in Czech Republic (UCT Prague). Details on fabrication process are given in Chapter IV, V and VI. In addition, complementary information regarding pure phases microstructure is gathered in Appendix 3.

Table 3: Phases weight and molar composition and supplier

Phases	Composition / wt. %	Supplier
Al	≈ 100	GoodFellow
Zn(Al)	-	UCT Prague
Zn_2Mg	84(Zn) 16(Mg)	UCT Prague

2. Characterization of phases after corrosion

Different characterization techniques were used to obtain complementary information. Scanning Electronic Microscopy (SEM) coupled with EDS, Energy Dispersive Spectroscopy [2], [3], was used to verify the presence or absence of CC on ZnAlMg coatings or corrosion products on painted ZnAlMg coated steels. It wa also used to check the surface state as well as to obtain a first idea of the elemental composition of the observed phase or CC. For semi quantitative elemental analysis, 15 keV acceleration tension was used. In order to reduce electronic interaction volume EDS measurement were also made at 5keV. Depth penetration of electrons (R) can be calculated with Kanaya-Okayama Formula [4] (obtained from Bethe Formula [5]):

$$R = \frac{0.0276\, A\, E_0^n}{(Z^{0.89}\, \rho)} \tag{2-1}$$

where R is the depth penetration, A is the Atomic Weight (g/mole), n is a constant (=1.68), E_0 is the electron beam energy (keV), Z is the atomic number and ρ is the density (g/cm^3). This equation applied to pure Zn-based substrate gives R ~ 1.2 µm at 15 keV and R ~ 180 nm at 5keV.

3. Conversion coating distribution determination

Auger Emission Spectroscopy (AES) was also used to evaluate elemental concentrations of TiCC on ZnAlMg surfaces and can be used to obtain chemical state information from ZnAlMg surfaces after TiCC treatment. In association with Ar^+ sputtering, a depth distribution evaluation of the TiCC on each phase of ZnAlMg coatings was performed thanks to the high spatial resolution achievable with AES (≈ 10 nm). Using this technique, quantitative elemental information can also be calculated.

The AES principle is based on the Auger effect and schematized in Figure 11 [6]. A high energy electron beam (2-10 keV) is used to ionize the sample surface. A core level electron is then ejected creating an inner-shell vacancy on the L_3 level as visible on Figure 11. To fill in the energy gap on that level, a higher energy electron is transferred from the M_1 level to the L_3 one. The released energy causes the emission of an Auger electron from the $M_{2,3}$ level.

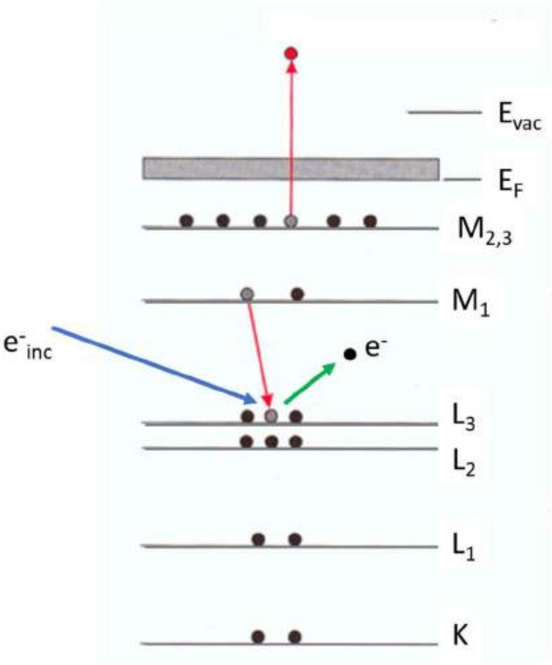

Figure 11: Auger electron emission principle in AES

Auger electrons are collected by an electron energy analyzer which measures the kinetic energy of the emitted Auger electrons based on the following equation:

$$E_{ka} = E_{L3} - E_{M1} - E_{M2,3} \quad (2\text{-}2)$$

Where E_{ka} is the kinetic energy of an Auger electron, E_{L3} the energy of the L3 level, E_{M1} the energy of the M1 one and $E_{M2,3}$, the energy level of the M2,3 level.

4. Conversion coating chemical composition evaluation

X-ray photoelectron spectroscopy (XPS), is a characterization tool used for extreme surface analysis (5 - 10 nm) [7]. It gives access to the composition of the TiCC as well as the oxidation state of the element present on the surface. The principle relies on the irradiation of the sample with an X-ray beam generated by an electron gun bombarding a metallic target.

From the photon irradiation, the atoms of the sample surface are ionized by a photoelectric effect. The excited atoms will emit photoelectrons during their relaxation and their kinetic energy E_k is measured. According to Einstein's relation, the characteristic binding energy E_b can be calculated:

$$E_b = \mathrm{h\nu} - (E_k + \phi) \quad (2\text{-}3)$$

where $h\nu$ is the energy of the photon from the X-ray source and ϕ the energy required to extract the electron from vacuum which depends on the spectrometer (considered as negligible for the calculations). XPS can be used to determine the surface composition, evaluate elements and contamination concentrations quantitatively but also the chemical state of elements and their local bonding environment.

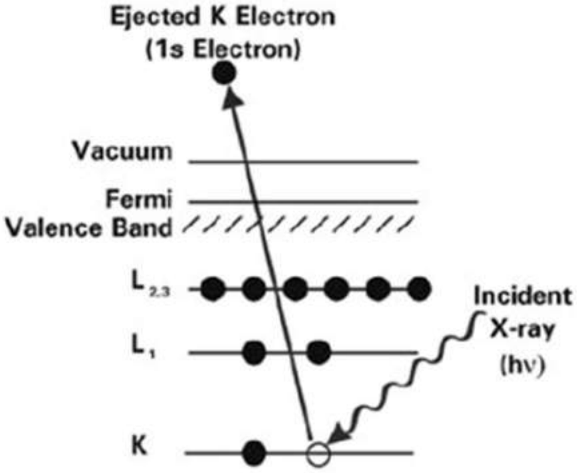

Figure 12: Principle of X-ray photoelectron spectroscopy [7]

5. Conversion coating thickness measurement

GD-OES (Glow-Discharge Optical Emission Spectroscopy) in association with DiP (Differential interferometry Profiling) operation was used to perform elemental depth profiles of the TiCC on a ZnAlMg surface and evaluate its thickness. Samples are exposed to a plasma in a primary vacuum chamber, slowly sputtered by argon ions and neutral species accelerated into the plasma. The extracted elements are then excited by the plasma and will, in return, emit a characteristic photon out of which the wavelength can be calculated using Max Planck's equation [8]:

$$E = \frac{hc}{\lambda} \tag{2-4}$$

where E is the photon energy, h the Planck's constant (h = 3.336 x 10^{-11} s.cm^{-1}), c the speed light (X) and λ the wavelength.

From this technique it is possible to identify the nature of the material, perform quantification and determine the elemental depth distribution (Figure 13).

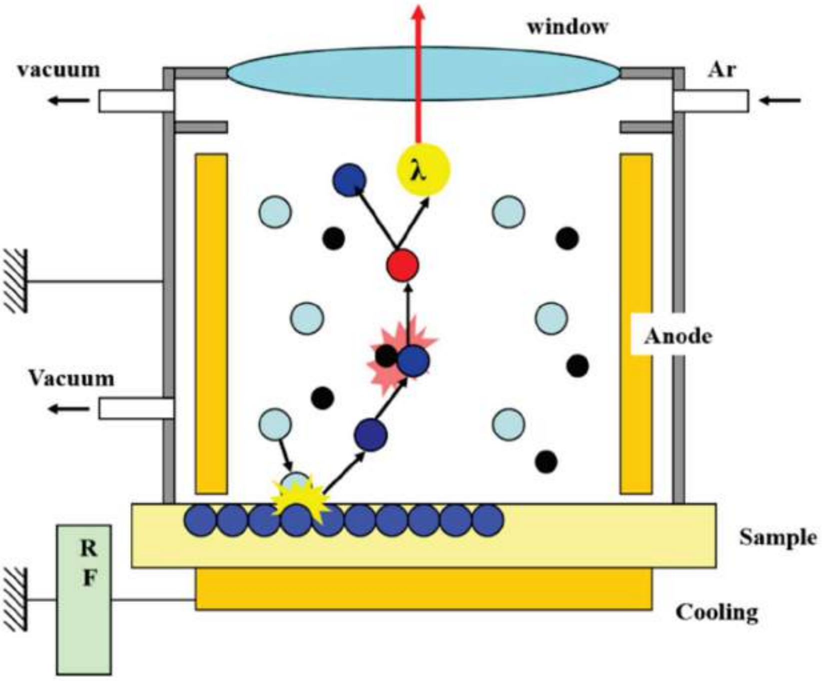

Figure 13: Scheme of the Glow Discharge Optical Emission Spectroscopy principle

6. Electrochemical measurements

6.1. Global electrochemistry

Electrochemical experiments as Open Circuit Potential (OCP) and polarization measurements were done in a classic thermostatic (25 °C) three-electrode cell (Appendix 4). Samples were used as working electrodes, the reference was a Saturated Calomel Electrode, and the counter electrode was a platinum wire. In case of coupling experiments, working and counter electrodes were two different pure phases.

The precise description of the used electrochemical sequence is given in the experimental section of each part chapter of this manuscript.

6.2. Local electrochemical analyses: Scanning Kelvin Probe (SKP) and local Electrochemical Impedance Mapping (LEIM)

LEIM is a local electrochemical technique used in this work to appreciate local surface reactivity's evolution impacted by corrosion and corrosion products formation. Local Electrochemical Impedance Spectroscopy (LEIS) and Local Electrochemical Impedance Mapping (LEIM) [9], [10] set up is composed of a potentiostat coupled with a lock-in amplifier. A three-electrode configuration is used with a metallic sample as working electrode, a Ag/AgCl electrode as reference and a platinum wire as counter electrode. Impedance measurements are carried out with a homemade local probe composed of two Ag wires of 250 µm diameter in a glass capillary (sealed in two joined capillaries with the distance between the two Ag wires centers d = 1.3 mm). The probe was positioned at 150 ± 25 µm above the WE and moved with a 3-axis positioning system driven by a motion encoder.

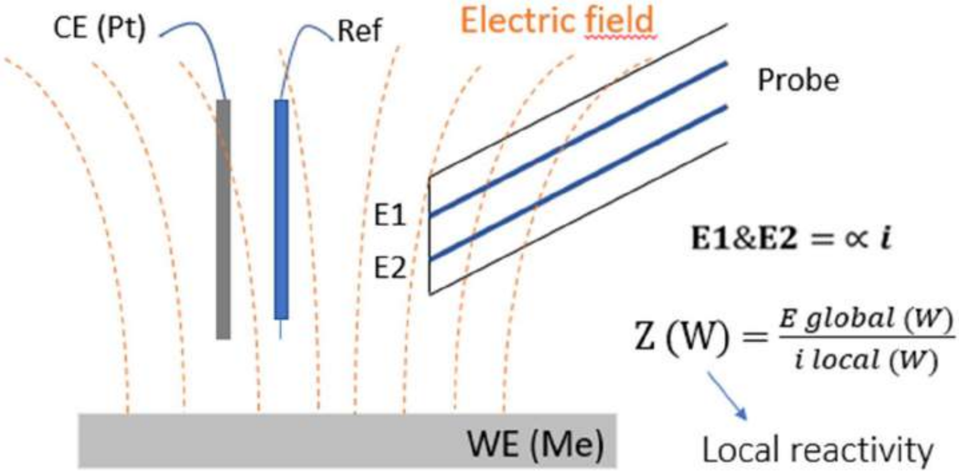

Figure 14: Local Electrochemical Impedance Spectroscopy (LEIS) explanatory diagram

This technique gives the same information than Electrochemical Impedance Spectroscopy (EIS) but the scanned area is of 300x300 µm². Local current density component normal to the WE surface ($\boldsymbol{i_{loc}(r)}$) is calculated from the potential difference sensed between the two Ag wires composing the probe:

$$\boldsymbol{i_{loc}(r) = \frac{(\varphi_1(r) - \varphi_2(r))\sigma_s}{d}} \tag{2-5}$$

where $(\varphi_1(r) - \varphi_2(r))$ is the potential difference between the two microelectrodes and d is the distance between two Ag wires center. The local impedance was defined as:

$$\boldsymbol{z(r) = \frac{V - \Phi_{ref}}{i_{loc}(r)}} \tag{2-6}$$

where $V - \Phi_{ref}$ represents the potential difference between the WE and the RE in the solution. Scanning Kelvin Probe (SKP) is a non-destructive technique used to measure the Contact Potential Difference (CPD) between the Kelvin probe and the surface sample tested [11]. This potential corresponds to the opposite of the Volta Potential.

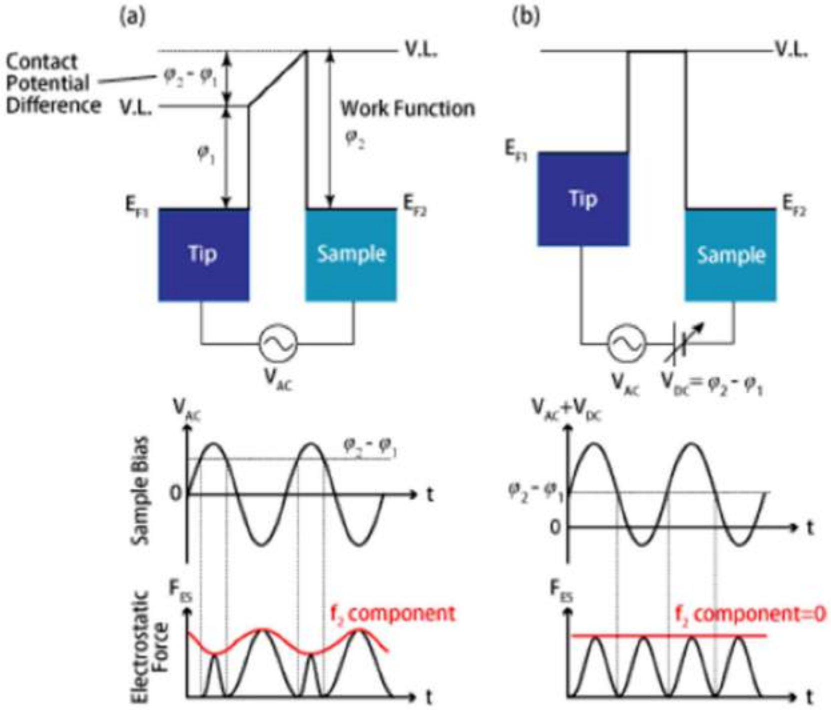

Figure 15:Scheme of the SKP principle

The probe tip and the sample surface near one another form a capacitor. The potential difference between the 2 metals, called the Volta Potential, induces the creation of an electric field from the electrons flow.

During the measurement, the probe tip vibrates at a specific frequency, generating an alternative current (to maintain the electric field between the 2 metal surfaces). Simultaneously, a DC voltage is applied to counter balance the Volta Potential and allow electrons to flow in both directions. The CPD is found when the applied DC voltage gives a nullified AC current.

References

[1] T. Machado Amorim, J. Richard, E. Jacqueson, A. Lhermeroult, P. Feltin, J-M. Lemaire, C. Allely, L. Diez, J-M. Mataigne, Method for Producing a Pre-Lacquered Metal Sheet Having Zn-Al-Mg Coatings, and Corresponding Metal Sheet, WO/2013/160567, 01-Nov-2013.

[2] A. E. Vladár, M. T. Postek, M. T. Postek, The Scanning Electron Microscope, Handbook of Charged Particle Optics, 24-Oct-2008. [Online]. Available: https://www.taylorfrancis.com/. [Accessed: 17-Oct-2018].

[3] J. I. Goldstein, D. E. Newbury, J. R. Michael, N. W. M. Ritchie, J. H. J. Scott, D. C. Joy, Scanning Electron Microscopy and X-Ray Microanalysis. Springer, 2017.

[4] K. Kanaya, S. Okayama, Penetration and energy-loss theory of electrons in solid targets, J. Phys. Appl. Phys., 5 (1972) 43.

[5] H. Bethe, Handbook of Physics, Springer., vol. XXIV. Berlin Heidelberg New York, 1933.

[6] M.-G. Barthés-Labrousse, The Auger Effect, Microsc. Microanal. Microstruct., 6 (1995) 253–262.

[7] ‘Thermo Scientific XPS: What is XPS’. [Online]. Available on: https://xpssimplified.com/whatisxps.php. [Accessed on: 12/07/2018].

[8] S. Lebouil, Etude et réalisation d’un couplage instrumental pour la mesure du dégagement d’hydrogène en temps réel : apports des outils microfluidiques, Université Pierre et Marie Curie, 2013.

[9] V. Shkirskiy, A. Maltseva, K. Ogle, P. Volovitch, Environmental effects on selective dissolution from ZnAlMg alloy under low frequency alternating current perturbations, Electrochimica Acta, 238 (2017) 397–409.

[10] V. Shkirskiy, P. Volovitch, V. Vivier, ‘Development of quantitative Local Electrochemical Impedance Mapping: an efficient tool for the evaluation of delamination kinetics, Electrochimica Acta, 235 (2017) 442–452.

[11] M. Nonnenmacher, M. P. O’Boyle, H. K. Wickramasinghe, Kelvin probe force microscopy, Appl. Phys. Lett., 58 (1991) 2921–2923.

Chapter 3: Environmental degradation of painted ZnAlMg coated steel with Ti-based conversion coating

Authors: Perrine Tanguy[a,b, 1], Christian Allély[b] and Polina Volovitch[a]

[a] *Chimie ParisTech, PSL Research University, CNRS, Institut de Recherche de Chimie Paris (IRCP), F-75005 Paris, France*

[b] *Global Research and Development, ArcelorMittal Maizières Research, France*

Abstract: This chapter introduces the morphology of degradation of painted ZnAlMg coated steel after natural exposures and galvanostatic polarization experiments and discusses probable degradation mechanisms. Natural exposures revealed blister formation in both, natural exposure and under anodic polarization, if samples have an initial artificial scratch through the whole thickness of the ZnAlMg coating while these phenomena were not observed for hot dip galvanized steels. Scanning Kelvin Probe maps of the surface and Scanning Electron Microscopy (SEM) of the cross sections demonstrated that blisters are connected between them and with the initial defect going down to steel via corroded zones. SEM observations showed a preferential Zn_2Mg lamellas oxidation at the delamination front, evidencing the anodic behavior of the Zn-Zn_2Mg phase in the coating. Blistering was proposed to be promoted by anodic under paint corrosion through Zn-Zn_2Mg phase from the down to steel defect associated with the presence of soluble salts or a lack of CC locally under the paint.

1. Introduction

Coil-coated steel sheets are largely used in the building and construction industry as cladding, sandwich panels, tiled roof etc. The coil coating process ensures a high cost efficiency as the production is run without interruption, a low environmental impact and a surface quality in the end line. In addition, the coating weight can be continuously checked. The coil-coating process of multiphase ZnAlMg sacrificial coatings replacing monophase Zn-based HDG coatings has led to the appearance of blisters distant from the down to steel scratch after several months of outdoor exposure.

Delamination from the cut edges and/or blistering randomly distributed on the surface are known phenomena in the event of outdoor exposure of coil coated materials [1]-[5]. Blisters are local defects characterized by the coating bulging and resulting from a weakness at the metal/polymer interface or between polymer layers [2]. This phenomenon has already been addressed in the literature, and numerous degradation mechanisms including chemical, electrochemical (anodic or cathodic undermining), osmotic, mechanical etc. were proposed [6]-[9].

One of the most common triggers for the blistering is surface contamination with soluble products, responsible for osmotic pressure [2], [8], [10] or corrosion process [6], [7].

Water, oxygen and local loss of adhesion between the polymer and the metal are required for blister development.

Under the blister, simultaneous electrochemical reactions can take place, creating corrosion products [6], [7]:

- Anodic dissolution:

$$\mathrm{Me} \rightarrow \mathrm{Me}^{n+} + ne^- \tag{3-1}$$

- Cathodic reduction leading to pH increase:

$$O_2 + 2H_2O + 4e^- \rightarrow 4OH^- \tag{3-2}$$

Blistering however had never been reported in the case of coil coated monophase Zn-based HDG with the same conversion coating and polymeric paints system. This indicates a possible link between the multiphase metal/polymer interface robustness and the emergence of blisters. The objective of the present chapter is to identify the degradation mechanisms of painted ZnAlMg coated steels which can occur in the presence of defects in the paint and sacrificial coating going down to the steel substrate. In order to localize the degradation and understand its formation, the morphology of the degraded samples was characterized using SKP and scanning electron microscopy while anodic galvanostatic polarization was used for an accelerated simulation of blistering for painted ZnAlMg coated steel.

2. Experimental

2.1. Materials

ZnAlMg multiphase coatings were used for blistering studies and individual pure phases were used to confirm galvanic coupling.

2.1.1. Painted ZnAlMg materials

The ZnAlMg coated steel with a thickness of 500 µm was supplied by ArcelorMittal in the skin-passed state with a roughness of 0.95 ± 0.03 µm. ZnAlMg coatings were produced by hot dip process with a total thickness around 10 µm. The selected composition contained Al < 5 wt. % and Mg < 3 wt. %. Details about microstructure characteristics are summed up in Table 4. The samples of HDG were twice thicker, however the corrosion resistance of both materials without paint is supposed to be equivalent [11]. Further details about ZnAlMg coatings microstructure are available in Appendix 2.

Samples are coated with a 10 nm-thick conversion coating before the application of a polymer coating by roll-coater (thickness: 45 µm).

Table 4: Composition of pure phases and ZnAlMg

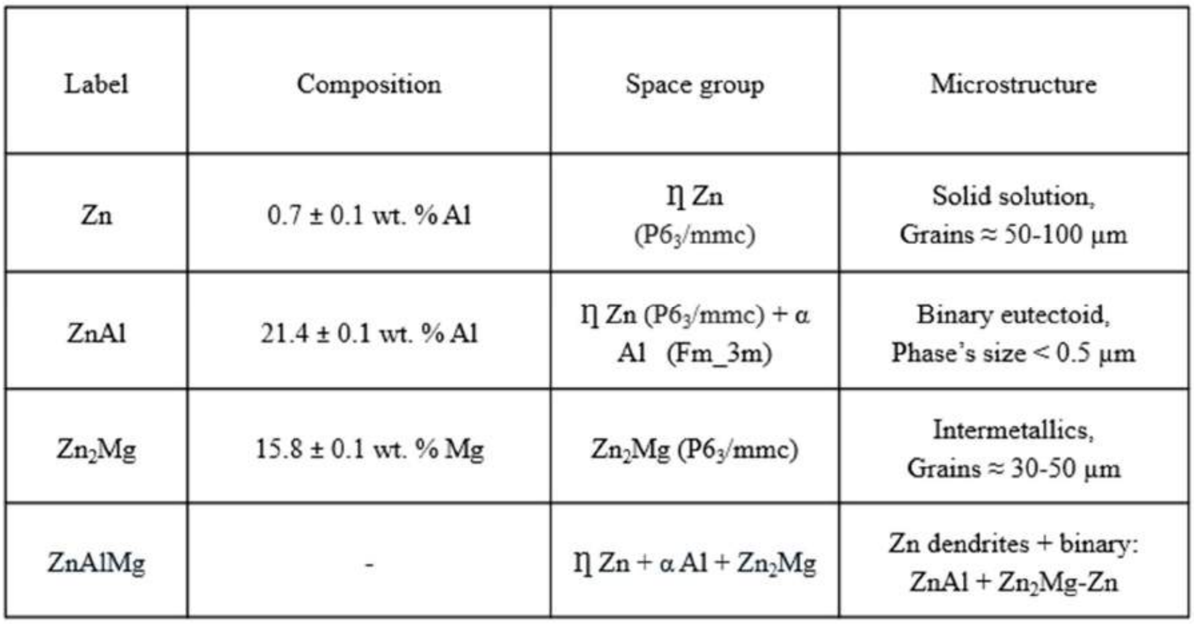

Label	Composition	Space group	Microstructure
Zn	0.7 ± 0.1 wt. % Al	η Zn ($P6_3/mmc$)	Solid solution, Grains ≈ 50-100 µm
ZnAl	21.4 ± 0.1 wt. % Al	η Zn ($P6_3/mmc$) + α Al (Fm_3m)	Binary eutectoid, Phase's size < 0.5 µm
Zn_2Mg	15.8 ± 0.1 wt. % Mg	Zn_2Mg ($P6_3/mmc$)	Intermetallics, Grains ≈ 30-50 µm
ZnAlMg	-	η Zn + α Al + Zn_2Mg	Zn dendrites + binary: ZnAl + Zn_2Mg-Zn

Samples dimensions for the outdoor natural exposure were 100x200 mm.

2.1.2. Model phases

For mechanistic purposes, Zn, ZnAl (21.4 wt. % of Al) and Zn_2Mg model phases with compositions matching the different phases contained in ZnAlMg coatings were prepared. Characteristics regarding the pure phases are displayed in Table 4 and complementary information regarding pure phases microstructure is gathered in Appendix 3. The preparation of the phases is detailed in chapter 5 in which they are used as main materials. In addition, Al (99.999 % purity) supplied by GoodFellow was used.

2.2. Outdoor natural exposure

Samples were exposed in a marine environment with a corrosivity index of C3 (for pure Zn) or C5 (for steel) according to the ISO 9223 standard for 24 months under a 5°-slope to evaluate their corrosion resistance when simulating the water retention occurring on tiled roofing. Prior to the exposure, a 6-cm long down to steel scratch was made manually with 1 mm Sikken blade and scratches depth were controlled using a Surtronic S 128 portable device. Two replicates were exposed for reproducibility purposes.

2.3. Electrochemical measurements

A three-electrode cell was used with a saturated calomel electrode (SCE) as the reference electrode, a platinum wire as the counter electrode and the sample as the working electrode. Open Circuit Potential (OCP) measurements were performed using a Biologic VSP potentiostat.

The sacrificial coating dissolution was simulated by galvanostatic polarization of painted HDG and ZnAlMg pellets with a diameter of 32 mm with preliminary made artificial scratches. Scratches up to the steel (length: 15 mm) were made manually with a 1 mm Sikken blade. The scratches depth was in average 50 µm controlled using a Surtronic S 128 portable device. Samples were immersed in 1 L of NaCl 1 wt. % pH 7 electrolyte and a +1500 $\mu A.cm^{-2}$ current was applied for 72 h on the coating. This current density is typical of what can be measured during a galvanic coupling between ZnAlMg coatings and steel when considering an oxygen reduction current density of 30 $\mu A.cm^{-2}$ on the steel. Three replicates were tested in this experiment.

2.4. Surface characterization

Samples were cut using a hand shear to cut blisters in the center and observe their cross sections. Samples with a thickness of 1 mm were finally polished by ionic beam using a JEOL SM-09010 cross polisher starting on the inferior face, opposite to the observation one. Polishing was carried out for 15 h at a voltage of 6 kV and a current of 200 µA.

The distribution of the TiCC deposited on model phases was investigated using a Field Emission Gun Scanning Electron Microscopy (FEG-SEM) on a JEOL 7800F device at an accelerating voltage of 5 kV, coupled with a Brucker Xflash 6160 Energy Dispersive Spectroscopy (EDS) device using a Si(Li) detector and equipped with QUANTAX 1.9 software (Bruker AXS).

2.5. Scanning Kelvin Probe measurement

The surface potential evaluation was performed with a VersaSCAN Electrochemical Scanning system manufactured by AMETEK Scientific Instruments. A Kelvin probe with a diameter of 500 µm was placed at 150 ± 20 µm of the sample surface and a mapping was carried out with a step size of 500 µm along both X- and Y-directions and a probe moving at a 500 µm/sec between 2 measurements. The sensitivity threshold was chosen at 50 mV and the overall scanned surfaces were 20x11 mm. Data treatment was made using the VersaSCAN software.

3. Results

3.1. Blisters morphology after field exposure

First of all, one should note that no blister was visible on the samples for which the scratch did not reach the steel substrate after any exposure. For the samples with scratch down to steel and exposed for 24 months in marine environment, a cross section was carried out along blisters and up to the down to steel scratch as shown in Figure 16.

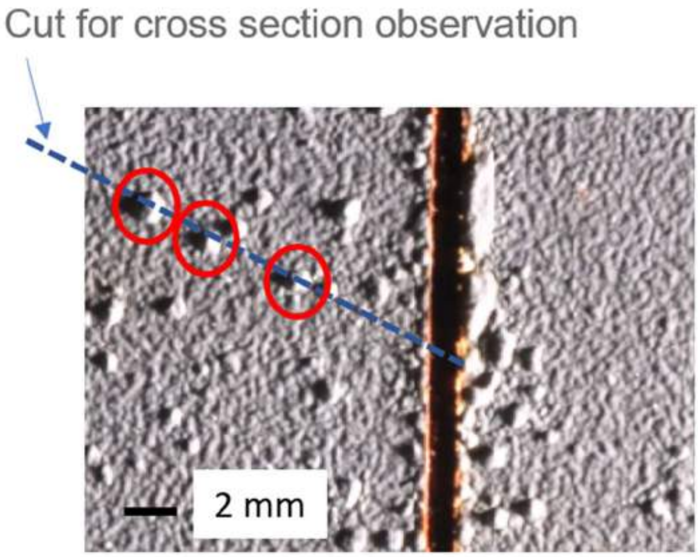

Figure 16: Photo of ZnAlMg material after 24 months of outdoor exposure in marine environment

An alignment of three selected blisters was cut as shown in the figure and polished. The obtained surface if shown in Figure 17 are displayed photos of the SEM characterization.

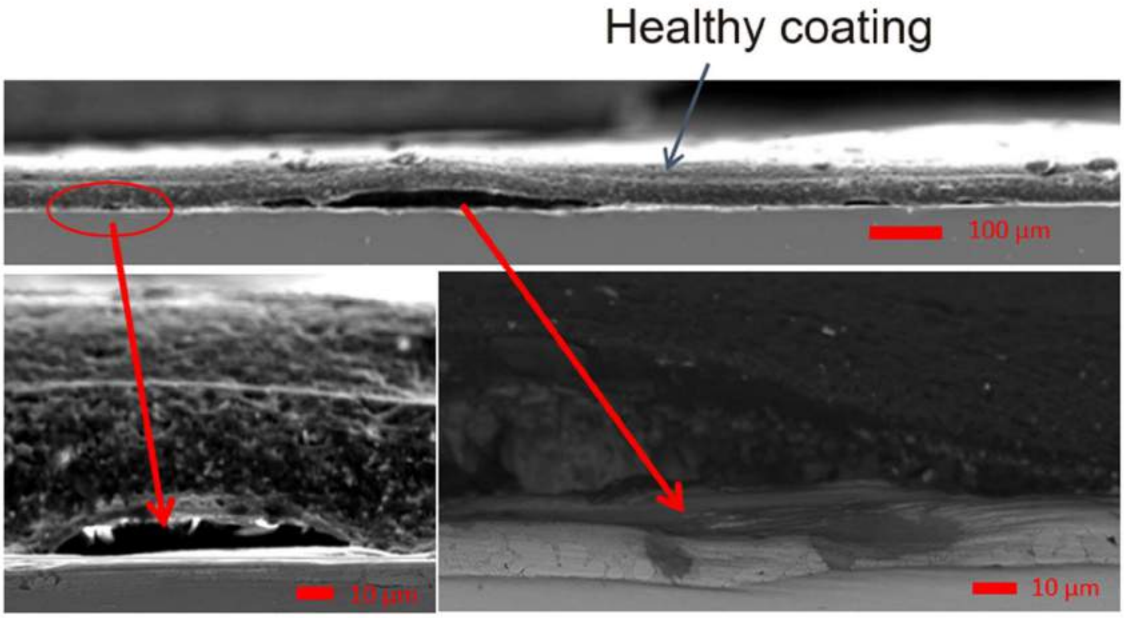

Figure 17: SEM images of cross sections of painted ZnAlMg with blisters

An example of mature blisters is visible in the top picture. Under these blisters, corrosion products are located at the interface between the metallic coating and the primer one. The cross section reveals that, under the blister, the corrosion of the ZnAlMg coating is incomplete as visible in the bottom right picture. The corrosion morphology follows microstructure features, probably due to a preferential corrosion of one of the phases. However, this corrosion could also be resulting from blistering. The local retention of water underneath the paint during dry periods can lead to local corrosion creating a corrosion path width considerably larger than the ZnAlMg microstructure itself.

The local paint decohesion is also visible near well-developed blisters although no paint blistering is detectable from the top (bottom left picture). These areas with a weak adherence could correspond to early stage blisters which could further grow due to hygroscopic behavior of corrosion products and the osmotic effect.

3.2. Connectivity between blisters after field exposure

To verify if the blisters are indeed connected with the artificial scratch and between each other, a SKP analysis was performed on a painted ZnAlMg material with large blisters distant from the scratch. The obtained map is shown in Figure 18.

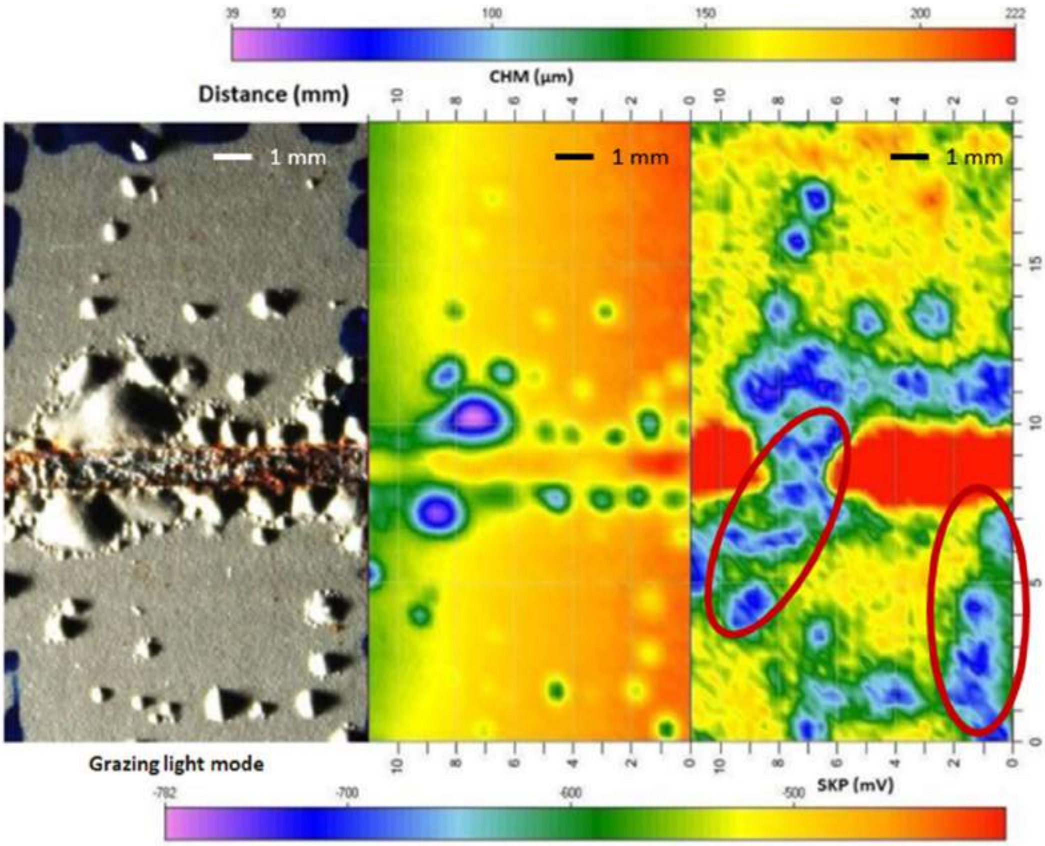

Figure 18: SKP mapping of painted and corroded ZnAlMg material with a down to steel scratch after 24 months of outdoor corrosion testing. The left figure shows optical image, the middle figure shows the topography and the right figure shows the values of Volta potential.

In Figure 18, the grazing light photo of the blistered surface is displayed at the left corner while the topography mapping is visible in the center with the associated scale being in the top of the figure. The potential mapping is shown on the right side and the corresponding scale is at the bottom of the image.

It is visible in the right image that the large blisters distant from the scratch match the low surface potential areas colored in green and blue while the yellow areas are consistent with an uncorroded coating and the red zone corresponds to the steel substrate. The corroded areas are substantially more extended than the blisters visible in grazing light. Some close but distinct blisters appear to be connected which confirms the presence of the corrosion path linking blisters. Finally, in the red-circled areas, a link between the down to steel scratch and blisters distant of 5-10 mm from the scratch is visible.

Considering that blisters do not form when no scratch is made, it is possible to suppose that galvanic coupling between the coating and steel enhances corrosion processes and that the blistering development is due to an enhanced anodic reactivity of the coating.

3.3. Artificial blisters formed under anodic polarization

To evaluate if indeed the anodic reactivity enhances blistering on multiphase substrate, galvanostatic anodic polarization tests were made on ZnAlMg coated and HDG steels with the same Ti-based conversion coating and industrial paint. The applied anodic current value was calculated in order to compensate the oxygen reduction current density (30 µA.cm^{-2}) in the exposed steel area in the scratch. Samples after 72 h of polarization are shown in Figure 19.

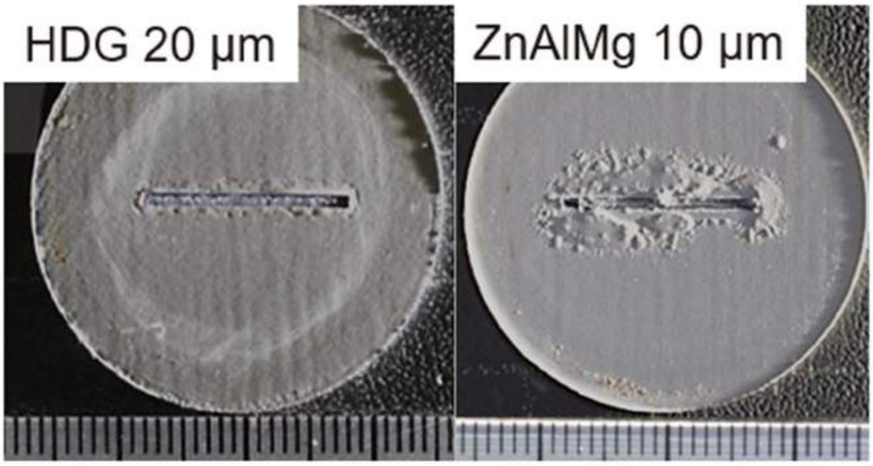

Figure 19: General view of painted HDG and ZnAlMg materials with an artificial defect down to steel after 72 h of anodic galvanostatic polarization in 1 wt. % NaCl solution with initial pH 7.

The polymer delamination from the ZnAlMg coated steel is considerably stronger than the HDG substrate. The only difference between the two materials being a multiphase structure of ZnAlMg one can conclude that this multiphase microstructure can significantly decrease anodic delamination resistance of painted materials.

The elemental distribution on the cross sections made at the delamination from by SEM-EDS mapping is displayed in Figure 20.

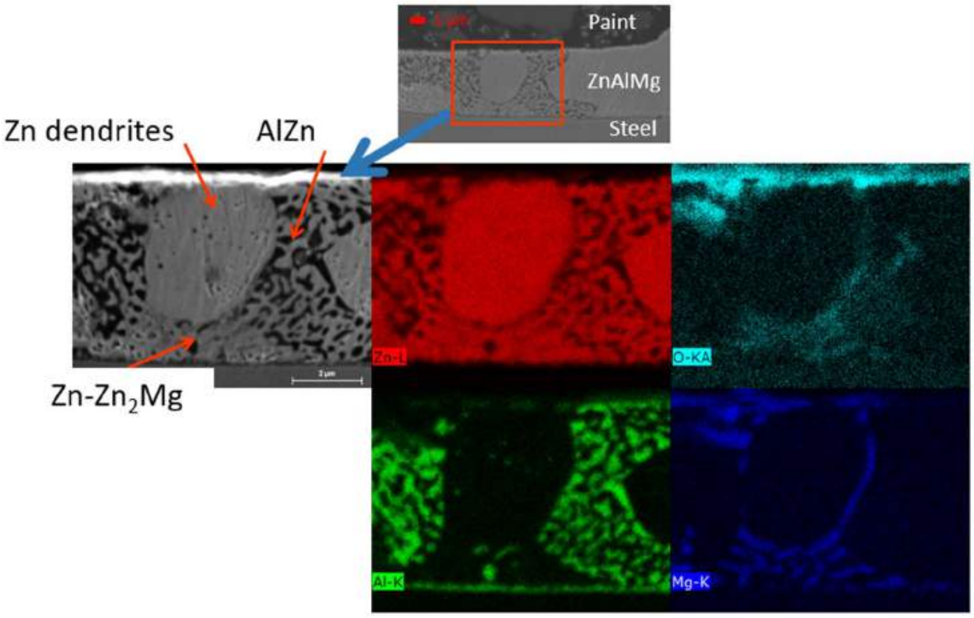

Figure 20: SEM-EDS mapping of ZnAlMg material after 72 h of anodic galvanostatic polarization in 1 wt. % NaCl solution with initial pH 7

The mapping was done in the area of the delamination front where the corrosion is partial and no paint decohesion was detected. The oxygen signal in Figure 20 is associated with the presence of corrosion products and it is clear from Figure 20, that the oxygen distribution (light blue) closely follow the distribution of magnesium (dark blue) near the surface, confirming the selective corrosion of Zn_2Mg phase [12].

The anodic behavior of Zn_2Mg phase and its preferential corrosion is well known in the literature for unpainted ZnAlMg alloys and from electrochemical characterization of pure phases [12]. Measured in this work, corrosion potentials and OCP values presented in Figure

21 also confirm that the Zn_2Mg lamellas contained in the binary Zn-Zn_2Mg phase are more anodic than the Zn dendrites and the binary ZnAl phase.

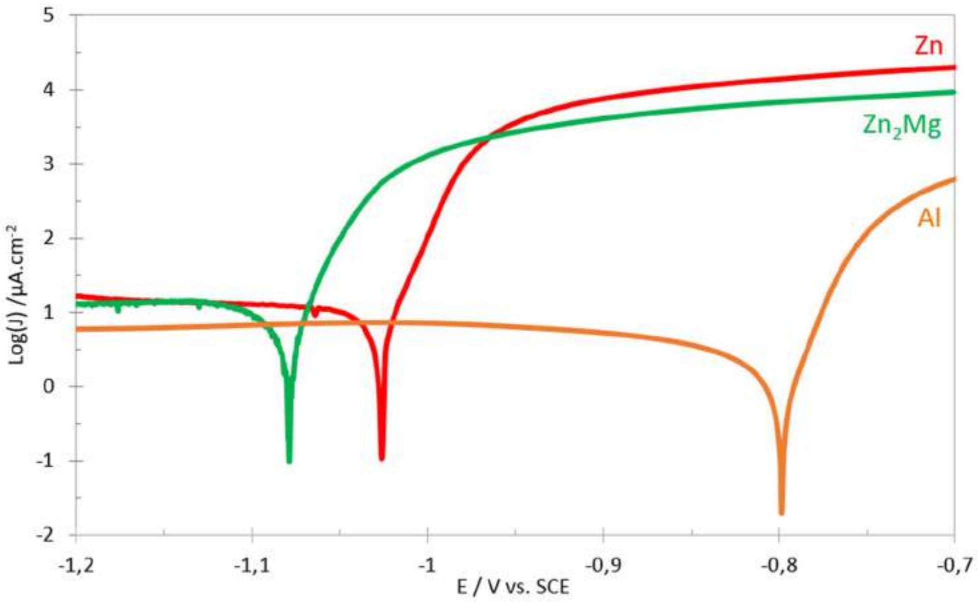

Figure 21: Anodic and cathodic polarization curves of pure phases relevant for ZnAlMg coating in 5 wt. % NaCl solution at a pH 7 and T=25 °C

Finally, it seems that under paint corrosion also promotes selective dissolution of Zn_2Mg.

4. Discussion

The presented results argue in favor of the enhancement of corrosion propagation on multiphase ZnAlMg coating by anodic polarization. Indeed, the corrosion developed under anodic polarization by an external current and in an initial defect in the coating were linked with the galvanic coupling between the steel substrate and the ZnAlMg coating. This anodic undermining leads to initial delamination around the scratch. Then both, anodic undermining and cathodic delamination can take place. The multiphase ZnAlMg microstructure induces a galvanic coupling between the anodic Zn-Zn_2Mg phase and the rest of the microstructure, fueling the anodic corrosion of Zn-Zn_2Mg. At the same time, in the confined zone, a gradient of oxygen concentration between the center of the delaminated zone and the edge of the delamination front induces a slowly renewed oxygen concentration zone with a higher pH resulting from the oxygen reduction. The production of hydroxyl ions can initiate a cathodic delamination process from damaging the polymer/metal interface bonding, dissolving oxides etc [6], [7], [9], [13], [14]. The transport of water, oxygen and cations is also facilitated by a defect in the coating [23].

The development of blisters will be also influenced by the presence of surface contamination with soluble products or a corrosion reaction on-going under the paint [2]. Indeed, because polymeric coatings act like semi-permeable membranes that will let water and oxygen flow [7], [8], [10], [12], water and oxygen can get in contact with the polymer/metal interface on every location of the surface and the presence of soluble species will enhance osmotic pressure [7], [8], [10] but also electrolyte conductivity and hence corrosion rate.

The inhomogeneous distribution of conversion coating or its low chemical stability can also contribute to the process leaving uncoated areas locally and enhancing the electrolyte uptake from the scratch [15]-[22]. Indeed, in the case of a multiphase coating, the conversion coating distribution can be heterogeneous on the surface, creating locally uncoated areas that could constitute weak points [15]-[22]. This hypothesis will be studied and confirmed in a following chapter of this PhD.

Globally, the combination degradation mechanisms leading to the formation of blisters is summed up in Figure 22 here after:

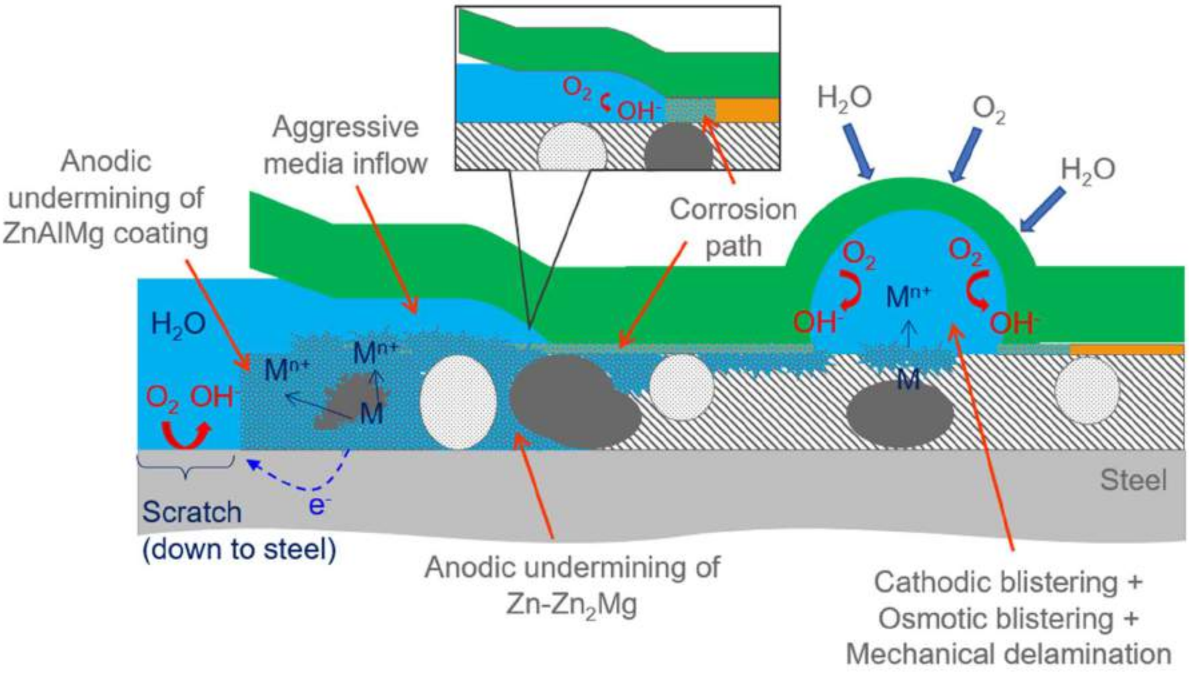

Figure 22: Scheme of the degradation mechanism of painted ZnAlMg material from the down to steel scratch

5. Conclusion

Painted ZnAlMg coatings can develop blisters in outdoor exposures if a defect in the paint and coating goes down to the steel substrate. Such blisters are not formed neither in absence of defect nor if the scratch does not go to the steel. No blistering was detected on HDG steel even if the scratch goes down to steel. This suggests the importance of multiphase microstructure and the key role of anodic processes in blistering observed on painted ZnAlMg with artificial defect down to steel.

The SKP mapping demonstrated the existence between the visually isolated blisters of the interconnected path characterized by lower than the surrounding matrix Volta potential values. SEM observations of cross sections revealed that these areas contain corroded ZnAlMg coating under intact paint and that initial lack of adherence can originate from these corroded areas. Similar to unpainted ZnAlMg corrosion, it seems that under paint corrosion of these coatings starts with selective corrosion of Zn_2Mg phase.

Galvanostatic anodic polarization confirmed that delamination from a multiphase ZnAlMg coated steel is more severe than from a monophase HDG steel. This fact is in favor of the hypothesis that a galvanic coupling between phases of the coating can enhance reactivity. Another hypothesis explaining the role of the multiphase microstructure can be related to non-homogeneous conversion coating on multiphase substrate resulting in local lack of adherence. The latter can contribute to easy access of water and oxygen to the ZnAlMg substrate but also to a localization of the corrosion process.

The exact role of the multiphase microstructure in the performance of painted ZnAlMg coated steel still needs to be understood. Indeed, it cannot be ruled out that the starting point of the corrosion propagation under the paint could be a combination of the initial inhomogeneity of the coating, its low chemical stability and the ZnAlMg substrate corrosion. Considering that the Ti-conversion coating thickness is nanometric, it is difficult to make a distinction between the degradation of the metallic substrate and of the conversion layer under the paint. The issue of conversion coating distribution on multiphase substrate will be addressed in the next chapters of the thesis.

References

[1] T. Prosek, A. Nazarov, J. Stoulil, D. Thierry, Evaluation of the tendency of coil-coated materials to blistering: Field exposure, accelerated tests and electrochemical measurements, Corros. Sci., 61 (2012) 92–100.

[2] T. Prosek, A. Nazarov, M.-G. Olivier, C. Vandermiers, D. Koberg, D. Thierry, The role of stress and topcoat properties in blistering of coil-coated materials, Prog. Org. Coat., 68 (2010) 328-333.

[3] R. M. Souto, D. J. Scantlebury, Cathodic delamination of coil coatings produced with different Zn-based intermediate metallic layers, Prog. Org. Coat., 53 (2005) 63-70.

[4] R. M. Souto, Y. González-García, S. González, Evaluation of the corrosion performance of coil-coated steel sheet as studied by scanning electrochemical microscopy, Corros. Sci., 50 (2008) 1637-1643.

[5] J. N. Murray, L. D. Stephenson, A. Kumar, Electrochemical and physical evaluations of coil coatings on metal-coated steels for roofing applications, Prog. Org. Coat., 47 (2003) 136-146.

[6] A. Amirudin, D. Thierry, Corrosion mechanisms of phosphated zinc layers on steel as substrates for automotive coatings, Prog. Org. Coat., 28 (1996) 59-76.

[7] P. Marcus, Corrosion Mechanisms in Theory and Practice. CRC Press, 2011.

[8] M. Doherty, J. M. Sykes, A quantitative study of blister growth on lacquered food cans by scanning acoustic microscopy, Corros. Sci., 50 (2008) 2755-2772.

[9] W. Funke, Toward a unified view of the mechanism responsible for paint defects by metallic corrosion, Ind. Eng. Chem. Prod. Res. Dev., 24 (1985) 343-347.

[10] M. Morcillo, Soluble salts: their effect on premature degradation of anticorrosive paints. Prog. Org. Coat. 36 (1999) 137–147.

[11] Brochure of Tata Steel, Magizinc ® Auto, the new high-performance coating, 2012

[12] J. Han, K. Ogle, Dealloying of $MgZn_2$ Intermetallic in Slightly Alkaline Chloride Electrolyte and Its Significance in Corrosion Resistance, J. Electrochem. Soc. 164 (2017) 952–961.

[13] T. Nguyen, J.W. Martin, Modes and mechanisms for the degradation of fusion-bonded epoxy-coated steel in a marine concrete environment, JCT Res., 1 (2004) 81-92.

[14] D. Greenfield, D. Scantlebury, The protective action of organic coatings on steel: A review, J. Corros. Sci. Eng., 3 (2000).

[15] T. Lostak, A. Maljusch, B. Klink, S. Krebs, M. Kimpel, J. Flock, S. Schulz, W. Schuhmann, Zr-based conversion layer on Zn-Al-Mg alloy coated steel sheets: insights into the formation mechanism, Electrochim. Acta, 137 (2014) 65-74.

[16] F. Andreatta, A. Turco, I. de Graeve, H. Terryn, J. H. W. de Wit, L. Fedrizzi, SKPFM and SEM study of the deposition mechanism of Zr/Ti based pre-treatment on AA6016 aluminium alloy, Surf. Coat. Technol., 201 (2007) 7668-7685.

[17] J. H. Nordlien, J. C. Walmsley, H. Østerberg, K. Nisancioglu, Formation of a zirconium-titanium based conversion layer on AA 6060 aluminium, Surf. Coat. Technol., 153 (2002) 72-78.

[18] O. Lunder, C. Simensen, Y. Yu, K. Nisancioglu, Formation and characterisation of Ti–Zr based conversion layers on AA6060 aluminium, Surf. Coat. Technol., 184 (2004) 278-290.

[19] L. Fedrizzi, F. Deflorian, P. L. Bonora, Corrosion behaviour of fluotitanate pretreated and painted aluminium sheets, Electrochim. Acta, 42 (1997) 969-978.

[20] J. Cerezo, I. Vandendael, R. Posner, K. Lill, J.H.W. de Wit, J.M.C. Mol, H. Terryn, Initiation and growth of modified Zr-based conversion coatings on multi-metal surfaces, Surf. Coat. Technol., 236 (2013) 284-289.

[21] I. Milosev, G. S. Frankel, Review—Conversion Coatings Based on Zirconium and/or Titanium, J. Electrochem. Soc., 165 (2018) C127-C144.

[22] I. Schoukens, I. Vandendael, J. De Strycker, A. A. Saleh, H. Terryn, I. De Graeve, Effect of surface composition and microstructure of aluminised steel on the formation of a titanium-based conversion layer, Surf. Coat. Technol., 235 (2013) 628-636.

[23] H. Leidheiser, Towards a Better Understanding of Corrosion beneath Organic Coatings, Corrosion, 39 (1983) 189-201.

Chapter 4: On the effect of multiphase microstructure of ZnAlMg substrate on the Ti-based activation and phosphate conversion coating distribution

Authors: Perrine Tanguy[a,b, 1], Christian Allély[b], Diana Dragoe[c], Vaclav Sefl[d] and Jan Stoulil[d] and Polina Volovitch[a]

[a] *Chimie ParisTech, PSL Research University, CNRS, Institut de Recherche de Chimie Paris (IRCP), F-75005 Paris, France*

[b] *Global Research and Development, ArcelorMittal Research Maizières, France*

[c] *Institut de Chimie Moléculaire et des Matériaux d'Orsay, CNRS, Université Paris-Sud 11, 91405 Orsay Cedex, France*

[d] *University of Chemistry and Technology Technicka 5, Prague, Czech Republic*

Abstract: The paper verifies the impact of multiphase microstructure of ZnAlMg coatings on the distribution of bi-cation phosphate conversion coating (PCC). Three ZnAlMg coatings and three pure phases (Zn, Zn_2Mg and ZnAl) relevant for these coatings were characterized after Ti-based activation and after complete PCC procedure. Highly alloyed ZnAl and Zn_2Mg were more sensitive to the ageing of activator bath than Zn. X-ray photoelectron spectroscopy demonstrated that Ti concentration on the surface after Ti-containing activation step decreased in order Zn>Zn_2Mg>>ZnAl and that Ti-O group is chemically bound to the Zn surface while for the alloyed phases mainly TiO_2 was formed. Scanning electron microscopy demonstrated that for the coatings with a fine microstructure, the complete covering by PCC was achieved in standard conditions despite the differences in the activation state of different phases and different kinetics of PCC formation. This was explained by the hypothesis that the variance in the reactivity of different phases which constituent the coating can be leveled by the phosphate crystal size, exceeding the substrate microstructure inhomogeneity.

1. Introduction

Phosphate conversion coatings (PCC) are among the most used conversion coating for galvanized steel and have been broadly studied on various substrates [1-6]. PCC are inorganic layers of micrometric thickness applied for pre-painted materials in order to improve corrosion resistance and ensure paint adherence on metallic substrates.

The PCC composition consists of a phosphate source, Zn cations and accelerators (NO_3^-, NO_2^- etc.) [1], [7]. Additional cations (Ni^{2+}, Mn^{2+} etc.) can be added to the basic formulation. While both, Mn^{2+} and Ni^{2+}, decrease the grain size of the precipitated phosphates, Ni^{2+} is expected to accelerate the surface reaction during the phosphating process and seal the pores of the PCC, limiting the anodic undermining [8]-[11].

The PCC formation mechanism is a complex series of processes. For HDG, the following reactions were proposed [1-4], [10], [12]-[14]:

1. Anodic dissolution:

$$Zn \rightarrow Zn^{2+} + 2e^- \tag{4-1}$$

2. Cathodic reduction leading to pH increase:

$$NO_3^- + 2H^+ + 2e^- \rightarrow NO_2^- + H_2O \tag{4-2}$$

Or

$$NO_2^- + 8H^+ + 6e^- \rightarrow NH_4^+ + H_2O \tag{4-3}$$

3. PCC precipitation in pH range from 4.7 to 8.5 [15]):

$$2PO_4^{3-} + 3Zn^{2+} + H_2O \rightarrow Zn_3(PO_4)_2 . nH_2O \tag{4-4}$$

Additionally, the formation of ZnNi alloys at the Zn/PCC interface was communicated [11]:

$$xZn^{2+} + yNi^{2+} + 2(x+y)e^- \rightarrow Zn_xNi_y \tag{4-5}$$

The PCC process consists of several steps, including alkaline degreasing, rinsing, activation, phosphating and final rinsing. The Ti-based activation plays an important role for nucleation of PCC crystals on HDG [12], [16], [17].

Nowadays, HDG steel is more and more replaced by multiphase ZnAl and ZnAlMg coatings which offer longer corrosion resistance and reduction of the coating weight [18]-[21]. New ZnAlMg coatings have a complex multiphase microstructure composed of Zn dendrites, and binary and ternary eutectics formed by Zn and Al-rich phase and/or intermetallic Zn_2Mg [19], [22], [23]. The reactivity of these phases being different [24]-[30], it can result in a micro galvanic coupling between phases and a heterogeneous spatial distribution of cathodes and anodes. The inhomogeneous surface reactivity can impact the PCC formation at different steps, including alkaline degreasing, activation or phosphating.

In the present work, we aim to verify if the interactions of PCC with multiphase ZnAlMg substrates are homogeneous and if the activator has an impact on the homogeneity of the layer via surface characterizations at different surface treatment steps of model ZnAlMg multiphase coatings and pure phases simulating ZnAlMg microstructures.

2. Experimental

2.1. Materials

Two types of materials were tested: model ZnAlMg multiphase coatings and individual pure phases.

2.1.1. Model ZnAlMg materials

Three types of ZnAlMg coated steel with a thickness of 500 µm were supplied by ArcelorMittal. ZnAlMg coatings were produced by hot dip process with thickness ranging between 5 and 10 µm. 3 different compositions with different microstructures were selected containing Al < 5 wt. % and Mg < 3 wt. %. The difference between the three compositions was in their phase composition which is summed up in Table 5. In coatings B and C, the typical size of phase was up to10 µm. In coating A, the microstructure was finer with phases below 1 µm. Only the composition A possessed the binary eutectoid ZnAl. All coatings were skin-passed resulting in a roughness comprised between 0.6 and 1.3 µm. Further details about ZnAlMg coatings microstructure is available in Appendix 2.

Table 5: Fraction of the surface (%) covered by Zn dendrites, binary phases Zn-Zn2Mg and Zn-Al, and ternary eutectic Zn-Al-Zn2Mg determined from the SEM images of top surface of coatings A, B and C and the typical linear size (µm) of phases

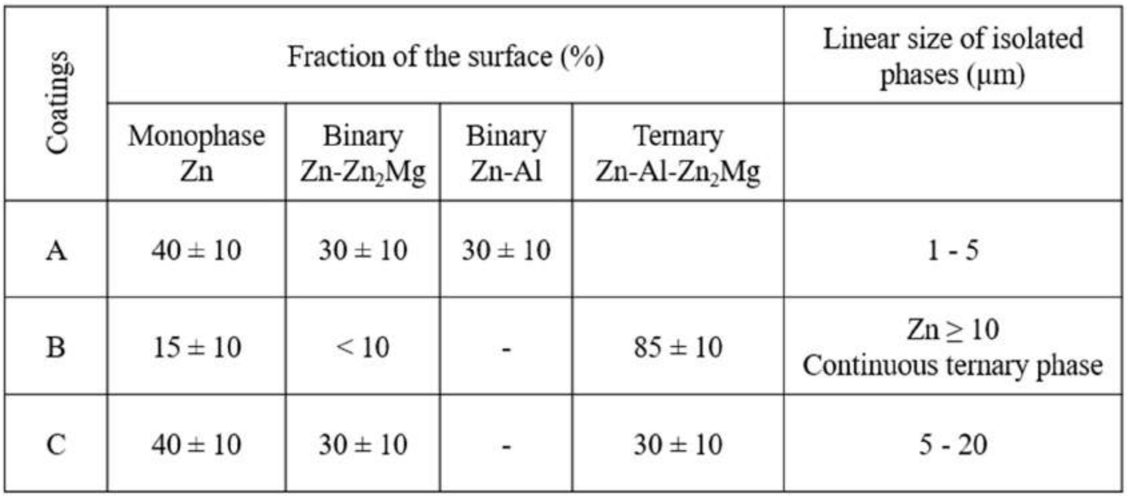

Coatings	Fraction of the surface (%)				Linear size of isolated phases (µm)
	Monophase Zn	Binary $Zn\text{-}Zn_2Mg$	Binary Zn-Al	Ternary $Zn\text{-}Al\text{-}Zn_2Mg$	
A	40 ± 10	30 ± 10	30 ± 10		1 - 5
B	15 ± 10	< 10	-	85 ± 10	Zn ≥ 10 Continuous ternary phase
C	40 ± 10	30 ± 10	-	30 ± 10	5 - 20

Samples with a size of 100 mm × 200 mm were cut from the supplied substrate and cleaned with a petroleum ether solvent to ensure complete removal of any oils or surface contamination.

2.1.2. Pure phases

For mechanistic purposes, Zn, ZnAl and Zn_2Mg model phases with compositions matching the different phases contained in ZnAlMg coatings were prepared. Alloys were weighed in masses according to their planned composition and heated at 500 °C in furnace. Liquid mixtures were then filtered through ceramic filters (61 wt. % Al_2O_3 + 39 wt. % SiO_2) with 10 pores per square inch porosity. The composition of the obtained phases is summarized in Table 6. The composition, crystallinity, grain size and orientation and hardness of all model phases were characterized by atomic absorption spectroscopy, SEM, EBSD, XRD and nanoindentation techniques. Complementary information regarding pure phases microstructure is gathered in Appendix 3.

Table 6: Model phases relevant for ZnAlMg coatings: their chemical composition (from AAS), phase crystallography (from XRD) and microstructure (from SEM) as well as open circuit potential (OCP) in PCC bath at 60 °C after 12 sec and 100 sec of immersion

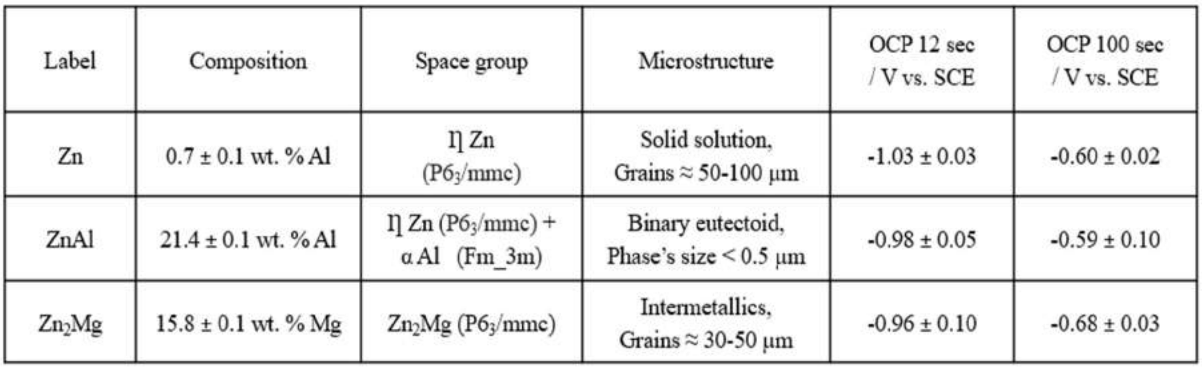

Label	Composition	Space group	Microstructure	OCP 12 sec / V vs. SCE	OCP 100 sec / V vs. SCE
Zn	0.7 ± 0.1 wt. % Al	η Zn ($P6_3/mmc$)	Solid solution, Grains ≈ 50-100 μm	-1.03 ± 0.03	-0.60 ± 0.02
ZnAl	21.4 ± 0.1 wt. % Al	η Zn ($P6_3/mmc$) + α Al (Fm_3m)	Binary eutectoid, Phase's size < 0.5 μm	-0.98 ± 0.05	-0.59 ± 0.10
Zn_2Mg	15.8 ± 0.1 wt. % Mg	Zn_2Mg ($P6_3/mmc$)	Intermetallics, Grains ≈ 30-50 μm	-0.96 ± 0.10	-0.68 ± 0.03

Samples were polished with SiC polishing discs (up to 4000 grit). After polishing, all samples were rinsed using ethanol and dried with compressed air.

2.2. Bication Zn-Ni phosphating solutions

Solutions used to prepare PCC on pure phases and model ZnAlMg materials are listed in Table 7. To determine the total concentration of phosphoric acid in the bath and the one available for the phosphating, total and free acidity were controlled. Titrations were performed using a 0.1 N NaOH aqueous solution for 10 mL of PCC bath reaching values of 30-32 mL for total acidity and 2-3 mL for free acidity respectively. Phenolphtalein and bromophenol blue indicator solutions were used to observe the color change during the titration of the total and free acidity respectively.

All baths were used maximum 12 h after mixing and renewed every 24 h. Fresh activator baths were used maximum 4 h after preparation while in order to verify the impact of the activator bath ageing on PCC distribution, the aged bathes were used 19 days after mixing.

Table 7: Main components and their concentration in solutions used for the bication (Zn-Ni) phosphating procedure

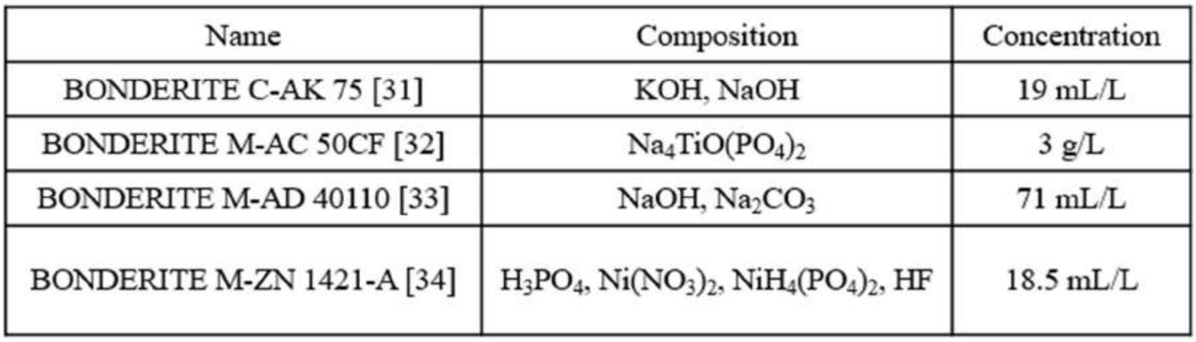

Name	Composition	Concentration
BONDERITE C-AK 75 [31]	KOH, NaOH	19 mL/L
BONDERITE M-AC 50CF [32]	$Na_4TiO(PO_4)_2$	3 g/L
BONDERITE M-AD 40110 [33]	NaOH, Na_2CO_3	71 mL/L
BONDERITE M-ZN 1421-A [34]	H_3PO_4, $Ni(NO_3)_2$, $NiH_4(PO_4)_2$, HF	18.5 mL/L

2.2.1. Bication Zn-Ni phosphating procedure

The exposed area (A= 1 cm²) of the samples was defined using insulating tapes containing precut portholes (PortHoles ™ Electrochemical Sample Masks). The following procedure was used to precipitate phosphate conversion layers on pure phases and model ZnAlMg materials:

- Alkaline degreasing in BONDERITE C-AK 75 at 55 °C for 30 sec
- Osmosis water rinsing at 50 °C and at ambient temperature
- Immersion in surface activation bath (Bonderite M-AC 50CF) at room temperature for 5 sec
- Immersion in bication Zn-Ni PCC bath (BONDERITE M-AD 40110 + BONDERITE M-ZN 1421-A) at 40 °C or 60 °C with immersion time between 0 and 40 sec.
- Osmosis water rinsing at room temperature
- Drying in hot air stream

For ZnAlMg coatings, the alkaline degreasing was made by spraying on both faces of the sample for 12 sec. Three replicates were performed to control the reproducibility.

2.3. Electrochemical measurements

Open Circuit Potential (OCP) measurements were performed using a Biologic VSP potentiostat. A three-electrode cell was used with a saturated calomel electrode (SCE) as the reference electrode, a platinum wire as the counter electrode and the sample as the working electrode. Three replicates were made for this experiment.

2.4. Surface characterization

The morphology and distribution of the Zn-Ni phosphate conversion coating deposited on model phases were investigated using a Field Emission Gun Scanning Electron Microscopy (FEG-SEM) on a JEOL 7800F device at an accelerating voltage of 15kV. Samples were observed not later than 4 h after the phosphating procedure. Several dozens of pictures of the sample surface were taken to evaluate the phosphating homogeneity.

The titanium-based compound contained in the activator after immersion of the model ZnAlMg coatings and pure phases in the activator bath were studied by X-ray Photoelectron

Spectroscopy (XPS). The XPS spectrometer (K Alpha, Thermo Fisher Scientific, base pressure in the low 10^{-9} mbar range) was equipped with a monochromatic aluminium source (Al K_{α}, 1486.68 eV). A spot size of 400 µm corresponding to an irradiated zone of approximately 1 mm^2 was used. The hemispherical analyzer was operated at 0° take off angle in the Constant Analyzer Energy (CAE) mode, with a pass energy of 200 eV and an energy step of 1 eV for the acquisition of wide scans, while narrow scan spectra centered on the Ti 2p region were recorded at a pass energy of 100 eV and an energy step of 0.1 eV due to the very low Ti signal concentration on the surface. Charge compensation was achieved by means of a “dual beam” flood gun, using low energy electrons (5 eV) and argon ions. Samples were fixed on the support using adhesive conducting tape.

The recorded spectra were processed by means of the Avantage software, using a peak-fitting routine with Shirley background and symmetrical 70 %-30 % mixed Gaussian-Lorentzian peak shapes. The atomic ratios were evaluated following normalizations of the peak areas with the Scofield sensitivity factors.

The binding energy scale was calibrated on the neutral carbon set at 284.8 eV. Regarding reproducibility, the majority of quantitative and qualitative measurements were replicated at least 5 times.

3. Results

3.1. Characterization of the activated surface before immersion in PCC bath

The SEM and EDS are inefficient to evaluate the presence and the density of the activator nuclei on different phases of ZnAlMg coatings because the size of the nuclei is less than several nm and the total quantity of detected Ti is significantly less than the detection limit of EDS. Hence, the Ti concentration on different model phases and chemical form were evaluated by X-Ray Photoelectron Spectroscopy after alkaline degreasing and immersion in the activator bath. To verify if the activator nuclei are deposited only by physical process or if a chemical modification is also possible, a reference non-reacted activator was also characterized after evaporation at 35 °C for 50 h to determine its composition, compare it with as-received powders and evaluate the water impact on the chemical composition.

Figure 23 shows the XPS spectra recorded on (a) as-received activator, (b) dissolved and solvent evaporated at 35 °C for 50 h activator and (c) ZnAl, (d) Zn and (e) Zn_2Mg phases after alkaline degreasing, immersion for 5 seconds at room temperature in the fresh activator bath and drying.

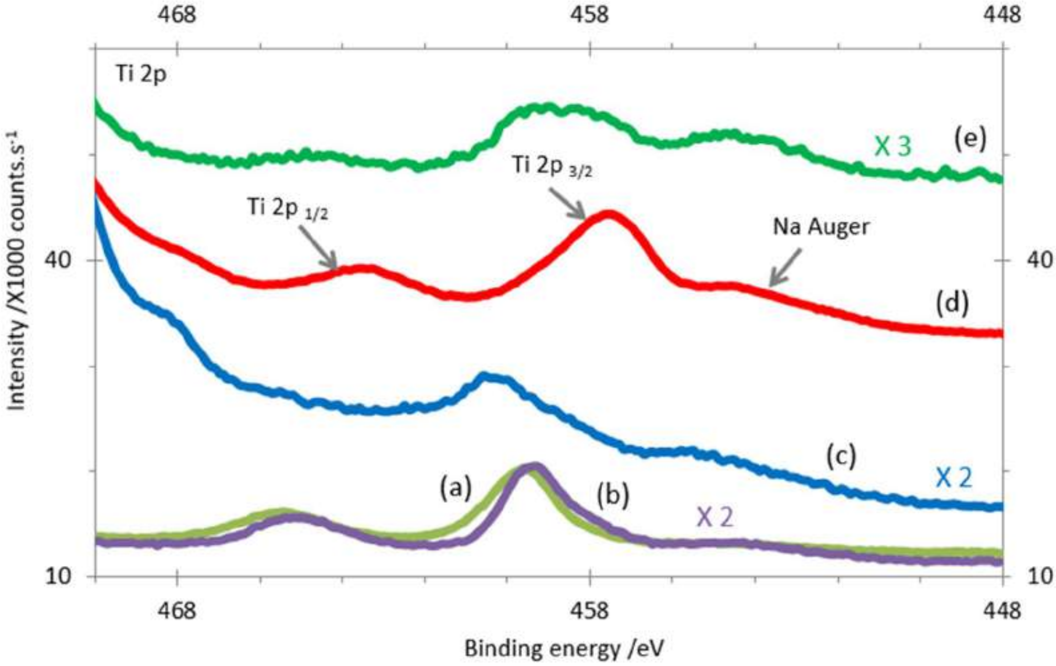

Figure 23: Comparison of Ti 2p XPS spectra of: (a) as-received activator, (b) dissolved and solvent evaporated activator, (c) ZnAl, (d) Zn and (e) Zn_2Mg

Even without peaks deconvolution, it can be seen from Figure 23, that Ti 2p $_{3/2}$ and Ti 2p $_{1/2}$ peaks are larger on model phases compared to as-received activator and dissolved + solvent evaporated activator, indicating that titanium is involved in several types of chemical bonding on model phases. Binding energies of Ti 2p $_{3/2}$ and Ti 2p $_{1/2}$ peaks for activator coated Zn_2Mg exhibit the initial Ti bonding amongst other while Zn and ZnAl show newly created bonds for the titanium.

The activator dissolved in water and solvent evaporated at 35 °C presents a peak asymmetry, indicating a possible new type of bonding created after the contact with water.

Spectra decomposition of (a) as-received activator, (b) dissolved and solvent evaporated activator, (c) Zn_2Mg and (d) Zn are presented on Figure 24. No curve-fitting was possible on ZnAl after immersion in activator due to a low signal/background ratio of Ti 2p. The details of the curve fitting can be seen in Appendix 5.

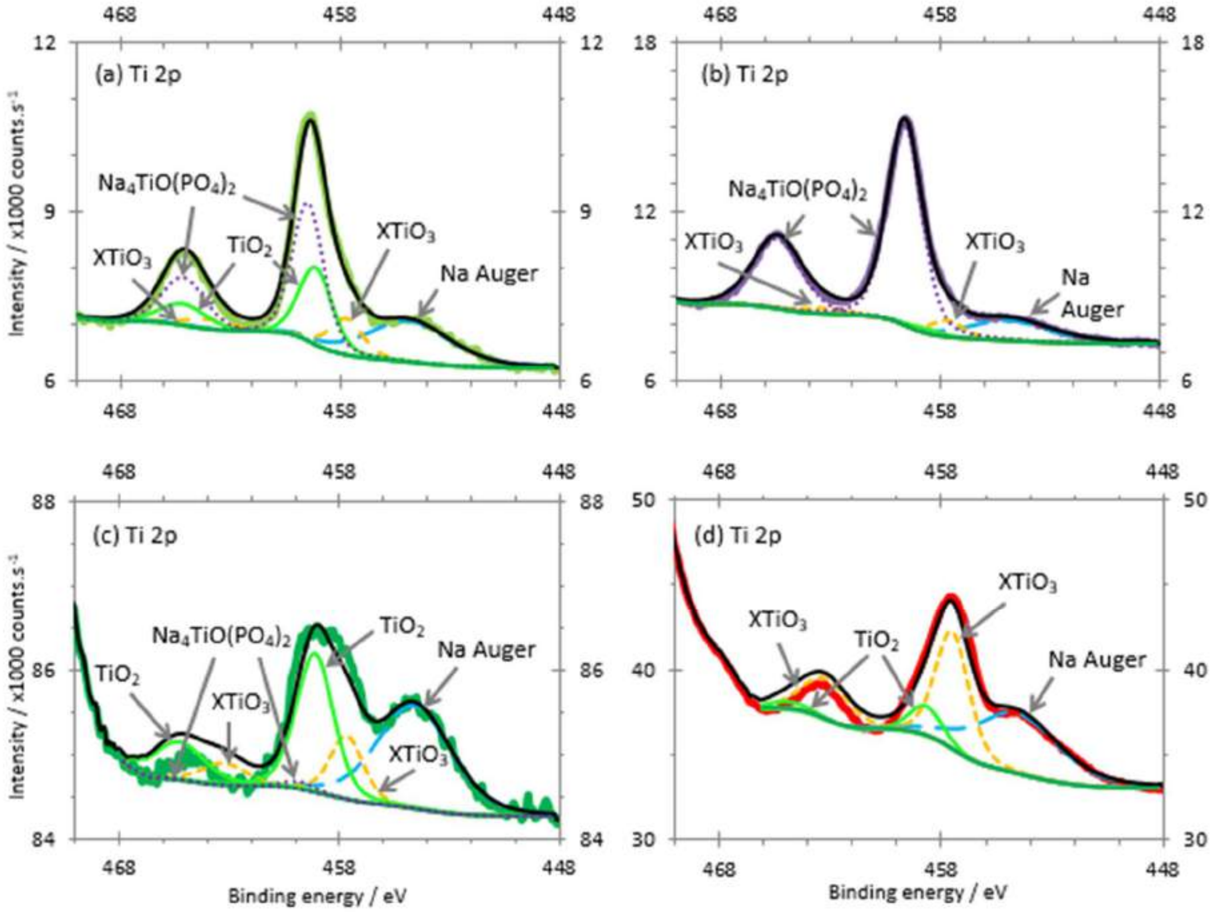

Figure 24: Ti 2p XPS spectra and respective curve-fittings of: (a) as-received activator, (b) dissolved and solvent evaporated activator, (c) Zn2Mg and (d) Zn

Curve-fitting for the (a) as-received activator and (b) dissolved and solvent evaporated activator show the presence of $Na_4TiO(PO_4)_2$ which is in accordance with the initial composition of the activator. An additional doublet at 457.7 eV ($Ti2p_{3/2}$) and 463.3 eV ($Ti2p_{1/2}$) could also be present as clearly indicates the spectrum in Fig. 24-d. This doublet is shifted comparing to both, $Na_4TiO(PO_4)_2$ and TiO_2 (which could be formed by hydrolysis of the initial solution) and was attributed to the formation of titanate-like compound, indicated as $XTiO_3$ because the shift direction compared to TiO_2 and binding energies are consistent with titanates ($ZnTiO_3$ or Na_2TiO_3) [35]-[38].

Curve fitting for Zn_2Mg (c) and Zn (d) after immersion in the activator bath reveals the presence of TiO_2 and $XTiO_3$-type of component at the surface indicating the complete transformation of $Na_4TiO(PO_4)_2$ and a chemical bonding of the activator to the surface. Because of the low intensity of Ti $2p_{1/2}$ peak and the Zn auger peak interference, the baseline fitting of (c) and (d) spectra led to an offset between the original signal and the curve-fitting in that region of the spectrum. In the case of Zn_2Mg phase in the activator, the noisy signal can be related to the high surface roughness of the sample.

The total quantity of Ti atoms on the surface was small enough, the ratio Ti/Zn of the atomic fractions of Ti and Zn detected by XPS on different phases is present in Table 8. The contribution of different forms of Ti in atomic concentration of total Ti on all model pure phases is also present. It was evaluated as a fraction of each type divided by a sum of the atomic concentrations of all the three Ti components, namely $Na_4TiO(PO_4)_2$, TiO_2 and $XTiO_3$. Considering the low Ti concentration, the quantification error could be high but the order of magnitude still can be considered.

Table 8: XPS analysis results of the atomic concentration of Ti measured on each phase (at. % Zn/ at. % Ti)

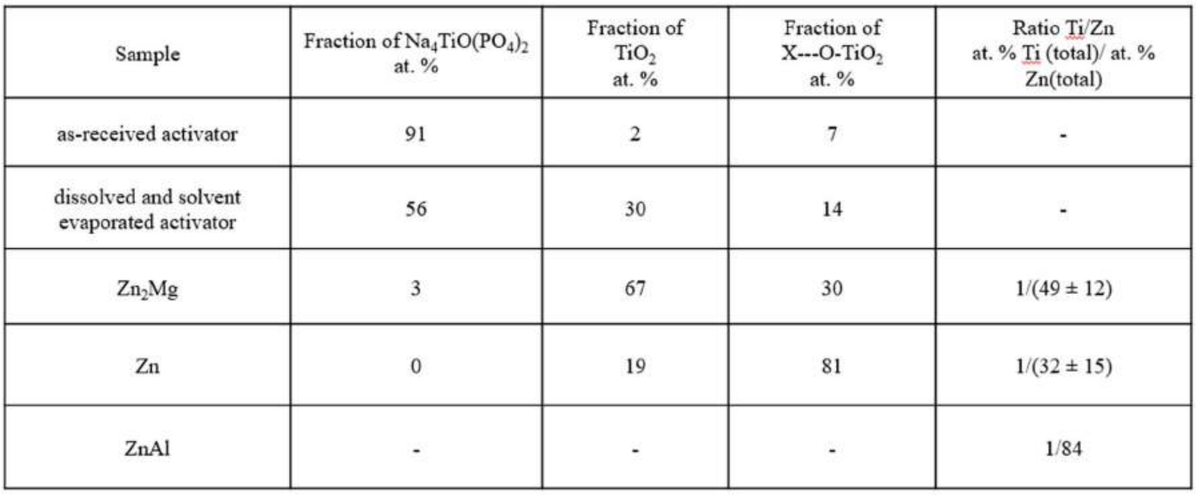

Sample	Fraction of $Na_4TiO(PO_4)_2$ at. %	Fraction of TiO_2 at. %	Fraction of X---O-TiO_2 at. %	Ratio Ti/Zn at. % Ti (total)/ at. % Zn(total)
as-received activator	91	2	7	-
dissolved and solvent evaporated activator	56	30	14	-
Zn_2Mg	3	67	30	1/(49 ± 12)
Zn	0	19	81	1/(32 ± 15)
ZnAl	-	-	-	1/84

As visible in Table 8, a higher concentration of Ti is measured on Zn compared to Zn_2Mg and ZnAl. On the ZnAl phase, only one measurement enabled the detection of Ti on the phase surface which is why more detailed work was performed only on Zn and Zn_2Mg phases. The chemical form of Ti is also different between Zn and Zn_2Mg as there is more TiO_3^{2-} than TiO_2 on Zn. Taking into account that the total quantity of Ti measured on Zn_2Mg is smaller than on Zn and that it also contains unreacted activator $Na_4TiO(PO_4)_2$, the proportion of the activator chemically bound with the surface is higher on Zn than on Zn_2Mg. In the case of dissolved and solvent evaporated activator, the proportion of TiO_2 is of 13.76 at. % which shows that the contact of the activator with the metallic substrate might not be necessary to ensure the formation of TiO_2.

3.2. OCP evolution in PCC bath

The evolution of the OCP of ZnAl, Zn and Zn_2Mg model phases with the immersion time in the PCC bath after alkaline degreasing and rinsing at 55 °C and room temperature respectively is shown in Figure 25.

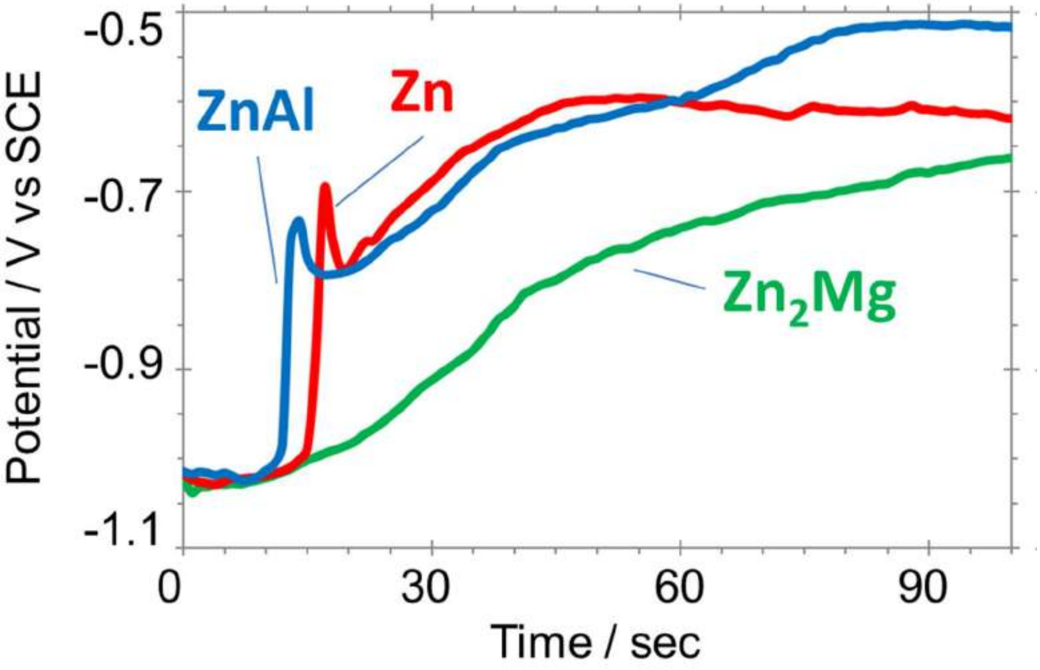

Figure 25: Evolution of open circuit potential of pure phases relevant for ZnAlMg coatings as a function of immersion time in PCC bath at 60 °C

After 12 sec of immersion in the PCC bath, all phases exhibit OCP value close to the potential of pure zinc in these conditions (E° = -1.0 V/SCE for $[Zn^{2+}] = 1$ M). In the early stages of the PCC formation, the measured potential can be attributed to the potential of the model phase substrate, mainly composed of zinc in all 3 cases.

After stabilization of the potential in the PCC bath, the increased potential of each phase demonstrates the barrier effect of the PCC. Both ZnAl and Zn are more anodic than Zn_2Mg.

The evolution of the OCP in a form of a sharp peak for Zn and ZnAl phases within the first 20 sec of immersion can be interpreted as a result of the fast precipitation kinetic of the phosphate conversion layer on phases alloyed with Al compared to Mg-alloyed phases. The appearance of such a peak was associated in the literature to a Ni^{2+} diffusion limitation as the phosphating is carried out without stirring [39]. A similar experiment carried out on ZnAlMg model materials exhibited an OCP evolution close to the evolution of pure Zn_2Mg phase. As for

Zn_2Mg, the OCP evolution is slower than for the other 2 phases owing to the preferential Mg dissolution in the phase, [13], delaying the formation of hopeite because of the lower dissolution of Zn and hence lower supersaturation rate by Zn^{2+}. Mg phosphates solubility being more than 10 times higher than the solubility of hopeite [40], [41], the formation of the PCC layer can be delayed.

3.3. Surface observations by SEM

3.3.1. PCC crystals morphology

Figure 26 and Figure 27 illustrate typical morphologies of PCC crystals formed on the coatings (Figure 26) and pure phases (Figure 27) at different PCC treatment conditions - with and without activation step, varied temperature and treatment time.

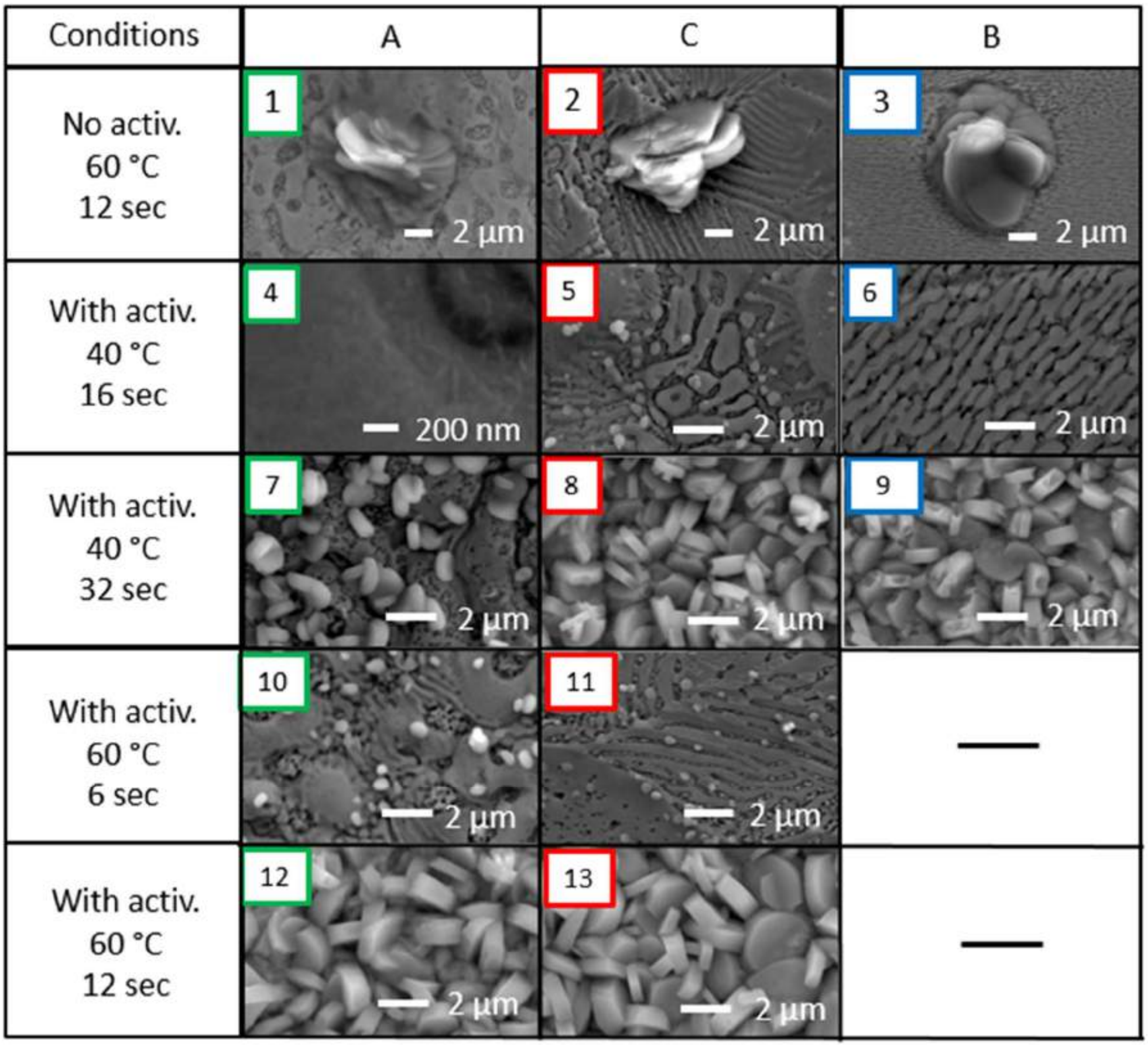

Figure 26: PCC grains density and morphology on ZnAlMg surfaces as a function of the use of a fresh activator, bath temperature and immersion time (as indicated)

To evaluate the distribution of PCC at early stages of crystallization, some experiments were made at 40 °C instead of 60 °C. At 40 °C, a complete coverage of the surface of compositions B and C is achieved after 32 sec (Figure 26) while at 60°C the complete coverage of the composition C is achieved at 12 sec (composition B was not tested). The composition A exhibits a partial coverage after 32 sec at 40 °C but is completely covered at 60 °C after 12 sec. The slower deposition kinetics of the material A will be considered in the discussion section. PCC grains look homogeneously distributed on all ZnAlMg phases at different treatment times whether the immersion in the PCC bath was carried out at 40 or 60 °C.

Concerning the importance of the activator, it is visible in Figure 26, that without activator, the precipitation of scattered and large PCC grains is observed on all ZnAlMg compositions. For composition A, it is not possible to determine if there is a preferential precipitation on a specific phase as the grain size is on average 10 times larger than each phase of the microstructure. A comparable observation can be made for composition B as the surface locally contains Zn dendrites with a smaller size than PCC grains. No preferential precipitation of phosphate grains on a specific phase was observed on composition C. Generally, the grain size is unchanged from one ZnAlMg composition to the other.

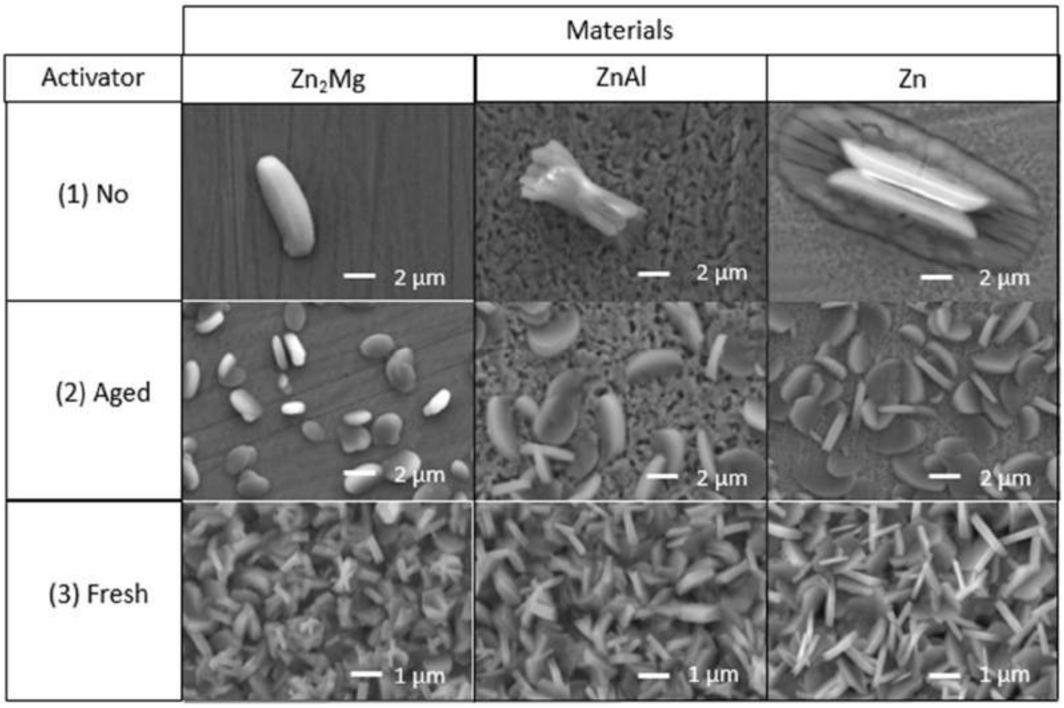

Figure 27: PCC grains density and morphology on different materials as indicated after immersion in the PCC bath for 12 sec at 60 °C using: (1) no activation, (2) aged activation and (3) fresh activation (see text for detail)

Like on ZnAlMg materials, phosphates on model pure phases exhibited large and scattered grains of variable diameter (Figure 27). In contrast, a significant PCC grain size variation on Zn, ZnAl and Zn_2Mg pure phases is visible, highlighting the different interaction between the PCC bath and the model phase depending on whether the phase is highly alloyed (ZnAl and Zn_2Mg) or almost mono-component (Zn).

By comparison of the fully covered surfaces on model phases (Figure 27) and coatings (Figure 26) treated with a fresh activator, the grains look thinner and noticeably smaller on pure phases. Still, a similar PCC grain density and morphology is observed on all pure phases and grains diameter is ranging between 1 and 2 µm. As for HDG coatings, for ZnAlMg coatings the activator seems to be a key factor to favor nucleation vs grain growth to ensure homogeneous distribution of the coating on different ZnAlMg materials and pure phases.

3.3.2. Surface coverage evolution with time and T°C of PCC treatment

From the analysis of a large number of SEM photos of PCC on all ZnAlMg materials after different times of PCC treatment (see Figure 26 for typical examples), the surface coverage by PCC at different immersion times was determined. As without activator, incomplete coverage at short immersion times does not reveal any preferential PCC deposition, but in contrast with the phosphating w/o the activator, grains are smaller (photos 5, 7, 10 and 11). Grains are more or less spherical at the initial steps of the PCC formation while they exhibit a more angular shape once the surface full coverage is completed.

The evolution of the covering rate as a function of immersion time for different coatings and immersion conditions is in a form of the precipitation kinetics in Figure 28.

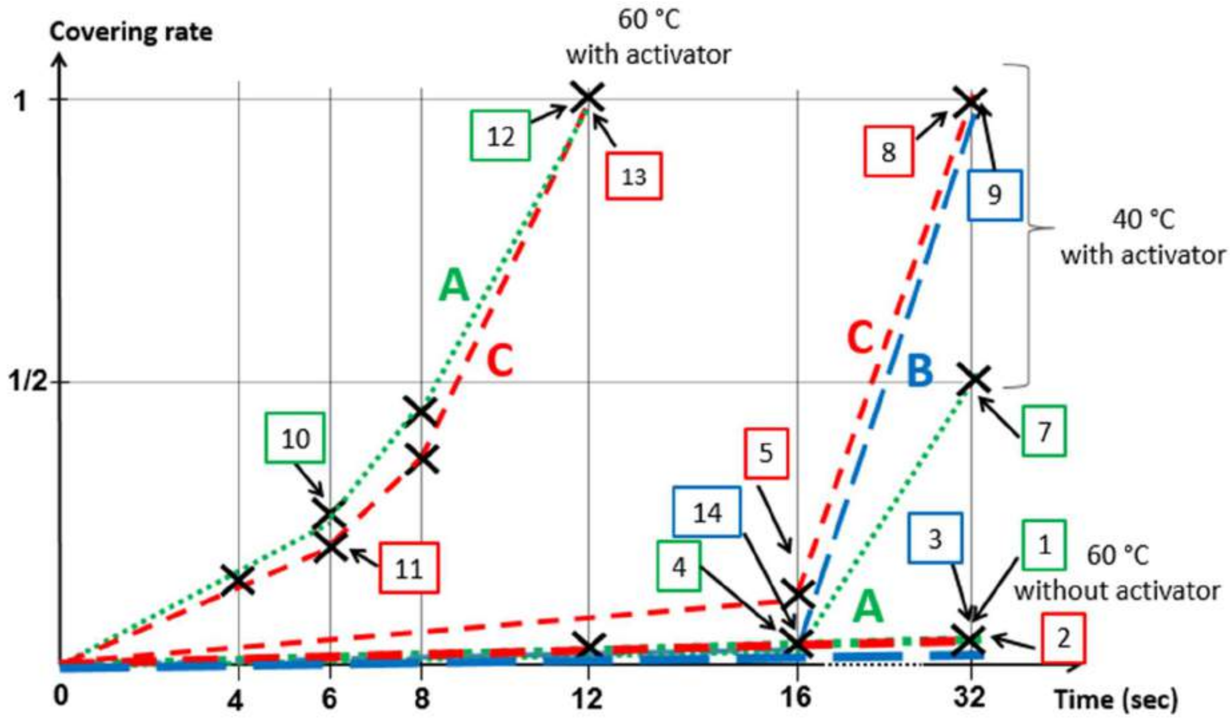

Figure 28: Surface coverage evolution as a function of immersion time, ZnAlMg substrate composition, bath temperature and use of activator (as indicated)

Without activator, the PCC kinetics is very slow. PCC treatment at 40 °C instead of 60 °C increases the time necessary for a complete coverage of the coatings B and C to 32 sec instead of 12 sec at 60 °C, while the composition A is still uncovered even after 32 sec. However, although different ZnAlMg materials and pure phases demonstrated differences in PCC grain morphology and PCC layer growth kinetics, a complete coverage by the PCC can be achieved on all multiphase coatings after 12 sec of immersion at 60 °C.

4. Discussion

4.1. Impact of the activator on the PCC growth mechanism and grain shape

The role of the activation step in the phosphating process has already been studied for various types of PCC on HDG, steel [12], [16], [17] and Al [42]. The literature attributes the mechanism of activation in several steps

- Adsorption of nano-particles of $Na_4TiO(PO_4)_2$ activator to the surface [16].
- Transformation of $Na_4TiO(PO_4)_2$ into $Zn_2Ti(PO_4)_2$ when the activated surface gets in contact with Zn^{2+} ions contained in the PCC bath [12], [16].

The growth of $Zn_3(PO_4)_2.4H_2O$ on the formed nuclei is reported to be epitaxial on the $Zn_2Ti(PO_4)_2$ nuclei [12], [16], [42].

This mechanism and the idea of the epitaxial growth are commonly accepted but we were not able to find a published result confirming the hypothesis of the epitaxial growth with the activator nuclei, except the reference [42] demonstrating that on Al substrates and with disc-like Ti-based activator, the PCC grains grow directionally keeping a disc-like form. The results presented in this paper for alloyed substrates in conditions when PCC is not yet covering demonstrate that the disc-like and platelet-like shape of crystals can be obtained on the Zn-based materials without activator (Figure 26 and Figure 27). Additionally, in case of aged activator (ageing decreases the concentration of potential nuclei), the PCC formed discs with diameter of about 1 μm on the model Zn_2Mg phase while significantly better formed hexagonal platelets with diameter about 2 μm were formed on Zn and ZnAl substrates.

By consequence, the effect of the nucleating agent on the grain shape is not necessarily related to the epitaxy between the activator nuclei and the hopeite forming on it. The role of the activator for the shape of the PCC crystals can be hence limited to an increased number of PCC crystals which nucleate in the first seconds of the phosphating process regardless of the exact chemical composition of the nucleus. By consequence, $ZnTiO_3$ and TiO_2 present on the surface after activation step can serve as nuclei even if they do not exhibit a similar crystallography or stoichiometry as $Zn_xNi_y(PO_4)_2$ and in this case, the first nuclei of hopeite can be spherical. Titanium phosphates can be also formed by the reaction of TiO_2 or Ti salts with phosphoric acid in phosphating bath [43-46] favoring the epitaxial growth and formation of disc-like crystals from the first moments of grain growth.

In case of ZnAlMg substrates, at initial stages of PCC formation even with previous activation step, the visible PCC crystals on these materials were spherical. Such a morphology has never been reported for PCC on Zn. The apparent incoherence however can be a consequence of the fact that the surface observations reported in the literature were usually made in conditions of high surface coverage (typical observation times were from 10 seconds to several minutes). In such conditions the nucleation processes are already less important and the grain growth is well advanced. From our results, it seems that the induction period before the nucleation and the exponential crystal growth [47] on Zn_2Mg phase and ZnAlMg materials is slower than on pure Zn and that the minimum size for a stable spherical nucleus on Mg-rich substrates is higher than on Zn. Indeed, spherical PCC crystals were observed on the alpha Mg phase in AZ31 Mg-Al alloy treated without preliminary activation [48]. The reason of longer induction period can be in a selective Mg dissolution from Mg-containing Zn materials [13] [24] which delays the increase of Zn concentration near the surface. The solubility of Mg phosphates being 10 times higher than the solubility of hopeite, more time is necessary to reduce Mg concentration in solution and to achieve Zn access to the surface.

To sum up, the most important characteristic of the activator for multiphase substrate should be hence its homogeneous distribution on different phases. From this point of view, the differences in the Ti chemistry and its quantity on the activated surfaces of different pure phases is important: the total quantity of Ti deposited on different phases decreases in order $Zn>Zn_2Mg>>ZnAl$ and the fraction of the chemically bound Ti decreases in the same order. As a result, the phase sensitivity to the activator ageing (by agglomeration of colloids [16] or by pH increase [49]) increases in order: $Zn<Zn_2Mg<ZnAl$. The weakest activation of ZnAl phase can also explain why after 32 seconds of "slowed" PCC treatment at 40 °C, the multiphase coating with the composition A, which contained high surface fraction of ZnAl phase present as a binary eutectoid, was not completely covered while the compositions B and C, exempt of the ZnAl binary eutectoid, had been already completely covered by PCC.

4.2. Impact of the activator on the PCC distribution

As presented in section 4.1, the interaction of the activator with the phases composing ZnAlMg alloyed coatings looks different however it does not disturb the formation of a homogeneous layer of PCC on coatings with different microstructures. In this section, we will try to formulate some hypotheses explaining the apparent incoherence between the incongruent interaction of the activator with different ZnAlMg constituents and a formation of the homogeneous PCC layer with similar morphology on the coatings.

The good coverage of Zn dendrites could be explained by a high concentration of Ti-activator chemically bound to the surface. However, on ZnAl phase and on the eutectic phases in coatings, including the binary eutectoid-containing ZnAl phase, despite a lower activator concentration expected on ZnAl, a full coverage is achieved. This effect can be attributed to the size of the PCC grains after completion of the PCC procedure compared to the ZnAl phase dimensions in the material. As schematically represented in Fig. 7, at an advanced stage of the conversion reaction, PCC crystals are significantly bigger than the size of the phase which is not activated. This phase can be protected by the crystals deposited on the neighboring phases. In case of eutectic phases with micrometric lamellas width and in case of ZnAl phase with the size less than the size of the PCC grains (about 1.5 μm diameter after 12 sec of immersion at 60 °C), these phases can be hence covered by PCC even if their interaction with the activator is not efficient. Such an observation can be through for both, ZnAl and Zn-Zn_2Mg binary phases.

The proposed scheme can explain how, despite the ZnAlMg substrate and the activator deposition heterogeneities, a complete coverage of the multiphase ZnAlMg substrate can be ensured by the combination of the coarse size of PCC grains and relatively fine microstructure of the coating. It also reveals that, potentially, the formation of nanometric conversion layers on multiphase substrates might be more complex than the PCC formation.

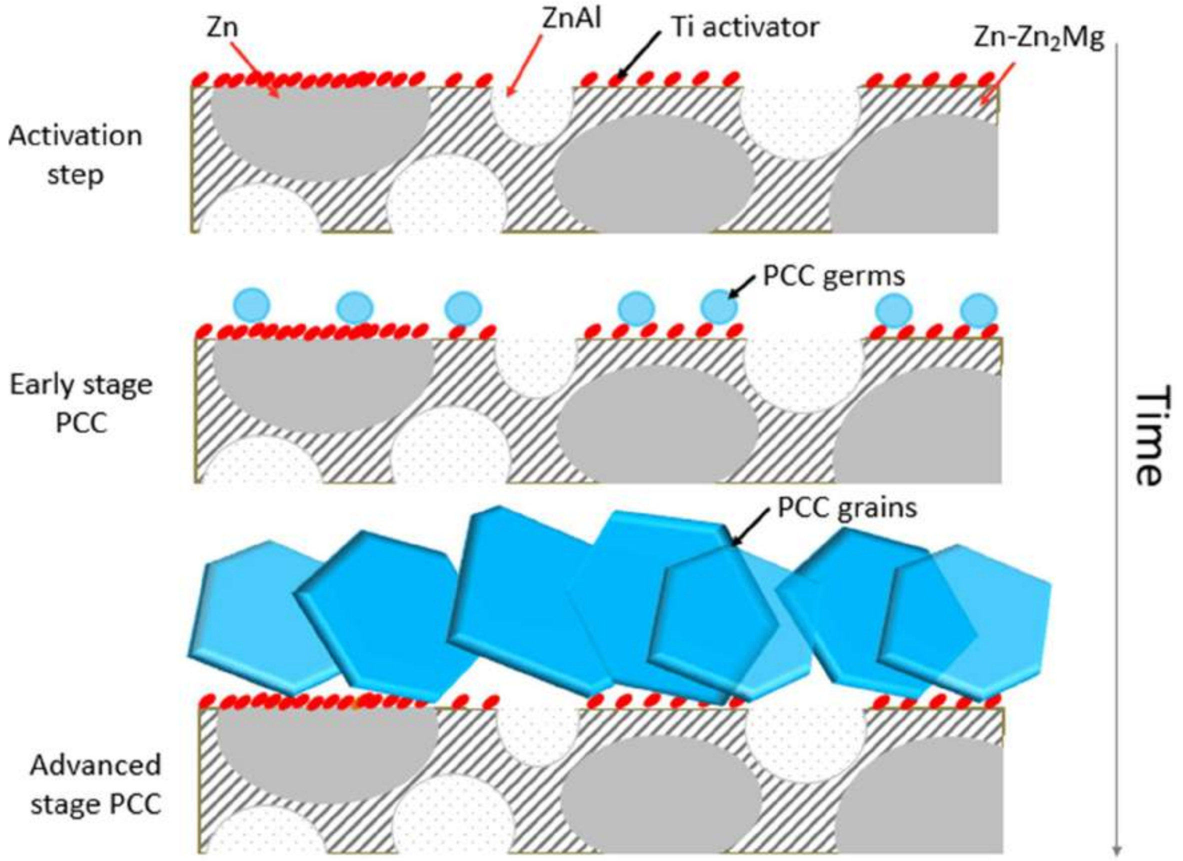

Figure 7: Scheme of the Ti-activator and PCC distributions explaining homogeneous precipitation

5. Conclusion

In this work, the distribution of PCC at different surface treatment steps on model ZnAlMg materials as well as model phases simulating the different phases of ZnAlMg microstructures was characterized and the effect of the substrate microstructure on the phosphating process was understood.

- **No preferential deposition** of PCC on a specific phase was detected when working in **standard conditions** (with activator – immersion for 12 sec in PO_4 ZnNi bath at 60 °C).
- **Highly alloyed phases** (ZnAl and Zn_2Mg) were found to be more **sensitive to the activator bath ageing** than Zn. The impact was measured on both **grain density and shape** (round-like grains instead of plates) leading to different **PCC nucleation kinetics** between all 3 model phases

PCC nucleation kinetics: Zn > ZnAl > Zn_2Mg

The variation of reactivity of the model phases with the PCC bath was attributed to the concentration and type of Ti-based compounds formed on the surface during the activation step.

- During activation step, a variation of **types of bonding** on all 3 model phases were highlighted by XPS

Highest Ti concentration: Zn > Zn_2Mg > ZnAl

Zn: Formation of $XTiO_3$ ($ZnTiO_3$ etc) favored compared to TiO_2

Zn_2Mg: Formation of TiO_2 favored compared to $XTiO_3$ ($ZnTiO_3$ etc)

Fast nucleation kinetics + grain shape favored on Zn by **high Ti concentration** associated to the **formation of $XTiO_3$** on the surface

In general, the slower interaction of Zn_2Mg with the activator does not seem to be critical during the PCC formation step, probably due to the relatively small size binary eutectic Zn_2Mg phases in studied ZnAlMg materials.

References

[1] K. Ogle, R. Buchheit, Conversion Coatings, in : A.J. Bard, M. Stratmann, J. Frankel (Eds.), Encyclopedia of Electrochemistry, vol. 4, Corrosion and Oxide Films, Wiley-VCH, 2003, p. 460.

[2] K. Ogle, M. Wolpers, Phosphate conversion coatings, in : S.D. Cramer, B.S. Covino (Eds.), ASM Handbook, vol. 13A, Corrosion : Fundamentals, Testing, and Protection, ASM International, 2003, p. 712.

[3] L. Jiang, M. Wolpers, P. Volovitch, K. Ogle, The degradation of phosphate conversion coatings by electrochemically generated hydroxide, Corros. Sci. 55 (2012) 76-89.

[4] K. S. Fernandes, E. de A. Alvarenga, P. R. G. Brandão, V. de F. C. Lins, Análise por espectroscopia no infravermelho das camadas de fosfato de zinco e de zinco modificado com níquel e manganês em aço eletrogalvanizado, Rem Rev. Esc. Minas. 64 (2011) 45–49.

[5] W. Zhou, D. Shan, E.-H. Han, W. Ke, Structure and formation mechanism of phosphate conversion coating on die-cast AZ91D magnesium alloy, Corros. Sci. 50 (2008) 329–337.

[6] A. Losch, E. Klusmann, J. Schulze, Electrochemical investigations of phosphate layers by metal deposition and cataphoretic painting, Electrochim. Acta. 39 (1994) 1183–1187.

[7] J. Donofrio, Zinc phosphating, Met. Finish. 108 (2010) 40–56.

[8] A. S. Akhtar, K. C. Wong, K. A. R. Mitchell, The effect of pH and role of Ni^{2+} in zinc phosphating of 2024-Al alloy: Part I: Macroscopic studies with XPS and SEM, Appl. Surf. Sci. 253 (2006) 493–501.

[9] A. S. Akhtar, D. Susac, P. C. Wong, K. A. R. Mitchell, The effect of pH and role of Ni^{2+} in zinc phosphating of 2024-Al alloy: Part II: Microscopic studies with SEM and SAM, Appl. Surf. Sci. 253 (2006) 502-509.

[10] A. S. Akhtar, K. C. Wong, P. C. Wong, K. A. R. Mitchell, Effect of Mn^{2+} additive on the zinc phosphating of 2024-Al alloy, Thin Solid Films. 515 (2007) 7899-7905.

[11] D. Zimmermann, A. G. Muñoz, J. W. Schultze, Formation of Zn–Ni alloys in the phosphating of Zn layers, Surf. Coat. Technol. 197 (2005) 260–269.

[12] M. Wolpers, J. Angeli, Activation of galvanized steel surfaces before zinc phosphating - XPS and GD-OES investigations, Appl. Surf. Sci. 179 (2001) 281–291.

[13] L. Jiang, P. Volovitch, M. Wolpers, K. Ogle, Activation and inhibition of Zn–Al and Zn–Al–Mg coatings on steel by nitrate in phosphoric acid solution, Corros. Sci. 60 (2012) 256–264.

[14] M. Pourbaix, Atlas d'équilibres électrochimiques à 25 °C, Gauthier-Villars & Cie, Paris, 1963. p. 494-495.

[15] L. Jiang, Application of atomic emission spectroelectrochemistry to the formation and degradation of conversion coatings on galvanized steel (Zn and Zn-Al-Mg)', PhD thesis, Université Pierre et Marie Curie, Paris, 2012.

[16] P.-E. Tegehall, Colloidal titanium phosphate, the chemical activator in surface conditioning before zinc phosphating, Colloids Surf. 42 (1989) 155–164.

[17] P.-E. Tegehall, The mechanism of chemical activation with titanium phosphate colloids in the formation of zinc phosphate conversion coatings, Colloids Surf. 49 (1990) 373–383.

[18] T. Prosek, A. Nazarov, A. Le Gac, D. Thierry, Coil-coated Zn–Mg and Zn–Al–Mg: Effect of climatic parameters on the corrosion at cut edges, Prog. Org. Coat. 83 (2015) 26–35.

[19] N. Le Bozec, D. Thierry, M. Rohwerder, A. Koavcs, A. Peltola, G. Luckeneder, L. Luxem, G. Marchiaro, « Advanced Zinc-based hot dip coatings for automotive applications (AUTOCOAT) », Technical report No. EUR 26323 to European comission - Directorate general for research and innovation (2013).

[20] P. Volovitch, T. N. Vu, C. Allély, A. Abdel Aal, K. Ogle, Understanding corrosion via corrosion product characterization: II. Role of alloying elements in improving the corrosion resistance of Zn–Al–Mg coatings on steel, Corros. Sci. 53 (2011) 2437–2445.

[21] T. Prosek, N. Larché, M. Vlot, F. Goodwin, D. Thierry, Corrosion performance of Zn–Al–Mg coatings in open and confined zones in conditions simulating automotive applications, Mater. Corros. 61 (2010) 412–420.

[22] M. Salgueiro Azevedo, C. Allély, K. Ogle, P. Volovitch, Corrosion mechanisms of Zn(Mg,Al) coated steel: 2. The effect of Mg and Al alloying on the formation and properties of corrosion products in different electrolytes, Corros. Sci. 90 (2015) 482–490.

[23] T. Prosek, N. Larché, M. Vlot, F. Goodwin, D. Thierry, Corrosion performance of Zn-Al-Mg coatings in open and confined zones in conditions simulating automotive applications, Mater. Corros. 61 (2009) 412-420.

[24] J. Han, K. Ogle, Dealloying of $MgZn_2$ Intermetallic in Slightly Alkaline Chloride Electrolyte and Its Significance in Corrosion Resistance, J. Electrochem. Soc. 164 (2017) 952–961.

[25] J. Han, K. Ogle, Cathodic Dealloying of α-Phase Al-Zn in Slightly Alkaline Chloride Electrolyte and Its Consequence for Corrosion Resistance, J. Electrochem. Soc. 165 (2018) 334–342.

[26] P. Qiu, C. Leygraf, I. Odnevall Wallinder, Evolution of corrosion products and metal release from Galvalume coatings on steel during short and long-term atmospheric exposures, Mater. Chem. Phys. 133 (2012) 419–428.

[27] I. Odnevall Wallinder, W. He, P.-E. Augustsson, C. Leygraf, Characterization of black rust staining of unpassivated 55% Al–Zn alloy coatings. Effect of temperature, pH and wet storage, Corros. Sci. 41 (1999) 2229–2249.

[28] X. Zhang, C. Leygraf, I. Odnevall Wallinder, Atmospheric corrosion of Galfan coatings on steel in chloride-rich environments, Corros. Sci. 73 (2013) 62–71.

[29] X. Zhang, T.-N. Vu, P. Volovitch, C. Leygraf, K. Ogle, and I. Odnevall Wallinder, The initial release of zinc and aluminium from non-treated Galvalume and the formation of corrosion products in chloride-containing media, Appl. Surf. Sci. 258 (2012) 4351–4359.

[30] T.-N. Vu, M. Mokaddem, P. Volovitch, K. Ogle, The anodic dissolution of zinc and zinc alloys in alkaline solution. II. Al and Zn partial dissolution from 5% Al–Zn coatings, Electrochim. Acta, 74 (2012) 130–138.

[31] Henkel AG & Co, BONDERITE C-AK 75 known as Ridoline 75, MSDS, No. 234097 V002.2 (2015).

[32] Henkel AG & Co, BONDERITE M-AC 50 CF known as Fixodine 50 CF, MSDS, No. 47026 V002.4 (2015).

[33] Henkel AG & Co, BONDERITE M-AD 40110 known as primaire M, MSDS, No. 73533 V001.6 (2015).

[34] Henkel AG & Co, BONDERITE M-Zn 1421-A R (EU) BU, MSDS, No. 579603 V001.0 (2016).

[35] D. P. Dutta, A. Singh, A. K. Tyagi, Ag doped and Ag dispersed nano $ZnTiO_3$: Improved photocatalytic organic pollutant degradation under solar irradiation and antibacterial activity, J. Environ. Chem. Eng. 2 (2014) 2177–2187.

[36] Y. Wang, P.-H. Yuan, C.-M. Fan, Y. Wang, G.-Y. Ding, Y.-F. Wang, Preparation of zinc titanate nanoparticles and their photocatalytic behaviors in the photodegradation of humic acid in water, Ceram. Int. 38 (2012) 4173–4180.

[37] S. Wu, X. Liu, Y.L. Chan, C.Y. Chung, P.K. Chu, C.L. Chu, K.O. Lam, K.W.K. Yeung, W.W. Lu, K.D.K. Luk, K.M.C. Cheung, In vitro bioactivity and osteoblast response on chemically modified biomedical porous NiTi synthesized by capsule-free hot isostatic pressing, Surf. Coat. Technol. 202 (2008) 2458–2462.

[38] M. T. Pham, W. Matz, H. Reuther, E. Richter, G. Steiner, Hydroxyapatite nucleation on Na ion implanted Ti surfaces, J. Mater. Sci. Lett. 19 (2000) 1029–1031.

[39] D. Zimmermann, A. G. Muñoz, J. W. Schultze, Microscopic local elements in the phosphating process, Electrochim. Acta 48 (2003) 3267–3277.

[40] A. W. Taylor, A. W. Frazier, E. L. Gurney, J. P. Smith, Solubility products of di- and trimagnesium phosphates and the dissociation of magnesium phosphate solutions, Trans. Faraday Soc., 59 (1963) 1585-1589.

[41] D. L. Felker, P. M. A. Sherwood, Zinc phosphate (Zn3(PO4)2) by XPS, Surf. Sci. Spectra, 9 (2012) 106-113.

[42] I. Van Roy, H. Terryn, et G. Goeminne, Study of the phosphating treatment of aluminium surfaces: role of the activating process, Colloids Surf. Physicochem. Eng. Asp., 136 (1998) 89-96.

[43] P. A. Connor, A. J. McQuillan, Phosphate Adsorption onto TiO $_2$ from Aqueous Solutions: An in Situ Internal Reflection Infrared Spectroscopic Study, Langmuir. 15 (1999) 2916–2921.

[44] H. Onoda, A. Matsukura, Influence of pH-control in phosphoric acid treatment of titanium oxide and their powder properties, Mater. Res. Bull. 66 (2015) 151–155.

[45] D. Zhao, C. Chen, Y. Wang, H. Ji, W. Ma, L. Zang, J. Zhao, Surface Modification of TiO_2 by Phosphate: Effect on Photocatalytic Activity and Mechanism Implication, J. Phys. Chem. C. 112 (2008) 5993–6001.

[46] H. Onoda, S. Fujikado, T. Toyama, Preparation of titanium phosphate white pigments with titanium sulfate and their powder properties, J. Adv. Ceram. 3 (2014) 132–136.

[47] T. S. N. Sankara Narayanan, Surface pretreatment by phosphate conversion coatings_ a review, Rev. Adv. Mater. Sci, 9 (2005) 130-177.

[48] W. Zhou, D. Shan, E.-H. Han, W. Ke, Structure and formation mechanism of phosphate conversion coating on die-cast AZ91D magnesium alloy, Corros. Sci., 50 (2008) 329-337.

[49] H. Khan, Sol–gel synthesis of TiO_2 from $TiOSO_4$: characterization and UV photocatalytic activity for the degradation of 4-chlorophenol, React. Kinet. Mech. Catal., 121 (2017) 811-832.

Chapter 5: On the uneven distribution of Ti-based conversion coating on multiphase ZnAlMg coating

Authors: Perrine Tanguy[a,b, 1], Christian Allély[b], Diana Dragoe[c], Michel Lahaye[d], Vaclav Sefl[e] and Jan Stoulil[e] and Polina Volovitch[a]

[a] *Chimie ParisTech, PSL Research University, CNRS, Institut de Recherche de Chimie Paris (IRCP), F-75005 Paris, France*

[b] *Global Research and Development, ArcelorMittal Maizières Research, France*

[c] *Institut de Chimie Moléculaire et des Matériaux d'Orsay, CNRS, Université Paris-Sud 11, 91405 Orsay Cedex, France*

[d] *PLateforme Aquitaine CAractérisation de MATériaux Placamat, CNRS, Université de Bordeaux, 33600 Pessac*

[e] *University of Chemistry and Technology Technicka 5, Prague, Czech Republic*

Corresponding author: Polina Volovitch

Tel.: (+33) 1 44 27 20 74 Fax: (+33) 1 46 34 07 53

Email: polina.volovitch@chimieparistech.psl.eu

Abstract: The chemical composition, speciation and spatial distribution of Ti-based conversion coating (TiCC) on multiphase ZnAlMg coating on steel was studied by SEM-EDS, XPS, nano AES, GD-OES. A ZnAlMg coating containing Zn dendrites, binary eutectoid Zn-Al and binary eutectic Zn_2Mg-Zn as well as three pure phases (Zn, ZnAl and Zn_2Mg) simulating the ZnAlMg microstructure were characterized after alkaline degreasing and TiCC procedure. XPS demonstrated the presence of TiO_2, Mn-modified hopeite, F-doped ZnO on all phases and MgF_2 on Mg-containing substrates. Electron microscopy and nano-AES spectroscopy and mapping demonstrated a heterogeneous TiCC distribution on the multiphase substrate, binary eutectoid ZnAl and binary eutectic Zn_2Mg phases being covered with thicker CC than monophase Zn dendrites. Galvanic coupling inside binary eutectic phases was proposed to be responsible for the enhanced TiCC precipitation kinetics on these phases because of the closely spaced anodes and cathodes on ZnAl and Zn_2Mg compared to Zn dendrites. Electrochemical tests of model phases consolidated this hypothesis.

1. Introduction

Ti-based conversion coatings (TiCC) are nanometric coatings providing corrosion resistance and paint adherence to HDG [1], [2], aluminium [2-6] or ZnAlMg substrates [7]. It is generally assumed that thin Zr-based CC (ZrCC) and TiCC, deposited by immersion procedure [8] or by coil coating [9], follow a similar precipitation mechanism as they both exhibit a partial orbital-d filling (Ti: [Ar] $3d^2\ 4s^2$; Zr: [Kr] $4d^2\ 5s^2$). The precipitation of TiCC on HDG is considered as a multi-step process consisting of 1) the metal substrate dissolution (5-1) accompanied by local alkalization from cathodic reactions (5-2 and 5-3) leading to 2) the CC precipitation as titanium oxide (5-4) at pH = 2.5 – 8.5 [10].

- Anodic dissolution:

$$\mathrm{Zn} \rightarrow \mathrm{Zn}^{2+} + 2\mathrm{e}^{-} \tag{5-1}$$

- Cathodic reduction leading to pH increase:

$$\mathrm{O}_2 + 4\mathrm{H}^{+} + 4\mathrm{e}^{-} \rightarrow 2\mathrm{H}_2\mathrm{O} \tag{5-2}$$

$$2\mathrm{H}^{+} + 2\mathrm{e}^{-} \rightarrow \mathrm{H}_2 \tag{5-3}$$

- TiCC precipitation:

$$\mathrm{TiF_6}^{2-} + 4\mathrm{OH}^{-} \rightarrow \mathrm{TiO}_2.\mathrm{H}_2\mathrm{O} + 6\mathrm{F}^{-} \tag{5-4}$$

The TiCC procedure consists of several steps, including alkaline degreasing, rinsing, immersion in the TiCC bath and final rinsing.

Considering the low thickness of TiCC and the large number of elements composing the formulation, it is challenging to define the precise chemical composition of the conversion coating and its distribution on multiphase substrates. However, several works were published for Al-based [4]-[6] and Zn-based substrates [11]-[12].

ZnAlMg coatings have a complex multiphase microstructure composed by Zn dendrites, and binary and ternary eutectics formed by Zn and Al-rich phase and/or intermetallic Zn_2Mg [13-15]. The reactivity variation between phases can result in a micro-galvanic coupling between phases and a heterogeneous spatial distribution of cathodes and anodes on the multiphase substrate and by consequence an inhomogeneous coating deposition [4]-[7], [16].

On Al alloys [4], [5], the ZrCC preferential precipitation was observed on and in the vicinity of cathodic intermetallic particles.

Recent work on ZnAlMg substrates has also shown the preferential precipitation of ZrCC on Zn-rich phases at the expense of Al-rich and Mg-rich ones [7].

The impact of the microstructure on the CC precipitation and spatial distribution over multiphase substrates had already been reported for chromate-based CC [16].

However, the thickness of chromate CC, around 100 nm [16], is about 10 times higher than for TiCC or ZrCC. The impact of a heterogeneous distribution of CC on ZnAlMg on the paint adherence and local under paint corrosion hence can be more critical for TiCC and ZrCC.

The objective of the present work is to evaluate the impact of the phase composition and distribution in the ZnAlMg substrate on the distribution and chemical composition of TiCC. To do so, the distribution and chemical composition of the precipitated TiCC was studied on synthetic pure phases composing ZnAlMg and on a multiphase coating combining different surface analytical techniques.

The reactivity of the ZnAlMg material phases during the TiCC precipitation and possible effect of galvanic coupling between and inside phases were evaluated through electrochemical measurements.

2. Experimental

2.1. Materials

Two types of materials were tested including model ZnAlMg multiphase coatings and individual pure phases.

2.1.1. Model ZnAlMg materials

ZnAlMg coated steel with a thickness of 500 µm were supplied by ArcelorMittal in the skin-passed state with a roughness of 0.95 ± 0.03 µm. ZnAlMg coatings were produced by hot dip process with thickness around 10 µm. The selected composition contained Al ≤ 5 wt. % and Mg < 3 wt. %. Phase composition and details about microstructure of the materials are summed up in Table 9. Further details about ZnAlMg coatings microstructure is available in Appendix 2.

Samples with a size of 100 mm × 200 mm were cut from the supplied substrate and subjected to a petroleum ether solvent cleaning process to ensure complete removal of any oils or surface contamination. During OCP measurements, the exposed area ($A = 3\ cm^2$) of the ZnAlMg samples was defined using insulator tapes containing precut portholes (PortHoles ™ Electrochemical Sample Masks).

2.1.2. Model phases

For mechanistic purposes, Zn, ZnAl and Zn_2Mg model phases with compositions relevant to the ZnAlMg coating were synthetized. Depending on their composition, alloys were weighed in masses and heated at 500 °C. Liquid mixtures were then filtered through ceramic filters consisting of 61 wt. % Al_2O_3 and 39 wt. % SiO_2 (10 pores per square inch porosity). The composition, crystallinity, grain size and orientation and hardness of all synthetized phases were characterized using atomic absorption spectroscopy, SEM, EBSD, XRD and nanoindentation techniques. The composition of the obtained phases is summarized in Table 9. Complementary information regarding pure phases microstructure is gathered in Appendix 3. In addition, Al (99.999 % purity) supplied by GoodFellow was used. It should be noted that the studied ZnAlMg material and ZnAl phase are multiphase while Zn and Zn_2Mg are monophase.

Table 9: Composition of ZnAlMg and pure phases relevant for ZnAlMg coating

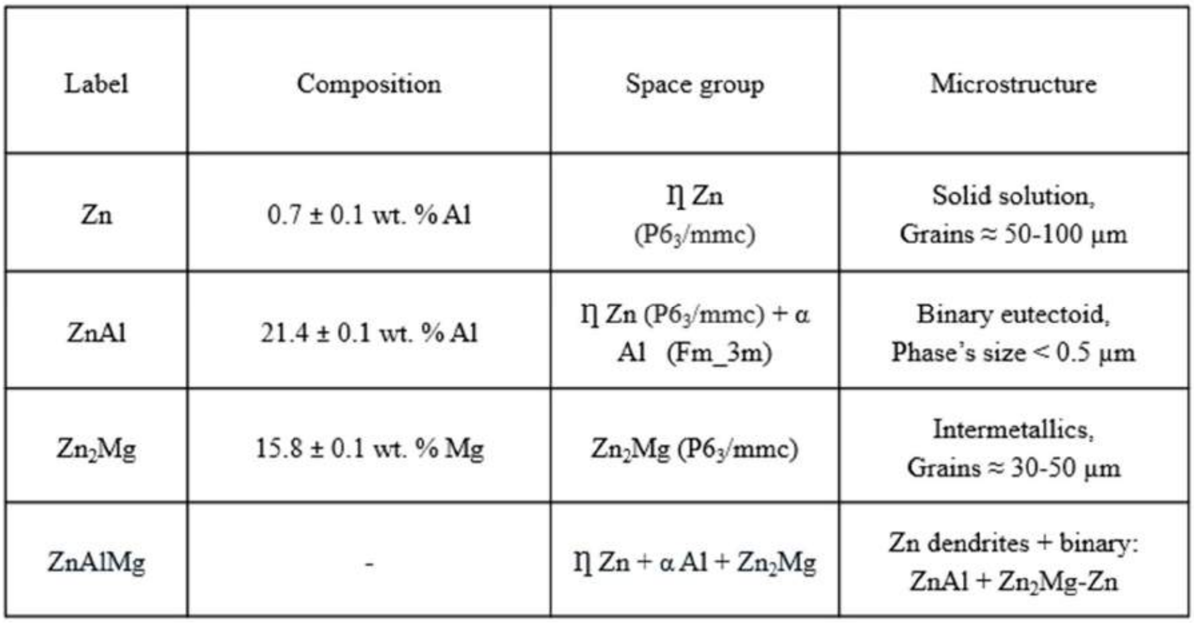

Label	Composition	Space group	Microstructure
Zn	0.7 ± 0.1 wt. % Al	η Zn ($P6_3/mmc$)	Solid solution, Grains ≈ 50-100 µm
ZnAl	21.4 ± 0.1 wt. % Al	η Zn ($P6_3/mmc$) + α Al (Fm_3m)	Binary eutectoid, Phase's size < 0.5 µm
Zn_2Mg	15.8 ± 0.1 wt. % Mg	Zn_2Mg ($P6_3/mmc$)	Intermetallics, Grains ≈ 30-50 µm
ZnAlMg	-	η Zn + α Al + Zn_2Mg	Zn dendrites + binary: ZnAl + Zn_2Mg-Zn

Samples were polished with SiC polishing discs (up to 4000 grit). After polishing, all samples were rinsed using ethanol and dried with compressed air. Prior to immersion, the reacting area (A= 1 cm²) of the pure phases was defined using insulator tapes containing precut portholes (PortHoles ™ Electrochemical Sample Masks).

2.2. TiCC solutions

Solutions used to deposit TiCC on pure phases and model ZnAlMg material are listed in Table 10.

Table 10: Main components and their concentration in solutions used for the TiCC procedure

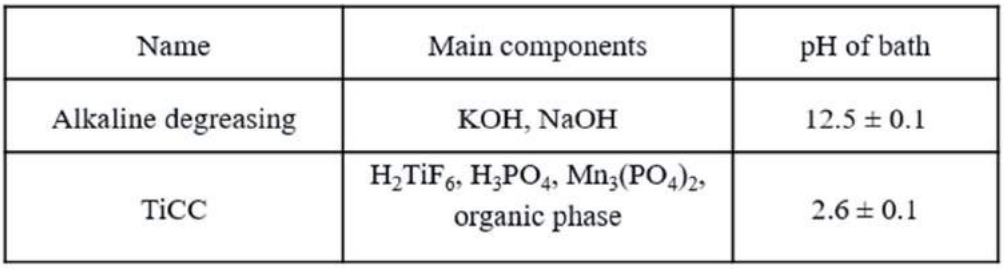

Name	Main components	pH of bath
Alkaline degreasing	KOH, NaOH	12.5 ± 0.1
TiCC	H_2TiF_6, H_3PO_4, $Mn_3(PO_4)_2$, organic phase	2.6 ± 0.1

2.3. TiCC procedure

2.3.1. Bication Zn-Ni phosphating procedure

The following general procedure was used to precipitate Ti-based conversion layers on pure phases:

- Alkaline degreasing at 55 °C for 2 min
- Osmosis water rinsing at 50 °C and at ambient temperature
- Immersion in TiCC bath at 60 °C
- Osmosis water rinsing at room temperature
- Drying in hot air stream

For ZnAlMg coating, the alkaline degreasing was performed by spraying on both faces of the sample for 12 sec. All baths were used maximum 12 h after mixing and renewed every 24 h. The immersion of the ZnAlMg substrate in the TiCC bath followed by an osmosis water rinsing enabled the conversion of insoluble CC elements on ZnAlMg without having to consider the possible impact of the application procedure on the TiCC on ZnAlMg phases and minimized the effect of unreacted and/or soluble products. Three replicates were performed to control the reproducibility.

2.3.2 Bath composition determination for Hydra-Medusa calculations

The predominant equilibrium species which could be expected from thermodynamics were calculated using the Hydra-Medusa software [17]. For the calculation, the concentrations of Ti^{4+}, PO_4^{3-} and Mn^{2+} in the 20 wt. % TiCC-bath were evaluated using ICP-AES. It was assumed that the totality of the fluoride ions available in the bath originate from the hexafluoro titanic acid (H_2TiF_6). Hence, the fluoride concentration was defined as 6 times the Ti^{4+} one. Details about elements concentration are available in Appendix 6.

Concentrations of the substrate elements (Zn^{2+}, Al^{3+} and Mg^{2+}) getting dissolved during the TiCC precipitation and incorporated in the conversion coating thickness were determined from the titration of the TiCC bath by a NaOH 1M solution. When reaching pH=7, the total acidity contained in the TiCC bath is neutralized. Considering that the neutralized acidity is twice the Zn concentration dissolved at the anodes (see reactions 5-1 and 5-2), it is possible to evaluate the total Zn concentration that is susceptible to be dissolved in the bath. The evaluation of the Zn/Al and Zn/Mg ratios was made by bath analysis using ICP-AES after the immersion of a ZnAlMg material sheet in the TiCC bath.

The resulting elemental concentrations used for the Hydra-Medusa software simulation are shown in Table 11.

Table 11: Elemental concentrations for the Hydra-Medusa software simulation of the precipitated species in TiCC

Elements	Concentration / mM
Zn^{2+}	113
Al^{3+}	57
Mg^{2+}	57
PO_4^{3-}	112
Ti^{4+}	66
Mn^{2+}	88
F^-	420

2.4. Electrochemical measurements

Open Circuit Potential (OCP) measurements were performed using a Biologic VSP potentiostat. A three-electrode cell was used with a saturated calomel electrode (SCE) as the reference electrode, a platinum wire as the counter electrode and the sample as the working electrode. Anodic and cathodic polarizations were carried out at a 2 mV/sec sweeping rate without stirring. Three replicates were made for this experiment.

2.5. Surface characterization

The distribution of the Ti-based conversion coating deposited on model phases was investigated using a Field Emission Gun Scanning Electron Microscope (FEG-SEM) JEOL 7800F at an accelerating voltage of 15 kV, coupled with a Brucker Xflash 6160 Energy Dispersive Spectroscopy (EDS) device using a Si(Li) detector and equipped with QUANTAX 1.9 software (Bruker AXS). Samples were observed not later than 4 h after the conversion coating procedure. A minimum of 4 replicates were made to control the reproducibility.

GD-OES chemical analyses were performed using a Horiba Jobin Yvon GD-Profiler 2 GD-OES instrument to evaluate the distribution of P, Ti, Mn and F within the thickness of TiCC. Samples were analyzed under a pressure of 700 Pa and a power of 30 W. The sampling time interval was 0,01 sec for the first 3 min then 0,1 sec until the end of the profile acquisition. Parameters that could possibly influence the eroded mass of material per sec are the relative sputtering rate, the material density, the interaction with Ar^+ ions etc. Analyses were reproduced twice for reproducibility purposes.

The distribution and thickness of TiCC on all phases of ZnAlMg material was evaluated by nano Auger Electron Spectroscopy (AES) with electron microscopy, using a PHI 170 setup. The primary electron beam voltage was 20 kV and the beam current was 1 nA. A CMA analyzer with an incident angle of 30° with respect to the surface normal was used and experiments were performed at a pressure of $2{,}3.10^{-6}$ Pa. Depth profiles were carried out in a sequential mode with an Ar^+ ion beam sputtering the surface at a voltage of 2 kV and a current of 1 µA. The ion beam sputtered a 4 mm^2 surface at an angle of 60 ° with respect to the surface normal. The TiCC thickness was defined at 50 % of the inflection zone of TiCC markers (Ti, P, Mn and F), to avoid the figure overload hence a less effective readability. A minimum of 2 replicates were made to control the reproducibility.

The chemistry of the deposited layer and the average concentrations after immersion of the model ZnAlMg coating and pure phases in the TiCC bath were studied by X-ray Photoelectron Spectroscopy (XPS) using K Alpha, Thermo Fisher Scientific spectrometer, (base pressure in the low 10^{-9} mbar range) equipped with a monochromatic aluminium source (Al K_α, 1486.68 eV). A spot size of 400 µm corresponding to an irradiated zone of approximately 1 mm^2 was used. The hemispherical analyzer was operated at 0 ° take off angle in the Constant Analyzer Energy (CAE) mode, with a pass energy of 200 eV and an energy step of 1 eV for the acquisition of wide scans, while narrow scan spectra centered on the Ti 2p region were recorded at a pass energy of 100 eV and an energy step of 0.1 eV. Charge compensation was achieved by means of a “dual beam” flood gun, using low energy electrons (5 eV) and argon ions. The determination of the type of phosphate precipitates created during the conversion reaction was performed using the P 2s region as the P 2p region is interfered by Zn 3s. Samples were fixed on the support using adhesive conducting tape.

The recorded spectra were processed by means of the Avantage software, using a peak-fitting routine with Shirley background and symmetrical 70 % - 30 % mixed Gaussian-Lorentzian peak shapes. The atomic ratios were evaluated following normalizations of the peak areas with the Scofield sensitivity factors.

The binding energy scale was calibrated on the neutral carbon set at 284.8 eV. Regarding reproducibility, the majority of quantitative and qualitative measurements were replicated at least 5 times.

3. Results

3.1. Depth profiles distribution of TiCC by GD-OES

3.1.1. Erosion profiles of TiCC on ZnAlMg

To detect the TiCC and evaluate the average depth distribution on ZnAlMg material after alkaline degreasing followed by immersion in the TiCC bath at 60 °C for 30 sec, GD-OES profiles were performed showing the distribution of TiCC tracers within the CC thickness as visible on Figure 29.

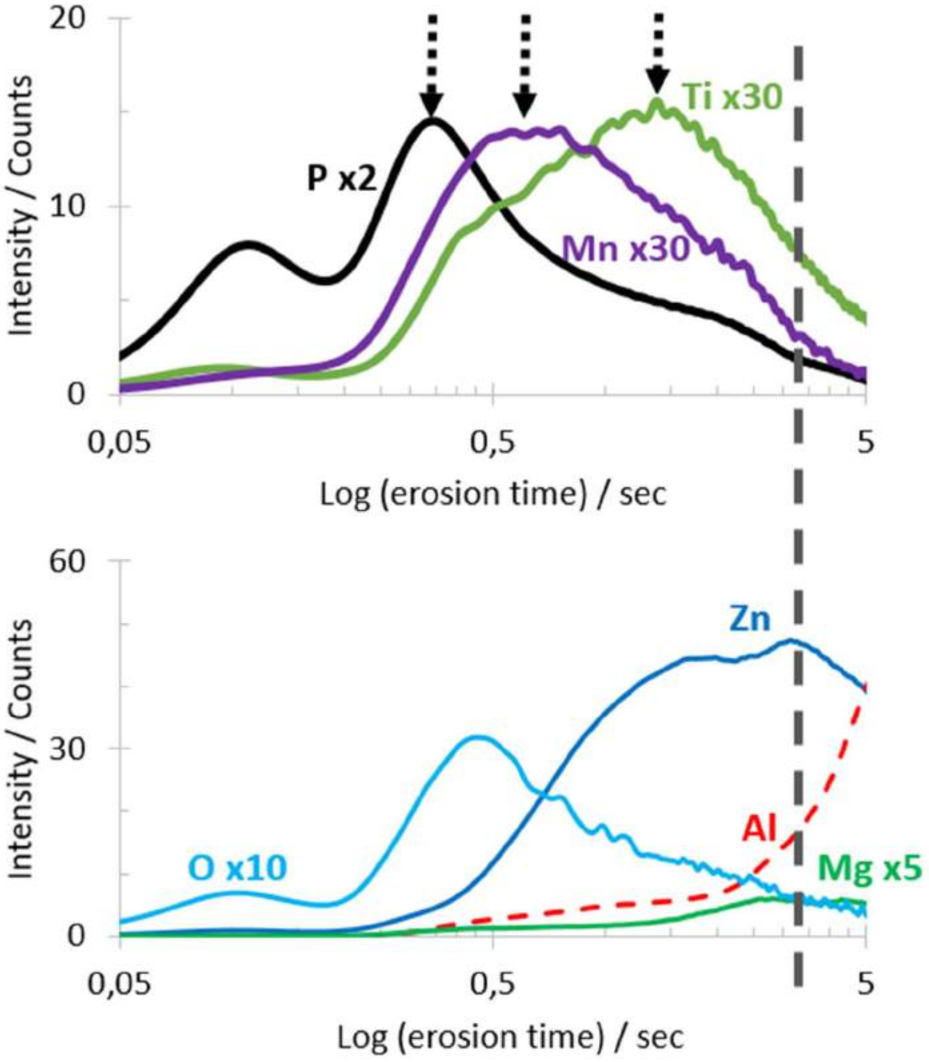

Figure 29: Distribution of P, Ti, Mn and F by GD-OES profile on ZnAlMg after alkaline degreasing followed by immersion in TiCC bath at 60 °C for 30 sec

The figure presents the intensity of different elemental signals as a function of the sputtering time and not the eroded depth because the average thickness of TiCC evaluated from DiP was in the range of 10 nm and the exact calibration of erosion rate for such a thin layer on the top surface with significant rugosity is impossible. Black arrows in the figure designate the maximum intensity of each component of TiCC. All tracers do not reach their maximum intensity at the same time. This way, the CC/substrate interface was defined as a position at 50 % of the inflection zone of the most in-depth tracer, Ti. Regarding the distribution of the tracers visible in the figure, Ti is located at the interface with the ZnAlMg substrate while P is concentrated in the outer layer. The presence of Mn is detected in the center of the layer. The P enrichment in the outer layer of the CC is coherent with the results communicated for an industrial HDG substrate [12].

From the distribution of TiCC tracers within the CC thickness, it is possible to formulate some hypothesis about the composition of the TiCC. On one hand, it seems unlikely to have a $Ti_x(PO_4)_y$ precipitate because the maximums of P and Ti do not appear at the same time. However, it is in accordance with the formation of TiO_2 on the surface.

The juxtaposition of P and Mn signals in the GD-OES profile is consistent with the previously reported $Mn_x(PO_4)y$ presence in the TiCC bath [18].

3.2. Surface distribution of TiCC by SEM-EDS

A typical example of TiCC distribution on ZnAlMg after immersion in TiCC bath at 60 °C for 30 sec is present in Figure 30. Tracers used to detect the presence of TiCC on the surface are P, Ti, Mn and F. Although the surface rugosity of the skin-passed ZnAlMg material can interfere quantitative analysis of TiCC tracers, some observations can be made.

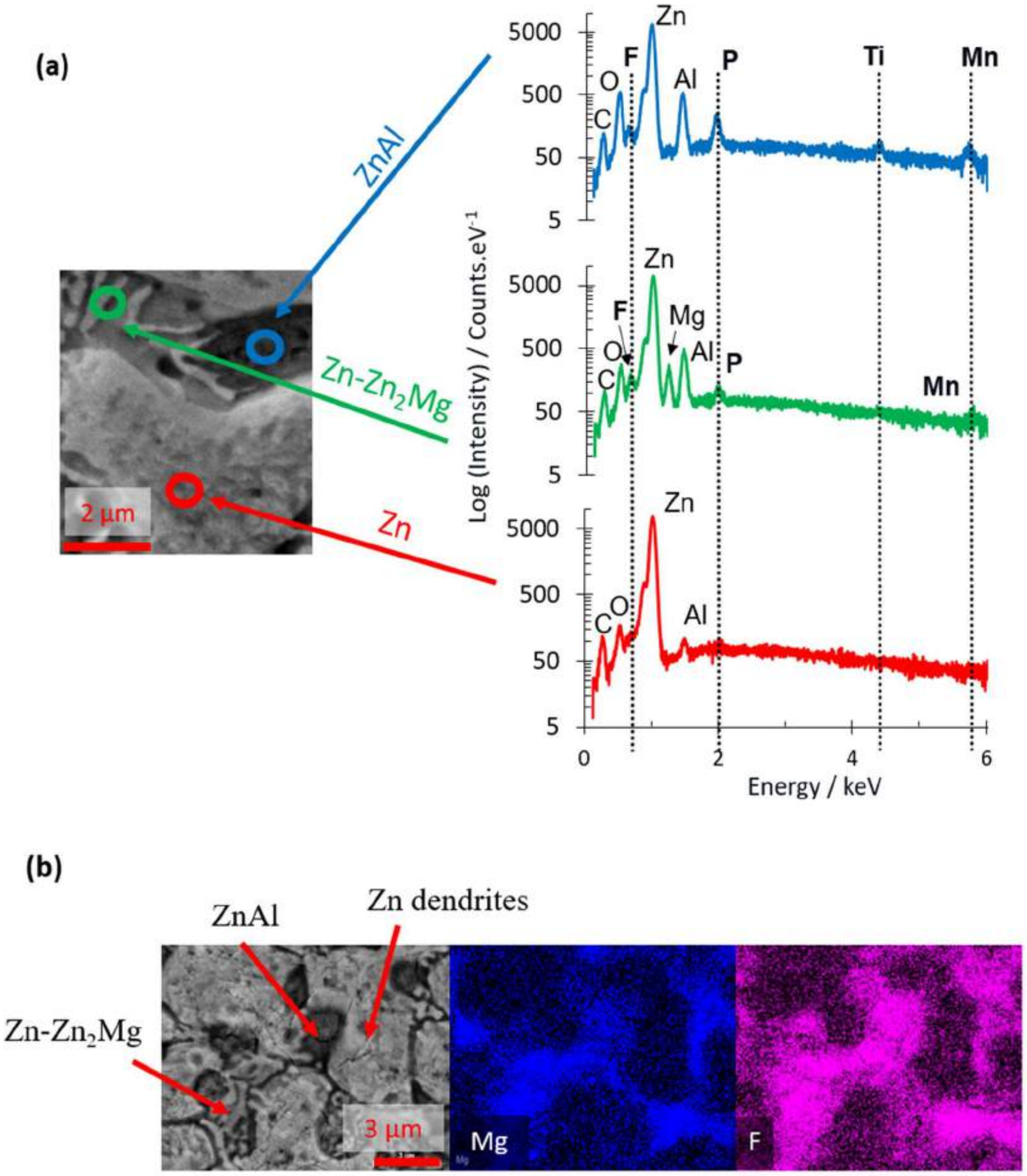

Figure 30: (a) SEM image of ZnAlMg coating (as indicated) after immersion in TiCC at 60 °C for 30 sec and EDS distribution of P, Ti, Mn and F on different phases and (b) SEM image of ZnAlMg and EDS mapping of Mg and F distribution after immersion in TiCC at 60 °C for 30 sec

First of all, the preferential precipitation of TiCC tracers was observed on Al-rich phase at the expense of Zn dendrites in Figure 30-a. While the highest concentrations of P, Ti and Mn are observed on the Al-rich phase, the fraction of P and Ti were near the detection limit of the method on Zn dendrites. Only a small concentration of P and Mn were measured on Zn-Zn_2Mg binary eutectic, but no Ti. The highest concentrations of F were measured on AlZn and Zn-Zn_2Mg. The similarity of Mg and F distribution patterns was confirmed through an EDS mapping of the ZnAlMg surface as shown in Figure 30-b. The difference in the distribution of Ti, P, Mn and F between phases let us suppose that very complex and non-homogeneous precipitation mechanisms take place on the ZnAlMg surface depending on the phase exposed to the conversion coating.

To sum up, SEM-EDS demonstrated inhomogeneous local distribution of different components of TiCC, varying from one phase to the other.

3.3. Local distribution of TiCC thickness on ZnAlMg phases by AES

3.3.1. Nano-AES profiles of TICC thickness on ZnAlMg phases

To complement the EDS profiling allowing the average TiCC thickness measurement, nano-AES analyses were carried out on each phase of the multiphase ZnAlMg material to evaluate the homogeneity of the TiCC. For reproducibility purpose, 3 distinct areas were measured for each phase.

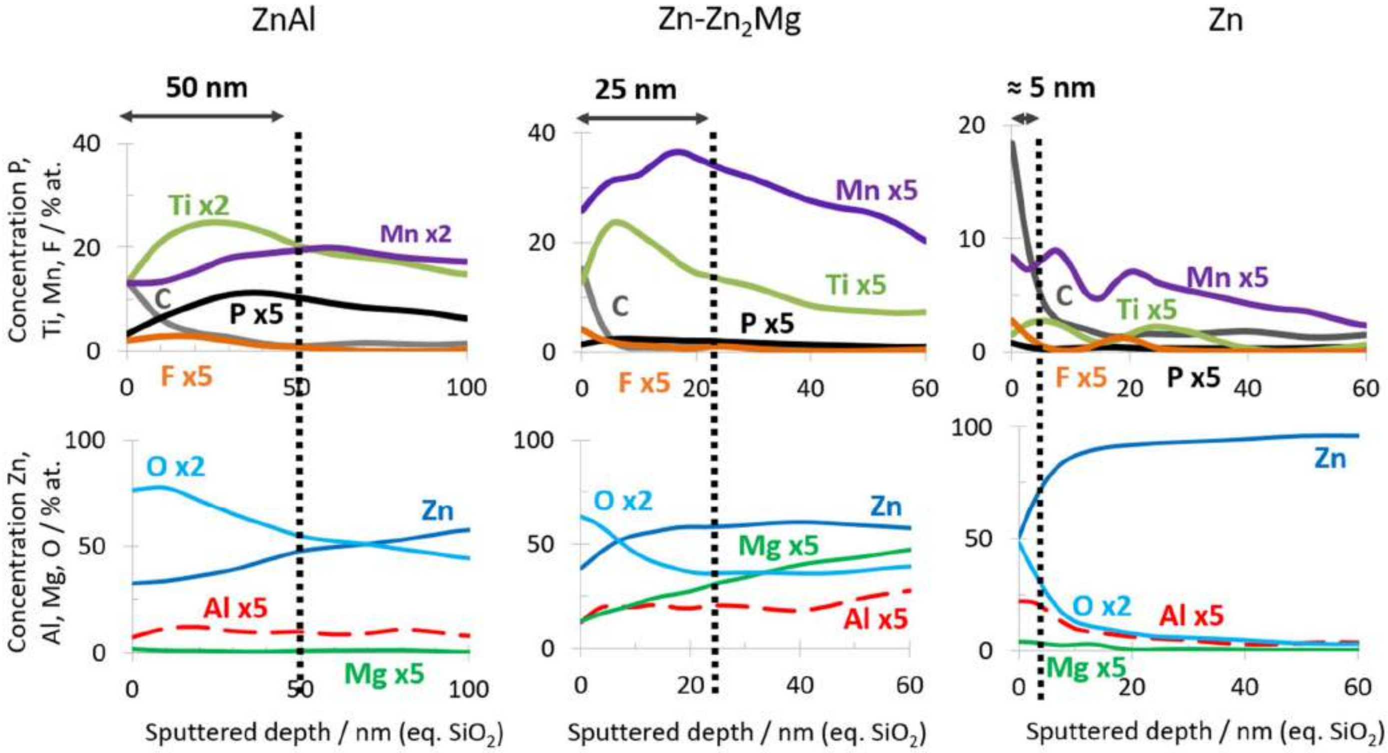

Figure 31: AES profiles of different phases of ZnAlMg after immersion in TiCC bath at 60 °C for 30 sec after standard cleaning

Figure 31 presents typical AES depth profiles obtained on different phases of ZnAlMg coating. The thinnest TiCC is detected on Zn dendrites (< 10 nm). In fact, the signal of TiCC tracers was so fluctuating, as shown by the corresponding AES profile, that the interface was placed using the Zn and O concentration profiles, at 50 % of the inflection zone for conveniency. The Al-rich phase exhibits the thickest CC with an estimated thickness close to 50 nm. On Zn-Zn_2Mg, the measured TiCC thickness was close to 25 nm. Globally, AES analyses confirmed the preferential precipitation occurring on Al-rich phase compared to Zn-Zn_2Mg and Zn dendrites. The evolution of F was hardly detectable using AES. The distribution of Ti and Mn with the CC thickness follows a similar trend as detected by GD-OES. The position of P seems to be closer to the ZnAlMg coating interface compared to GD-OES characterization. To explain this difference of distribution, it is essential to remember that the ZnAlMg substrate is rough (Ra = 0,95 µm in average) due to the skin pass operation. The GD-OES measurement reveals a spread interface where both plateaus and valleys are analyzed at the same time.

It is worth noticing that, during the erosion process, a variation of sputtering rate from one phase to the other was observed, which is illustrated by SEM images after different erosion times by AES as presented in Figure 32.

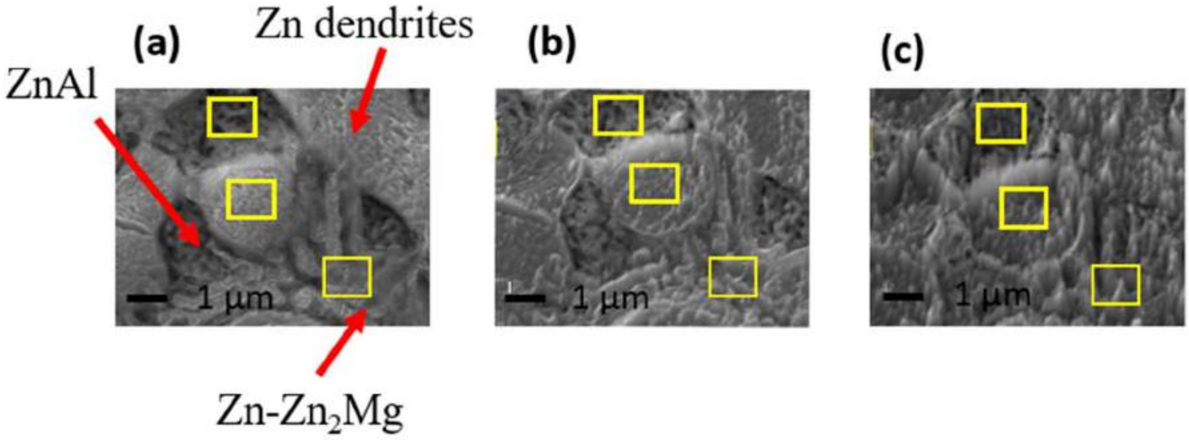

Figure 32: SEM images of ZnAlMg surface after alkaline degreasing and immersion in TiCC bath at 60 °C for 30 sec : (a) before sputtering, (b) after theoretical 70 nm of depth sputtering and (c) after theoretical 300 nm of depth sputtering

After a theoretical depth sputtering of 300 nm, one can observe that Zn-Zn_2Mg phase is fully eroded. The Zn dendrites are also highly eroded as the level difference between ZnAl and Zn dendrites shows while the ZnAl one seems to be less impacted by the Ar^+ beam. This selectively low erosion rate is in line with the thickest oxidized layer present on the ZnAl phase. Indeed, the erosion of oxides is known to be slower than the erosion of corresponding metals. Differences in erosion rates of different phases composing ZnAlMg coating by Ar^+ was also verified by GD-OES erosion and following profilometry described in the next section.

3.3.2. Erosion rates variation between Zn, ZnAl and Zn_2Mg by GD-OES

To evaluate the impact of the erosion process on ZnAlMg phases, erosion profiles of the pure phases simulating the ZnAlMg microstructure were carried out by GD-OES at 0.1 keV. The Figure 33 shows the calculated sputtering rates after 3 min of erosion from the crater depth measured with a profilometer.

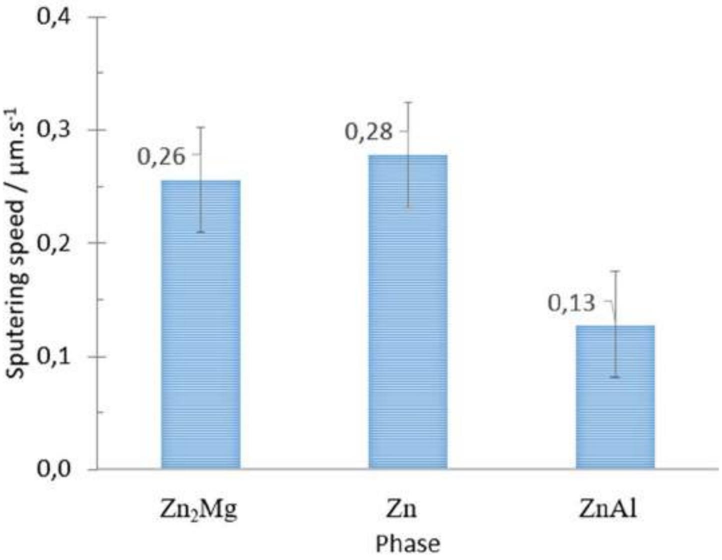

Figure 33: Mean sputtering rates of untreated and polished (4000 SiC) Zn, ZnAl and Zn2Mg

The calculated sputtering rates show that the Zn phase simulating Zn dendrites exhibits the highest sputtering rate, close to the one of the Zn_2Mg intermetallic phase. The ZnAl phase has the lowest sputtering rate, at least twice slower than for Zn and Zn_2Mg. The difference in sputtering rate between all pure phases is to be kept in mind when evaluating the thickness of the TiCC from sputtering profiles. However, it is important to keep in mind that the sputtering rates calculated by GD-OES cannot be directly applied to evaluate selective sputtering during AES profiling. Indeed, the beam energy is 2 keV for AES while it is 0.1 keV for GD-OES and the relative sputtering rate will not evolve linearly as a function of the beam energy.

3.4. TiCC chemical speciation and Ti concentration on pure phases with XPS

To characterize the chemical speciation and the total concentration of Ti (at. %) on ZnAlMg and each pure model phase simulating ZnAlMg, the chemical forms of Ti, P, Mn and F were determined by X-Ray Photoelectron Spectroscopy on model pure phases and ZnAlMg after alkaline degreasing, immersion in the TiCC bath at 60 °C for 30 sec, surface rinsing and drying. The measured atomic concentration of Ti on model phases are available in Table 12.

Table 12: Atomic concentration of Ti measured on model phases (at. % Ti)

Label	$\frac{\%\,at.\ Ti}{\%\,at.\ Ti + \%\,at.\ \ P + \%\,at.\ Mn + \%\,at.\ \ F + \%\,at.\ Zn}$
Zn	7.2 ± 0.8
ZnAl	14.3 ± 1.5
Zn_2Mg	10.8 ± 1.0

XPS confirmed the highest amount of Ti on ZnAl and the lowest on the Zn phase. This observation is consistent with EDS and AES results.

To ensure a suitable XPS signal intensity for the chemical composition identification, an additional analysis was made on ZnAlMg substrate immersed in TiCC bath at 60 °C for 1 min instead of 30 °C after the alkaline degreasing. For Zn_2Mg, a charge compensation was necessary because all peaks were shifted towards higher energy binding. Spectra of (a) Ti 2p, (b) P 2s, (c) Mn 2p and (d) F 1s obtained on this sample are displayed in Figure 34.

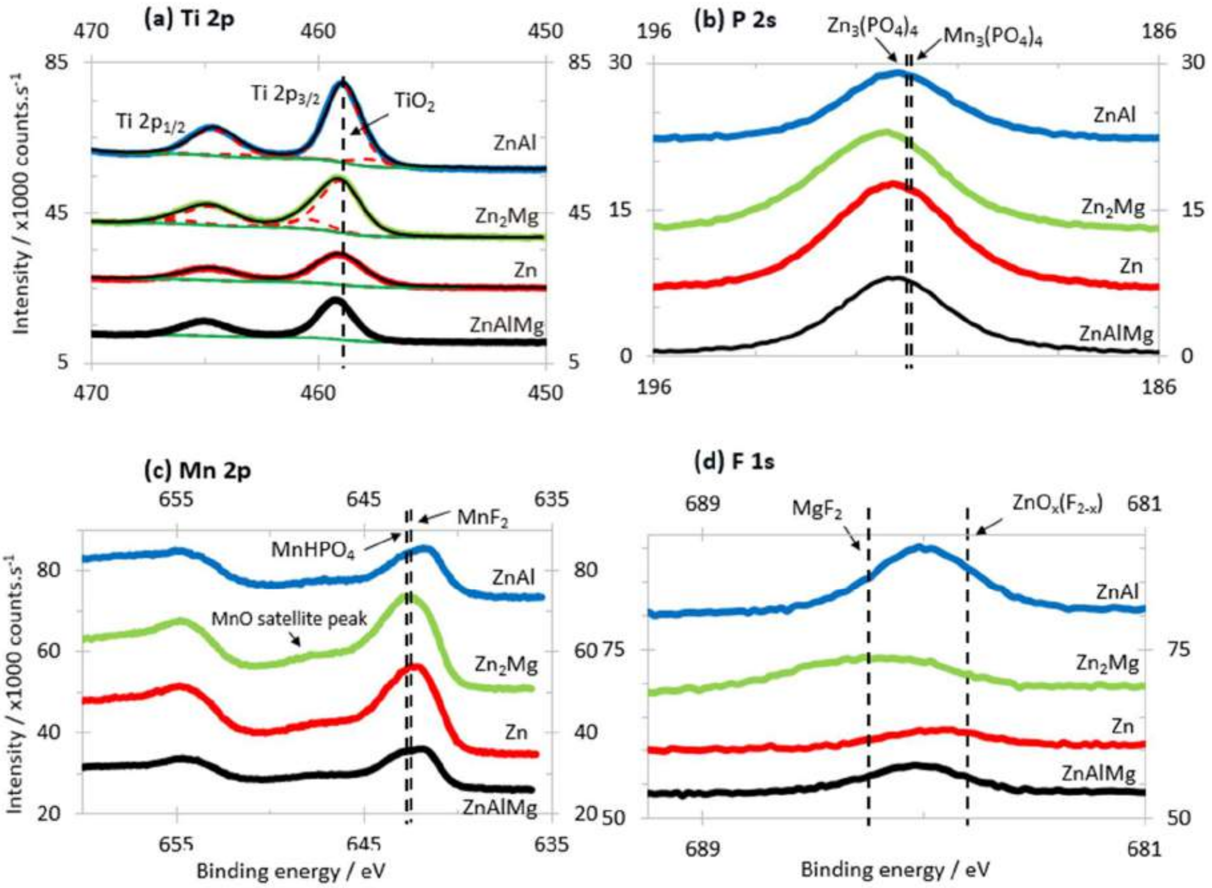

Figure 34: XPS spectra windows of TiCC tracers on pure phases and multiphase ZnAlMg substrates as indicated after standard degreasing and immersion in the TiCC bath at 60 °C for 30 sec

From Figure 34, one can notice that the binding energy for P 2s and Mn 2p regions look similar for ZnAlMg, Zn and ZnAl substrates. In F 1s region, ZnAlMg and ZnAl show a similar peak. However, the Zn peak is shifted towards lower binding energies.

For Ti 2p region, a peak fitting was carried out. The type of bonding involving Ti evidences the presence of TiO_2 at 458.9 eV on all the substrates. The formation of TiO_2 is consistent with the fact that in GD-OES profiles, the Ti is located at the metal/CC interface and not bound with P. This is also consistent with the observation that anodic titanium oxide films obtained under galvanostatic conditions in phosphate buffer consist of TiO_2 while phosphates are incorporated only at the external surface [19]. In the case of ZnAl and Zn_2Mg phases, additional components containing Ti were detected. For Zn_2Mg phase, the highest binding energy seems to correspond to the presence of a mix between Ti-F (e.g. TiF_4) and Ti-O-F compounds [20]. This is a reasonable assumption considering that Ti is present initially as TiF_6^{2-}. For both substrates, the existence of mixed compounds can be interpreted by a pollution or by incomplete transformation of TiF_6^{2-} into TiO_2 (reaction 5-4).

The Mn 2p peaks are of lower intensity on ZnAl phase compared to the other two. It could be due to the lower Mn concentration on that specific phase but it can also be linked to the position of the element inside the TiCC layer. Indeed, as suggested by the GD-OES analysis, Mn is not located near the surface but more in depth. The ZnAl phase exhibits the thickest TiCC layer and it can be expected that quantities of P and Mn should also be the highest. Hence, a big fraction of Mn can be hindered from the XPS analysis. No metallic Zn was detected on any phase confirming that the X-ray beam did not penetrate the sample up to the substrate.

The P 2s peak measured at 191 eV can be associated with the presence of $Mn_3(PO_4)_2$ but also $Zn_3(PO_4)_2$ as their difference in binding energy is only 0.1 eV apart [21], [22].

In the Mn 2p region spectra, the satellite peak at 647.7 eV is typical of Mn^{II} (MnO). The Mn 2p3 peak can be attributed to both Mn^{II} or Mn^{III} [23]. The binding energy of Mn 2p3 is in good agreement with the presence of MnF_2 [24] or $MnHPO_4$, particularly on Zn_2Mg [25].

In the F 1s area, peaks measured on all substrates exhibit a specific binding energy, indicating that several F-based products were probably formed during the conversion reaction. The F 1s peak is extremely large. To understand this, it is important to keep in mind that the binding energies reported for MgF_2 vary in a large range comprised between 684.2 eV and 686.1 eV [26]-[29]. A reference at 686 eV was selected to illustrate it [29] as it fits well the peak measured on Zn_2Mg.

The presence of F-doped ZnO, ZnO_x-(F_{2-x}), could explain the width of the F 1s peak and is consistent with the peak measured on the Zn phase, shifting towards lower binding energies. The F concentration in the TiCC is in large excess. According to the literature and Hydra-Medusa simulations, the other possible F-containing products, except for MgF_2 [29] are soluble and their presence after the surface was rinsed can be only due to their retention in the porosities of the oxide.

Finally, it is interesting to notice that concentrations evolution of Ti and F are similar from one phase to another. A similar observation can be made about Mn and P. This can be attributed to the fact that the CC bath contains H_2TiF_6 and $Mn_3(PO_4)_4$ in its formulation [18].

The complete list of the compounds considered for the analysis is given in Appendix 7.

3.5. Electrochemical behavior of pure phases in degreasing and TiCC baths

For better understanding of the reactivity of all ZnAlMg phases during the TiCC procedure, the open circuit potential of model phases relevant to the ZnAlMg composition was recorded in the degreasing bath after 2 min at 55 °C as visible in Table 13.

Table 13: Open circuit potential (OCP) of pure phases after 2 min in the degreasing bath at 55 °C

Label	OCP in degreasing bath after 2 min at 55 °C / V vs. SCE
Zn_2Mg	-1.43 ± 0.02
ZnAl	-1.63 ± 0.02
Zn	-1.41 ± 0.02

From the degreasing step, ZnAl and ZnAlMg exhibit a much lower potential than Zn and Zn_2Mg. The anodic behavior of ZnAl and ZnAlMg can be attributed to the higher concentration of Al in both materials, Al being highly anodic in highly alkaline environments [30].

Additional OCP measurement were carried out in (a) TiCC bath at 60 °C for 1 min after 2 min of alkaline degreasing and (b) in 5 wt. % Na_2SO_4 solution with the same pH as TiCC but without ions which could precipitate as shown in Figure 35.

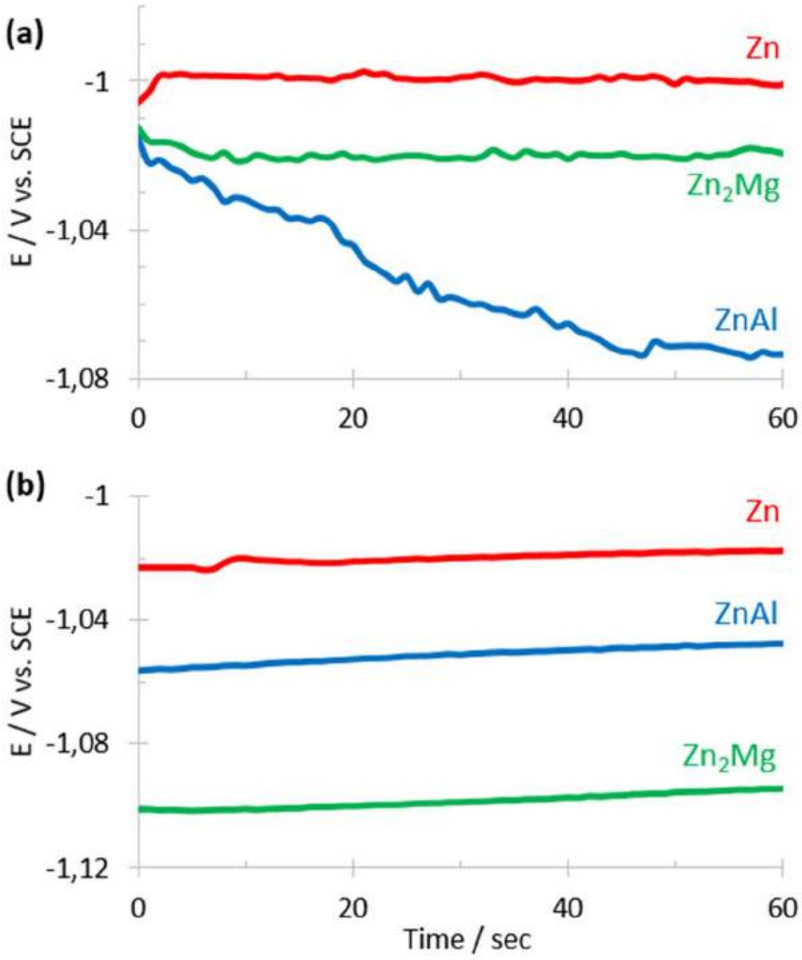

Figure 35: Open Circuit Potentials (OCP) of pure phases in (a) TiCC bath pH 2.6, T=60 °C after 2 min of alkaline degreasing and (b) 5 wt. % Na_2SO_4 pH 2.6, T=60 °C

During the immersion in the TiCC bath, Zn and Zn_2Mg phases reach a significantly similar and stable potential value close to the potential of pure zinc in these conditions (E° = -1 V/SCE for $[Zn^{2+}]$ = 1 M) within seconds of immersion in the TiCC bath.

ZnAl is more anodic than other phases with a potential varying from -1,01 V/SCE to -1,07 V/SCE after 1 min of immersion in the TiCC bath.

A similar measurement was carried out in 5 wt. % Na_2SO_4 pH 2.6 at 40 °C. For Zn phase, the potential remains in the same range as what was measured in TiCC bath after alkaline degreasing. On the contrary, Zn_2Mg is more anodic in 5 wt. % Na_2SO_4 pH 2.6 compared to the TiCC bath at the same pH. The OCP decreased in order Zn>ZnAl>Zn_2Mg.

From the OCP evolution values, a strong galvanic coupling between Zn dendrites and ZnAl eutectoid is not expected. The galvanic coupling between different phases cannot hence explain the better coverage of binary phases and their reactivity should be approached considering the possibility of galvanic coupling inside the phase.

To simulate the reactivity of binary phases (ZnAl and Zn/Zn_2Mg), galvanic coupling experiments were made. The results of galvanic coupling of Zn with Zn_2Mg are shown in Figure 36 a. For ZnAl eutectoid [31], the behavior was simulated by the galvanic coupling of the Zn phase with pure Al, as shown in Figure 36 b. It is expected that all tendencies observed from the coupling will be aggravated compared to the actual intensity of the intra-phase coupling occurring within ZnAl phase.

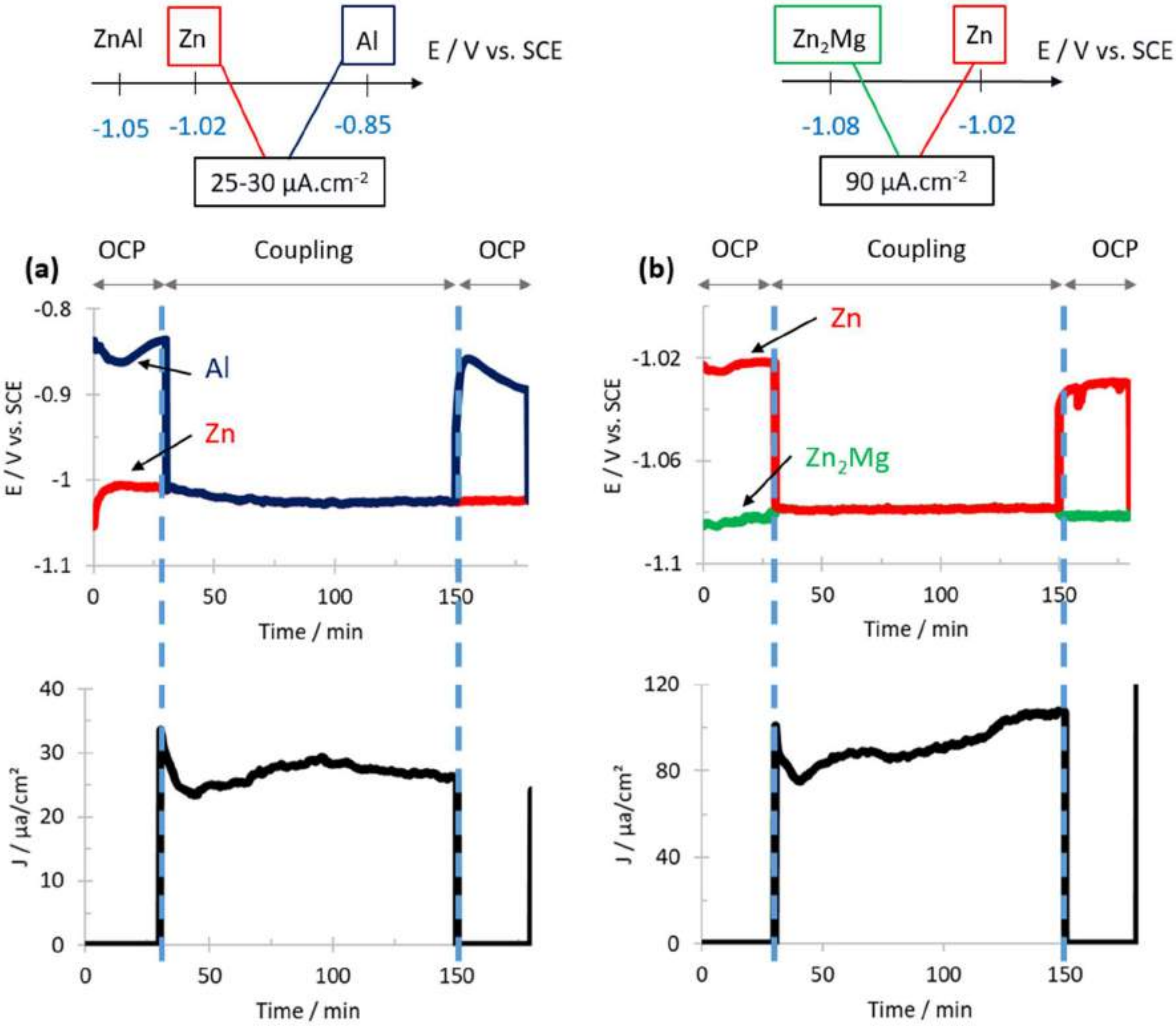

Figure 36: Potential evolution and current density of (a) Zn/Al coupling and (b) Zn/Zn2Mg coupling after respectively 30 min of immersion and 2 h of phase coupling in 5 wt. % Na2SO4 pH 2,6 at 25 °C

When coupling Zn with Zn_2Mg, the Zn phase plays the role of cathode while Zn_2Mg becomes the anode and current density reaches 100 µA.cm^{-2}. Although, a low potential variation exists between Zn and Zn_2Mg (≈ 70 mV/SCE), the high current density measured indicates that a non-negligible local galvanic coupling can occur between Zn and Zn_2Mg lamellas within the ZnAlMg material. A heterogeneous precipitation of the TiCC inside the phase and starting preferentially on Zn lamellas before being extended to Zn_2Mg ones can be assumed.

A similar observation can be made for the coupling of the cathodic pure Al and the anodic Zn phase although a lower current density ranging between 25 and 30 µA.cm^{-2} was measured, probably due to the low reactivity of pure Al observed in 5 wt. % Na_2SO_4 pH 2.6.

4. Discussion

4.1. TiCC chemical composition on all ZnAlMg phases

Using the Hydra-Medusa software calculation, the predominant species formed by each ion during the TiCC are shown in Figure 37.

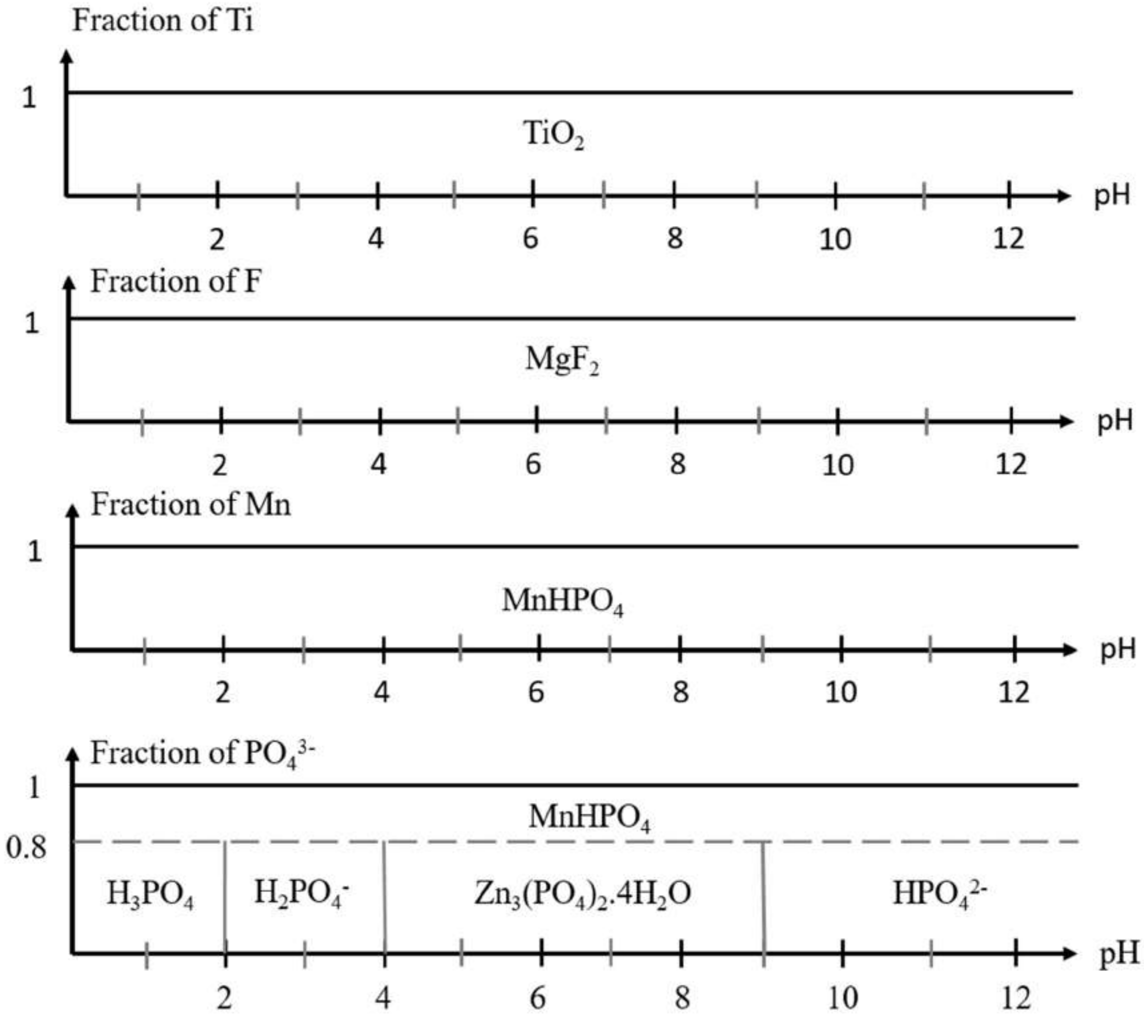

Figure 37: Predominant equilibrium species for 113 mM Zn^{2+} + 57 mM Al^{3+} + 57 mM Mg^{2+} + 112 mM PO_4^{3-} + 66 mM Ti^{4+} + 88 mM Mn^{2+} + 420 mM F^- using the Hydra-Medusa software and associated database of

equilibrium constants at 25 °C. Complexes used in the simulation include (a) for Zn species alone: ZnO (cr), $Zn(OH)_2$, $Zn(OH)_3^-$, $Zn(OH)_4^{2-}$, $Zn_4(OH)_4^{4+}$, $ZnOH^+$, $Zn_2(OH)_6^{2-}$, $ZnOH^{3+}$; (b) for Al species alone: $Al(OH)_3$, AlOOH, $Al(OH)_4^-$, $AlOH_2^+$, $Al_{13}O_4(OH)_{24}^{7+}$, $Al_2(OH)_2^{4+}$, $Al_3(OH)_4^{5+}$, $AlOH_2^+$; (c) for Mg species alone: MgO, $Mg(OH)_2$, $MgOH^+$, $Mg_4(OH)_4^{4+}$; (d) for Ti species alone: TiO_2, $TiO(OH)_2$, $TiO(OH)_3^-$, $TiOOH^+$; (e) for Mn species alone: $Mn(OH)_2$, $MnOH^+$, $Mn(OH)_3^-$, $Mn(OH)_4^{2-}$, $Mn_2(OH)_3^+$, $Mn_2OH_3^+$; (f) for P species alones: H_3PO_4, $H_2PO_4^-$, HPO_4^{2-}; (g) for F species alone: HF, H_2F_2, HF_2^-; (h) mixed species: $Zn_3(PO_4)_2.4H_2O$, $Mn_3(PO_4)_2$, $MnHPO_4$, ZnF_2, ZnF^+, AlF_2^+, AlF_3, AlF_4^-, AlF_5^{2-}, AlF_6^{3-}, $MgAlO_4$, MgF_2, MgF^+, MnF^+, MnF_2, $AlPO_4$, TiF_6^{2-}.

Simulations show that Zn and Mn tend to react with the phosphate groups present in the bath. The preferential formation of hopeite ($Zn_3(PO_4)_2$) is in accordance with the XPS analyses and depth profiles by AES and GD-OES. However, it is possible to assume that the substitution of Mn by Zn leads to the formation of a mixed phosphate compound $Zn_xMn_{3-x}(PO_4)_2$ during the TiCC precipitation which should also be considered.

Regarding Mn^{2+} ions, the precipitation of $MnHPO_4$ is described as the only Mn-based compound to be formed on the surface for all pH conditions. This result was also consistent with the XPS analyses and the binding energy reported for $MnHPO_4$ in the literature [25].

The titanium contained in the conversion coating is precipitating only as TiO_2 for all pH at this concentration which is also consistent with the surface characterization. Various studies focusing on the precipitation mechanisms of TiCC on HDG or Al alloys have highlighted the formation of TiO_2 [4], [6], [11], [32] as well as $Mn_xTi_y(PO_4)_z$ although it is unclear if P is involved in $Mn_xTi_y(PO_4)_z$ or $Mn_xZn_y(PO_4)_z$.

Finally, the Mg^{2+} ions dissolved in the TiCC bath form insoluble MgF_2. Indeed, its solubility is 8 times lower than the one of ZnF_2 or MnF_2, all of which are possible formed precipitates from XPS analyses [33]. This hypothesis is not ruled out by XPS analyses results and is consistent with SEM-EDS observations.

Taking into the composition of each phase of ZnAlMg, the formation mechanism of TiCC can be summed up as follows in Figure 38:

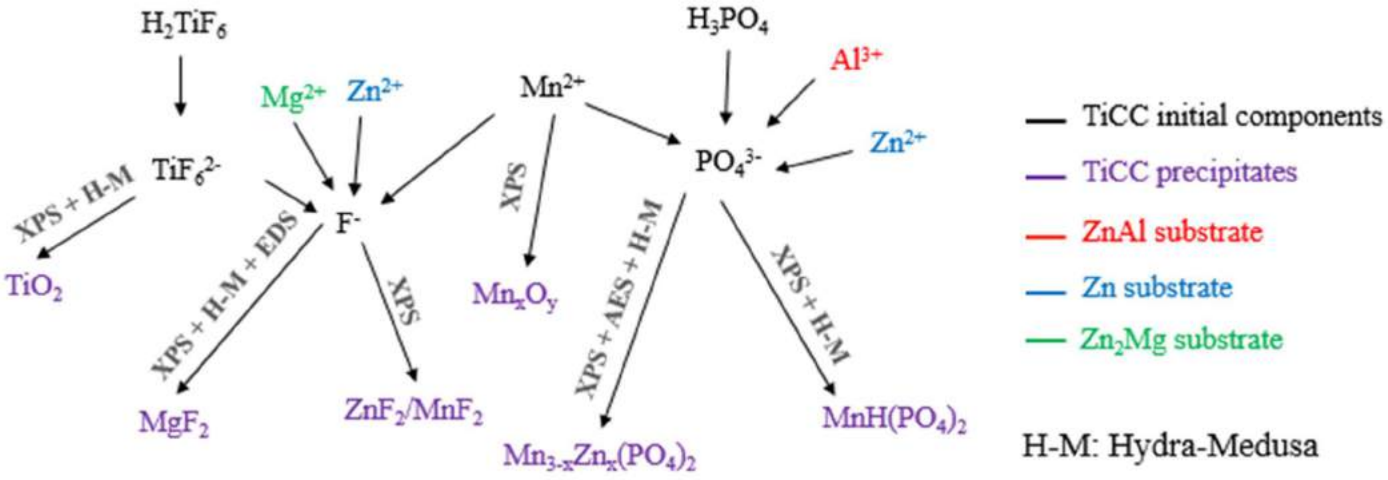

Figure 38: Schematic diagram of the TiCC precipitation on ZnAlMg

4.2. Distribution of TiCC on ZnAlMg phases

From the results presented here above, the TiCC distribution is not homogeneous on ZnAlMg phases where the surface coverage decreases in order: ZnAl > Zn-Zn_2Mg > Zn dendrites. A TiCC precipitation mechanism on all ZnAlMg phases is suggested in Figure 39.

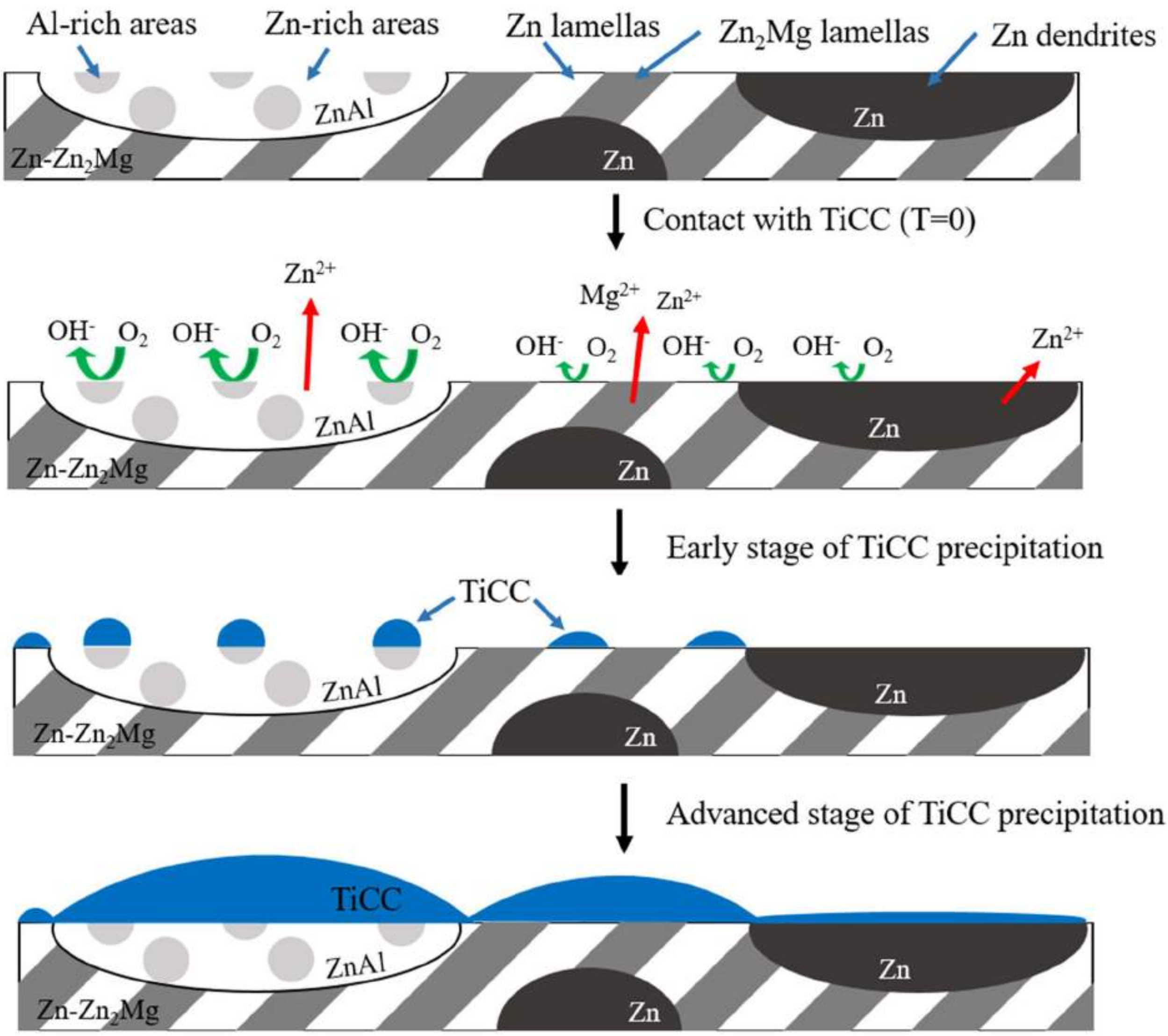

Figure 39: Scheme of the TiCC precipitation mechanism on ZnAlMg

From the contact between ZnAlMg and the TiCC bath, anodic and cathodic areas are locally formed where the substrate will get dissolved in anodic zones (Zn_2Mg lamellas and Zn-rich areas contained in ZnAl) while a pH increase occurs in cathodic zones.

After a prolongated contact of the substrate with the CC bath, the CC precipitation is extended from cathodic areas to more anodic areas of binary phases and then to monophase Zn dendrites with a lower reactivity towards the TiCC bath. The CC is self-extinguished when the local pH is not high enough anymore to enable more CC to precipitate due to the isolation of the substrate from the TiCC bath.

Electrochemical measurements indicate that a galvanic coupling is probable within ZnAlMg material that could explain the heterogeneous TiCC distribution on ZnAlMg.

Potential differences between ZnAlMg phases are not expected to induce a strong and predominant galvanic coupling between phases. Nevertheless, a galvanic coupling inside each binary phase can be strong enough and enhance the reactivity as the distance between the anodic and cathodic zones will be very small. It can hence play an important role in the TiCC precipitation kinetics. The local pH increase is expected to extend quickly from cathodic zones to anodic ones when they are closely spaced.

The dissolution of anodic areas leads to a local surface enrichment of the cathodic phase hence a faster alkalization of the media on Zn lamellas and Al-rich areas present in ZnAl respectively and a locally enhanced TiCC precipitation kinetics. This way, anodic and cathodic phases size could act as an accelerating factor regarding precipitation kinetics.

Finally, the lowest TiCC concentration measured on Zn dendrites contained in ZnAlMg could be explained by the phase homogeneity in the center of dendrites. The coupling within Zn/Zn_2Mg or ZnAl induces a dissolution and a more homogeneous pH increase at the interface resulting in a faster precipitation kinetics and an overall higher TiCC thickness on the surface. One might also consider that a conversion coating concentration gradient between the center of the Zn phase and the phase edges in direct contact with the neighboring ZnAl and Zn/Zn_2Mg phases might exist. However, no EDS or AES measurements were carried out to confirm nor infirm this hypothesis.

In the case of ZnAl, an internal coupling was also evidenced from coupling pure Al with Zn phase. To explain why the concentration of TiCC is the highest on this phase, it is important to remember that the microstructure of this phase is the finest between all the phases relevant for ZnAlMg coatings which can enhance the TiCC precipitation kinetics on ZnAl.

5. Conclusion

The distribution and chemical composition of TiCC on the multiphase ZnAlMg substrate was evaluated and the role of individual phases for TiCC distribution was approached with additional study of model pure phases corresponding to ZnAlMg.

- A heterogeneous distribution of TiCC on ZnAlMg material after alkaline degreasing and immersion in the conversion bath at 60°C for 30 sec was demonstrated by EDS, AES and XPS measurements.

The quantity of precipitated TiCC, which can be considered as a measure of precipitation kinetics, decreases in order: binary ZnAl > binary Zn/Zn_2Mg > Zn

- The improved CC precipitation kinetics on binary phases was explained by a galvanic coupling inside these phases (Zn/Zn_2Mg and Zn/Al), contributing to stronger reactivity and more rapid pH increase on these phases. The fineness of the microstructure distribution is expected to play a key role for the local pH distribution and hence homogeneity of the deposition. It is expected that the galvanic coupling inside binary phases prevails over the coupling between the phases and Zn dendrites.
- The TiCC chemical composition from XPS, AES, GD-OES, EDS and Hydra-Medusa software precipitation simulations enabled the identification of the following products:

  - **TiO_2** (sometimes doped with F). No phosphates of Ti was detected
  - **$Mn_{3-x}Zn_x(PO_4)_2$** $0 < x < 3$ (with possibility of some **$MnHPO_4$** and **Mn_xO_y**
  - **MgF_2** and some F-doped ZnO

References

[1] V. Saarimaa, E. Kauppinen, A. Markkula, J. Juhanoja, B.-J. Skrifvars, P. Steen, Microscale distribution of Ti-based conversion layer on hot dip galvanized steel, Surf. Coat. Technol., 206 (2012) 4173-4179.

[2] J. Cerezo, I. Vandendael, R. Posner, K. Lill, J.H.W. de Wit, J.M.C. Mol, H. Terryn, Initiation and growth of modified Zr-based conversion coatings on multi-metal surfaces, Surf. Coat. Technol., 236 (2013) 284-289.

[3] L. Fedrizzi, F. Deflorian, P. L. Bonora, Corrosion behaviour of fluotitanate pretreated and painted aluminium sheets, Electrochim. Acta, 42 (1997) 969-978.

[4] J. H. Nordlien, J. C. Walmsley, H. Østerberg, K. Nisancioglu, Formation of a zirconium-titanium based conversion layer on AA 6060 aluminium, Surf. Coat. Technol., 153 (2002) 72-78.

[5] O. Lunder, C. Simensen, Y. Yu, K. Nisancioglu, Formation and characterisation of Ti–Zr based conversion layers on AA6060 aluminium, Surf. Coat. Technol., 184 (2004) 278-290.

[6] F. Andreatta, A. Turco, I. de Graeve, H. Terryn, J. H. W. de Wit, L. Fedrizzi, SKPFM and SEM study of the deposition mechanism of Zr/Ti based pre-treatment on AA6016 aluminium alloy, Surf. Coat. Technol., 201 (2007) 7668-7685.

[7] T. Lostak, A. Maljusch, B. Klink, S. Krebs, M. Kimpel, J. Flock, S. Schulz, W. Schuhmann, Zr-based conversion layer on Zn-Al-Mg alloy coated steel sheets: insights into the formation mechanism, Electrochim. Acta, 137 (2014) 65-74.

[8] N.K. Akafuah, S. Poozesh, A. Salaimeh, G. Patrick, K. Lawler, K. Saito, Evolution of the Automotive Body Coating Process - A Review, Coatings, 24 (2016) 1–22.

[9] User manual, Organic coated steel, ArcelorMittal Flat Carbon Europe 19, avenue de la Liberté L-2930 Luxembourg.

[10] L. Li, B. W. Whitman, G. M. Swain, Characterization and performance of a Zr/Ti pretreatment conversion coating on AA2024-T3, J. Electrochem. Soc., 162 (2015) C279-C284.

[11] B. Wilson, N. Fink, G. Grundmeier, Formation of ultra-thin amorphous conversion films on zinc alloy coatings: Part 2: Nucleation, growth and properties of inorganic–organic ultra-thin hybrid films, Electrochim. Acta, 51 (2006) 3066-3075.

[12] V. Saarimaa, A. Markkula, J. Juhanoja, B.-J. Skrifvars, Determination of Surface Topography and Composition of Cr-Free Pretreatment Layers on Hot Dip Galvanized Steel, J Coat Sci Technol, 1 (2014) 88-95.

[13] N. Le Bozec, D. Thierry, M. Rohwerder, A. Kovacs, A. Peltola, G. Luckeneder, L. Luxem, G. Marchiaro, Advanced Zinc-based hot dip coatings for automotive applications (AUTOCOAT), European comission - Directorate general for research and innovation, EUR 26323, 2013.

[14] M. Salgueiro Azevedo, C. Allély, K. Ogle, P. Volovitch, Corrosion mechanisms of Zn(Mg, Al) coated steel: 2. The effect of Mg and Al alloying on the formation and properties of corrosion products in different electrolytes, Corros. Sci., 90 (2015) 482-490.

[15] T. Prosek, A. Nazarov, M.-G. Olivier, C. Vandermiers, D. Koberg, D. Thierry, The role of stress and topcoat properties in blistering of coil-coated materials, Prog. Org. Coat., 68 (2010) 328-333.

[16] P. Campestrini, E. P. M. van Westing, J. H. W. de Wit, Influence of surface preparation on performance of chromate conversion coatings on Alclad 2024 aluminium alloy: Part I: Nucleation and growth, Electrochim. Acta, 46 (2001) 2553-2571.

[17] I. Puigdomenech, Hydra/Medusa Chemical Equilibrium Database and Plotting Software KTH Royal Institute of Technology, 2004

[18] S. Le Manchet, (2010). Mécanismes de corrosion et de délamination d’un composite acier/polymère pour le marché automobile. Université de Technologie de Compiègne : PhD Thesis., Université de Technologie de Compiègne, 2010.

[19] C. E. B. Marino, P. A. P. Nascente, S. R. Biaggio, R. C. Rocha-Filho, N. Bocchi, XPS characterization of anodic titanium oxide films grown in phosphate buffer solutions, Thin Solid Films, 468 (2004) 109-112.

[20] J. Halim, An X-Ray Photoelectron Spectroscopy Study of Multiplayered Transition Metal Carbides (MXenes), PhD Thesis, Drexel University, Philadelphia, USA, 2016.

[21] R. Franke, T. Chassé, P. Streubel, A. Meisel, Auger parameters and relaxation energies of phosphorus in solid compounds, J. Electron Spectrosc. Relat. Phenom., 56 (1991) 381-388.

[22] D. L. Felker, P. M. A. Sherwood, Zinc phosphate (Zn3(PO4)2) by XPS, Surf. Sci. Spectra, 9 (2002) 106-113.

[23] Thermofisher, Manganese - Interpretation of XPS data. [Online]. Disponible sur : https://xpssimplified.com/elements/manganese.php. [Consulted on : 25-sept-2018].

[24] A. Aoki, X-Ray Photoelectron Spectroscopic Studies on ZnS: MnF2 Phosphors, Jpn. J. Appl. Phys., 15 (1976) 305.

[25] G. Wang, N. Cao, Y. Wang, Characteristics and corrosion studies of Zn-Mn PCC on Mg-Li alloy, RSC Adv., 4 (2014) 59772-59778.

[26] M. D. Pereda, C. Alonso, L. Burgos-Asperilla, J. A. del Valle, O. A. Ruano, P. Perez, M. A. Fernandez Lorenzo de Mele, Corrosion inhibition of powder metallurgy Mg by fluoride treatments, Acta Biomater., 6 (2010) 1772-1782,

[27] J. Dong, L. Wu, L. Zhao, W. Ke, X. Li, Influence of the KF concentration on the coating process and properties of potentiostatic deposited fluoride conversion film on AZ31 Mg alloy, Res. Rev. J. Mater. Sci., 3 (2015) 1-22.

[28] L. Wu, J. Dong, W. Ke, Potentiostatic deposition process of fluoride conversion film on AZ31 magnesium alloy in 0.1M KF solution, Electrochim. Acta, 105 (2013) 554-559.

[29] S. Da-Ming, S. Zhao-Qi, L. Ai-Xia, X. Zhi-Yuan, XPS analysis of the oxidation of Ag–MgF2 cermet film, Vacuum, 52 (1999) 383-386.

[30] N. R. Short, S. Zhou, J. K. Dennis, Electrochemical studies on the corrosion of a range of zinc alloy coated steel in alkaline solutions, Surf. Coat. Technol., 79 (1996) 218-224.

[31] American Society for Metals (ASM), Aluminium-Zinc Binary Phase Diagram, ASM Alloy Phase Diagram Database. [Online]. Available on: https://matdata.asminternational.org/apd/index.aspx. [Consulted on: 08-aug-2018].

[32] S. Le Manchet, D. Verchère, J. Landoulsi, Effects of organic and inorganic treatment agents on the formation of conversion layer on hot-dip galvanized steel: An X-ray photoelectron spectroscopy study, Thin Solid Films, 520 (2012) 2009-2016.

[33] Aqion, Solubility Product Constants Ksp at 25 *°C,* aqion. [Online]. Available on : http://www.aqion.de/site/16#name. [Consulted on: 02-oct-2018].

Chapter 6: Improvement of TiCC homogeneity on multiphase ZnAlMg substrate using surface activation by Cu^{2+} modified alkaline degreasing

Authors: Perrine Tanguy[a,b, 1], Christian Allély[b], Diana Dragoe[c], Michel Lahaye[d], Anna Krasnova[a] and Polina Volovitch[a]

[a] *Chimie ParisTech, PSL Research University, CNRS, Institut de Recherche de Chimie Paris (IRCP), F-75005 Paris, France*

[b] *Global Research and Development, ArcelorMittal Maizières Research, France*

[c] *Institut de Chimie Moléculaire et des Matériaux d'Orsay, CNRS, Université Paris-Sud 11, 91405 Orsay Cedex, France*

[d] *PLateforme Aquitaine CAractérisation de MATériaux Placamat, CNRS, Université de Bordeaux, 33600 Pessac*

Corresponding author: Polina Volovitch

Tel.: *(+33) 1 44 27 20 74* Fax: *(+33) 1 46 34 07 53*

Email: polina.volovitch@chimieparistech.psl.eu

Abstract: In the previous chapter, the inhomogeneous coverage of multiphase ZnAlMg substrates by Ti-conversion coating (TiCC) was ascribed to a variation of local reactivity between phases. In order to overcome this problem and activate the whole surface of the multiphase substrate, a Cu^{2+}-modified alkaline pretreatment is proposed and its effect on the chemical speciation and spatial distribution of TiCC on the multiphase substrate is described in the present chapter. After the degreasing step, EDS and AES confirmed the presence of metallic Cu nanoparticles on all phases of ZnAlMg. Following the TiCC deposition, AES revealed a similar TiCC thickness on all ZnAlMg phases. X-ray Photoelectron Spectroscopy (XPS) confirmed the homogeneity of the TiCC chemistry on the ZnAlMg surface after using the Cu^{2+}-modified alkaline cleaner. The origin of the TiCC improved homogeneity was proposed to be in the cathodic nature of the cemented metal versus all phases of ZnAlMg, which induced a finer and homogeneous distribution of local cathodes and anodes, accelerated and homogenized the local pH increase necessary for the TiCC precipitation. Local Electrochemical Impedance

Mappings evidenced the enhanced corrosion resistance of TiCC coated and painted ZnAlMg coated steel pretreated with the Cu^{2+}-modified cleaner compared to the sample prepared with a conventional alkaline cleaner.

1. Introduction

In the pre-painted and automotive industries, nanometric TiCC and ZrCC are promising conversion coatings for providing corrosion resistance and paint adherence to painted cold rolled steel, HDG, Al alloys etc [1]-[9].

Simultaneously, monophase HDG coated steels are being replaced by multiphase ZnAlMg ones exhibiting an improved corrosion resistance, thus allowing a coating thickness reduction [10]-[14].

The use of ZrCC on multiphase ZnAlMg materials as well as aluminium alloys containing intermetallic particles has been reported to lead to a heterogeneous conversion coating distribution due to the spatially located anodes and cathodes on the surface [5], [6], [8], [15]. The chapter 5 of this manuscript focusing on the distribution and chemical composition of TiCC on ZnAlMg confirmed this hypothesis highlighting that monophase Zn dendrites are the least covered ZnAlMg phase from the absence of galvanic coupling inside the phase.

One of the possible solutions to homogenize the conversion coating distribution is to induce the deposition/cementation of more noble elements such as Cu or Fe [16]-[21] during conversion coating procedure, in order to create local galvanic coupling between the Cu/Fe particles and the ZnAlMg phase. This is expected to accelerate the precipitation kinetics leading to a more homogeneous coating thickness on the overall surface. Indeed, it was observed by Cerezo et al. that the cementation of Cu particles during the ZrCC procedure on an AA1050 surface promoted the formation of the ZrCC [8]. This observation was also confirmed by Lostak et al. although it was reported that the addition of Cu^{2+} to the conversion bath led to a thicker but less homogeneously distributed ZrCC on HDG steel compared to Fe^{3+}, especially for short immersion times in the conversion coating bath. Regarding the corrosion resistance of samples treated with the Cu/Fe-modified conversion bath, they reported that the OCP was shifted to more noble values by the addition of Cu^{2+}/Fe^{3+} [16]. Adhikari et al. noted an enhanced delamination resistance of samples treated with ZrCC containing Cu particles compared to those not containing Cu particles [17].

In the automotive industry, ferric and cupric ions are already part of the formulation of some conversion coatings, including $Fe(NO_3)_3.9H_2O$ or $Cu(NO_3)_3.9H_2O$ [16]. During the immersion of a HDG substrate in the conversion coating bath, the first step consists in the deposition of noble metallic (Fe or Cu) particles on the substrate [16]:

$$3\mathrm{Zn} + 2\mathrm{Fe}^{3+} \rightarrow 3\mathrm{Zn}^{2+} + 2\mathrm{Fe} \tag{6-1}$$

Or

$$\mathrm{Zn} + \mathrm{Cu}^{2+} \rightarrow \mathrm{Zn}^{2+} + \mathrm{Cu} \tag{6-2}$$

Simultaneously, anodic and cathodic reactions occur on the HDG surface creating a substrate dissolution followed by local alkalization, leading to the CC precipitation as titanium oxide [4]-[6], [8], [22]-[25]:

1. Anodic dissolution:

$$\mathrm{Zn} \rightarrow \mathrm{Zn}^{2+} + 2\mathrm{e}^- \tag{6-3}$$

2. Cathodic reduction leading to pH increase:

$$\mathrm{O}_2 + 4\mathrm{H}^+ + 4\mathrm{e}^- \rightarrow 2\mathrm{H}_2\mathrm{O} \tag{6-4}$$

$$2\mathrm{H}^+ + 2\mathrm{e}^- \rightarrow \mathrm{H}_2 \tag{6-5}$$

3. TiCC precipitation (pH range= 2.5 – 8.5 [26]):

$$\mathrm{TiF_6}^{2-} + 4\mathrm{OH}^- \rightarrow \mathrm{TiO_2.H_2O} + 6\mathrm{F}^- \tag{6-6}$$

In this chapter, the use of Cu^{2+} ions at the pretreatment step is considered as a possible solution of the problem of inhomogeneous TiCC precipitation on multiphase substrates.

The objective of the work is to evaluate if the pretreatment resulting in the cementation of Cu particles can lead to a homogenization of TiCC distribution on all phases of ZnAlMg and if the stability of painted ZnAlMg treated TiCC after this modified pretreatment is improved compared to the painted ZnAlMg with conventional TiCC.

Firstly, the distribution and chemical form of Cu particles after the degreasing step as well as the TiCC were evaluated on all phases of ZnAlMg using surface analysis techniques. Then, a model epoxy paint was deposited on ZnAlMg coated steels with TiCC prepared after standard alkaline cleaning and after Cu-modified procedure and the stability of formed systems during immersion and polarization in a 0.1 M NaCl solution was compared. Local Electrochemical Impedance Mapping (LEIM) was used to detect degradation, identify the delamination front position and the delamination front propagation.

The applied interest of the study is that Cu^{2+}-modified alkaline degreasing bath has never been associated with a TiCC dedicated to the pre-painted market as part of a 2-step procedure. In addition, the precipitation of Cu cathodes aiming at homogenizing the conversion coating distribution has never been reported on multiphase ZnAlMg in the literature.

2. Experimental

2.1. Materials

Two types of materials were tested including model ZnAlMg multiphase coatings and individual pure phases.

2.1.1. Model ZnAlMg materials

ZnAlMg coated steel with a thickness of 500 µm were supplied by ArcelorMittal in the skin-passed state with a roughness of 0.95 ± 0.03 µm. ZnAlMg coatings were produced by hot dip process with thickness around 10 µm. The selected composition contained Al $\leq$ 5 wt. % and Mg $<$ 3 wt. %. Phase composition and details about microstructure of the materials are summed up inTable 14. Further details about ZnAlMg coatings microstructure is available in Appendix 2.

Samples with a size of 100 mm × 200 mm were cut from the supplied substrate and subjected to a petroleum ether solvent cleaning process to ensure complete removal of any oils or surface contamination.

2.1.2. Pure phases

For the delamination studies, samples were covered with 10 µm of epoxy using spin-coater (Spin150, The Netherlands) and dried at air overnight. Scratches up to the steel (length: 15 mm) were made manually with a 1 mm Sikken blade and scratches depth were controlled using a Surtronic S 128 portable device.

For mechanistic purposes, Zn, ZnAl and Zn_2Mg model phases with compositions relevant to the ZnAlMg coating were synthetized. Depending on their composition, alloys were weighed in masses and heated at 500 °C. Liquid mixtures were then filtered through ceramic filters consisting of 61 wt. % Al_2O_3 and 39 wt. % SiO_2 (10 pores per square inch porosity). The composition, crystallinity, grain size and orientation and hardness of all synthetized phases were characterized using atomic absorption spectroscopy, SEM, EBSD, XRD and nanoindentation techniques. The composition of the obtained phases is summarized in Table 14. Complementary information regarding pure phases microstructure is gathered in Appendix 3. In addition, Al (99.999 % purity) supplied by GoodFellow was used. It should be noted that the studied ZnAlMg material and ZnAl phase are multiphase while Zn and Zn_2Mg are monophase.

Table 14: Composition of ZnAlMg and pure phases corresponding to ZnAlMg

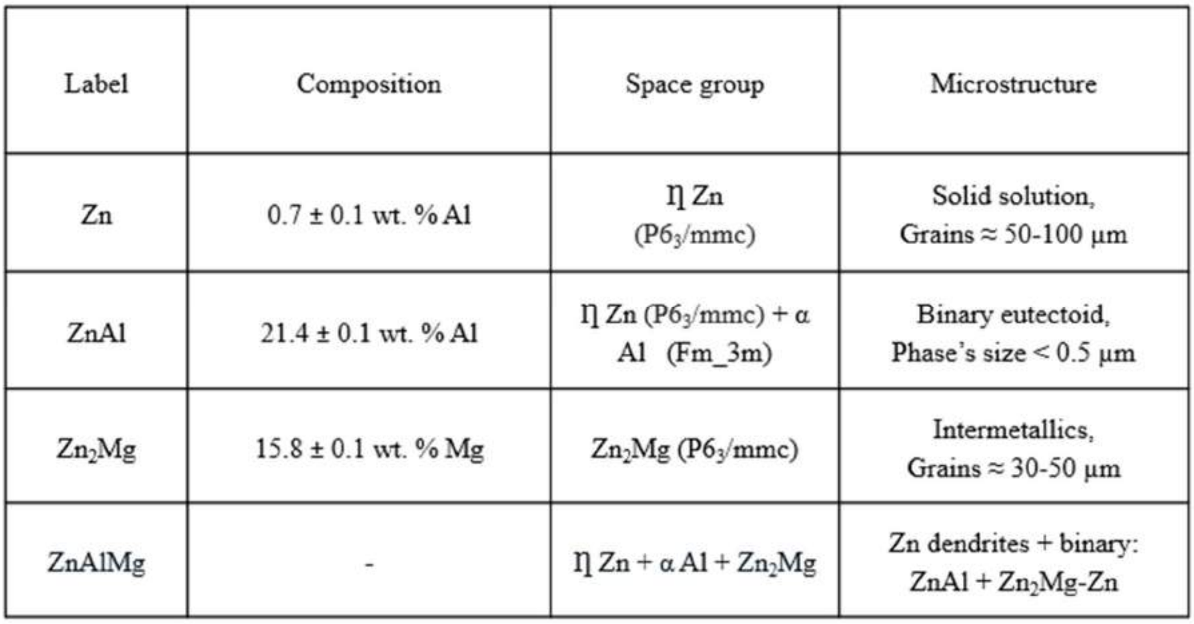

Label	Composition	Space group	Microstructure
Zn	0.7 ± 0.1 wt. % Al	η Zn ($P6_3/mmc$)	Solid solution, Grains ≈ 50-100 µm
ZnAl	21.4 ± 0.1 wt. % Al	η Zn ($P6_3/mmc$) + α Al (Fm_3m)	Binary eutectoid, Phase's size < 0.5 µm
Zn_2Mg	15.8 ± 0.1 wt. % Mg	Zn_2Mg ($P6_3/mmc$)	Intermetallics, Grains ≈ 30-50 µm
ZnAlMg	-	η Zn + α Al + Zn_2Mg	Zn dendrites + binary: ZnAl + Zn_2Mg-Zn

Samples were polished with SiC polishing discs (up to 4000 grit). After polishing, all samples were rinsed using ethanol and dried with compressed air. Prior to immersion, the reacting area (A= 1 cm^2) of the pure phases was defined using insulator tapes containing precut portholes (PortHoles ™ Electrochemical Sample Masks).

2.2. TiCC solutions

Solutions used to prepare TiCC on pure phases and model ZnAlMg material are listed in Table 15. For convenience, the commercial TiCC remained unchanged. The Cu addition was carried out in the degreasing bath prior to the conversion coating step. A new formulation was created based on the necessity to keep Cu^{2+} ions soluble in an alkaline media. To prevent Cu from precipitating in the alkaline degreasing bath (pH = 12.5), 2 types of chelating agents were used, sodium gluconate ($C_6H_{11}NaO_7$) and sodium citrate ($C_6H_5Na_3O_7$) in large excess compared to the Cu concentration (0.026 M) [27], [28]. EDTA was not a suitable choice as it can complex Cu only in acidic and neutral pH [29].

Table 15: Main components and their concentration in solutions used for the TiCC procedure

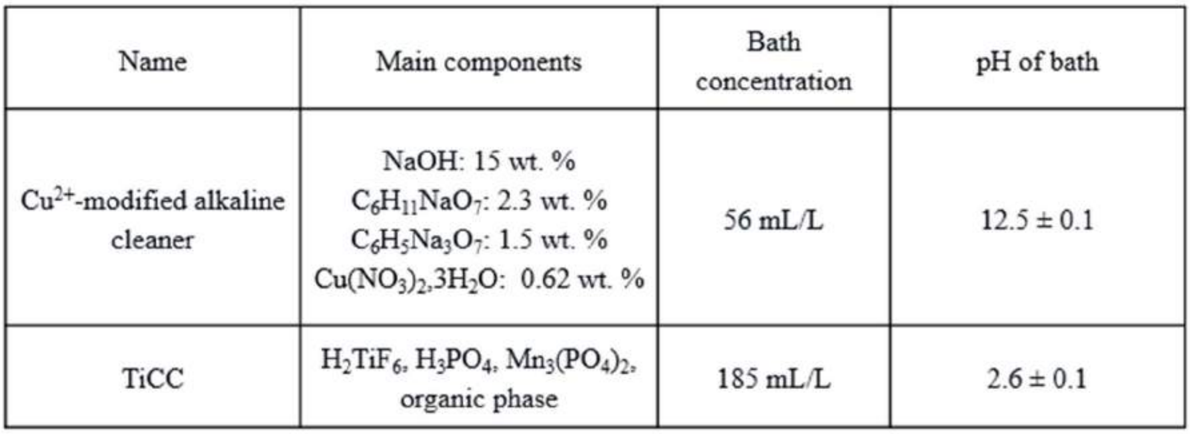

Name	Main components	Bath concentration	pH of bath
Cu^{2+}-modified alkaline cleaner	NaOH: 15 wt. % $C_6H_{11}NaO_7$: 2.3 wt. % $C_6H_5Na_3O_7$: 1.5 wt. % $Cu(NO_3)_2.3H_2O$: 0.62 wt. %	56 mL/L	12.5 ± 0.1
TiCC	H_2TiF_6, H_3PO_4, $Mn_3(PO_4)_2$, organic phase	185 mL/L	2.6 ± 0.1

2.3. TiCC procedure

The following general procedure was used to precipitate TiCC on pure phases:

1. Immersion in Cu^{2+}-modified alkaline degreasing bath at 55 °C for 30 sec or 2 min
2. Osmosis water rinsing at 50 °C and at ambient temperature
3. Immersion in the TiCC bath at 60 °C for 30 sec
4. Osmosis water rinsing at room temperature
5. Drying in hot air stream

All baths were used maximum 12 h after mixing and renewed every 24 h.

2.4. Local Electrochemical Impedance Spectroscopy and Mapping

Local Electrochemical Impedance Spectroscopy (LEIS) and Local Electrochemical Impedance Mapping (LEIM) were performed using a potentiostat (Solartron ModuLab XM ECS, Princeton Applied Research). Samples were epoxy-coated (polymer thickness: 10 µm) with a spin-coater (Spin150, The Netherlands) and dried at air overnight. An artificial down to steel scratch (scratch dimension: 15 mm x 1 mm x 100 µm) was manually made on samples before they were mounted as working electrodes (WE) at the bottom of a 3D printed electrochemical cell. The counter-electrode was a platinum wire and the reference one was an Ag/AgCl sat. electrode where a 0.1 s per sample integration period with 20 mV peak-to-peak potential perturbation was applied. The electrochemical cell was filled up with a 0.1 M NaCl solution where samples were immersed 1 h before the beginning of the measurement to saturate the polymer coating with water, allowing the ionic flow through the polymer. A homemade set-up using a Solartron potentiostat was used. Measurements were done with a homemade local probe composed of two Ag wires of 250 µm diameter in a glass capillary (sealed in two joined capillaries with the distance between the two Ag wires centers d = 1.3 mm). The probe was positioned at 150 ± 25 µm above the WE and moved with a 3-axis positioning system (UTM25, Newport) driven by a motion encoder (MM4005, Newport). The data treatment was made with a homemade software. All impedance maps were measured on 8x3 cm^2 areas with steps of 200 µm along both X- and Y-directions which required about 15 minutes for each map.

Each step included global and local impedance measurements in two points above the polymer (A) and the scratch (B) with frequencies ranging from 100 kHz to 1 Hz and a LEIM mapping at a constant frequency of 500 Hz for the sample treated with the unmodified cleaner. For the one degreased with the Cu^{2+}-modified alkaline one, 4 mappings were performed at 500 Hz while the last one was made at 300 Hz to avoid an inductivity phenomenon.

Measurements of global and local impedances were performed at the OCP for 1 h to study their evolution. First, a LEIM analysis was performed at OCP followed by global and local impedance measurements in points A and B (in the same conditions). Then, an anodic polarization of the sample at -0.7 V vs Ag/AgCl saturated reference electrode was applied before performing the LEIM analysis, global and local impedances measurements in points A and B. This alternating OCP-anodic polarization procedure was repeated 3 times for the reference sample degreased using an unmodified alkaline degreasing and 5 times for samples degreased with the Cu^{2+}-modified alkaline degreasing until the darkened area around the artificial defect under the polymer became approximately twice wider than the initial defect. In a second step, a cathodic polarization (-1.5 V vs Ag/AgCl saturated) and anodic one (-0.6 V vs Ag/AgCl saturated) were applied alternately for both samples. An additional mapping was performed on the sample treated with the unmodified alkaline cleaner due to the delamination propagation.

The typical output used so far in the literature to report on LEIM experiments is mapping of the local impedance, $z(r)$, or the local admittance, $z^{-1}(r)$, at a fixed frequency. In the present work, the gradient of the local admittance is used to present the results [30].

2.5. Electrochemical measurements

Open Circuit Potential (OCP) measurements were performed using a Biologic VSP potentiostat. A three-electrode cell was used with a saturated calomel electrode (SCE) as the reference electrode, a platinum wire as the counter electrode and the sample as the working electrode.

A Pt electrode was used to carry out imposed potential polarization experiments in the Cu^{2+}-modified alkaline degreasing bath at 55 °C in order to determine the precipitation potential of Cu particles. After an OCP measurement for 5 min, potentials ranging between -0.8 and -1.4 V vs. SCE were applied for 30 min to the sample. For all measurements, freshly prepared electrolyte was stirred at 200 rpm. After imposed potential polarizations, the Cu mass gain was measured with an OHAUS Explorer EX1103 precision scale (sensitivity: 0.001 g). Two replicates were made for this experiment.

2.6. Surface characterization

The distribution and thickness of TiCC on all phases of ZnAlMg material was evaluated by Auger Electron Spectroscopy (AES), using a PHI 170 setup. The primary electron beam voltage was 20 kV and the beam current was 1 nA. A CMA analyzer with an incident angle of 30° with respect to the surface normal was used and experiments were performed at a pressure of $2,3.10^{-6}$ Pa. Depth profiles were carried out in a sequential mode with an Ar^{+} ion beam sputtering the surface at a voltage of 2 kV and a current of 1 µA. The ion beam sputtered a 4 mm^2 surface at an angle of 60 ° with respect to the surface normal. The interface between the CC and the substrate was defined as the inflection point in the Ti profiles or for complex profiles as a point at 50 % height of the maximal signal, A peak with a kinetic energy of 776 eV was selected to follow Cu evolution because the main auger peaks of Cu are interfered by Zn. For the differentiation of the Cu forms contained in the Cu peak, the Target Factor Analysis (TFA) methods was used. First, a Principal Component Analysis was performed to identify the two most differentiated shapes of the Cu peak and define them as metallic Cu and oxidized Cu forms. Using the 2 peaks, a deconvolution was made as a function of the erosion depth to determine the concentration of each form of the Cu element in the erosion profile. A minimum of 2 replicates were made to control the reproducibility.

The TiCC composition and concentration after immersion of the model ZnAlMg coating and pure phases in the TiCC bath were studied by X-ray Photoelectron Spectroscopy (XPS). The XPS spectrometer used (K Alpha, Thermo Fisher Scientific, base pressure in the low 10^{-9} mbar range) was equipped with a monochromatic aluminium source (Al K_{α}, 1486.68 eV). A spot size of 400 µm corresponding to an irradiated zone of approximately 1 mm^2 was used. The hemispherical analyzer was operated at 0° take off angle in the Constant Analyzer Energy (CAE) mode, with a pass energy of 200 eV and an energy step of 1 eV for the acquisition of wide scans, while narrow scan spectra centered on the Ti 2p region were recorded at a pass energy of 100 eV and an energy step of 0.1 eV. Charge compensation was achieved by means of a “dual beam” flood gun, using low energy electrons (5 eV) and argon ions. Samples were fixed on the support using adhesive conducting tape.

The recorded spectra were processed by means of the Avantage software, using a peak-fitting routine with Shirley background and symmetrical 70 %-30 % mixed Gaussian-Lorentzian peak shapes. The atomic ratios were valuated following normalizations of the peak areas with the Scofield sensitivity factors.

The binding energy scale was calibrated on the neutral carbon set at 284.8 eV. Regarding reproducibility, the majority of quantitative and qualitative measurements were replicated at least 5 times.

3. Results

3.1 Preliminary verification of Cu deposition from the modified cleaner by potentiostatic cathodic polarization

Imposed cathodic potentials experiments were performed on a Pt electrode immersed in the Cu^{2+}-modified alkaline bath to evaluate the mass of electrodeposited Cu on the Pt surface. In addition, it enabled testing if the chelating agents, sodium gluconate and sodium citrate were not too strong and would not prevent a proper Cu deposition. The tested potentials were chosen to represent the potentials, which can be reached by all the ZnAlMg phases in the Cu^{2+}-modified alkaline bath (table (a) in Figure 40) and confirm if the potential gap between Cu and ZnAlMg phases enables the Cu^{2+} ions reduction. The measured OCP values and Cu mass gains measured with a scale as a function of the imposed potential are displayed in Figure 40.

(a)

Phase	Zn_2Mg	Zn	ZnAl
OCP in Cu^{2+}-modified alkaline cleaner at 55 °C / V vs. SCE	- 1.44 ± 0.03	-1.46 ± 0.02	-1.63 ± 0.02

(b)

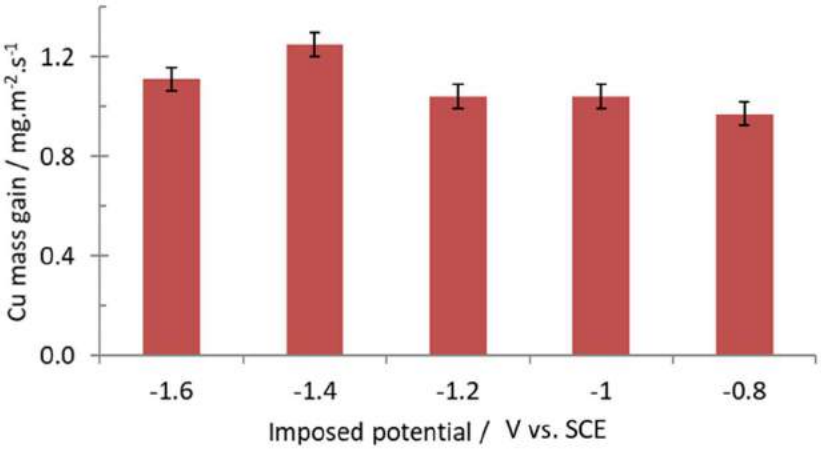

Figure 40: a) Measured OCP of different phases in Cu-modified alkaline cleaner and b) Cu mass gain measured on the Pt electrode as a function of the imposed potential in the Cu-modified alkaline degreasing bath at 55 °C

From Figure 40, it can be noticed that the rate of Cu cementation is not strongly influenced by the deposition potential in the range of potentials relevant for ZnAlMg phases which is coherent with Cu^{2+} ions diffusion limited kinetics. The type of chelating agents selected for the degreasing bath formulation appears hence to be a convenient choice for the rest of the study.

3.2 Cu distribution and chemical composition on ZnAlMg

Typical AES mapping of the ZnAlMg surface after immersion in the Cu^{2+}-modified alkaline degreasing bath at 55 °C for 2 min is shown in Figure 41.

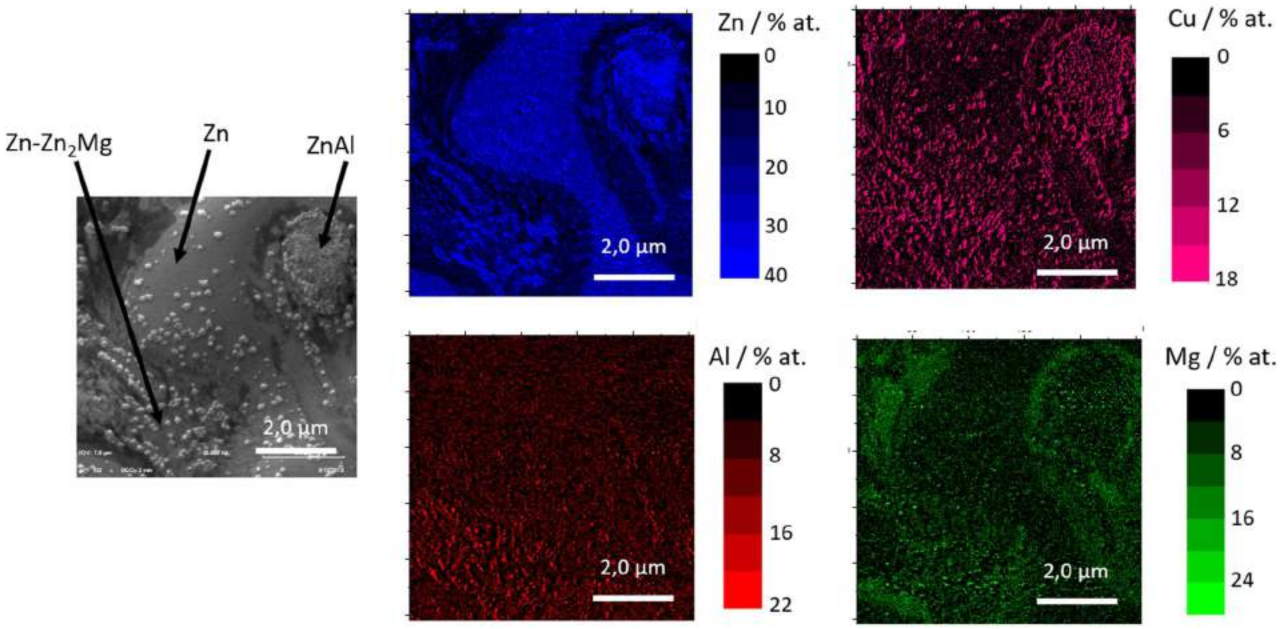

Figure 41: AES mapping of ZnAlMg surface after immersion in Cu alkaline cleaning at 55 °C for 2 min

From Figure 41, the white particles present on all phases of the ZnAlMg material contain Cu. This is consistent with the observation made by Cerezo et al. of similarly shaped Cu particles on Al alloys [19]. Cu concentrations at the extreme surface reached 18 at. % on the overall surface. Regarding the distribution of Cu between the phases, particles were found on all phases, in particular on the binary eutectoid ZnAl and Zn dendrites. More scattered particles were visible on Zn_2Mg lamellas, showing that Cu nucleate on all phases, with local concentration variations. Further details regarding the Cu precipitation mechanisms will be given in the discussion part.

After determining that Cu particles were precipitated on every phase of the ZnAlMg material, a complementary analysis to evaluate its chemical form on the surface was carried out with the AES technique. In this case, the XPS analysis did not provide sufficient information regarding Cu chemical form as Cu° and Cu^I exhibit binding energies closer than 0.2 eV for both Cu2p $_{3/2}$ and Cu2p $_{1/2}$ peaks [31]. Auger peaks of both species exhibit different energies but they are interfered by the Zn auger peak which makes the identification of Cu chemical form difficult using XPS.

However, using AES and the peak at a kinetic energy of 776 eV, it was possible to differentiate contributions coming from the metallic and oxidized Cu chemical form, although no further identification between CuO/Cu_2O would be possible using this technique.

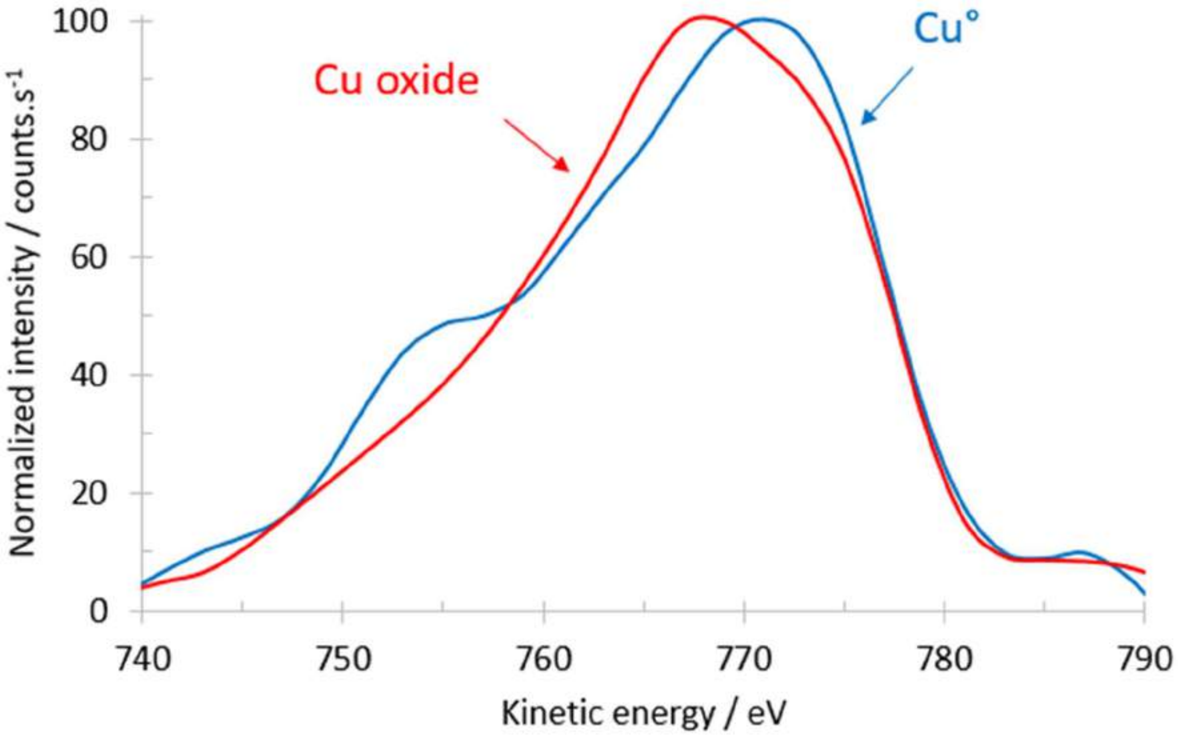

Figure 42: AES deconvolution of Cu auger peak of ZnAlMg after Cu alkaline degreasing for 2 min at 55 °C

On Figure 42 are displayed the normalized Cu auger peaks at 2 distinct sputtering steps. One can observe that the Cu auger peak is shifting from a kinetic energy of 769 to 771 eV throughout the sputtering process, highlighting that Cu is present in its oxidized form on the surface and its metallic one, closer to the ZnAlMg coating. This is coherent with the results of Sarfraz et al. [18] but also Khun who both worked with a Cu^{2+}-modified ZrCC baths [20]. For short immersion times, the formation was CuO was reported to be favorable while at long immersion times (180 sec), an increasing Cu_2O concentration and a decreasing CuO one was noted. The kinetic energy variation of metal Cu from 776 to 771 eV is due to the working mode used, either direct or derivative. Indeed, the theoretical kinetic energy peak value is 776 eV when working with the derivative mode. However, the data treatment was carried out on peaks displayed with the direct mode where the peak value corresponds to half of the peak height, hence 771 eV.

3.3. TiCC thickness distribution on ZnAlMg phases measured by AES

To evaluate if the cementation of Cu particles can lead to a homogenization of the TiCC distribution on all phases of ZnAlMg, AES profiles were performed on all ZnAlMg phases after its immersion in a TiCC bath at 60 °C for 30 sec following a Cu^{2+}-modified alkaline cleaning.

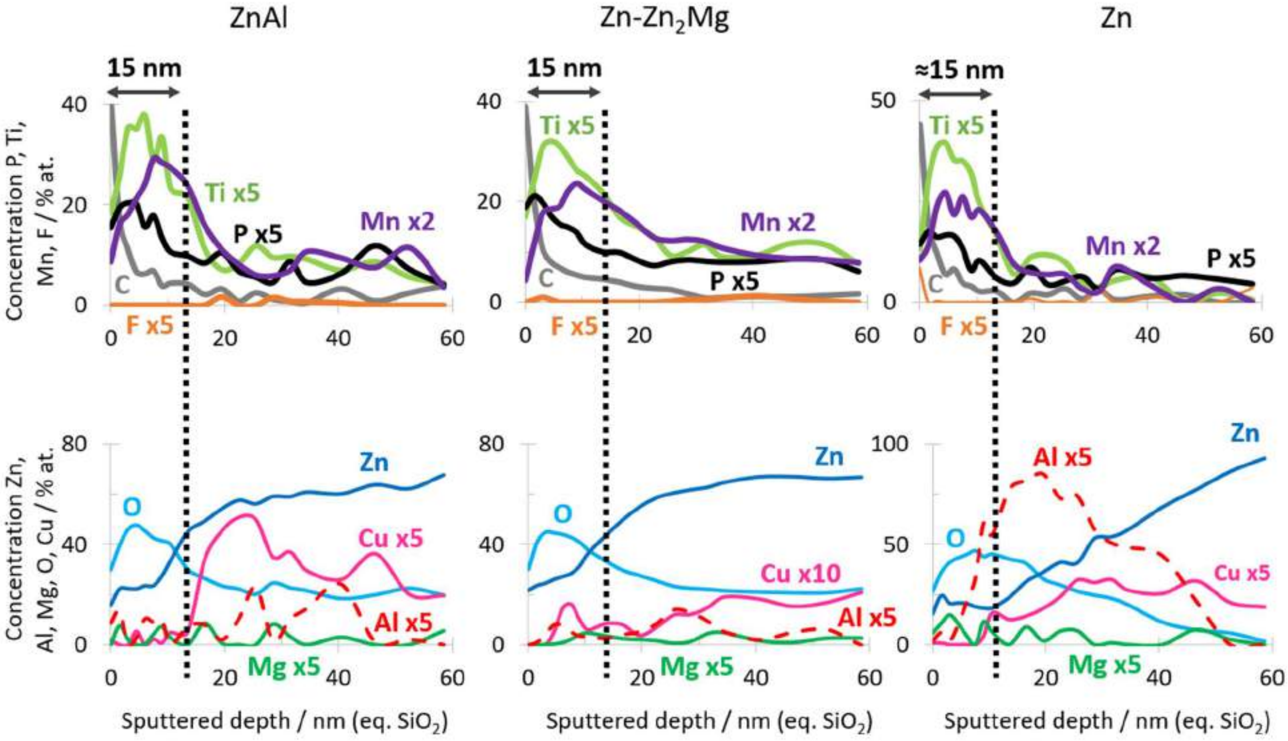

Figure 43: AES profile of ZnAlMg after immersion in TiCC bath at 60 °C for 30sec after Cu alkaline cleaning

As visible on Figure 43, profiles of Ti, P, Mn and F on the 3 ZnAlMg phases show that the TiCC thickness is comparable for all phases with an average thickness of 15 nm. On the overall, there is an improved coverage of Zn dendrites with the Cu^{2+}-modified alkaline cleaner compared to the unmodified one where a thickness of 5 nm was measured (Chapter 5). On the other hand, thinner conversion coating layers are measured on both binary phases. However, this can be explained by the relatively simple nature of the formulation which was not optimized and does not contain any additives etc. No optimization of the elements concentrations was performed to increase the Cu concentration on the surface in this study. In general, the enhanced conversion coating homogeneity from using Cu noble particles is confirmed.

The presence of Cu underneath the TiCC was also detected with AES profiles and the highest concentration seems to be measured on the binary ZnAl phase compared to the other 2 phases.

This is consistent with the results displayed on Figure 41 where a high concentration of white Cu particles is precipitated on the ZnAl phase.

3.4. TiCC chemical speciation on ZnAlMg after Cu^{2+}-modified alkaline degreasing

To evaluate the chemical composition of the TiCC on ZnAlMg when using a Cu^{2+}-modified alkaline cleaner at 55 °C for 2 min prior to the immersion in the TiCC bath at 60 °C for 30 sec, a XPS analysis was performed. Spectra of (a) Ti 2p, (b) P 2s, (c) Mn 2p and (d) F 1s are shown in Figure 44.

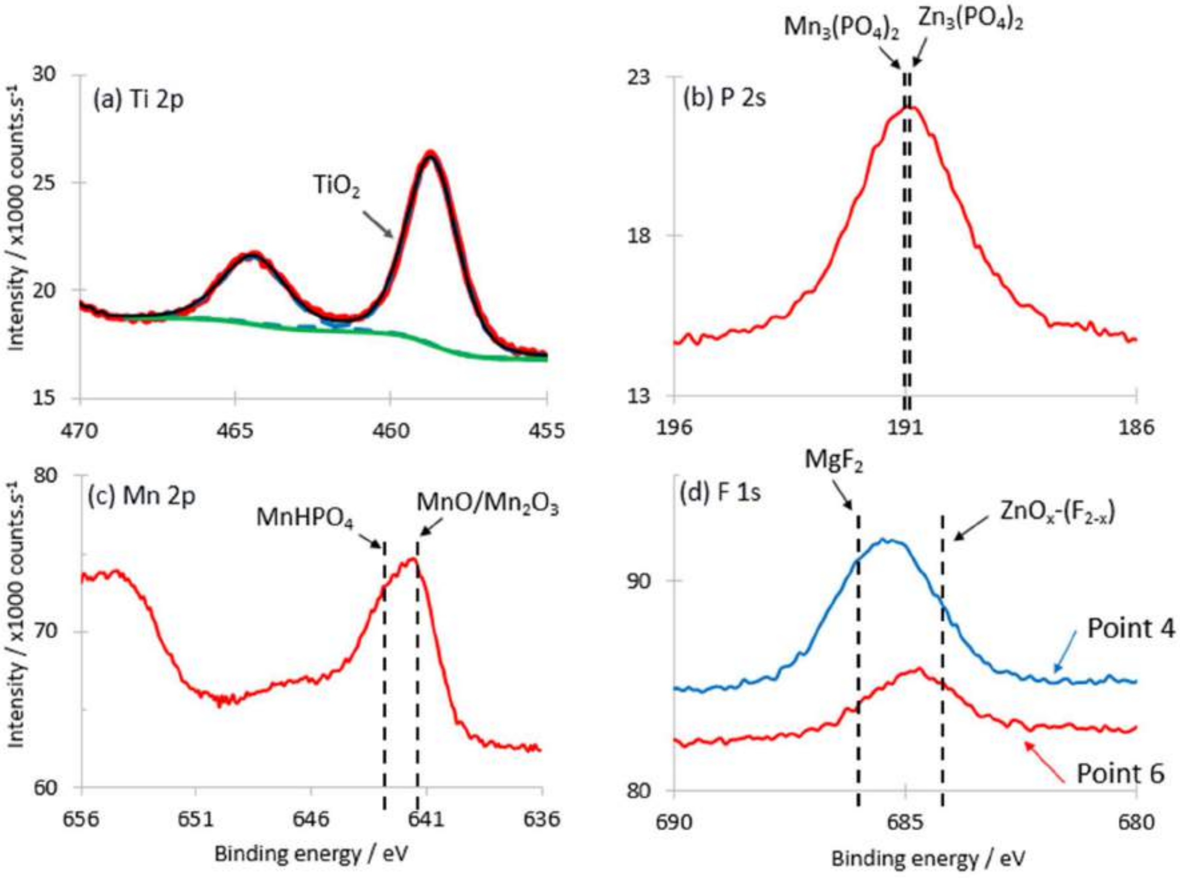

Figure 44: a) Ti 2p, b) P 2s, c) Mn 2p and d) F 1s XPS window spectra of ZnAlMg after Cu^{2+}-modified alkaline degreasing and immersion in the TiCC bath at 60 °C for 30 sec

A similar conversion coating chemical composition was detected in all the points selected for measurements except in the F 1s region (Figure 44 d). Generally, the peaks position for all studied elements is similar to the positions found on samples treated with an unmodified alkaline cleaner prior to the TiCC precipitation described in Chapter 5.

In the Ti 2p region, a peak fitting highlighted the presence of TiO_2 on the surface.

The determination of the type of phosphate precipitate created during the conversion reaction was performed using the P 2s region spectra as the P 2p region is interfered by Zn 3s.

In the P 2s region, the peak measured at 191 eV could be attributed to $Mn_3(PO_4)_2$ but also $Zn_3(PO_4)_2$ as they are 0.1 eV apart [32]-[33].

In the Mn 2p region spectra, the satellite peak at 647.7 eV is typical of the presence of MnO. The Mn 2p3 peak can be attributed to the presence of Mn^{II} or Mn^{III} [34]. It was also noticed that the binding energy of Mn 2p3 is in good agreement with the presence of $MnHPO_4$ on ZnAlMg [35].

For the F 1s region, a distinction must be made between both peaks. Indeed, for the Point 6, a lower binding energy was measured which highlights the presence of compounds such as $ZnO_xF_{(2-x)}$ [36].

On the other hand, on the Point 4, the higher binding energy suggests the formation of MgF_2 considering its binding energy and solubility product. [37]. On the Point 4, the intensity and peak width are larger compared to the Point 6. It can be assumed that both MgF_2 and $ZnO_xF_{(2-x)}$ are present in that sample surface area.

The list of all the compounds with a binding energy matching the peaks detected in the P 2s, Mn 2p and F 1s regions are gathered in Appendix 8.

3.5. Surface reactivity of epoxy coated samples by LEIM

The under-paint reactivity was studied by LEIM after separated OCP-anodic polarization, OCP-cathodic polarization cycles and a combination of both of them and following immersion. Two epoxy polymer coated ZnAlMg samples immersed in the TiCC bath at 60 °C for 30 sec after degreasing in a standard unmodified alkaline cleaner and Cu^{2+}-modified alkaline one respectively were compared. Both samples were scratched prior to the experiment and tested in 5 cycles of alternating anodic and cathodic polarization and overnight immersion. The purpose of this experiment was to compare the delamination resistance of both samples when immersed in a 0.1 M NaCl solution after alternating cathodic and anodic polarizations. The Figure 45 shows the maps of the values of the gradient of the admittance modulus obtained on these samples.

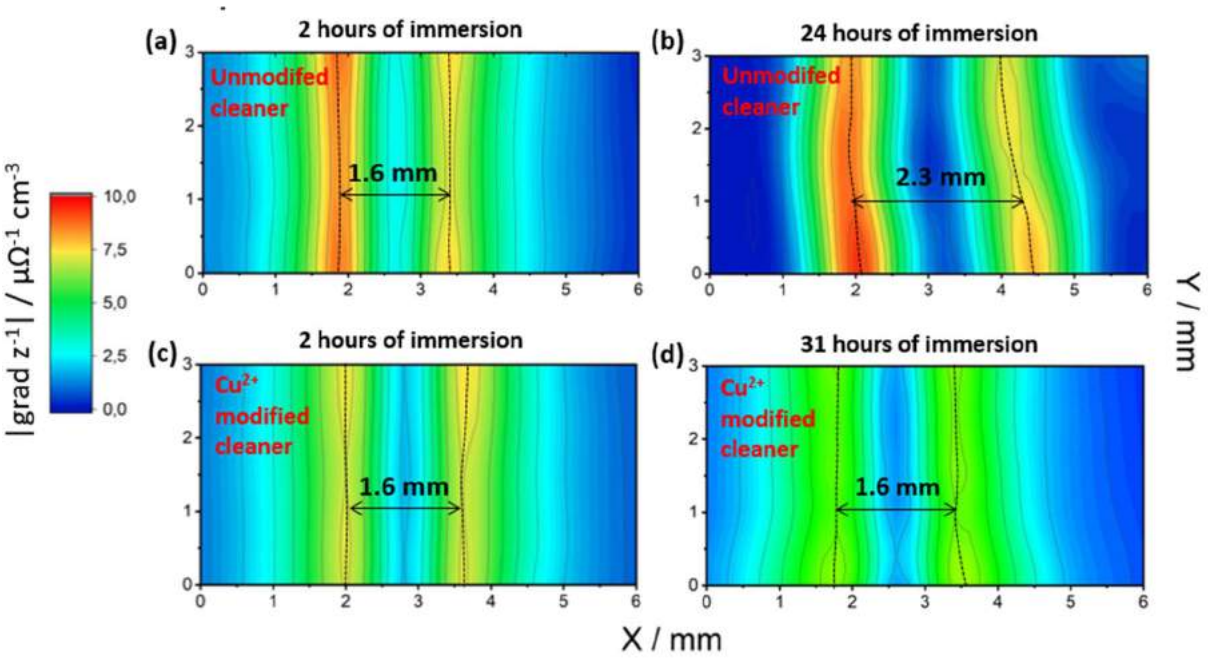

Figure 45: Gradient of the admittance modulus for ZnAlMg degreased with the standard cleaner: (a) after 2 h of immersion, (b) after 24 h of immersion and for ZnAlMg degreased with the Cu^{2+} modified cleaner: (c) after 2 h of immersion with alternating, (d) after 31 h of immersion

As shown by an admittance gradient map on Figure 45, at the beginning of the measurement, the delaminated zone width corresponds to the 1.6 mm-wide scratch (maps (a) and (c)). However, after alternating anodic and cathodic polarizations and 24 h of immersion in the electrolyte, the sample degreased with the unmodified alkaline cleaner exhibit a delaminated zone as large as 0.675 mm, corresponding to 42 % of its initial width (map (b)). On the other hand, the sample treated with the Cu^{2+}-modified alkaline cleaner, showed a barely worsened scratch (1.625 mm) after alternating cycles and 31 h of immersion as shown in the map (d). From this experiment, it was highlighted that the addition of Cu^{2+} ions to the degreasing bath leads to an enhanced delamination resistance of the epoxy-coated ZnAlMg sample.

Interestingly, even if the surface darkened around the scratch after anodic polarization (visible because the polymer was transparent), the under-paint reactivity was detected by LEIM only after a combination of both, anodic and cathodic polarizations and the following overnight immersion. This indicates the importance of both, anodic and cathodic reactions for the degradation of the interface in case of TiCC.

4. Discussion

4.1. Cu precipitation mechanism on ZnAlMg phases

Results in Figure 41 displayed an uneven distribution of Cu particles over all ZnAlMg phases. The binary ZnAl phase was largely covered with particles. Zn dendrites exhibited a partial coverage while Zn_2Mg lamellas showed very little amount of Cu on its surface. A possible explanation for this singularity comes from the necessity of an electron exchange from the metal substrate to Cu^{2+} ions to initiate the Cu precipitation.

During the alkaline degreasing step, the ZnAlMg phases have a different reactivity in alkaline conditions. The Al-containing phase ZnAl is easily dissolved at pH 12.5 which produces electrons available for Cu^{2+} ions to precipitate [38]. A similar statement can be made about Zn dendrites since Zn is sensitive to alkaline conditions, although in a less pronounced way than Al [38]. Zn_2Mg can form Mg hydroxides in alkaline media, limiting the Cu^{2+} reduction on its surface. From all these observations, one can conclude that Cu precipitation is triggered by the surface etching.

It was confirmed by Cerezo et al. as they noted that the nucleation of Cu particles was preferentially occurring on and around intermetallics contained in the microstructure of Al alloys which were preferentially getting dissolved during the alkaline surface etching [19].

4.2. Effect of Cu cementation on TiCC precipitation mechanism

The TiCC thickness seems to be affected by the coverage rate of Cu particles on ZnAlMg surface after the degreasing step. Indeed, the improved homogeneity of the conversion coating is based on the precipitation of noble cathodes on ZnAlMg. However, a complete coverage of the ZnAlMg surface is not aimed as it would inhibit the galvanic coupling between Cu and ZnAlMg phases. In this case, ZnAl phases are highly covered with Cu particles which isolate the phase from the surrounding TiCC solution during the conversion coating precipitation. A higher conversion coating thickness could have been achieved if a lower concentration of Cu was to be cemented on the phase surface. On the other hand, the precipitation of Cu on Zn dendrites was partial which favors the formation of a galvanic coupling between the Cu particles and the Zn dendrites and accelerate the precipitation kinetics of the conversion coating.

Based on the results observed on Figure 43, a new TiCC precipitation mechanism is suggested here after in Figure 46, taking into consideration the Cu precipitation after the degreasing step.

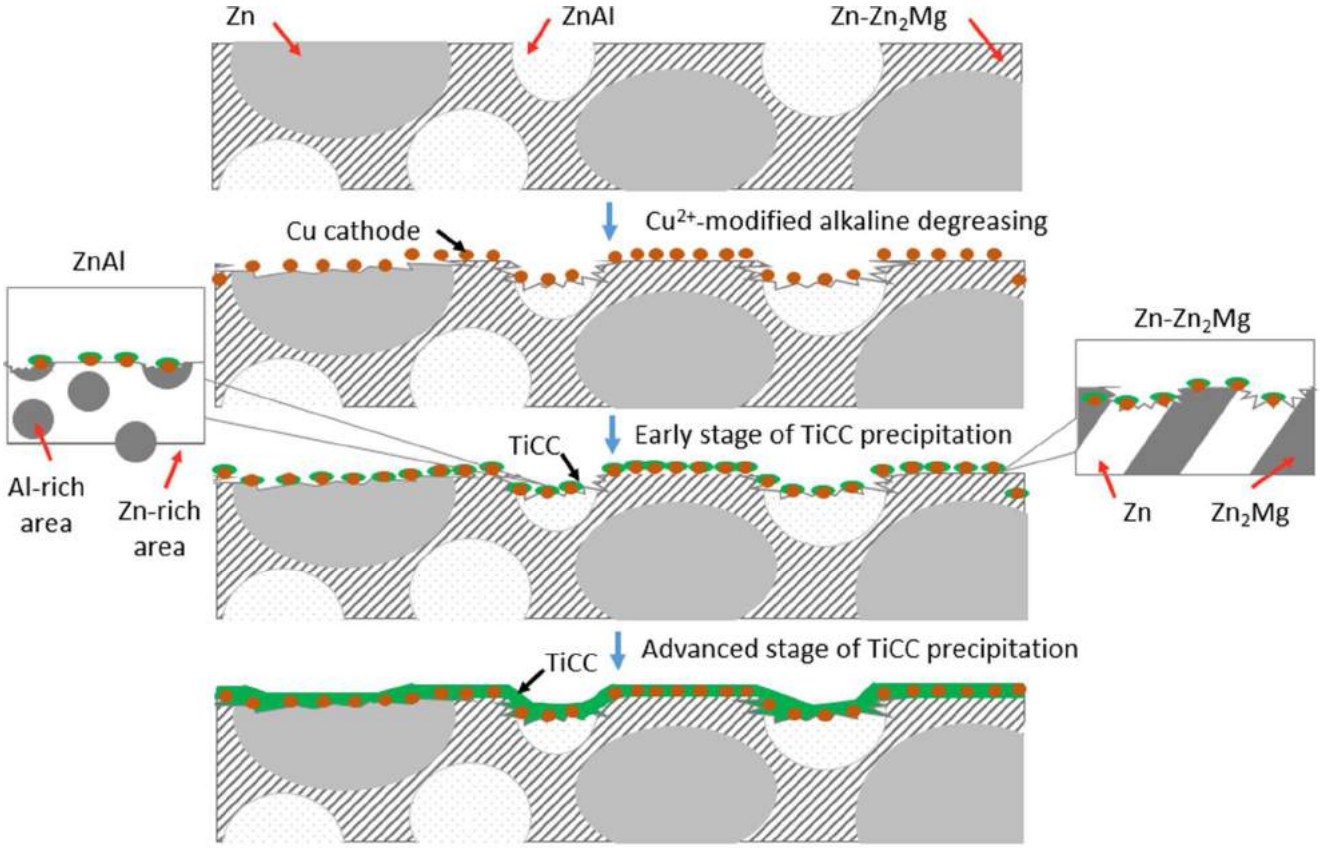

Figure 46: Scheme of the TiCC precipitation mechanism on ZnAlMg after Cu2+-modified alkaline degreasing procedure

For conveniency, an even Cu concentration is represented on all ZnAlMg phases as Cu particles are much smaller than the phase itself. Visible amounts like in Figure 41 are only revealing local overconcentration of Cu while Cu is precipitating all over the surface, even where it is not visible using electron microscopy.

During the degreasing step, the surface etching dissolves substrate elements such as Zn, Al and some Mg which makes it possible for the Cu^{2+} ions to precipitate. Considering that a large potential difference exists between all ZnAlMg phases and Cu^{2+}/Cu couple in the degreasing bath (~ 1 V/SCE), it is believed that Cu will precipitate homogeneously on the surface.

During the TiCC formation, the presence of Cu particles on the surface defines the cathodic sites where the oxygen and protons reductions can take place. In parallel, ZnAlMg phases exhibiting a much more anodic surface potential, the whole sacrificial coating serves as an anode. There is a fine distribution of cathodic and anodic sites on the whole surface thanks to the presence of Cu. When no Cu is precipitated, cathodes correspond to the ZnAlMg phases with the highest potential. However, from the moment Cu particles are precipitated, the potential gap between Cu and the sacrificial coating is so large that ZnAlMg most cathodic phases turn into anodes. The distribution of cathodes and anodes on the surface corresponds to a smaller scale lattice with distances between neighboring cathodes or anodes ranging about 100 nm. If no Cu precipitation, the distance between anodes and cathodes is in the micrometric scale, defined by the ZnAlMg microstructure size.

One can believe that the TiCC homogeneity lies in the distance separating the Cu particles. Since they are much smaller than ZnAlMg phases themselves, they are closely spaced, creating many local alkalization spots on the surface. Knowing that the TiCC formation will start at cathodes before extending itself to anodes, the little distance between anodes and cathodes will induce a much faster surface coverage by the TiCC.

5. Conclusion

In this chapter, a solution was proposed to obtain a homogeneous TiCC distribution on multiphase ZnAlMg substrate. This solution included a pretreatment resulting in the cementation of Cu particles on ZnAlMg. The impact of this pretreatment on the homogenization of TiCC distribution was investigated.

Even if the solution was inspired from CC formulations used in the automotive industry, where Cu^{2+} ions are incorporated to the CC baths to precipitate and create local and homogeneously distributed cathodes on metal surface, the main difference lies in the fact that Cu is not added to the conversion coating bath formulation but to the alkaline cleaner. The Cu precipitation occurs as a **distinct step**, prior to the TiCC precipitation.

The results demonstrated that the formulation of a Cu^{2+}-modified alkaline cleaner lead to the cementation of metallic Cu nanoparticles on all ZnAlMg phases. The **Cu precipitation is triggered by the surface etching** hence the electron exchange as represented here after:

$$\mathrm{Zn} + \mathrm{Cu}^{2+} \rightarrow \mathrm{Zn}^{2+} + \mathrm{Cu} \qquad (6\text{-}7)$$

Local concentration of deposited Cu decreased in order: binary ZnAl > Zn > Zn_2Mg intermetallics

- The cementation of Cu induces a new distribution of cathodes and anodes on ZnAlMg, more closely spaced. Many local alkalization spots are created on the surface leading to a more homogenized TiCC distribution on ZnAlMg phases.

The TiCC chemical composition remains unchanged on the overall for ZnAlMg samples treated with the Cu^{2+}-modified alkaline cleaner compared to those degreased with the unmodified one and TiCC contains: **TiO_2, $Zn_xMn_{3-x}(PO_4)_2$, $MnH(PO_4)_2$, Mn_xO_y,** and **MgF_2,**

- Preliminary tests of the interface stability of polymer-coated ZnAlMg materials treated with the Cu^{2+}-modified alkaline cleaner showed that the **addition of Cu^{2+} ions** to the alkaline cleaning bath led to slower degradation of the system compared to the systems prepared with standard cleaner.

Further tests aiming at optimizing the Cu concentration to be precipitated on the substrate surface would be interesting to perform. Indeed, since the TiCC homogeneity is closely linked with the distance separating cathodes and anodes on the surface, it is expected that a full coverage of the ZnAlMg surface is not to be achieved at the risk of obtaining an even surface potential and an inhibited galvanic coupling. Local alkalization is not initiated hence limiting the TiCC precipitation mechanism.

Deeper understanding of degradation mechanisms at the ZnAlMg/TiCC/polymer interface and the interpretation of all the results of local EIS measurements at different steps of ageing are also necessary.

.

References

[1] Ocupational Safety and Health Administration, Occupational Safety and Health Standards - Toxic and Hazardous Substances, United States Department of Labor. [Online]. Available on: https://www.osha.gov/pls/oshaweb/owadisp.show_document?p_table=STANDARDS&p_id=13117. [Accessed on: 09/08/2018].

[2] European Chemicals Agency, Substances restricted under REACH, *ECHA*, 2006. [Online]. Available on: https://echa.europa.eu/substances-restricted-under-reach/-/dislist/details/0b0236e1807e2bc1. [Accessed on: 09/08/2018].

[3] L. Fedrizzi, F. Deflorian, P. L. Bonora, Corrosion behaviour of fluotitanate pretreated and painted aluminium sheets, Electrochim. Acta, 42 (1997) 969-978.

[4] J. H. Nordlien, J. C. Walmsley, H. Østerberg, K. Nisancioglu, Formation of a zirconium-titanium based conversion layer on AA 6060 aluminium, Surf. Coat. Technol., 153 (2002) 72-78.

[5] O. Lunder, C. Simensen, Y. Yu, K. Nisancioglu, Formation and characterisation of Ti–Zr based conversion layers on AA6060 aluminium, Surf. Coat. Technol., 184 (2004) 278-290.

[6] F. Andreatta, A. Turco, I. de Graeve, H. Terryn, J. H. W. de Wit, L. Fedrizzi, SKPFM and SEM study of the deposition mechanism of Zr/Ti based pre-treatment on AA6016 aluminium alloy, Surf. Coat. Technol., 201 (2007) 7668-7685.

[7] V. Saarimaa, E. Kauppinen, A. Markkula, J. Juhanoja, B.-J. Skrifvars, P. Steen, Microscale distribution of Ti-based conversion layer on hot dip galvanized steel, Surf. Coat. Technol., 206 (2012) 4173-4179.

[8] J. Cerezo, I. Vandendael, R. Posner, K. Lill, J.H.W. de Wit, J.M.C. Mol, H. Terryn, Initiation and growth of modified Zr-based conversion coatings on multi-metal surfaces, Surf. Coat. Technol., 236 (2013) 284-289.

[9] V. Saarimaa, A. Markkula, J. Juhanoja, B.-J. Skrifvars, Determination of Surface Topography and Composition of Cr-Free Pretreatment Layers on Hot Dip Galvanized Steel, J Coat Sci Technol, 1 (2014) 88-95.

[10] P. Volovitch, T. N. Vu, C. Allély, A. Abdel Aal, K. Ogle, Understanding corrosion via corrosion product characterization: II. Role of alloying elements in improving the

corrosion resistance of Zn–Al–Mg coatings on steel, Corros. Sci., 53 (2011) 2437-2445.

[11] T. Prosek, A. Nazarov, U. Bexell, D. Thierry, J. Serak, Corrosion mechanism of model zinc–magnesium alloys in atmospheric conditions, Corros. Sci., 50 (2008) 2216–2231.

[12] T. Prosek, A. Nazarov, A. Le Gac, D. Thierry, Coil-coated Zn–Mg and Zn–Al–Mg: Effect of climatic parameters on the corrosion at cut edges, Prog. Org. Coat., 83 (2015) 26–35.

[13] W. Zhu, W. Li, S. Mu, N. Fu, Z. Liao, Comparative study on Ti/Zr/V and chromate conversion treated aluminium alloys: Anti-corrosion performance and epoxy coating adhesion properties, Appl. Surf. Sci., 405 (2017) 157–168.

[14] R.P. Edavan, R. Kopinski, Corrosion resistance of painted zinc alloy coated steels, Corros. Sci., 51 (2009) 2429–2442.

[15] T. Lostak, A. Maljusch, B. Klink, S. Krebs, M. Kimpel, J. Flock, S. Schulz, W. Schuhmann, Zr-based conversion layer on Zn-Al-Mg alloy coated steel sheets: insights into the formation mechanism, Electrochim. Acta, 137 (2014) 65-74.

[16] T. Lostak, S. Krebs, A. Maljusch, T. Gothe, M. Giza, M. Kimpel, J. Flock, S. Schulz, Formation and characterization of Fe^{3+}-/Cu^{2+}-modified zirconium oxide conversion layers on zinc alloy coated steel sheets, Electrochim. Acta, 112 (2013) 14-23.

[17] S. Adhikari, K.A. Unocic, Y. Zhai, G.S. Frankel, J. Zimmerman, W. Fristad, Hexafluorozirconic acid based surface pretreatments: Characterization and performance assessment. Electrochim. Acta 56 (2011) 1912–1924.

[18] A. Sarfraz, R. Posner, M.M. Lange, K. Lill, A. Erbe, Role of Intermetallics and Copper in the Deposition of ZrO2 Conversion Coatings on AA6014. J. Electrochem. Soc. 161 (2014) C509–C516.

[19] J. Cerezo, I. Vandendael, R. Posner, J.H.W. de Wit, J.M.C. Mol, H. Terryn, the effect of surface pre-conditioning treatments on the local composition of Zr-based conversion coatings formed on aluminium alloys., Appl. Surf. Sci., 366 (2016) 339–347.

[20] N.W. Khun, G.S. Frankel, Composition and corrosion protection of hexafluorozirconic acid treatment on steel: Composition and corrosion protection of hexafluorozirconic acid, Mater. Corros., 66 (2015) 1215–1222.

[21] J. Cerezo, P. Taheri, I. Vandendael, R. Posner, K. Lill, J.H.W. de Wit, J.M.C. Mol, H. Terryn, Influence of surface hydroxyls on the formation of Zr-based conversion coatings on AA6014 aluminium alloy, Coat. Technol., 254 (2014) 277-283.

[22] I. Milosev, G. S. Frankel, Review—Conversion Coatings Based on Zirconium and/or Titanium, J. Electrochem. Soc., 165 (2018) C127-C144.

[23] I. Schoukens, I. Vandendael, J. De Strycker, A.A. Saleh, H. Terryn, I. De Graeve, Effect of surface composition and microstructure of aluminised steel on the formation of a titanium-based conversion layer, Surf. Coat. Technol., 235 (2013) 628–636.

[24] R. Posner, N. Fink, M. Wolpers, G. Grundmeier, Electrochemical electrolyte spreading studies of the protective properties of ultra-thin films on zinc galvanized steel. Surf. Coat. Technol., 228 (2013) 286–295.

[25] X.-F. Xia, Y.-Y. Gu, S.-A. Xu, Titanium conversion coatings on the aluminium foil AA 8021 used for lithium–ion battery package. Appl. Surf. Sci., 419 (2017) 447–453.

[26] L. Li, B. W. Whitman, G. M. Swain, Characterization and performance of a Zr/Ti pretreatment conversion coating on AA2024-T3, J. Electrochem. Soc., 162 (2015) C279-C284.

[27] Ringbom, A. (1967). Les complexes en chimie analytique (Paris).

[28] R.L. Pecsok, R.S. Juvet, The Gluconate Complexes. I. Copper Gluconate Complexes in Strongly Basic Media1. J. Am. Chem. Soc., 77 (1955) 202–206.

[29] W.A. Norvell, W.L. Lindsay, Reactions of EDTA Complexes of Fe, Zn, Mn, and Cu with Soils 1, Soil Sci. Soc. Am. J., 33 (1969) 86–91.

[30] V. Shkirskiy, P. Volovitch, V. Vivier, ‘Development of quantitative Local Electrochemical Impedance Mapping: an efficient tool for the evaluation of delamination kinetics, Electrochimica Acta, 235 (2017) 442–452.

[31] Thermofisher, Copper - Interpretation of XPS data, [Online]. Available on: https://xpssimplified.com/elements/copper.php. [Consulted on: 25-sept-2018].

[32] R. Franke, T. Chassé, P. Streubel, A. Meisel, Auger parameters and relaxation energies of phosphorus in solid compounds, J. Electron Spectrosc. Relat. Phenom., 56 (1991) 381-388.

[33] D. L. Felker, P. M. A. Sherwood, Zinc phosphate (Zn3(PO4)2) by XPS, Surf. Sci. Spectra, 9 (2002) 106-113.

[34] Thermofisher, Manganese - Interpretation of XPS data. [Online]. Available on: https://xpssimplified.com/elements/manganese.php. [Consulted on: 25-sept-2018].

[35] G. Wang, N. Cao, Y. Wang, Characteristics and corrosion studies of Zn-Mn PCC on Mg-Li alloy, RSC Adv., 4 (2014) 59772-59778.

[36] C. D. Wagner, Handbook of X-Ray and ultraviolet Photoelectron Spectroscopy, D. Briggs.

[37] S. Da-Ming, S. Zhao-Qi, L. Ai-Xia, X. Zhi-Yuan, XPS analysis of the oxidation of Ag–MgF2 cermet film, Vacuum, 52 (1999) 383-386.

[38] M. Pourbaix, Atlas d’équilibres électrochimiques à 25 °C, Gauthier-Villars & Cie, Paris, 1963.

Conclusion and perspectives

1. Effect of microstructure on the formation of CC

The importance of the microstructure for conversion coating formation mechanisms and following performance was demonstrated. The hypothesis proposed during the PhD states that the microstructure effects become critical for the CC distribution if typical microstructure elements of the substrate, which can become local anodic sites during the CC formation, are significantly bigger than the elementary structural constituents of the formed conversion coating. This hypothesis was verified at different steps of PCC and TiCC procedures and a solution to improve the homogeneity of the TiCC distribution on the multiphase ZnAlMg substrate via cementation of metallic Cu was proposed. This way, corrosion mechanisms of painted ZnAlMg coated steel as well as the precipitation mechanism of TiCC and PCC on multiphase ZnAlMg coatings were understood.

Combining surface characterization of ZnAlMg coatings and pure phases, simulating ZnAlMg materials, at different steps of the CC procedure, it was confirmed that nanometric Ti-containing surface pretreatment (activator for PCC) and TiCC are heterogeneously distributed on ZnAlMg phases while micrometric PCC forms a homogeneous layer. The heterogeneous CC distribution was consistent with the worsened blistering resistance of TiCC-treated ZnAlMg surfaces compared to PCC-treated samples ones.

For PCC, the formation mechanism is described here after:

Anodic dissolution :

$$\mathrm{Me} \rightarrow \mathrm{Me}^{n+} + \mathrm{ne}^{-} \qquad (1)$$

Cathodic reduction leading to pH increase:

$$\mathrm{NO_3^-} + 2\mathrm{H}^{+} \rightarrow \mathrm{NO_2^-} + \mathrm{H_2O} \qquad (2)$$

Or

$$\mathrm{NO_2^-} + 8\mathrm{H}^{+} + 6\mathrm{e}^{-} \rightarrow \mathrm{NH_4^+} + \mathrm{H_2O} \qquad (3)$$

PCC precipitation in pH range from 4.7 to 8.5:

$$2PO_4^{3-} + 3Zn^{2+} + H_2O \rightarrow Zn_3(PO_4)_2.nH_2O \qquad (4)$$

Homogeneous PCC distribution covering all the phases despite a significant variation in the density of activator sites on different phases was attributed to the effect of PCC grains size, which is higher than the lateral dimensions of the constituents of binary phases and zinc dendrites. This way, during the PCC precipitation, grains initially formed on cathodic areas grow until they are in contact with each other and fully cover the substrate. The distribution of cathodes and anodes in ZnAlMg microstructure is fine enough compared to the PCC grains dimension to enable a full coverage of the surface as schematically represented in Figure 47

.

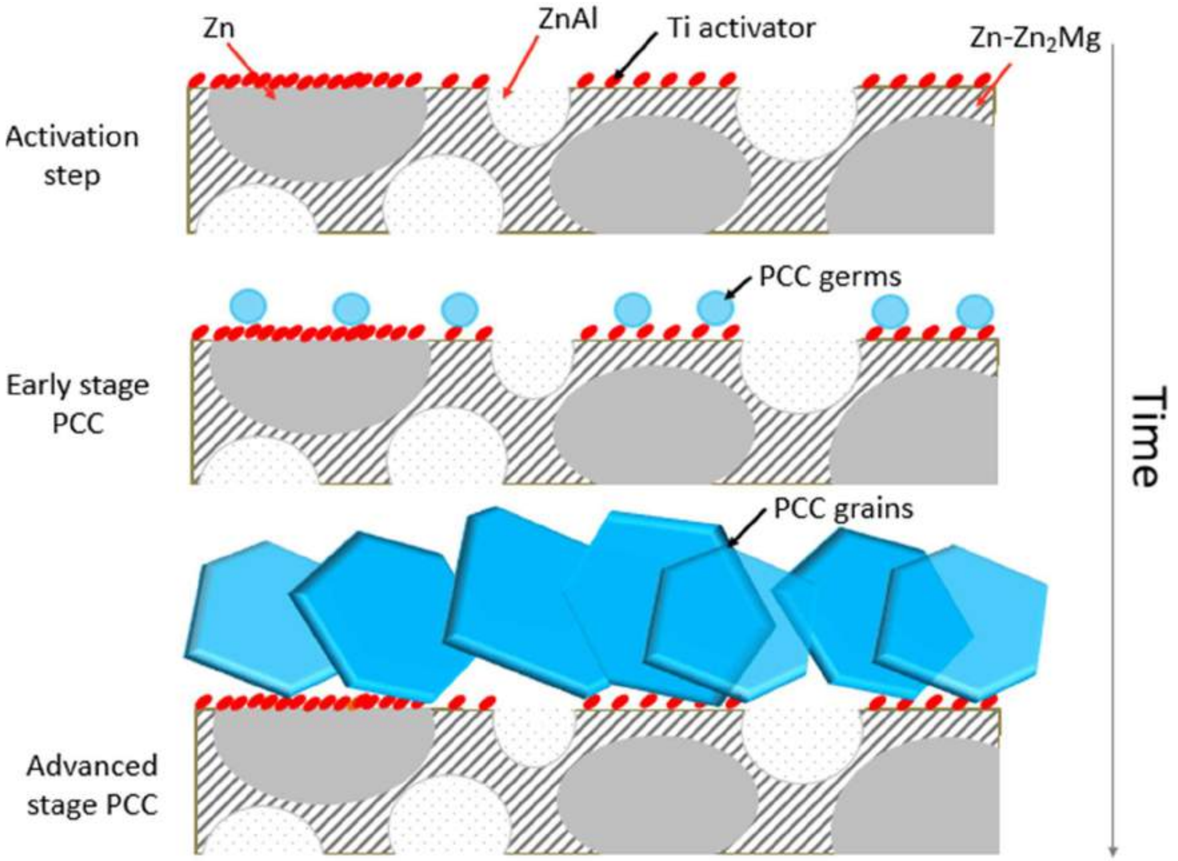

Figure 47: Scheme of the Ti-activator and PCC distributions explaining homogeneous precipitation

For TiCC, the CC formation mechanism can be summarized as follows:

- Anodic dissolution:

$$Me \rightarrow Me^{n+} + ne^- \qquad (1)$$

- Cathodic reduction leading to pH increase:

$$O_2 + 4H^+ + 4e^- \rightarrow 2H_2O \qquad (4)$$

and

$$2H^+ + 2e^- \rightarrow H_2 \qquad (5)$$

- TiCC precipitation (pH range= 2.5 – 8.5):

$$TiF_6^{2-} + 4OH^- \rightarrow TiO_2.H_2O + 6F^- \qquad (6)$$

The presence of galvanic coupling inside binary phases can enhance the phase reactivity in both, anodic and cathodic processes, and improve coating deposition kinetics. Experiments on model pure phases confirmed the possibility of coupling inside binary phases as illustrated in Figure 48

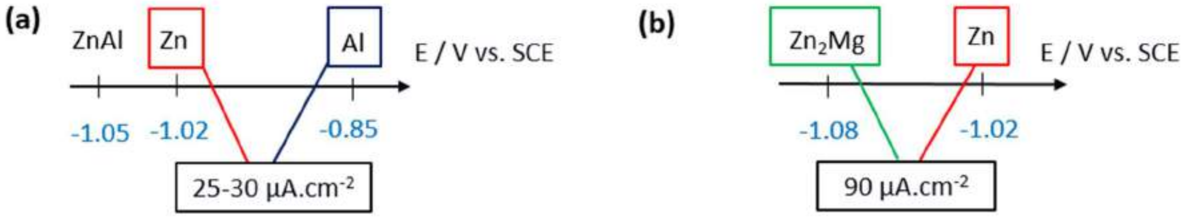

Figure 48: OCP of individual phases and current density measured for galvanic coupling of (a) Zn/Al and (b) Zn/Zn_2Mg phases relevant for binary eutectics. The measurement was made after 30 min of immersion of uncoupled phases in 5 wt. % Na_2SO_4 solution with initial pH 2,6 at 25 °C (OCP) followed by 2 h of phase coupling (galvanic current values).

More detailed specification of the TiCC components on different ZnAlMg phases and the methods permitting this specification are shown in Figure 49.

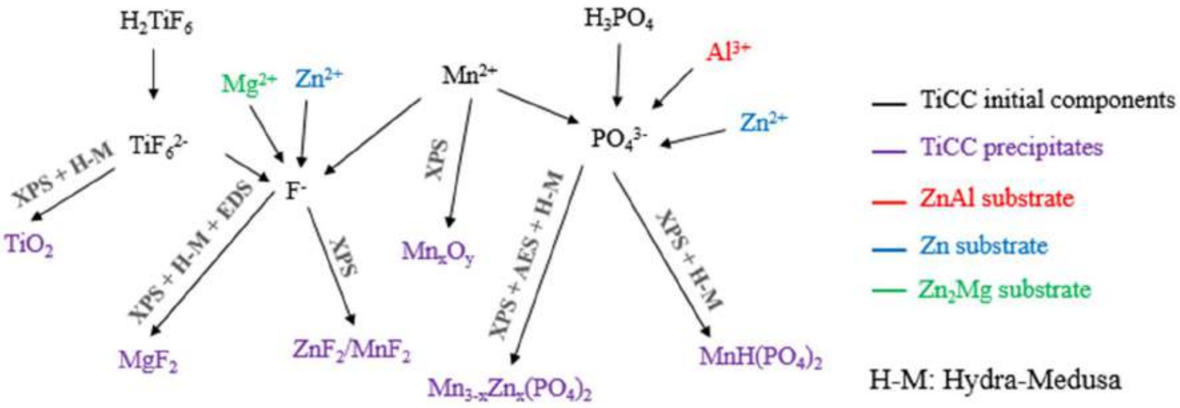

Figure 49: Schematic representation of formation of different CC species during reaction of Zn, ZnAl and Zn2Mg phases in TiCC bath

For TiCC, the CC elements are nanometric and hence significantly smaller than structural elements of binary and ternary phases as well as Zn dendrites, which makes critical the formation of a homogeneous layer during the CC precipitation step. Binary phases have an enhanced TiCC precipitation kinetics because of the closely spaced cathodic Zn dendrites/anodic Zn_2Mg lamellas in the Zn-Zn_2Mg phase and the anodic Zn-rich areas/ cathodic Al-rich zones in the ZnAl phase. On the contrary, monophase Zn dendrites are less covered than binary ZnAl and Zn/Zn_2Mg phases. As a result, after the completion of the TiCC procedure, the distribution is inhomogeneous, as illustrated in Figure 50.

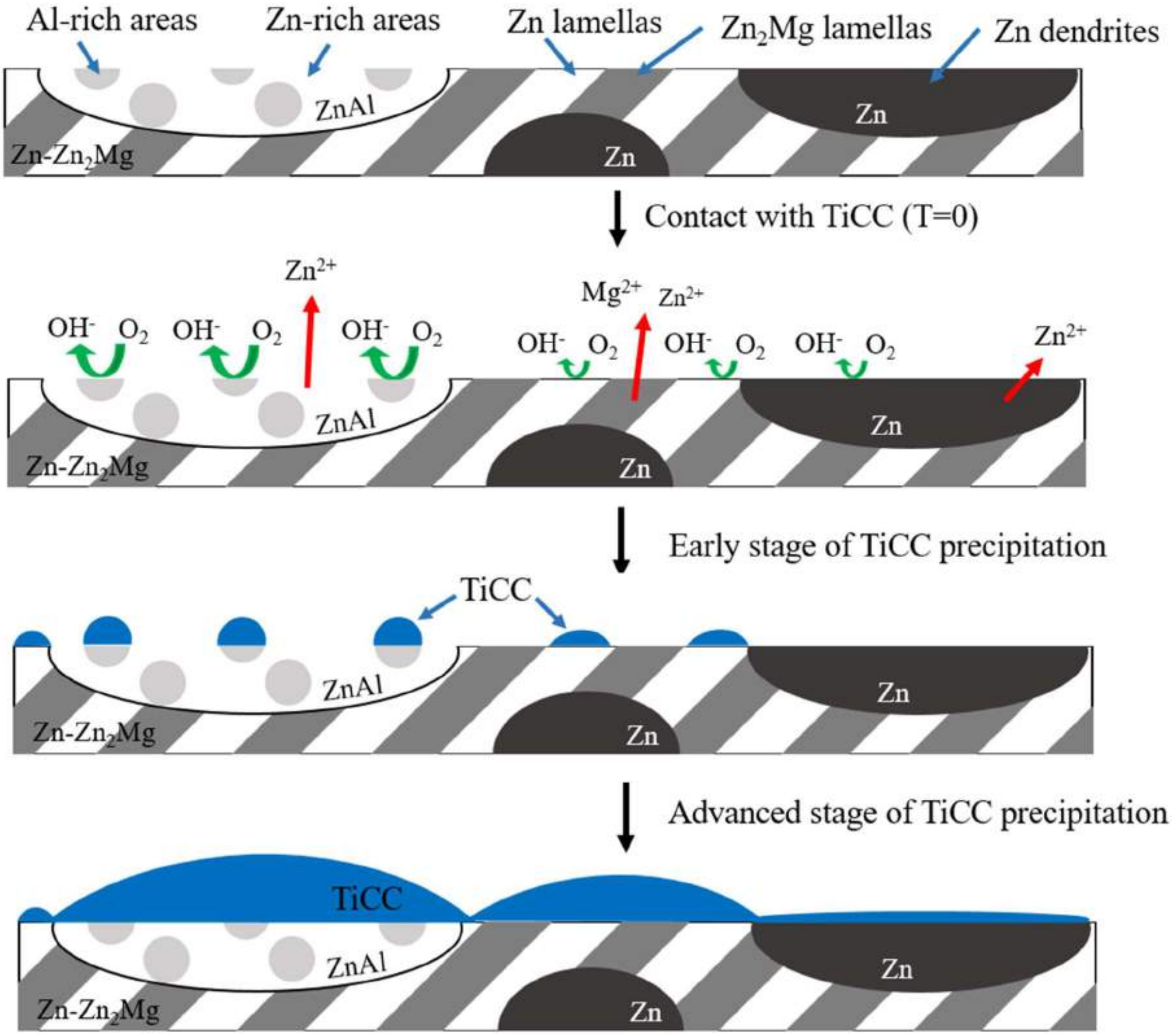

Figure 50: Schematic representation of inhomogeneous TiCC formation on the multiphase substrate

To overcome the influence of the microstructure/CC elements size ratio, it was proposed to achieve a Cu cementation on ZnAlMg phases during the degreasing step prior to the TiCC procedure. The cementation reaction can be described as follows:

$$\mathrm{Zn} + \mathrm{Cu}^{2+} \rightarrow \mathrm{Zn}^{2+} + \mathrm{Cu} \quad (7)$$

$$\mathrm{Zn_2Mg} + 3\mathrm{Cu}^{2+} \rightarrow 2\mathrm{Zn}^{2+} + \mathrm{Mg}^{2+} + 3\mathrm{Cu} \quad (8)$$

$$2\mathrm{Al} + 3\mathrm{Cu}^{2+} \rightarrow 2\mathrm{Al}^{3+} + 3\mathrm{Cu} \quad (9)$$

Considering the noble character of Cu/Cu^{2+} couple compared to the character of all the phases of ZnAlMg, the Cu cementation appears on all phases and enables a finer distribution of anodes and cathodes than the distribution induced by binary ZnAl and Zn/Zn_2Mg phases. AES confirmed that after the new pretreatment metallic Cu is present on all phases including Zn dendrites Figure 51.

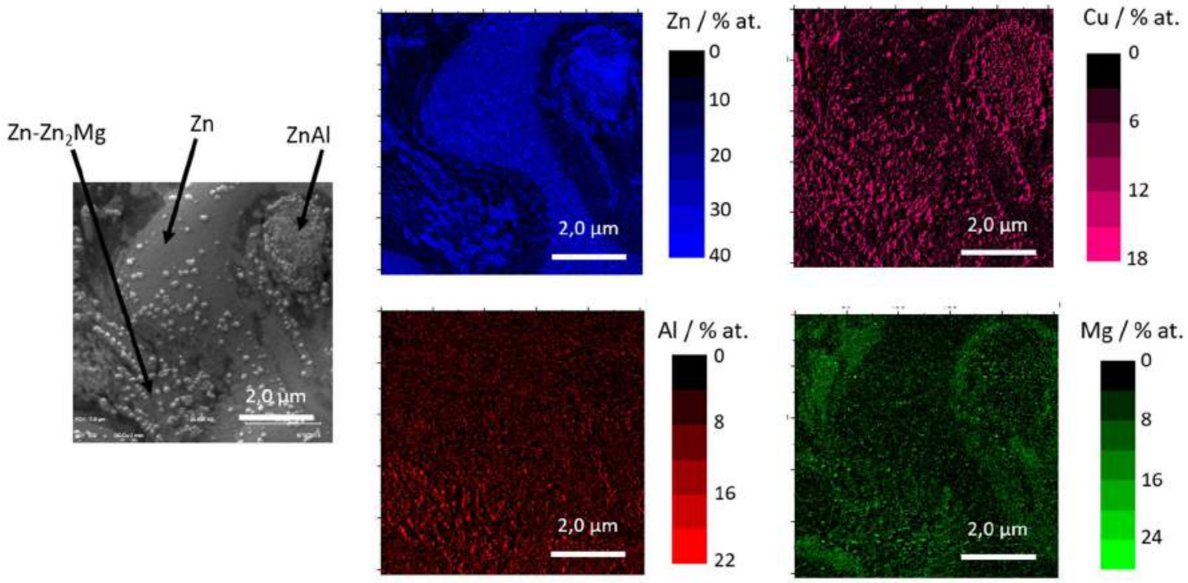

Figure 51: AES mapping of ZnAlMg surface after immersion in Cu alkaline cleaning at 55 °C for 2 min

The galvanic coupling between Cu particles and the substrate results in more rapid and more homogeneous pH increase in vicinity of the surface and hence in a more homogeneously distributed CC during the TiCC procedure as schematically displayed in Figure 52.

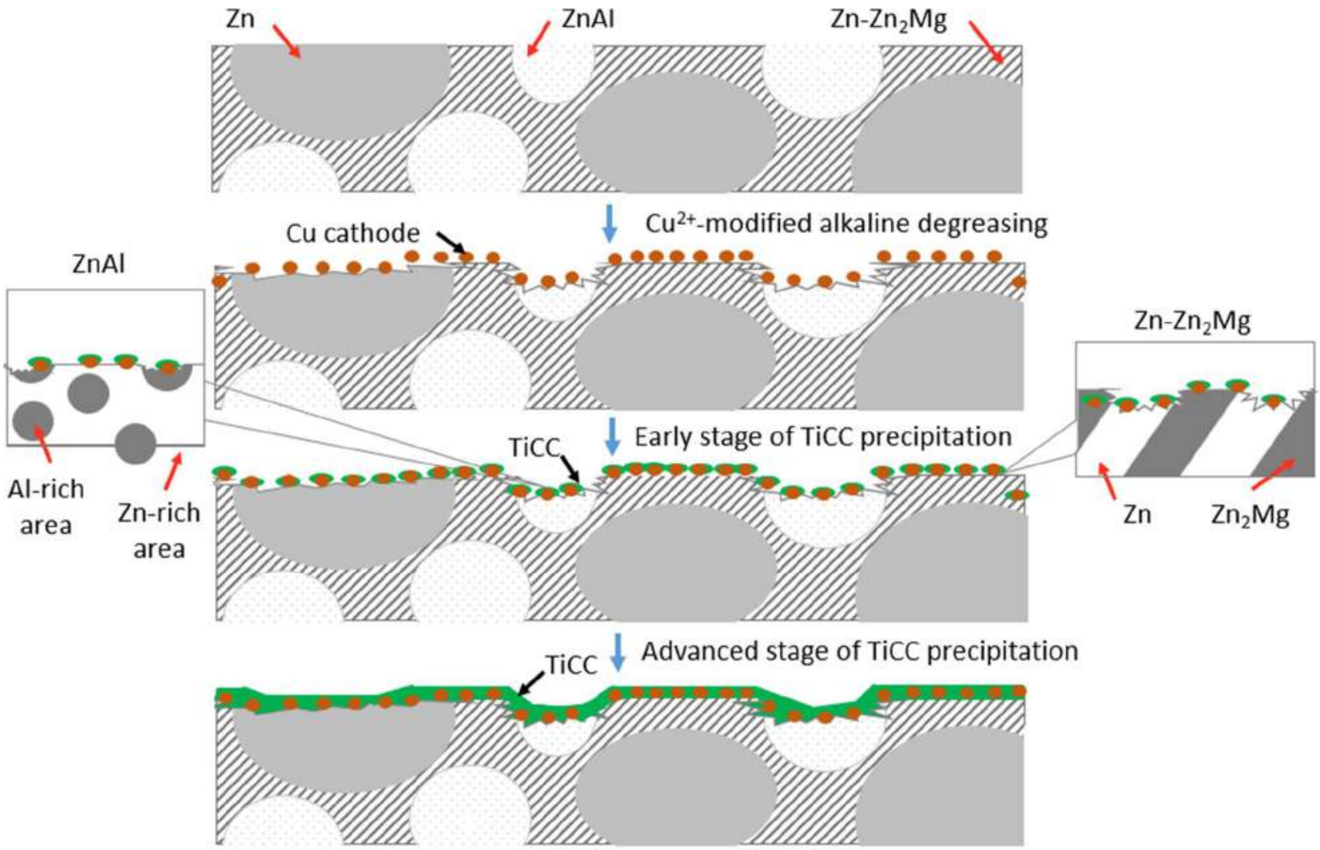

Figure 52: Scheme of the TiCC precipitation mechanism on ZnAlMg after Cu2+-modified alkaline degreasing procedure

Nano-AES confirmed that a well detectable homogeneous layer of TiCC can be formed on all phases of ZnAlMg substrate after Cu-containing degreasing (Figure 53), while after a standard alkaline degreasing, Zn dendrites were not covered at this temperature.

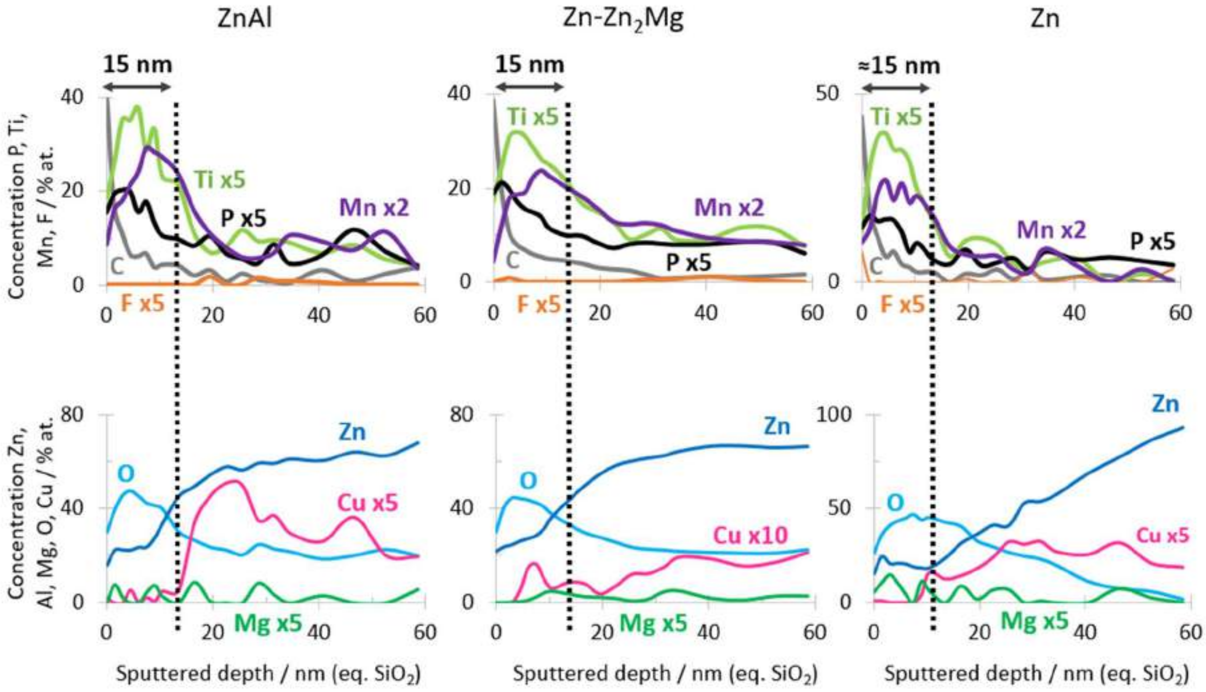

Figure 53: AES profile of ZnAlMg after immersion in TiCC bath at 60 °C for 30 sec after Cu alkaline cleaning

2. Effect of microstructure on the degradation mechanism of painted ZnAlMg

The importance of the microstructure on the degradation of painted ZnAlMg coatings is evidenced from the fact that painted ZnAlMg coated steel can develop blisters in outdoor exposure if a defect in the paint and coating goes down to the steel substrate while no blisters are formed in similar conditions on HDG steels. Moreover, the blisters are absent if the scratch does not go to the steel, which can be interpreted as a key role of anodic processes in blistering observed on painted ZnAlMg with artificial defect down to steel.

The SKP mapping demonstrated the existence of interconnected paths between the visually isolated blisters. The path is characterized by lower than the surrounding matrix Volta potential values. SEM observations of cross sections revealed that the path contains corroded ZnAlMg coating under intact paint and that the initial lack of adherence can originate from these corroded areas. Similar to corrosion of unpainted ZnAlMg, it seems that the underpaint corrosion of these coatings starts with selective corrosion of Zn_2Mg phase.

Two hypotheses explaining how the microstructure can affect the stability of the metal/polymer interface were formulated.

First, considering that galvanostatic anodic polarization is much more harmful for delamination in the case of a multiphase ZnAlMg coated steel than for a monophase HDG steel, the galvanic coupling between phases of the coating can enhance under paint reactivity and anodic undermining, giving easier access for water and oxygen to the cathodic areas.

Another hypothesis explaining the role of the multiphase microstructure can be related to the non homogeneous conversion coating on multiphase substrate resulting in a local lack of adherence. The latter can contribute to easy access of water and oxygen to the ZnAlMg substrate but also to a localization of the corrosion process. This hypothesis seems to be confirmed by the surface analysis (chapter 5) and by the fact that after the pretreatment enabling a homogeneous TiCC distribution, the stability of the interface metal/polymer in painted ZnAlMg seems to be significantly improved (chapter 6).

The exact role of the multiphase microstructure for the performance of painted ZnAlMg coated steel still needs to be understood. Indeed, it cannot be ruled out that the starting point of the corrosion propagation under the paint could be a combination of the initial inhomogeneity of the conversion coating, its low chemical stability and the ZnAlMg substrate corrosion, but the initial distribution of conversion coating seems to be a very important factor.

Finally, another pretreatment, also using the principle of metal cementation in order to homogenize TiCC distribution between ZnAlMg phases was proposed for industrial application and accelerated tests made in ArcelorMittal using this solution demonstrated significantly improved resistance to blister formation for the painted samples prepared with this new pretreatment.

3. Perspectives

Through the work about the mechanisms of TiCC formation, it was understood that the inhomogeneity of TiCC deposition is related to the inhomogeneity of the distribution of cathodic and anodic zones and a physico-chemical solution in which the surface activation can be achieved by a cementation of noble metal was proposed. This solution stays, however, at the level of laboratory tests and both, industrial application of the surface treatment procedure and a deep understanding of the improved blistering resistance should be made.

For the process application, it would be very interesting to optimize the formulation of the cleaner to enable an optimum distribution of Cu cathodes as a function of the substrate and to accelerate the deposition kinetics of the TiCC, therefore increasing the CC thickness.

To improve the understanding of blistering mechanisms, first of all more data are necessary concerning the stability of TiCC and the underlying substrate during the degradation of painted systems. Even if the SEM and SKP results demonstrated the presence of anodic dissolution under the paint and the presence of corroded “routes” between the blisters, the spatial resolution of SKP and the complexity of sample preparation for high resolution SEM were unable to elucidate the exact nature of the phases responsible for these routes. From the corrosion mechanisms of ZnAlMg alloys, one can expect that the binary and ternary eutectics containing Zn_2Mg should behave as the most anodic phases and dissolve preferentially, however a direct proof in the case of under paint corrosion is still missing. Moreover, in the present PhD, only the role of the substrate microstructure was considered. At the same time, the presence of soluble contamination trapped under the paint during the coil coating process due to the absence of rinsing step still needs to be addressed.

Deeper understanding of degradation mechanisms at the ZnAlMg/TiCC/polymer interface and the interpretation of all the results of local EIS measurements at different steps of ageing are also necessary.

Considering the improved adhesion after accelerated electrochemical corrosion testing of samples for which the surface preparation included Cu cementation pretreatment, it can be, firstly, attributed to a more homogeneous and thicker CC layer which improved initial adhesion limiting water diffusion between the substrate and the paint. However, it is not sufficient to explain the absence of locally propagating selective dissolution of anodic phases. One of the possible explanations is that a contact of all phases with homogeneously distributed cemented Cu metal forces a homogeneous dissolution around the scratch and formation of corrosion products blocking further corrosion propagation. The fact that adhesion is improved on the Zn dendrites limits the electrolyte access to their surface and the local pH increase once the electrolyte arrives. Another aspect of this work that needs to be extended is the evaluation of the corrosion resistance of painted ZnAlMg coated steels treated with the Cu^{2+}-modified alkaline cleaner in long term natural exposure to determine and quantify the gained corrosion resistance. The solution is under testing at the moment and a definite answer will be available in a few years.

Appendices

Appendix 1 (Chapter 1)

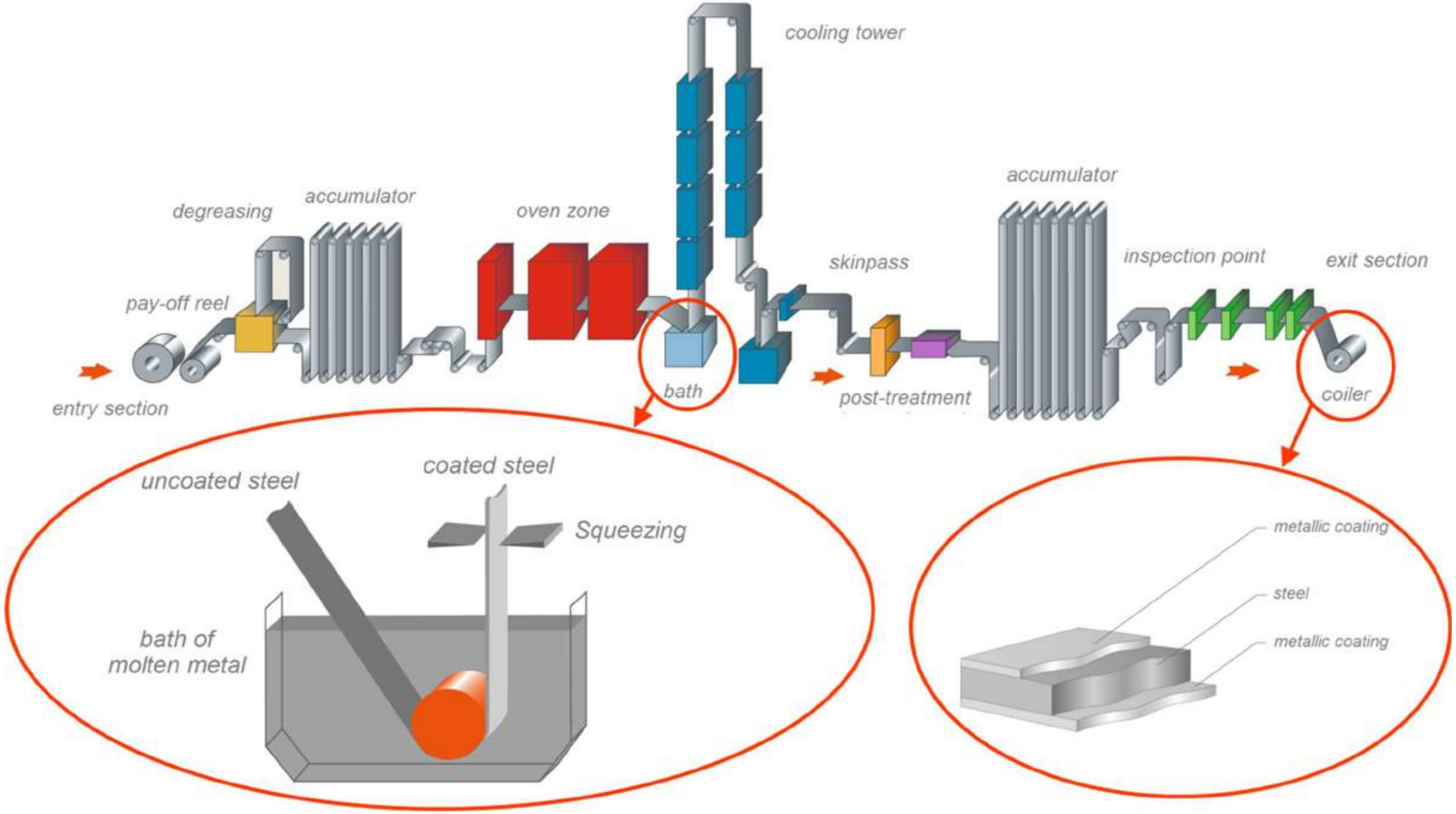

Figure 54: Schematic representation of a hot dip process for ZnAlMg coatings (1)

[1]: User manual, Organic coated steel, ArcelorMittal Flat Carbon Europe 19, avenue de la Liberté L-2930 Luxembourg.

Appendix 2 (Chapter 2)

ZnAlMg coatings

Composition A

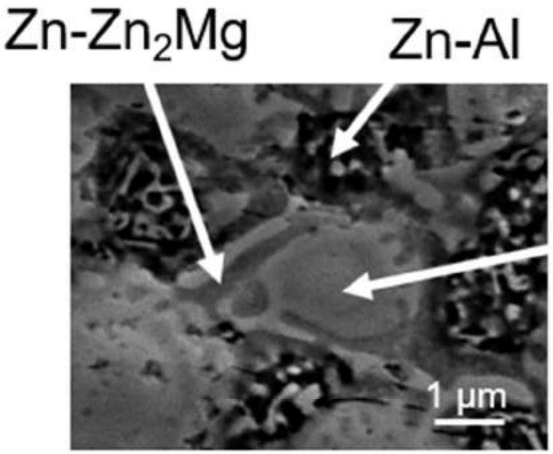

Composition C

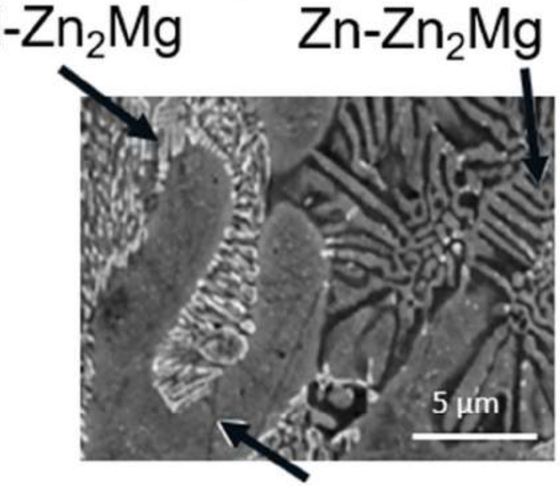

Composition B

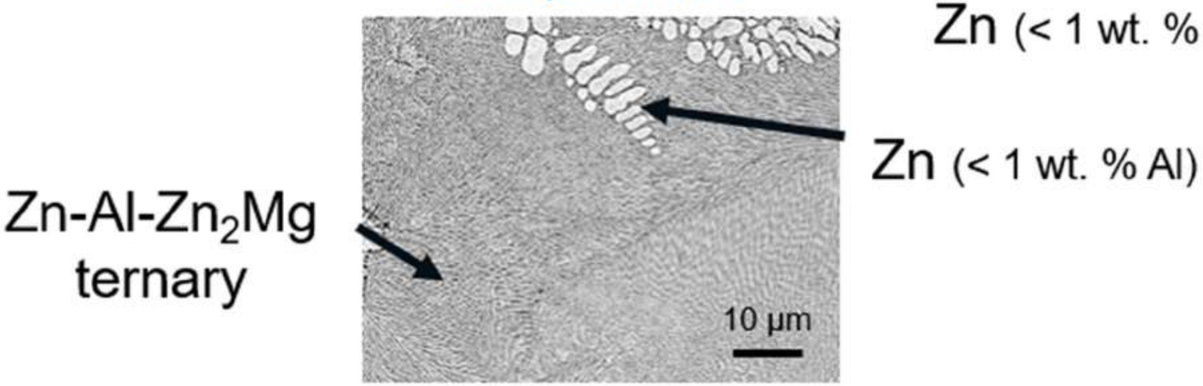

Appendix 3 (Chapter 2)

Pure phases relevant for ZnAlMg coatings

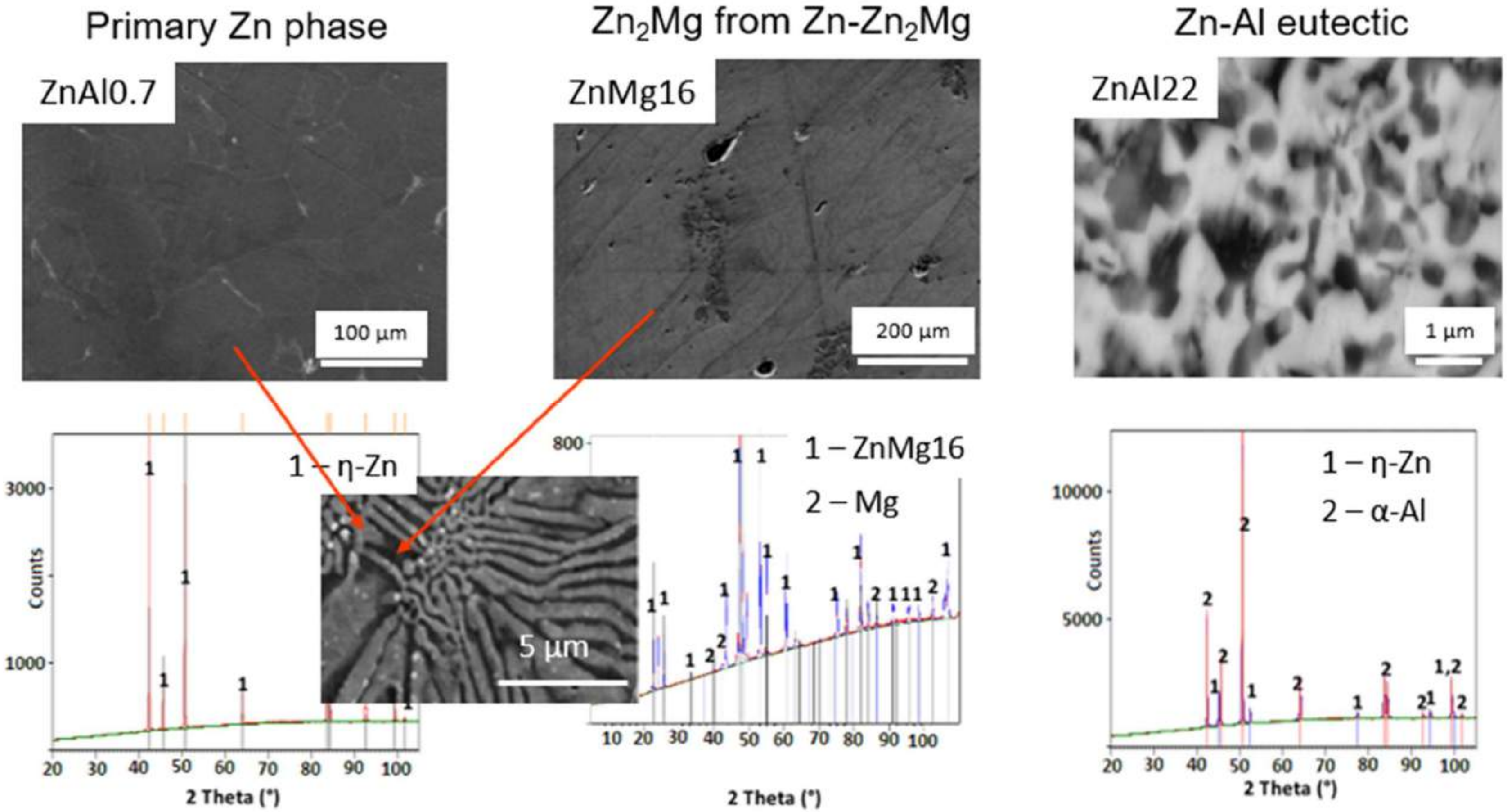

Appendix 4 (Chapter 2)

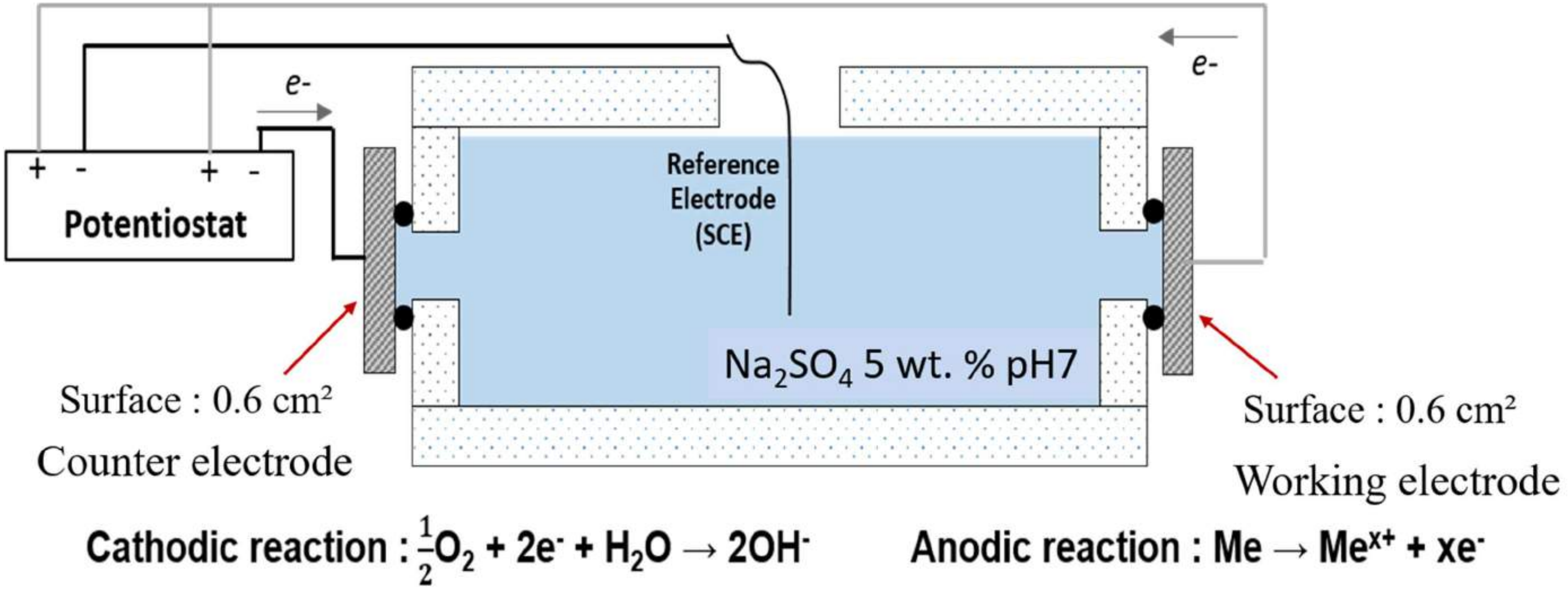

Figure 55: Electrochemical cell used for OCP measurements and galvanic couplings of pure phases (inspired by [2])

[2] C. Nicard, Corrosion mechanisms of AlSi(ZnMg) coated steel, PhD thesis, Université Paris Sciences & Lettres, Paris, 2018.

Appendix 5 (Chapter 4)

Table 16: XPS parameters used for Ti 2p peak deconvolution

Sample	Ref	Name	Peak BE (eV)	Height CPS	Area CPS.eV	Area Ratio	FWHM fit parameter (eV)
As-received activator	A	**Na Auger**	**454.88**	**717.45**	3713.54	0.23	**4.5**
							0.5 : 4.5
	B	**Ti2p3 XTiO$_3$**	**457.7**	**577.7**	1241.26	0.08	**1.8**
			457.50 : 457.70				1.8 : 2
	C	**Ti2p1 XTiO$_3$**	463.3	202.19	599.08	0.04	2.5
			B+5.80 (+0.4 - 0.2)	B*0.35			B*1.5 (±0.2)
	D	**Ti2p3 TiO$_2$**	**458.7**	**166.71**	358.41	0.02	**1.8**
			458.70 : 459.10	fixed			1.8 : 2
	E	**Ti2p1 TiO$_2$**	464.9	45.01	133.09	0.01	2.5
			D+5.80 (+0.4 - 0.2)	D*0.27			D*1.5 (±0.2)
	F	**Ti2p3 Na$_4$TiO(PO$_4$)$_2$**	**459.64**	**7130.9**	15804.62	1	**1.86**
			459.40 : 459.80	fixed			1.74 : 1.94
	G	**Ti2p1 Na$_4$TiO(PO$_4$)$_2$**	465.45	2495.82	7611.55	0.48	2.58
			F+5.80 (+0.4 - 0.2)	F*0.35			F*1.5 (±0.2)

Appendix 5

Sample	Ref	Name	Peak BE (eV)	Height CPS	Area CPS.eV	Area Ratio	FWHM fit parameter (eV)
Dissolved and solvent evaporated activator	A	**Na Auger**	**454.83**	**709.54**	3670.73	0.73	**4.5**
			454.83 : 455.03				0.5 : 4.5
	B	**Ti2p3 $XTiO_3$**	**457.7**	**634.15**	1362.56	0.27	**1.8**
			457.50 : 457.70				1.8 : 2
	C	**Ti2p1 $XTiO_3$**	463.9	171.22	506.99	0.1	2.5
			B+5.80 (+0.4 - 0.2)	B*0.27			B*1.5 (±0.2)
	D	**Ti2p3 TiO_2**	**459.1**	**1376.57**	2959.97	0.59	**1.8**
			458.70 : 459.10				1.8 : 2
	E	**Ti2p1 TiO_2**	465.13	371.67	1098.35	0.22	2.5
			D+5.80 (+0.4 - 0.2)	D*0.27			D*1.5 (±0.2)
	F	**Ti2p3 $Na_4TiO(PO_4)_2$**	**459.45**	**2460.64**	5002.64	1	**1.7**
			459.40 : 459.80				1.7 : 1.9
	G	**Ti2p1 $Na_4TiO(PO_4)_2$**	465.13	861.22	2396.46	0.48	2.35
			F+5.80 (+0.4 - 0.2)	F*0.35			F*1.5 (±0.2)

Sample	Ref	Name	Peak BE (eV)	Height CPS	Area CPS.eV	Area Ratio	FWHM fit parameter (eV)
Zn_2Mg	A	**Na Auger**	**454.58**	**1225.3**	5697.28	1	**4.04**
			454.38 : 454.58				4.02 : 4.04
	B	**Ti2p3 $XTiO_3$**	**457.65**	**762.76**	1636.01	0.29	**1.8**
			457.50 : 457.70				1.8 : 2
	C	**Ti2p1 $XTiO_3$**	463.25	266.96	785.56	0.14	2.5
			B+5.80 (+0.4 - 0.2)	B*0.35			B*1.5 (±0.2)
	D	**Ti2p3 TiO_2**	**459.1**	**1659.24**	3946.64	0.69	**2**
			458.70 : 459.10				1.8 : 2
	E	**Ti2p1 TiO_2**	465.3	448	1457.66	0.26	2.8
			D+5.80 (+0.4 - 0.2)	D*0.27			D*1.5 (±0.2)
	F	**Ti2p3 $Na_4TiO(PO_4)_2$**	**459.8**	**86.8**	180.59	0.03	**1.74**
			459.40 : 459.80				1.74 : 1.94
	G	**Ti2p1 $Na_4TiO(PO_4)_2$**	466	30.38	85.44	0.01	2.42
			F+5.80 (+0.4 - 0.2)	F*0.35			F*1.5 (±0.2)

Appendix 5

Sample	Ref	Name	Peak BE (eV)	Height CPS	Area CPS.eV	Area Ratio	FWHM fit parameter (eV)
ZnAl1	A	**Na Auger**	**454.58**	**3538.23**	18386.58	1	**4.5**
			454.38 : 454.58				0.5 : 4.5
	B	**Ti2p3 $XTiO_3$**	**457.5**	**6927.36**	14899.04	0.81	**1.8**
			457.50 : 457.70				1.8 : 2
	C	**Ti2p1 $XTiO_3$**	463.2	2424.58	7189.07	0.39	2.5
			B+5.80 (+0.4 - 0.2)	B*0.35			B*1.5 (±0.2)
	D	**Ti2p3 TiO_2**	**458.7**	**1791.39**	3854.79	0.21	**1.8**
			458.70 : 459.10				1.8 : 2
	E	**Ti2p1 TiO_2**	464.9	483.68	1430.86	0.08	2.5
			D+5.80 (+0.4 - 0.2)	D*0.27			D*1.5 (±0.2)
	F	**Ti2p3 $Na_4TiO(PO_4)_2$**	**459.45**	**0**	0	0	**1.8**
			459.40 : 459.80				1.74 : 1.94
	G	**Ti2p1 $Na_4TiO(PO_4)_2$**	465.05	0	0	0	2.91
			F+5.80 (+0.4 - 0.2)	F*0.35			F*1.5 (±0.2)

Appendix 6 (Chapter 5)

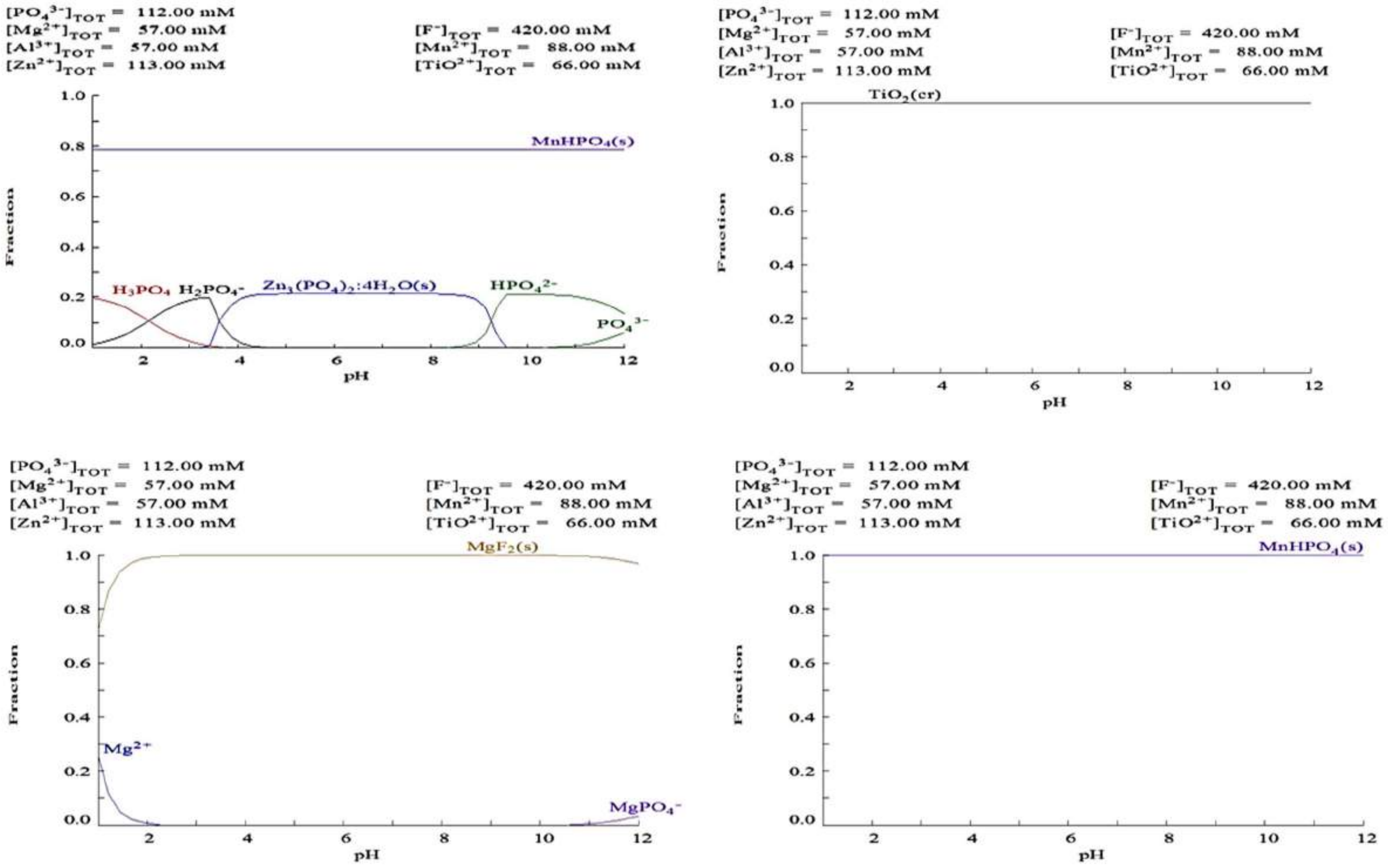

Figure 56: Predominant equilibrium species for 113 mM Zn2+ + 57 mM Al3+ + 57 mM Mg2+ + 112 mM PO43- + 66 mM Ti4+ + 88 mM Mn2+ + 420 mM F- using the Hydra-Medusa software and associated database of equilibrium constants at 25 °C

Appendix 7 (Chapter 5)

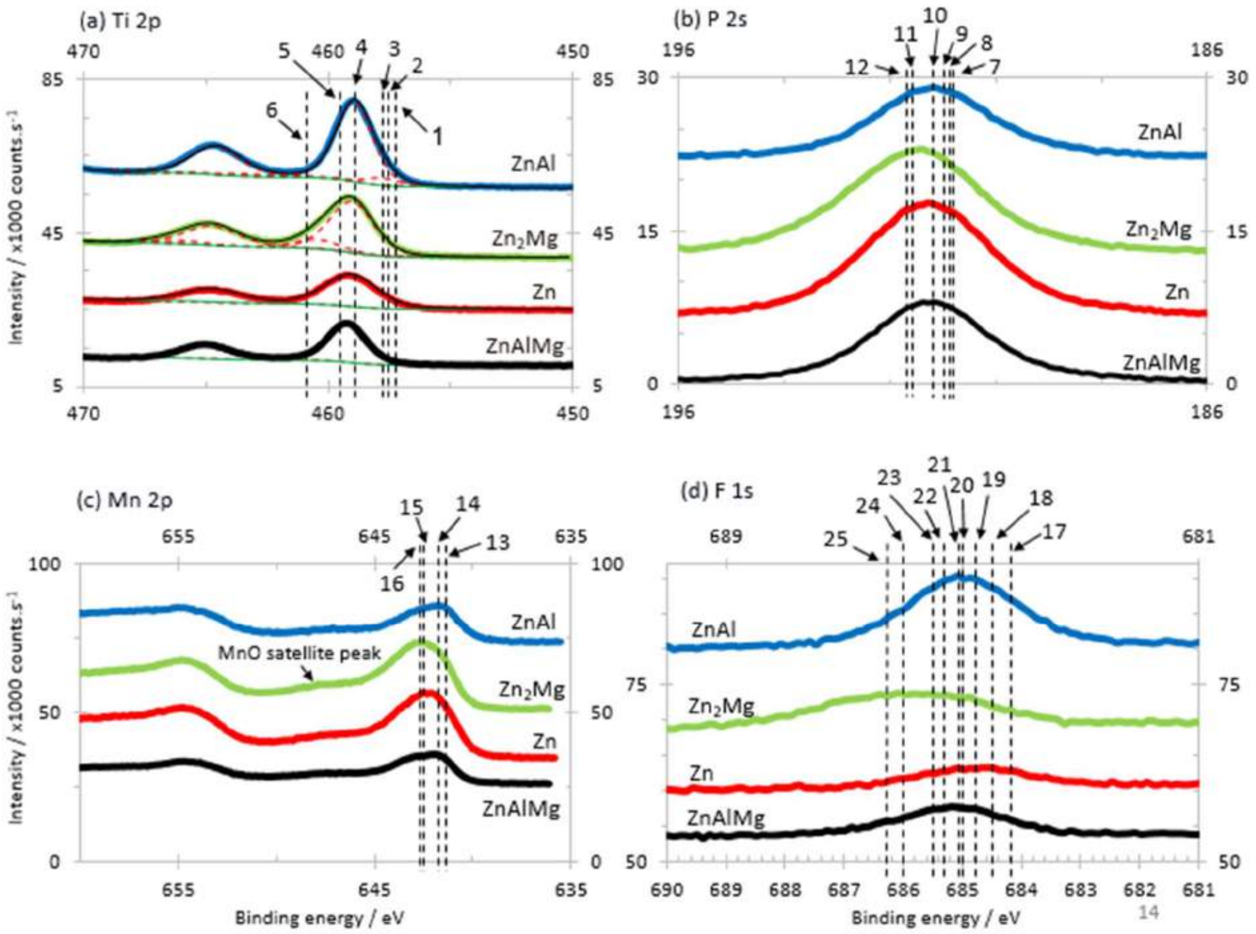

Figure 57: XPS spectra of pure phases and ZnAlMg after standard degreasing and immersion in the TiCC

The Table 17 shows the different compounds fitting the peaks measured by XPS on pure phases and ZnAlMg material and displayed in Figure 57.

Table 17: Binding energies of compounds with energies fitting pure phases and ZnAlMg peaks after standard degreasing and immersion in the TiCC bath

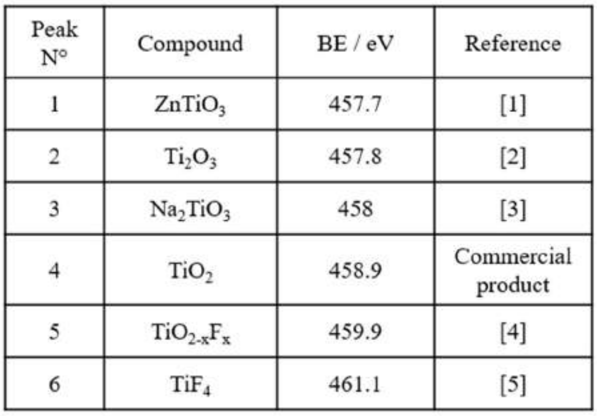

Peak N°	Compound	BE / eV	Reference
1	$ZnTiO_3$	457.7	[1]
2	Ti_2O_3	457.8	[2]
3	Na_2TiO_3	458	[3]
4	TiO_2	458.9	Commercial product
5	$TiO_{2-x}F_x$	459.9	[4]
6	TiF_4	461.1	[5]

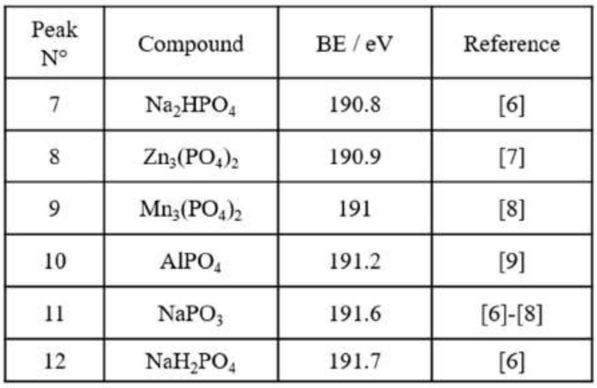

Peak N°	Compound	BE / eV	Reference
7	Na_2HPO_4	190.8	[6]
8	$Zn_3(PO_4)_2$	190.9	[7]
9	$Mn_3(PO_4)_2$	191	[8]
10	$AlPO_4$	191.2	[9]
11	$NaPO_3$	191.6	[6]-[8]
12	NaH_2PO_4	191.7	[6]

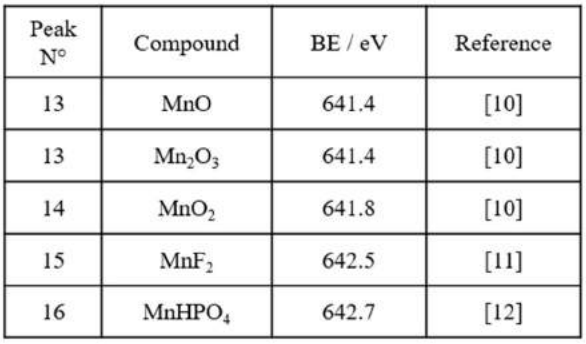

Peak N°	Compound	BE / eV	Reference
13	MnO	641.4	[10]
13	Mn_2O_3	641.4	[10]
14	MnO_2	641.8	[10]
15	MnF_2	642.5	[11]
16	$MnHPO_4$	642.7	[12]

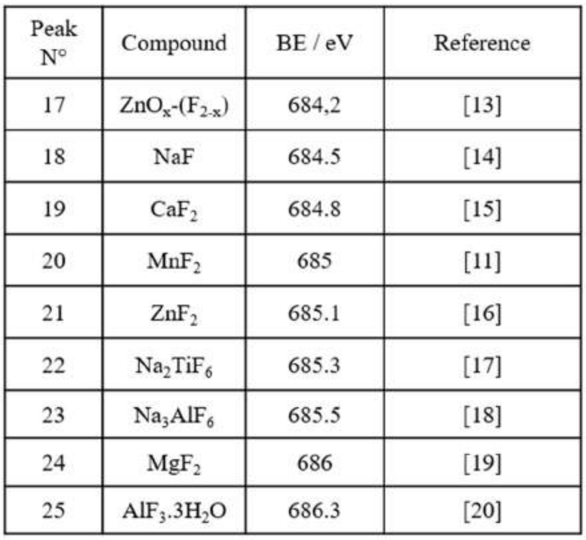

Peak N°	Compound	BE / eV	Reference
17	ZnO_x-(F_{2-x})	684,2	[13]
18	NaF	684.5	[14]
19	CaF_2	684.8	[15]
20	MnF_2	685	[11]
21	ZnF_2	685.1	[16]
22	Na_2TiF_6	685.3	[17]
23	Na_3AlF_6	685.5	[18]
24	MgF_2	686	[19]
25	$AlF_3.3H_2O$	686.3	[20]

References

[1] D.P. Dutta, A. Singh, A.K. Tyagi, Ag doped and Ag dispersed nano ZnTiO3: Improved photocatalytic organic pollutant degradation under solar irradiation and antibacterial activity, J. Environ. Chem. Eng., 2 (2014) 2177-2187.

[2] NIST X-ray Photoelectron Spectroscopy Database, Ti_2O_3. [Online]. Available on: https://srdata.nist.gov/xps/XPSDetailPage.aspx?AllDataNo=26605. [Accessed on: 17/08/2018].

[3] M.T. Pham, W. Matz, H. Reuther, E. Richter, G. Steiner, Hydroxyapatite nucleation on Na ion implanted Ti surfaces, J. Mater. Sci. Lett., 19 (2000) 1029–1031.

[4] J. Halim, An X-Ray Photoelectron Spectroscopy Study of Multilayered Transition Metal Carbides (MXenes), PhD thesis, Drexel University, Philadelphia, 2016.

[5] NIST X-ray Photoelectron Spectroscopy Database, TiF_4. [Online]. Available on: https://srdata.nist.gov/xps/XPSDetailPage.aspx?AllDataNo=67368. . [Accessed on: 17/08/2018].

[6] P. Swift, Adventitious carbon—the panacea for energy referencing? Surf. Interface Anal., 4 (1982) 47–51.

[7] D. L. Felker, P. M. A. Sherwood, Zinc phosphate (Zn3(PO4)2) by XPS, Surf. Sci. Spectra, 9 (2012) 106-113.

[8] R. Franke, T. Chassé, P. Streubel, A. Meisel, Auger parameters and relaxation energies of phosphorus in solid compounds, J. Electron Spectrosc., Relat. Phenom., 56 (1991) 381-388.

[9] T. Lindblad, B. Rebenstorf, Z.-G. Yan, S.L.T. Andersson, Characterization of vanadia supported on amorphous AlPO4 and its properties for oxidative dehydrogenation of propane, Appl. Catal. Gen., 112 (1994) 187–208.

[10] 'Thermo Scientific XPS: What is XPS'. [Online]. Available on: https://xpssimplified.com/whatisxps.php.[Accessed on: 12/07/2018].

[11] A. Aoki, X-Ray Photoelectron Spectroscopic Studies on ZnS: MnF2 Phosphors, Jpn. J. Appl. Phys. 15 (1976) 305.

[12] G. Wang, N. Cao, Y. Wang, Characteristics and corrosion studies of zinc–manganese phosphate coatings on magnesium–lithium alloy. RSC Adv. 4 (2014) 59772–59778.

[13] S. Ilican, M. Caglar, S. Aksoy, Y. Caglar, XPS Studies of Electrodeposited Grown F-Doped ZnO Rods and Electrical Properties of p-Si/n-FZN Heterojunctions, J. Nanomater, (2016).

[14] NIST X-ray Photoelectron Spectroscopy Database, NaF. [Online]. Available on: https://srdata.nist.gov/xps/XPSDetailPage.aspx?AllDataNo=20686. [Accessed on: 12/07/2018].

[15] NIST X-ray Photoelectron Spectroscopy Database, CaF_2. [Online]. Available on: https://srdata.nist.gov/xps/XPSDetailPage.aspx?AllDataNo=20763. [Accessed on: 12/07/2018].

[16] NIST X-ray Photoelectron Spectroscopy Database, ZnF_2. [Online]. Available on: https://srdata.nist.gov/xps/XPSDetailPage.aspx?AllDataNo=20680. [Accessed on: 12/07/2018].

[17] NIST X-ray Photoelectron Spectroscopy Database, Na_2TiF_6. [Online]. Available on: https://srdata.nist.gov/xps/XPSDetailPage.aspx?AllDataNo=20668. [Accessed on: 12/07/2018].

[18] NIST X-ray Photoelectron Spectroscopy Database, Na_3AlF_6. [Online]. Available on: https://srdata.nist.gov/xps/XPSDetailPage.aspx?AllDataNo=20710. [Accessed on: 12/07/2018].

[19] S. Da-Ming, S. Zhao-Qi, L. Ai-Xia, X. Zhi-Yuan, XPS analysis of the oxidation of Ag–MgF2 cermet film, Vacuum, 52 (1999) 383-386.

[20] NIST X-ray Photoelectron Spectroscopy Database, $AlF_3.3H_2O$. [Online]. Available on: https://srdata.nist.gov/xps/XPSDetailPage.aspx?AllDataNo=21603. [Accessed on: 12/07/2018].

Appendix 8 (Chapter 6)

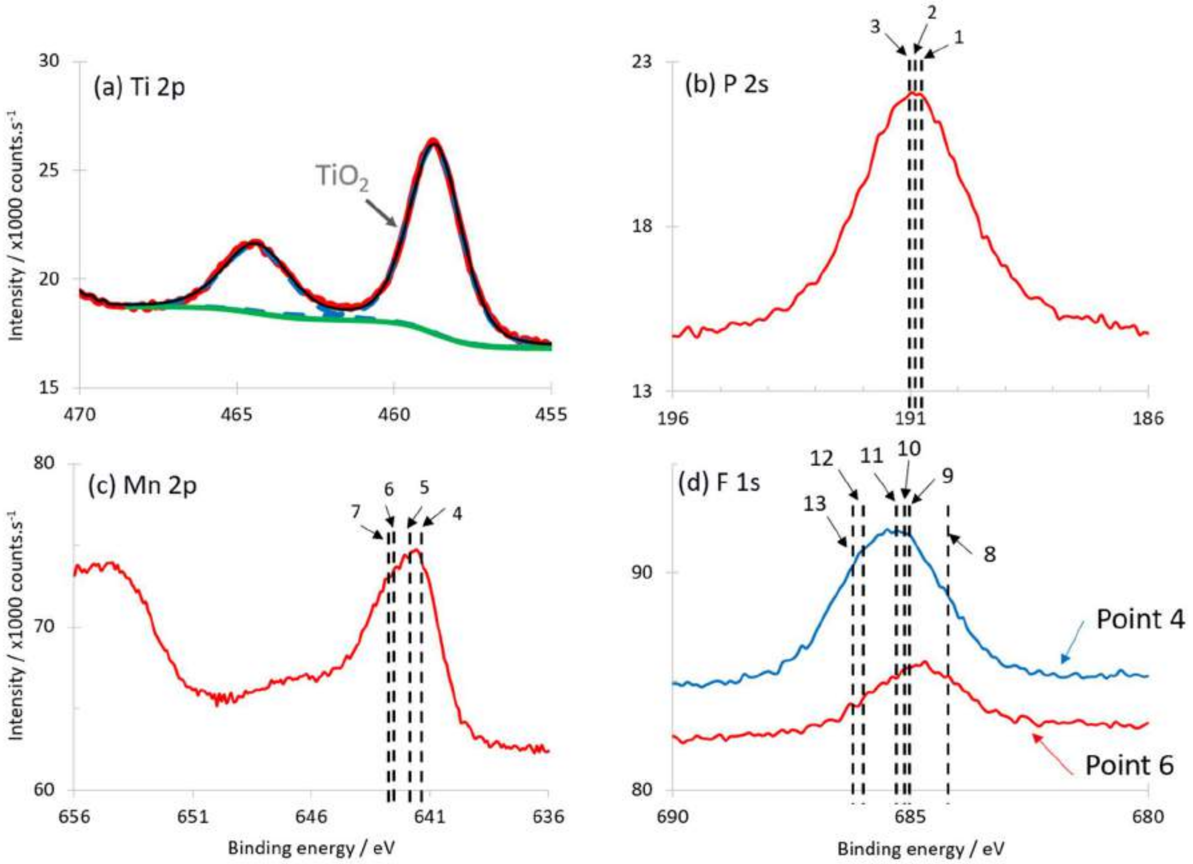

Figure 58: XPS spectra of ZnAlMg after Cu2+-modified alkaline degreasing and immersion in the Ti-based CC bath

The Table 18 shows the different compounds fitting the peaks measured by XPS on pure phases and ZnAlMg material and displayed in Figure 58.

Table 18: Binding energies of compounds with positions fitting P 2s, Mn 2p and F 1s peaks on ZnAlMg after Cu2+-modified alkaline degreasing and immersion in the TiCC bath

P 2s

Peak N°	Compound	BE / eV	Reference
1	Na_2HPO_4	190.8	[6]
2	$Zn_3(PO_4)_2$	190.9	[7]
3	$Mn_3(PO_4)_2$	191	[8]

Mn 2p

Peak N°	Compound	BE / eV	Reference
4	MnO	641.4	[10]
4	Mn_2O_3	641.4	[10]
5	MnO_2	641.8	[10]
6	MnF_2	642.5	[11]
7	$MnHPO_4$	642.7	[12]

F 1s

Peak N°	Compound	BE / eV	Reference
8	ZnO_x-(F_{2-x})	684,2	[13]
9	MnF_2	685	[11]
10	ZnF_2	685.1	[16]
11	Na_2TiF_6	685.3	[17]
12	MgF_2	686	[19]
13	$AlF_3.3H_2O$	686.3	[20]

References

[1] D.P. Dutta, A. Singh, A.K. Tyagi, Ag doped and Ag dispersed nano ZnTiO3: Improved photocatalytic organic pollutant degradation under solar irradiation and antibacterial activity, J. Environ. Chem. Eng., 2 (2014) 2177-2187.

[2] NIST X-ray Photoelectron Spectroscopy Database, Ti_2O_3. [Online]. Available on: https://srdata.nist.gov/xps/XPSDetailPage.aspx?AllDataNo=26605. [Accessed on: 17/08/2018].

[3] M.T. Pham, W. Matz, H. Reuther, E. Richter, G. Steiner, Hydroxyapatite nucleation on Na ion implanted Ti surfaces, J. Mater. Sci. Lett., 19 (2000) 1029–1031.

[4] J. Halim, An X-Ray Photoelectron Spectroscopy Study of Multilayered Transition Metal Carbides (MXenes), PhD thesis, Drexel University, Philadelphia, 2016.

[5] NIST X-ray Photoelectron Spectroscopy Database, TiF_4. [Online]. Available on: https://srdata.nist.gov/xps/XPSDetailPage.aspx?AllDataNo=67368. . [Accessed on: 17/08/2018].

[6] P. Swift, Adventitious carbon—the panacea for energy referencing? Surf. Interface Anal., 4 (1982) 47–51.

[7] D. L. Felker, P. M. A. Sherwood, Zinc phosphate (Zn3(PO4)2) by XPS, Surf. Sci. Spectra, 9 (2012) 106-113.

[8] R. Franke, T. Chassé, P. Streubel, A. Meisel, Auger parameters and relaxation energies of phosphorus in solid compounds, J. Electron Spectrosc., Relat. Phenom., 56 (1991) 381-388.

[9] T. Lindblad, B. Rebenstorf, Z.-G. Yan, S.L.T. Andersson, Characterization of vanadia supported on amorphous AlPO4 and its properties for oxidative dehydrogenation of propane, Appl. Catal. Gen., 112 (1994) 187–208.

[10] 'Thermo Scientific XPS: What is XPS'. [Online]. Available on: https://xpssimplified.com/whatisxps.php.[Accessed on: 12/07/2018].

[11] A. Aoki, X-Ray Photoelectron Spectroscopic Studies on ZnS: MnF2 Phosphors, Jpn. J. Appl. Phys. 15 (1976) 305.

[12] G. Wang, N. Cao, Y. Wang, Characteristics and corrosion studies of zinc–manganese phosphate coatings on magnesium–lithium alloy. RSC Adv. 4 (2014) 59772–59778.

[13] S. Ilican, M. Caglar, S. Aksoy, Y. Caglar, XPS Studies of Electrodeposited Grown F-Doped ZnO Rods and Electrical Properties of p-Si/n-FZN Heterojunctions, J. Nanomater, (2016).

[14] NIST X-ray Photoelectron Spectroscopy Database, NaF. [Online]. Available on: https://srdata.nist.gov/xps/XPSDetailPage.aspx?AllDataNo=20686. [Accessed on: 12/07/2018].

[15] NIST X-ray Photoelectron Spectroscopy Database, CaF_2. [Online]. Available on: https://srdata.nist.gov/xps/XPSDetailPage.aspx?AllDataNo=20763. [Accessed on: 12/07/2018].

[16] NIST X-ray Photoelectron Spectroscopy Database, ZnF_2. [Online]. Available on: https://srdata.nist.gov/xps/XPSDetailPage.aspx?AllDataNo=20680. [Accessed on: 12/07/2018].

[17] NIST X-ray Photoelectron Spectroscopy Database, Na_2TiF_6. [Online]. Available on: https://srdata.nist.gov/xps/XPSDetailPage.aspx?AllDataNo=20668. [Accessed on: 12/07/2018].

[18] NIST X-ray Photoelectron Spectroscopy Database, Na_3AlF_6. [Online]. Available on: https://srdata.nist.gov/xps/XPSDetailPage.aspx?AllDataNo=20710. [Accessed on: 12/07/2018].

[19] S. Da-Ming, S. Zhao-Qi, L. Ai-Xia, X. Zhi-Yuan, XPS analysis of the oxidation of Ag–MgF2 cermet film, Vacuum, 52 (1999) 383-386.

[20] NIST X-ray Photoelectron Spectroscopy Database, $AlF_3.3H_2O$. [Online]. Available on: https://srdata.nist.gov/xps/XPSDetailPage.aspx?AllDataNo=21603. [Accessed on: 12/07/2018].

« Impact de la microstructure des revêtements ZnAlMg sur les mécanismes de formation et la performance des couches de conversion sans Cr »

Par Perrine TANGUY
Thèse de doctorat en Chimie Physique et Chimie Analytique

RÉSUMÉ

Introduction

Contexte :

Actuellement, les aciers galvanisés (HDG) sont remplacés par des revêtements multiphasés de ZnAlMg dans les marchés du prélaqué et de l'automobile. Grâce à l'augmentation de la concentration en Al et l'ajout de Mg, une augmentation de la résistance à la corrosion est possible, réduisant l'épaisseur du revêtement sacrificiel et les coûts de production tout en allongeant la durée de vie des revêtements ZnAlMg. Pour assurer l'adhérence de la peinture sur les substrats ZnAlMg, des couches de conversion (CC), parmi lesquels des CC épaisses de phosphates (PCC) et des CC fines de Ti (TiCC), sont appliquées pour assurer l'adhérence de la peinture et améliorer la résistance à la corrosion des revêtements.

Des premiers tests de corrosion extérieurs ont montré qu'en présence d'une rayure à l'acier (tests industriels d'évaluation de la résistance à la corrosion cosmétique), des cloques peuvent se former sur des ZnAlMg peints avec des TiCC mais pas avec des PCC. Dans le même temps, les revêtements ZnAlMg traités avec les PCC ainsi que les aciers galvanisés traités avec les TiCC ne présentent pas de cloques. Le cloquage apparaît donc comme le résultat d'un manque d'adhérence entre le substrat ZnAlMg et le TiCC.

Une des raisons expliquant le cloquage sur ZnAlMg est la présence de multiples phases (Zn(Al)-Zn_2Mg-Zn) qui peuvent créer un couplage galvanique entre les phases durant la précipitation de la CC. Il est admis que la réaction de précipitation des CC se déroule selon un mécanisme en 2 étapes : (1) Dissolution du métal dans les zones anodiques associé à une alcalinisation dans les zones cathodiques due aux réactions cathodiques et (2) Précipitation de la CC quand le pH de précipitation est atteint. Un substrat multiphasé pourrait entraîner une distribution hétérogène des cathodes et anodes et changer la vitesse de nucléation et de croissance de la CC sur ces phases ainsi que les propriétés de la CC.

Objectifs :

Dans le contexte décrit précédemment, l'objectif de la thèse est de comprendre l'origine du phénomène de cloquage et en particulier :

- Les mécanismes de corrosion entraînant la formation de cloques sur les revêtements peints de ZnAlMg traités avec les TiCC.
- La différence de résistance à la corrosion entre les revêtements ZnAlMg peints traités avec les TiCC comparés aux PCC et en particulier, le rôle de l'activateur à base de Ti sur la formation de la PCC sur revêtements multiphasés de ZnAlMg.
- L'impact de la microstructure du ZnAlMg sur les mécanismes de formation des TiCC.
- La modification de la distribution du TiCC sur les phases de ZnAlMg par cémentation d'un métal noble.

Méthodologie :

Pour atteindre ces objectifs, la sonde de Kelvin, a révélé la présence de chemins de corrosion sous peinture liants les cloques depuis la rayure à l'acier jusqu'aux cloques les plus distantes. Des immersions de substrats ZnAlMg avec différentes microstructures et des phases pures simulant la microstructure des ZnAlMg dans des bains de TiCC ou de PCC ont été réalisées à différentes étapes de la procédure de conversion. Dans le cas de la PCC, l'impact du niveau de fraîcheur sur la formation de la PCC a aussi été étudiée. Les phases pures identifiées dans la microstructure des revêtements ont été synthétisées en partenariat avec l'Université technologique de Prague afin de les tester et de comprendre leur contribution individuelle aux mécanismes de formation des CC et de leur dégradation. La microscopie électronique à balayage et l'analyse dispersive en énergie ont permis d'observer la morphologie et distribution des grains de PCC sur les phases des revêtements ZnAlMg et phases pures. La spectroscopie de photoélectrons a permis de caractériser la concentration et la chimie de TiCC et de l'activateur à base de Ti nécessaire à la procédure de PCC sur les phases pures correspondant au ZnAlMg. La spectroscopie d'électrons Auger a permis l'évaluation de l'épaisseur de TiCC précipitée sur chaque phase du ZnAlMg. Des expériences de couplage galvanique entre phases pures ont été menées pour explorer les couplages galvaniques possibles dans les phases binaires et évaluer leur impact au moment de la formation des CC et distribution sur toutes les phases de ZnAlMg. La spectroscopie d'impédance électrochimique locale et la cartographie d'impédance électrochimique locale ont été utilisées pour déterminer le gain de résistance à la délamination et formation de cloques des revêtements ZnAlMg traités avec un dégraissant alcalin modifié au Cu permettant une précipitation plus homogène de TiCC sur ZnAlMg.

Structure :

Cette thèse est organisée en 4 parties et 7 chapitres.

La première partie est composée du chapitre d'introduction, de « l'état de l'art » (chapitre 1). La deuxième partie comprend la méthodologie expérimentale (chapitre 2) décrivant succinctement les techniques utilisées. La troisième partie comprend quatre chapitres de résultats sous formes de publications et qui se focalisent sur les thématiques suivantes :

Chapitre 3 (« **Compréhension des mécanismes de dégradation des revêtements ZnAlMg peints et traités aux TiCC** ») abord l'impact de la microstructure des substrats ZnAlMg dans le développement et la propagation de la délamination et des cloques sous peinture.

Chapitre 4 (« **Impact de la microstructure multiphasée des substrats ZnAlMg la distribution de l'activateur à base de Ti et la PCC** ») se focalise sur la distribution de la PCC à différentes étapes de la procédure de conversion et en fonction de la fraîcheur de l'activateur. Le rôle de l'activateur utilisé avant la PCC sur la formation de grains cristallins et couvrants sus les phases de ZnAlMg a été mis en avant.

Chapitre 5 (« **Impact des phases du revêtement ZnAlMg sur la distribution du TiCC** ») met en évidence l'origine de la distribution hétérogène du TiCC sur le ZnAlMg.

Chapitre 6 (« **Aperçu des mécanismes de formation et dégradation des TiCC sur ZnAlMg après utilisation d'un dégraissant alcalin contenant des ions Cu^{2+}** ») présente une solution choisie pour homogénéiser la distribution du TiCC sur les revêtements ZnAlMg qui est basée sur la cémentation de Cu pendant le dégraissage, permettant une distribution des cathodes et anodes plus fines.

La dernière partie est constituée du chapitre 7 « **Conclusions et perspectives** ».

Ce résumé en français reprend la même structure que la version en anglais en proposant à chaque fois une synthèse des conclusions majeures des différents chapitres du manuscrit.

1. État de l'art

Historiquement, les revêtements sacrificiels de l'acier utilisés dans le marché du bâtiment sont à base de zinc (Zn-0.2 wt. % Al) mais de nouveaux revêtements, ZnAlMg, sont en passe de les remplacer. Ils sont obtenus en utilisant le procédé de galvanisation (Hot Dip en anglais). La bande d'acier est immergée dans un bain de zinc, aluminium et magnésium liquide à des teneurs comprises entre 1 et 11 wt. % d'Al et jusqu'à 3 wt. % de Mg selon la composition visée.

Après refroidissement du revêtement, quatre phases solides peuvent se trouver dans la microstructure, à savoir une phase riche en Zn, une phase riche en Al, l'intermétallique Zn_2Mg et $Zn_{11}Mg_2$. Tandis que $Zn_{11}Mg_2$ est rarement présent dans la microstructure, les autres phases peuvent former des dendrites de Zn, des phases binaires eutectiques Zn-Al et Zn-Zn_2Mg et/ou un ternaire eutectique Zn-Al-Zn_2Mg selon la composition. Dans le cas des alliages à faible teneur en Mg, l'eutectique ternaire est considéré comme un eutectique binaire Zn-Al.

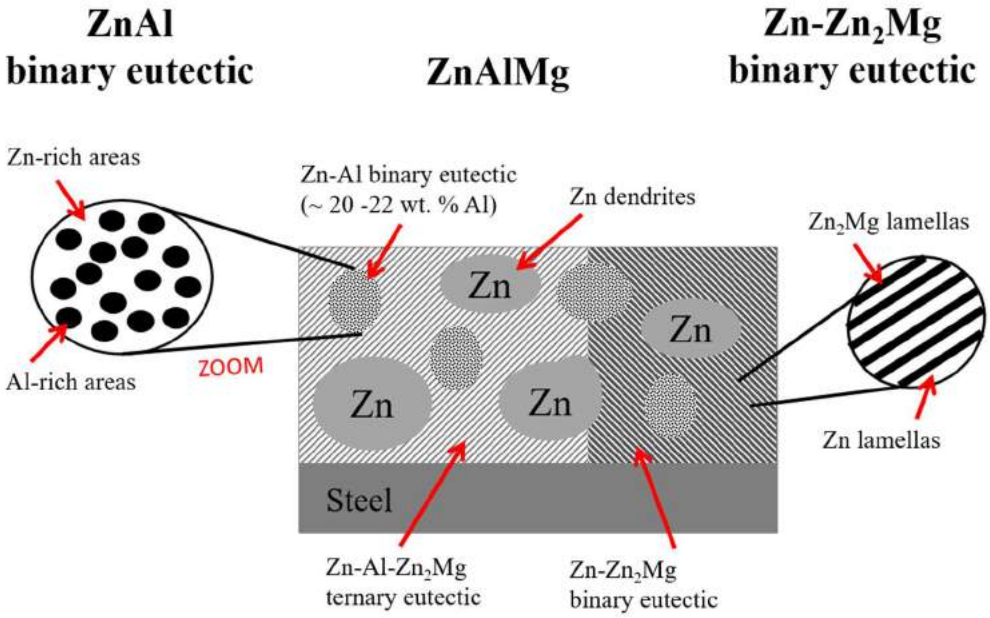

Figure 1: Schéma de la coupe d'un revêtement ZnAlMg. Le binaire Zn-Zn2Mg est composé de lamelles de Zn (claires) et de lamelles de Zn2Mg (foncées) tandis que le ternaire comprend Zn, Zn2Mg et une fine phase d'Al. Le binaire ZnAl est composé de zones riches en Zn (claires) et zones riches en al (foncées)

De nombreux tests de corrosion accélérés ou expositions naturelles (Test VDA, brouillard salin, scab test etc) ont permis de montrer que les revêtements de ZnAlMg possèdent une résistance à la corrosion améliorée comparé aux aciers galvanisés classiques. Il est communément admis que cela est en grande partie dû à la formation de produits de corrosion compact qui agissent comme une barrière physique à la réduction de l'oxygène sur la surface du ZnAlMg. Une réduction par deux de l'épaisseur du revêtement sacrificiel est possible tout en maintenant une résistance à la corrosion équivalente à celle des aciers galvanisés. Pour les revêtements ZnAlMg, l'épaisseur standard est de 10 µm tandis qu'elle est de 20 µm pour l'acier galvanisé.

Pour certaines applications dans l'automobile et le bâtiment, ces revêtements ZnAlMg sont peints comme présenté dans la Figure 2.

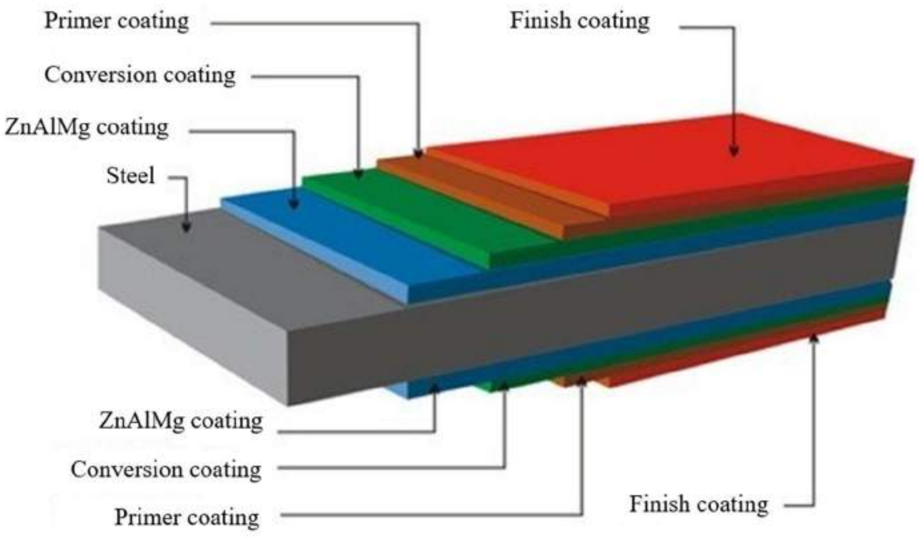

Figure 2: Structure d'un revêtement ZnAlMg peint

Différentes couches de peintures peuvent être appliquées selon les propriétés physiques, chimiques, électrochimiques etc désirées. L'épaisseur totale de peinture appliquée sur le revêtement est comprise entre 20 et 250 µm. L'adhérence de la peinture et la résistance à la corrosion du revêtement peint sont assurées par la présence d'une couche de conversion (CC) entre le revêtement ZnAlMg et la peinture. Ce sont des fines couches d'oxydes insolubles et inorganiques dont l'épaisseur varie entre 10 nm et 1 µm selon la nature de la CC utilisée. Ils agissent comme une barrière physique et insoluble limitant la réduction de l'oxygène sur la surface du ZnAlMg et ainsi la propagation de la corrosion.

La formation des CC est de nature électrochimique et suit un mécanisme général commun à toutes les formulations existantes. Avant l'application de la CC, un dégraissage alcalin est d'abord réalisé afin d'éliminer les traces d'huiles, d'oxydes etc résiduels à la surface de l'échantillon. La formation de la CC a lieu en 2 étapes. Tout d'abord, des zones anodiques et cathodiques sont définies au contact du traitement de conversion. Aux anodes, le métal est dissout tandis qu'aux cathodes, la réduction de l'oxygène et des protons sont les réactions majoritaires comme visible sur la figure 3.

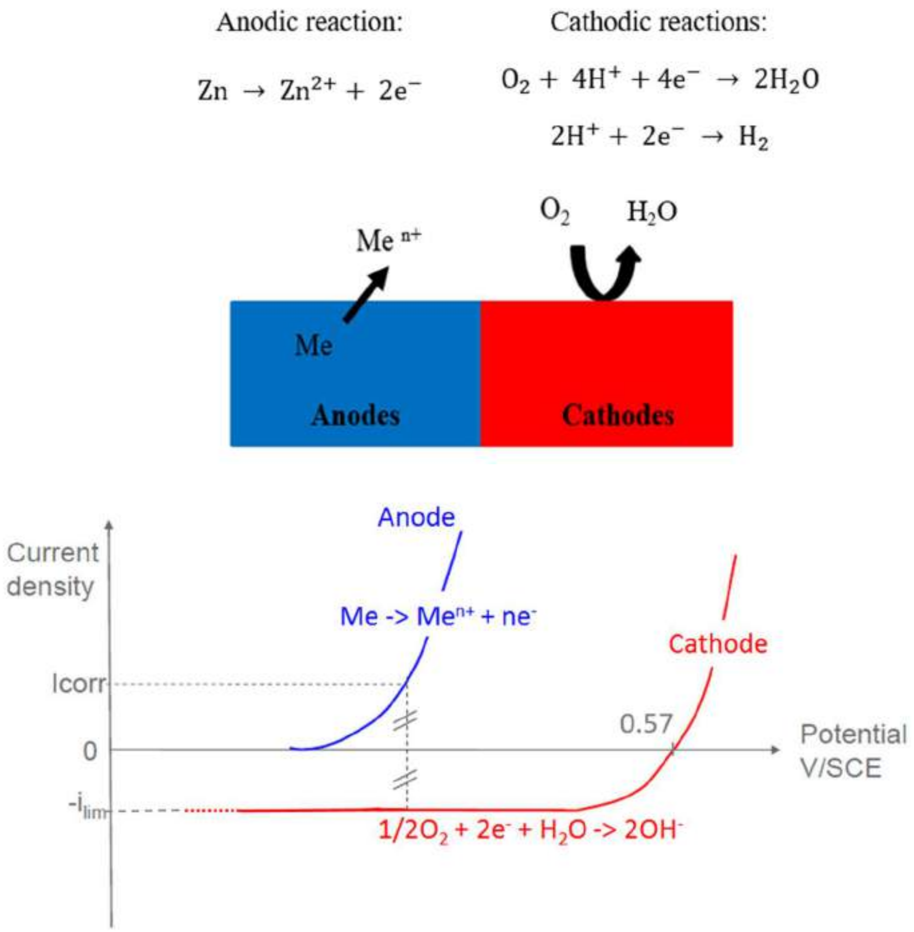

Figure 3:Schéma des réactions anodiques et cathodiques pendant le couplage galvanique

L'augmentation de pH est l'élément déclencheur de la precipitation de la CC. Dès que le pH seuil de précipitation de la CC est atteint, la formation de la couche d'oxydes a lieu, isolant le revêtement ZnAlMg de l'air ambiant.

Des tests de corrosion en milieu naturel (marin) sur des échantillons de ZnAlMg peints et traités avec une CC à base de Ti (TiCC) ont montré la présence de cloques après 22 mois d'expositions en présence d'un défaut à l'acier (Figure 4).

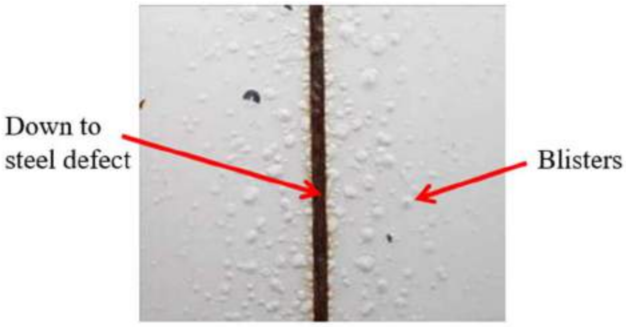

Figure 4 : Cloquage visible autour de la rayure à l'acier après 22 mois de test de corrosion en milieu naturel (marin)

Aucune cloque n'a été mesurée dans le cas des aciers galvanisés et traités avec les TiCC ce qui traduit le manque d'adhérence et de résistance à la corrosion des substrats ZnAlMg peints et traités avec le TiCC. L'objectif de la thèse est de comprendre l'origine de ce phénomène de cloquage et d'apporter une solution pour y remédier.

2. Expérimental

A partir de la bibliographie, différentes techniques ont été utilisées pour comprendre les mécanismes de dégradation des revêtements ZnAlMg peints ainsi que les mécanismes de formation des CC sur ZnAlMg. Dans un premier temps, les mécanismes de dégradation des revêtements ZnAlMg peints en utilisant la sonde de Kelvin, des cartographies d'Impédance Electochimique Locale (LEIM-LEIS) et de la chonopotentiométrie. D'un autre côté, l'étude des mécanismes de précipitation a été réalisée grâce à 2 approches complémentaires. La distribution des CC sur ZnAlMg a été déterminée par microscopie électronique à balayage et analyse dispersive en énergie. L'épaisseur globale de la CC sur ZnAlMg a été mesurée par Spectroscopie à Décharge Luminescente tandis que l'épaisseur locale dans chacune des phases du ZnAlMg fut mesurée par spectroscopie d'électrons auger. Des expériences électrochimiques sur des phases pures simulant la microstructure du ZnAlMg ont permis de confirmer les hypothèses émises à propos des mécanismes de formation des TiCC sur ZnAlMg. La chimie du TiCC a été évaluée par la spectroscopie de photoélectrons.

L'objectif de cette partie est de donner un aperçu des matériaux et techniques utilisées dans le cadre de la thèse.

Matériaux

Les revêtements d'acier galvanisé et de ZnAlMg ont été réalisés par une ligne de production ArcelorMittal. Les compositions des revêtements ZnAlMg sont comprises entre 0 et 5 wt. % d'Al et jusqu'à 3 wt. % de Mg. Les revêtements sont réalisés selon un procédé de galvanisation décrit dans le brevet N° WO 2013/160567 AI. Des phases pures représentant celles présentes à l'intérieur du revêtement de ZnAlMg ont été synthétisées par l'Université technologique de Prague.

Caractérisation des phases après corrosion

La microscopie électronique à balayage a permis d'évaluer la présence de produits de corrosion sur les revêtements ZnAlMg peints et la distribution des couches de conversion sur ZnAlMg après application. Les observations ont été faites avec une tension d'accélération de 15 keV ou de 5 keV pour réduire le volume de la poire d'interaction selon le besoin de l'analyse. Dans le cas d'un substrat à base de zinc, le volume de la poire est de 1.2 µm à 15 keV et de 180 nm à 5 keV.

Distribution des couches de conversion

La spectroscopie d'électrons auger a été utilisée pour évaluer la concentration en TiCC sur les phases de ZnAlMg. Une érosion aux ions Ar^+ a permis une évaluation de la distribution du TiCC en fonction de la profondeur d'érosion grâce à la haute résolution spatiale de la technique (≈ 10 nm).

Composition chimique de la couche de conversion

La spectroscopie de photoélectrons a donné accès à la composition chimique du TiCC, la nature des liaisons chimiques dans lesquelles les éléments de la CC sont impliqués ainsi que leur degré d'oxydation. Cette technique permet une analyse d'extrême surface sur 5-10 nm de profondeur.

Épaisseur globale de la couche de conversion

La spectroscopie à décharge luminescente a servi à réaliser une érosion de la surface avec des ions Ar^+ afin d'évaluer l'épaisseur de TiCC appliquée sur ZnAlMg. La surface analysée est de quelques mm² et donne une mesure moyenne de l'épaisseur, en prenant en compte toutes les phases du revêtement.

Mesures électrochimiques

- Électrochimie globale

Les mesures électrochimiques de mesure de potentiel à circuit ouvert ainsi que les polarisations anodiques et cathodiques des échantillons ont été réalisées dans une cellule à trois électrodes thermostatée à 40 °C. Les phases pures représentant le revêtement de ZnAlMg et le revêtement de ZnAlMg ont servis d'électrode de travail tandis qu'une électrode au calomel saturé a été choisie comme référence. La contre-électrode était représentée par un fil de platine.

- Électrochimie locale

La Cartographie d'Impédance Electrochimique Locale (LEIM) est une technique d'électrochimie locale utilisée pour caractériser l'évolution de la réactivité de surface locale au cours du processus de corrosion. Une configuration à trois électrodes est utilisé avec un subtrat métallique servant d'électrode de travail, une électrode Ag/AgCl comme électrode de référence et une contre-électrode de platine.

La sonde de Kelvin a aussi été utilisée pour identifier les zones corrodées du revêtement ZnAlMg sous peinture. Cette technique non destructive a permis de réaliser des cartographies de potentiel de surface grâce à une sonde de diamètre 500 µm révélant la propagation de la corrosion depuis la rayure à l'acier jusqu'aux cloques.

3. Compréhension des mécanismes de dégradation des revêtements ZnAlMg peints traités avec le TiCC

La formation de cloques sur des revêtements ZnAlMg peints et traités avec le TiCC n'est visible que pour les échantillons présentant une rayure à l'acier simulant un défaut profond accidentel.

Dans le même temps, l'acier galvanisé peint et traité avec le TiCC ne présente pas de cloque en présence d'un défaut à l'acier.

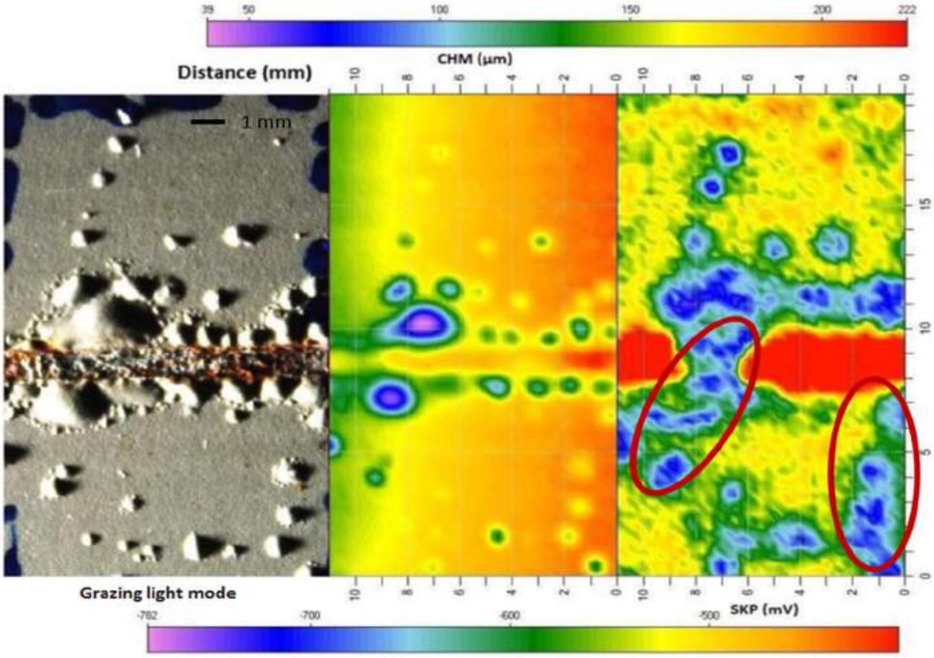

Figure 5: Cartographie SKP d'un revêtement ZnAlMg peint présentant un défaut à l'acier et après exposition en milieu naturel pendant 24 mois

La cartographie du potentiel de surface du revêtement ZnAlMg sous la peinture mesurée par sonde de Kelvin sur un échantillon cloqué permet de mettre en évidence les zones corrodées sous les cloques (Figure 5). Une observation plus fine de ces zones permet de réaliser que les zones corrodées sont plus étendues que les cloques elles-mêmes et lient plusieurs cloques entre elles. Dans certains cas, un chemin de corrosion partant de la rayure à l'acier jusqu'aux cloques distantes est visible.

Une expérience de chronopotentiométrie du revêtement de ZnAlMg peint et traité avec le TiCC au contact de NaCl a été réalisée pour caractériser la propagation de la corrosion au sein du revêtement (Figure 6).

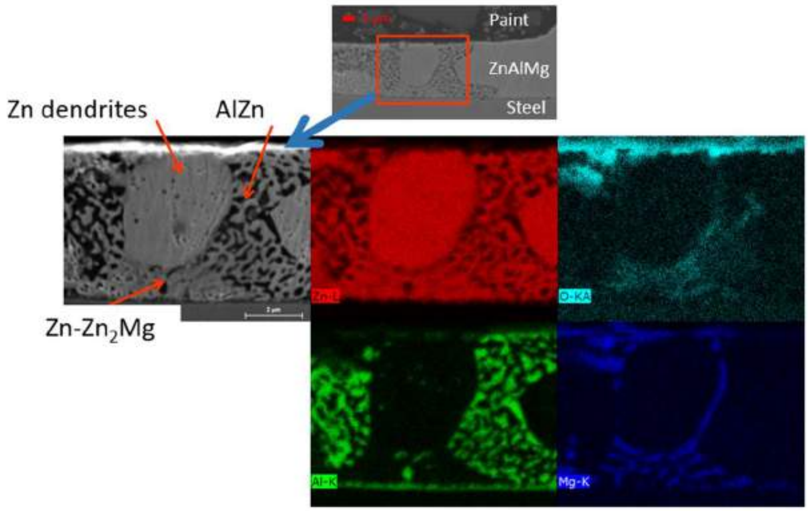

Figure 6: Cartographie MEB-EDS d'un revêtement ZnAlMg peint après 72 heures de chronopotentiométrie à 5 µA dans une solution de NaCl 1 wt. % pH 7

Au niveau du front de délamination, la cartographie de la microstructure montre la présence de corrosion à un stade peu avancée dans la microstructure. L'oxydation de la phase riche en Mg, Zn-Zn$_2$Mg semble indiquer le caractère anodique de cette phase qui pourrait corroder préférentiellement au contact de NaCl.

Des expériences de polarisations anodiques et cathodiques des phases pures simulant la microstructure du ZnAlMg ont été menées pour confirmer le comportement anodique de la phase Zn-Zn$_2$Mg comparé aux autres phases.

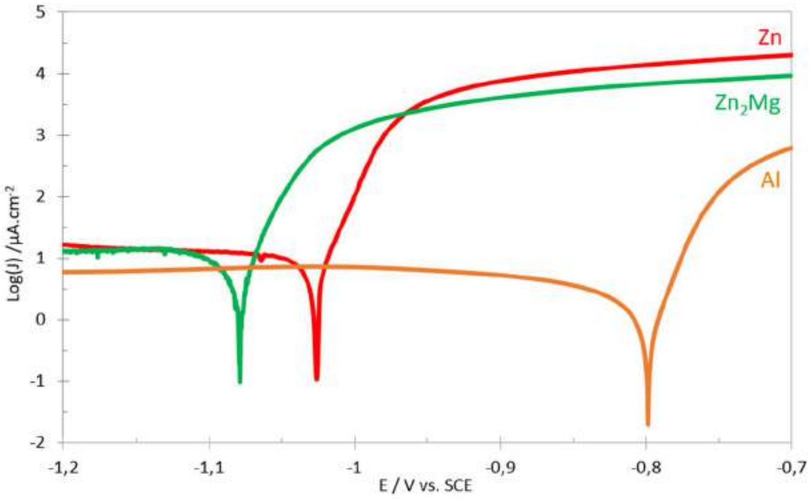

Figure 7: Courbes de polarisations anodiques et cathodiques des phases pures représentant le ZnAlMg dans une solution de NaCl 5 wt. % pH 7 T=25 °C

Les mécanismes de dégradations des revêtements de ZnAlMg peints et traités avec TiCC sont résumés de la manière suivante.

Au niveau de la rayure à l'acier, le couplage galvanique entre le revêtement sacrificiel de ZnAlMg et l'acier entraîne la dissolution du revêtement. Le couplage entre les matériaux étant fort, toutes les phases du revêtement sont impactées et se dissolvent. Cette dissolution anodique du revêtement forme une zone de délamination autour de la rayure. Au niveau de front de délamination, le confinement spatial permet à un autre type de mécanisme de dégradation d'entrer en jeu. En effet, le gradient de concentration en oxygène qui existe limite le renouvellement de l'oxygène au niveau du front de délamination et implique une augmentation du pH localement. La formation d'ions hydroxydes est responsable de la rupture des liaisons entre le polymère et le métal, favorisant la propagation d'électrolyte sous peinture.

Le contact entre l'électrolyte et le revêtement ZnAlMg conduit à la dissolution préférentielle de la phase de Zn-Zn_2Mg dans la microstructure, créant des chemins de corrosions depuis le défaut à l'acier.

Localement, la présence de produits solubles ou l'absence locale de couche de conversion peuvent être à l'origine du développement de cloques. L'absorption d'eau à travers la peinture va créer une solution ionique ou la formation de produits de corrosion qui peuvent entraîner la formation d'une cloque par effet osmotique. Sur les bords de la cloque, un effet combiné des mécanismes de délamination mécanique et cloquage cathodique pourrait expliquer leur croissance.

4. Effet de la microstructure multiphasée du ZnAlMg sur la distribution de l'activateur à base de Ti et la couche de conversion de phosphate

Les revêtements de ZnAlMg peints traités avec la couche de conversion de phosphates ne présentent pas de cloques sous peinture.

Pour ce type de CC, une étape d'activation à base de Ti est nécessaire avant l'étape de phosphatation

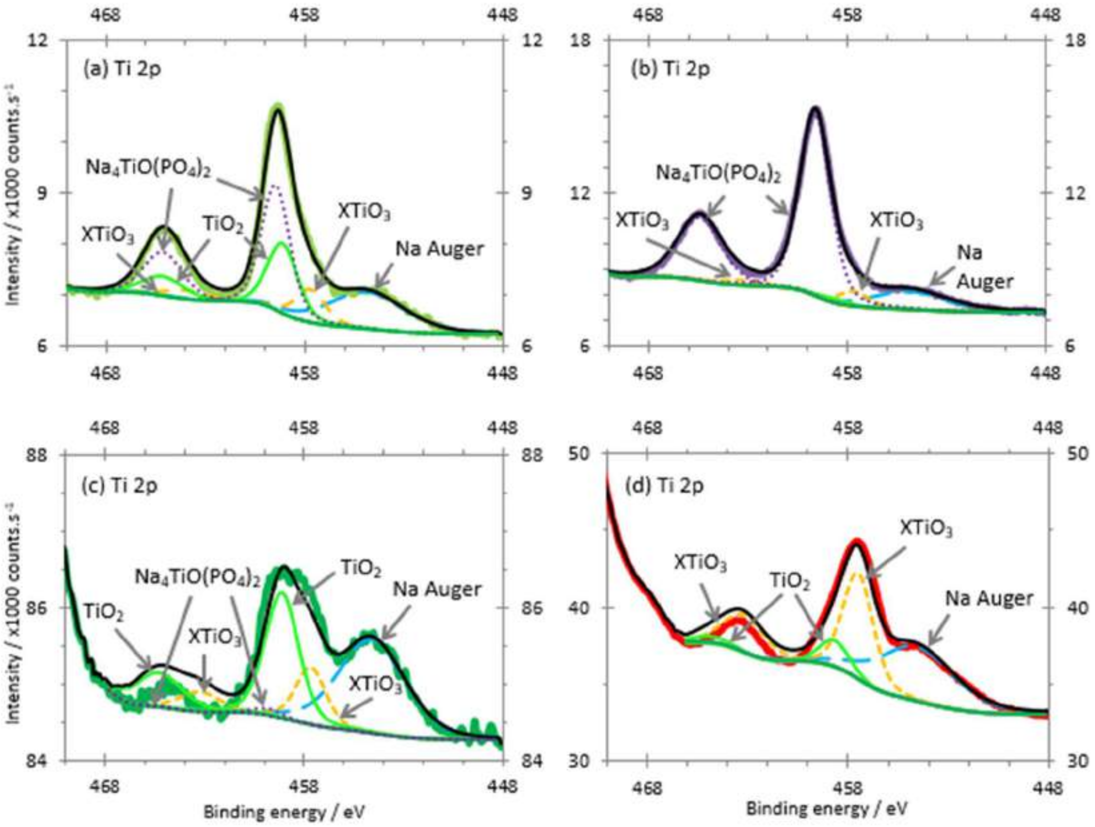

Figure 8: Spectre XPS Ti 2p et déconvolution : (a) activateur à l'état initial, (b) activateur après dissolution et évaporation du solvant, (c) Zn2Mg et (d) Zn

Après l'étape d'activation, la concentration et la forme chimique du Ti varient selon le substrat utilisé. Sur les phases pures représentant le ZnAlMg, le Ti est présent en plus forte concentration sur la phase de Zn que celle de Zn$_2$Mg, la concentration en Ti mesuré étant trop faible sur ZnAl pour permettre une déconvolution du pic de Ti 2p. Sur la phase Zn$_2$Mg, la présence de TiO$_2$ comme composant majoritaire a été mise en évidence tandis que sur Zn, c'est un composé de type XTiO$_3$ qui a été mesuré. Les énergies de liaisons mesurées favorisent la présence d'un TiO$_2$ lié chimiquement au substrat (ZnTiO$_3$).

L'impact de la concentration et la forme chimique de l'activateur à différentes étapes de la procédure de phosphatation est présentée sur la Figure 10.

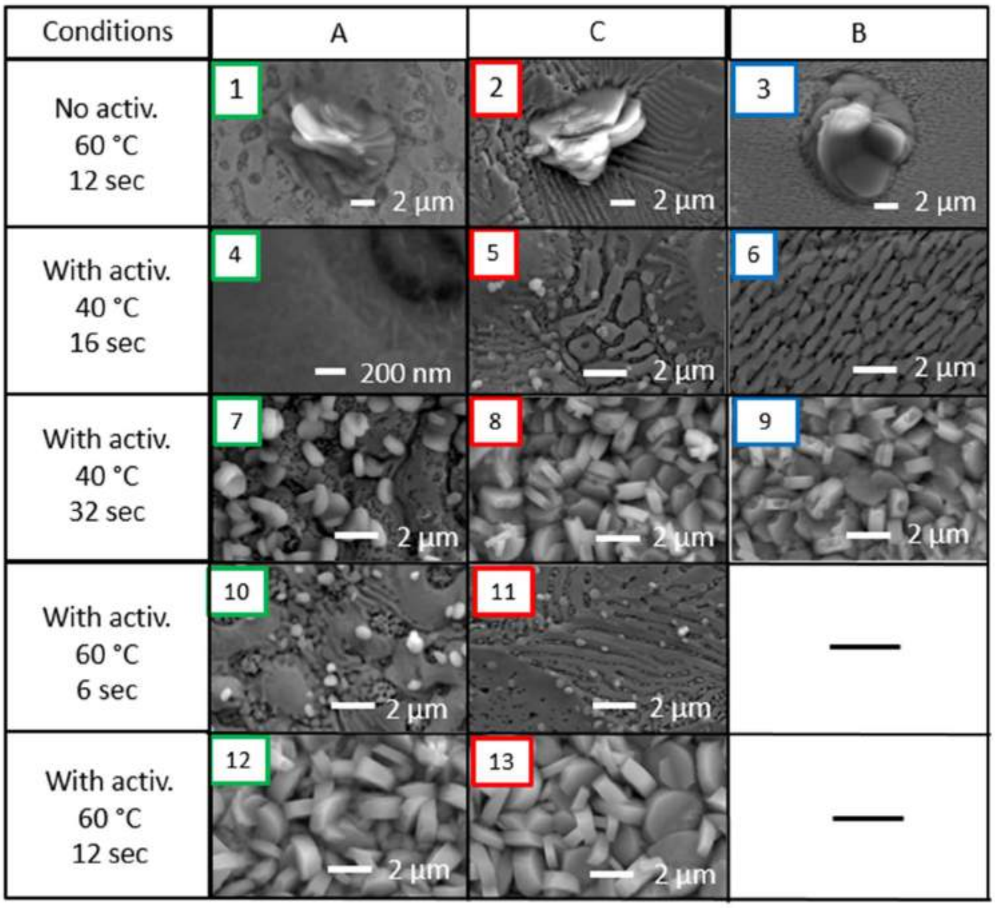

Figure 9: Morphologie et distribution des grains de PCC sur différents substrats de ZnAlMg en fonction de la présence de l'activateur, température du bain de phosphatation et temps d'immersion (voir figure)

L'absence d'activateur avant la phosphatation conduit à la formation d'amas de grains larges d'environ 10 nm permettant un recouvrement limité du revêtement. En présence d'activateur, une phosphatation à 60 °C pendant 12 sec permet la formation de petits grains d'1-2 µm, cristallins et couvrant 100 % de la surface. Aux stades intermédiaires de recouvrement du ZnAlMg, des grains de PCC peuvent être observés sur toutes les phases du revêtement, indiquant la distribution homogène de la CC sur la surface.

La formation de la PCC ne semble pas affectée par la distribution et composition chimique hétérogène de l'activateur à base de Ti. L'explication de ce phénomène réside dans le rapport de taille qui existe entre les grains de PCC et les dimensions des phases de la microstructure du ZnAlMg. En effet, les grains de PCC formés sont d'une taille au moins similaire à celle des phases du ZnAlMg ce qui permet un recouvrement de toutes les phases du revêtement, y compris celles présentant une faible concentration en activateur.

5. Impact des phases du revêtement ZnAlMg sur la distribution du TiCC

Pour comprendre l'origine du développement des cloques sur les revêtements ZnAlMg peints, une étude de la formation du TiCC sur le revêtement ZnAlMg par immersion du substrat dans le bain de TiCC suivi d'un rinçage de la surface a été réalisé.

Au cours de la réaction de conversion de TiCC sur un substrat de Zn, la formation de la CC se déroule en 2 étapes. La mise en contact du substrat avec le bain de TiCC entraîne l'apparition de zones anodiques et cathodiques à la surface du revêtement. Aux anodes ont lieu la dissolution du métal tandis qu'aux cathodes, la réduction de l'oxygène est la réaction majoritaire. Une augmentation du pH est observée qui entraîne la précipitation du TiCC dans un 2nd temps. Le mécanisme de précipitation de TiCC sur l'acier galvanisé est décrit ci-après :

- Dissolution anodique:

$$\mathrm{Zn} \rightarrow \mathrm{Zn}^{2+} + 2e^{-} \qquad (1\text{-}5)$$

- Réduction cathodique entraînant une alcalinisation :

$$\mathrm{O_2} + 4\mathrm{H}^{+} + 4e^{-} \rightarrow 2\mathrm{H_2O} \qquad (1\text{-}2)$$

$$2\mathrm{H}^{+} + 2e^{-} \rightarrow \mathrm{H_2} \qquad (1\text{-}3)$$

- Précipitation du TiCC:

$$\mathrm{TiF_6}^{2-} + 4\mathrm{OH}^{-} \rightarrow \mathrm{TiO_2.H_2O} + 6\mathrm{F}^{-} \qquad (1\text{-}4)$$

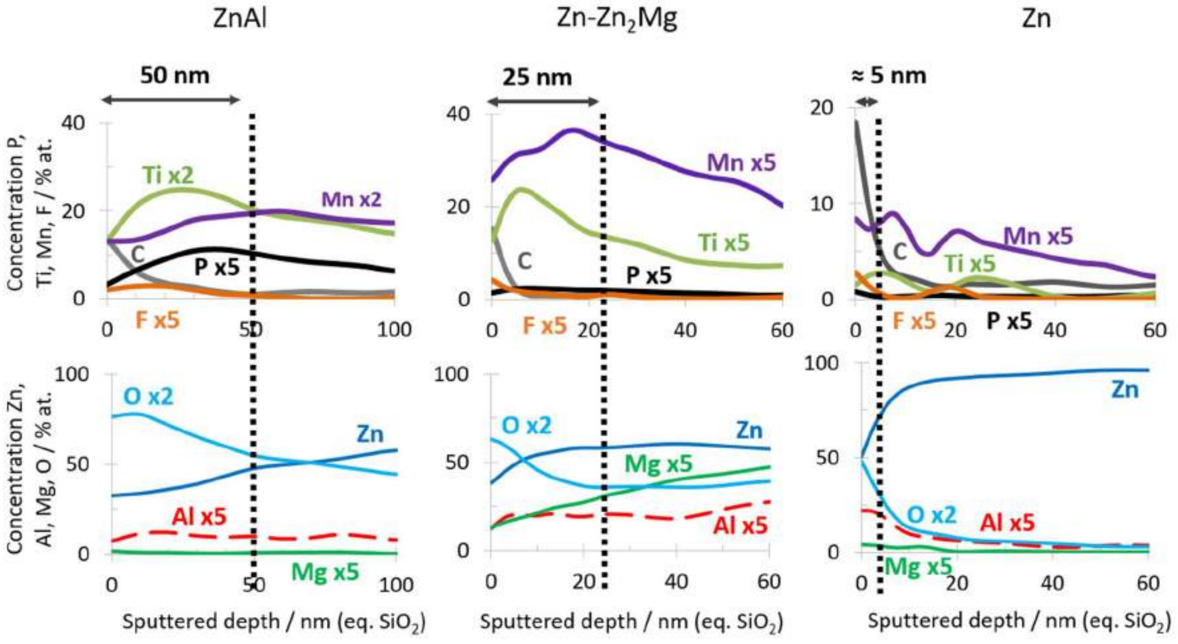

Figure 10: Profils d'érosion par spectroscopie auger des phases de ZnAlMg après immersion dans le bain de TiCC à 60 °C pendant 30 sec après un dégraissage alcalin

La mesure de l'épaisseur du TiCC sur chaque phase du revêtement ZnAlMg (Figure 10) montre une hétérogénéité de distribution du TiCC sur les phases. Les phases alliées ZnAl et Zn-Zn$_2$Mg sont mieux couvertes que les dendrites de Zn, ce qui n’est pas cohérent avec la réactivité des phases attendues dans le bain de TiCC.

La distribution hétérogène du TiCC a été attribuée à la microstructure du ZnAlMg et l’impact des phases pendant l’étape de conversion. En effet, les phases alliées ZnAl et Zn-Zn_2Mg sont des phases binaires à l’intérieur desquelles un couplage galvanique a lieu.

Les mesures de courant de couplage entre les phases pures Zn et Zn_2Mg puis Zn avec Al confirment la présence d’un couplage galvanique dans les phases binaires du revêtement (Figure 12)

Dans les phases alliées, le couplage galvanique au sein de la phase permet d’accélérer localement la cinétique de précipitation de TiCC et de recouvrir plus rapidement les phases binaires du revêtement, au détriment des dendrites de Zn monophasées.

.

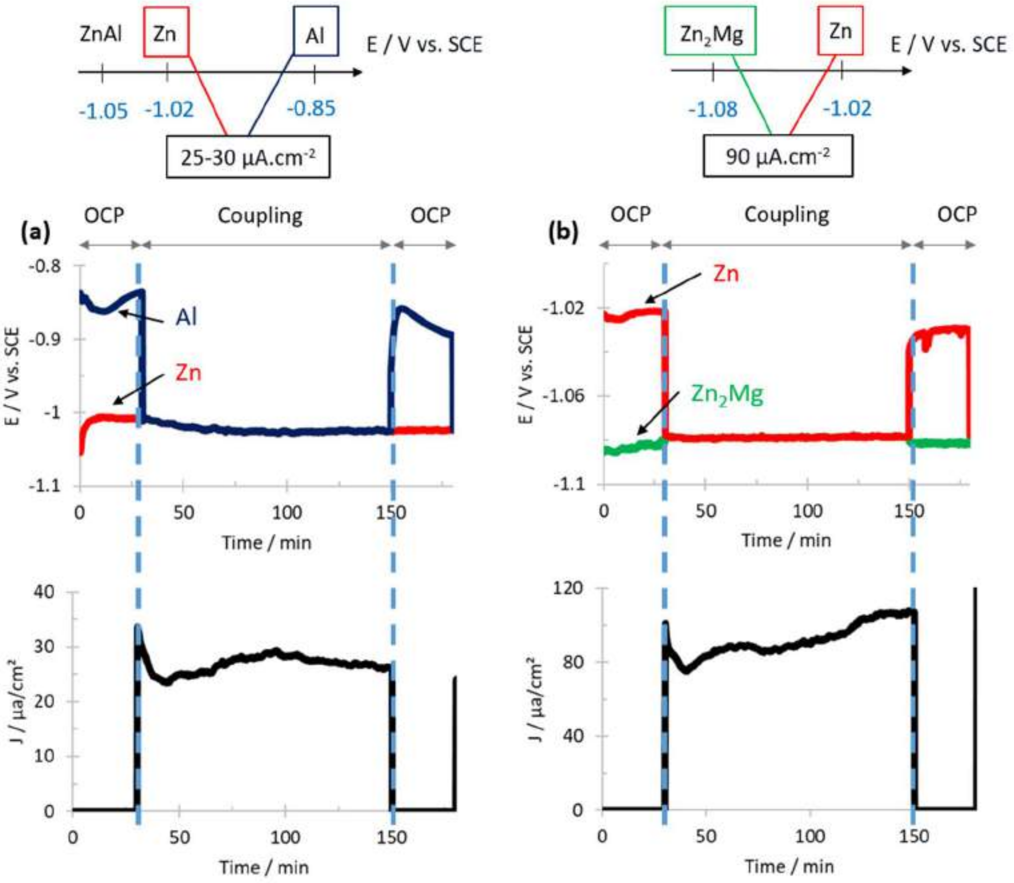

Figure 11: Evolution du potential et de la densité de courant de (a) Zn/Al et (b) Zn/Zn2Mg après 30 min d’immersion puis 2 h de couplage dans Na2SO4 5 wt. % pH 2,6 à 25 °C

6. Aperçu des mécanismes de formation et dégradation des TiCC sur ZnAlMg après utilisation d'un dégraissant alcalin contenant des ions Cu^{2+}

Pour homogénéiser la distribution de TiCC sur les phases de ZnAlMg, une solution basée sur la cémentation de métal noble Cu sur les phases de ZnAlMg a été testée. La précipitation de Cu a lieu pendant l'étape de dégraissage alcalin avant l'étape de conversion. Une formulation d'un dégraissant au Cu a été réalisée permettant la solubilisation du Cu en milieu alcalin grâce à une combinaison de complexants puissants du Cu.

La cémentation du Cu sur un substrat à base de Zn repose sur une réaction d'oxydo-réduction comme décrit ci-après :

$$\mathrm{Zn} + \mathrm{Cu}^{2+} \rightarrow \mathrm{Zn}^{2+} + \mathrm{Cu}$$

Des observations de microscopie électronique ont permis de vérifier la précipitation homogène du Cu sur toutes les phases de ZnAlMg. Après l'étape de conversion, des profils d'érosions par spectroscopie auger ont permis de confirmer que l'épaisseur de TiCC est plus homogène après un dégraissage alcalin permettant la cémentation de métal noble à la surface.

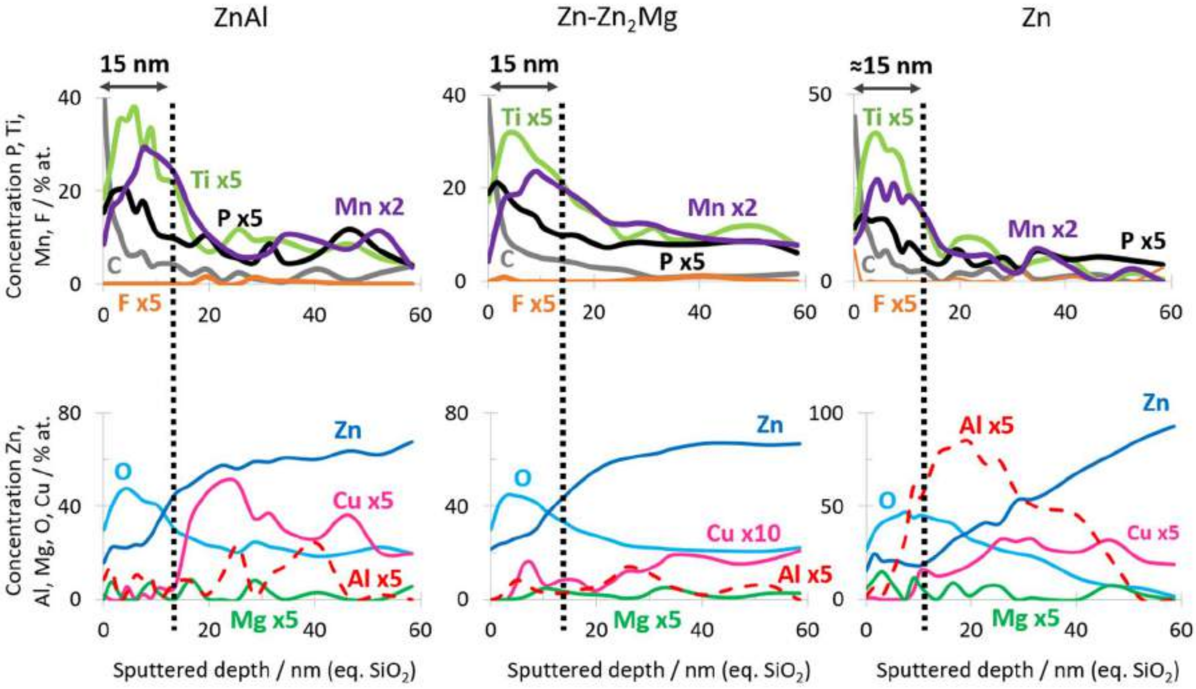

Figure 12: Profils d'érosion par spectroscopie auger des phases de ZnAlMg après immersion dans le bain de TiCC à 60 °C pendant 30 sec après un dégraissage alcalin contenant des ions Cu2+

La cémentation de Cu permet une distribution des anodes et cathodes plus fine ce qui permet un recouvrement plus rapide des zones anodiques et une distribution de TiCC plus homogène au final. Pour évaluer le gain de résistance à la corrosion du ZnAlMg après application de peinture, l'évolution du front de délamination d'un ZnAlMg traité avec le dégraissant au Cu puis le TiCC avant l'application d'un polymère modèle depuis un défaut à l'acier a été observée et comparée à celle d'un revêtement ayant subi un dégraissage standard. Les deux échantillons ont été immergés dans une solution de NaCl à 0.1 M (Figure 13).

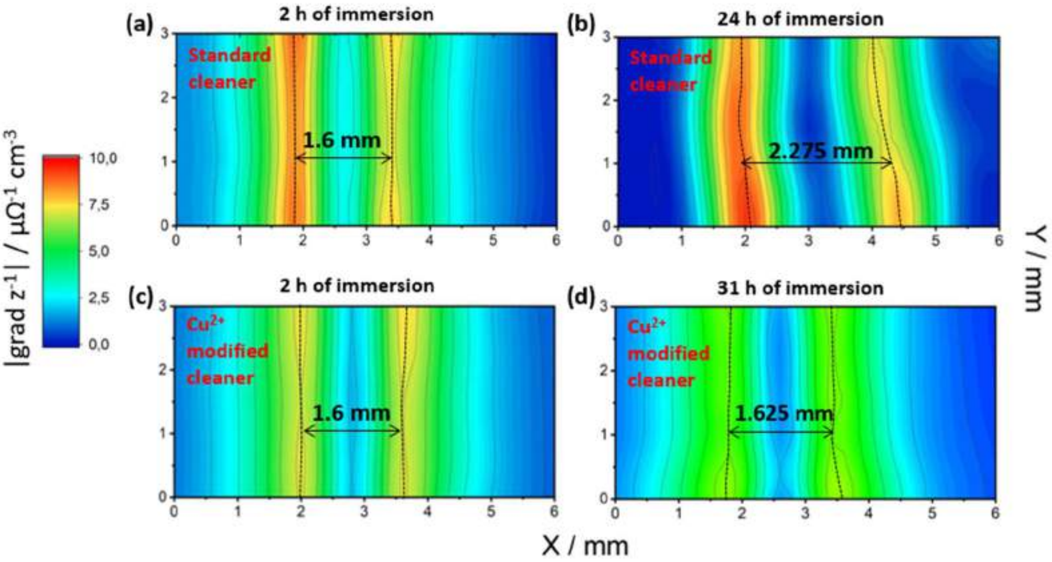

Figure 13: Gradient du module d'admittance de ZnAlMg revêtu de polymère modèle sur le TiCC après dégraissage alcalin standard: (a) après 2 h d'immersion, (b) après 24 h d'immersion et pour ZnAlMg traité avec le dégraissant aux ions Cu2+: (c) après 2 h d'immersion, (d) après 31 h d'immersion

Après 31 h d'immersion dans la solution de NaCl à 0.1 M, le front de délamination est à peine modifié pour l'échantillon traité avec le dégraissant au Cu alors que celui traité avec le dégraissant alcalin standard a subi une augmentation de la zone délaminée de 40 % par rapport à la largeur initiale.

7. Conclusions

L'étude du rôle de la microstructure des revêtements ZnAlMg sur le développement de cloques sur des ZnAlMg traités avec TiCC avant application de peinture a été vérifiée dans cette thèse. La présence de différentes phases dans le revêtement a un impact ou cours de la formation de la CC sur le ZnAlMg mais aussi pendant le processus de dégradation du revêtement peint.

En combinant des caractérisations de surface sur ZnAlMg et phases pures à différentes étapes de la réaction de conversion de PCC et TiCC, une compréhension des différences de résistance à la corrosion des 2 CC a été permise. En effet, la distribution de TiCC sur les différentes phases de ZnAlMg est hétérogène alors que dans le cas de la PCC, la distribution est homogène sur toutes les phases. Pour expliquer cette différence de distribution, le ratio entre la microstructure et la taille des éléments de la CC a été avancé.

Pour le PCC, l'activateur à base de Ti possède une réactivité différente face aux phases de ZnAlMg en termes de composés formés et de concentration mesurée. La distribution homogène était attribuée à la taille des grains de PCC qui sont d'une taille similaire à la microstructure. Pendant l'étape de conversion, les grains grandissent jusqu'à être en contact les uns avec les autres et recouvrir la surface. La distribution des anodes et cathodes dans la microstructure est assez fine comparé à la dimension des grains pour permettre un recouvrement complet de la surface.

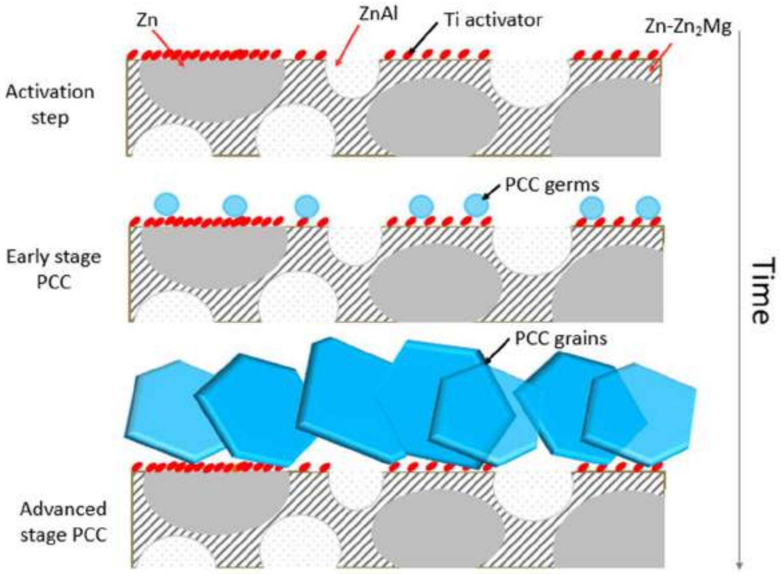

Figure14: Schéma de la distribution de l'activateur au Ti et de la PCC permettant une précipitation homogène

Pour le TiCC, la taille des éléments de la CC sont plus petits ce qui s'est révélé critique pendant l'étape de conversion. En effet, le couplage galvanique au sein des phases alliées entraîne une distribution bien définie des anodes et cathodes à la surface qui ont un impact sur la formation de TiCC. La cinétique de précipitation est plus rapide sur les phases binaires grâce à a distribution fine des zones anodiques et cathodiques. A l'inverse, les dendrites de Zn monophasées sont moins bien couvertes que les phases alliées.

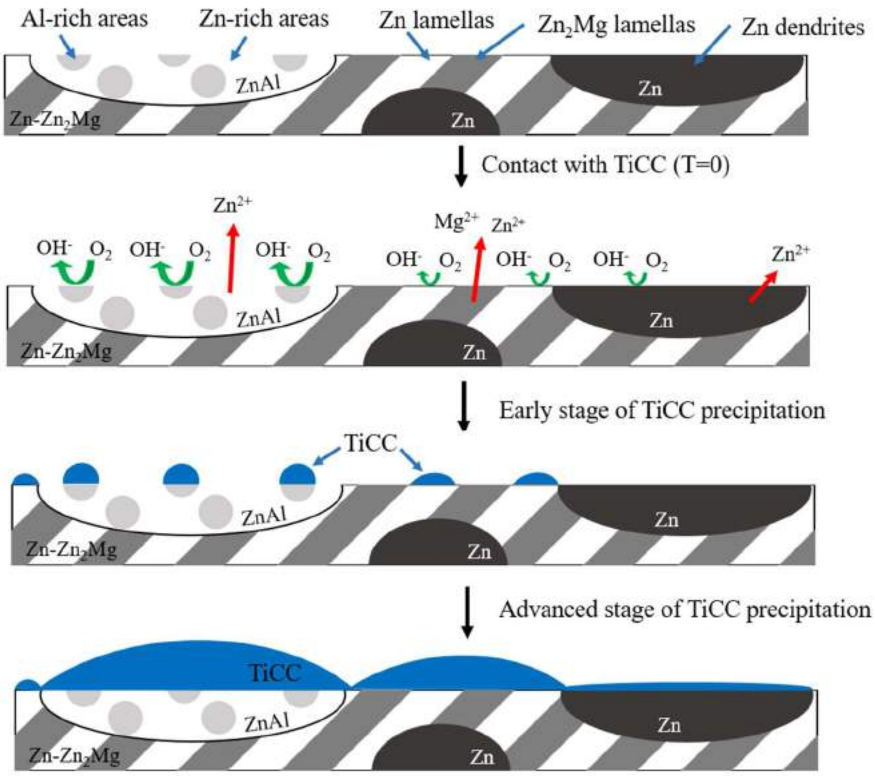

Figure 15: Schéma du mécanisme de précipitation de TiCC sur ZnAlMg

Pour homogénéiser la distribution de TiCC sur ZnAlMg, la cémentation de particules nobles de Cu a été testée en modifiant la nature du dégraissant alcalin pour permettre la solubilisation d'ions Cu^{2+}.

La précipitation du Cu sur toutes les phases de ZnAlMg entraîne une distribution très fine des cathodes et anodes sur la surface, permettant un couplage galvanique entre les particules de Cu cathodiques et le revêtement ZnAlMg anodique. La cémentation de Cu permet une homogénéisation du TiCC sur toute les phases de ZnAlMg.

Des tests de corrosion accélérés ont permis de confirmer le gain de résistance à la corrosion des échantillons ayant subi une cémentation de Cu à la surface.

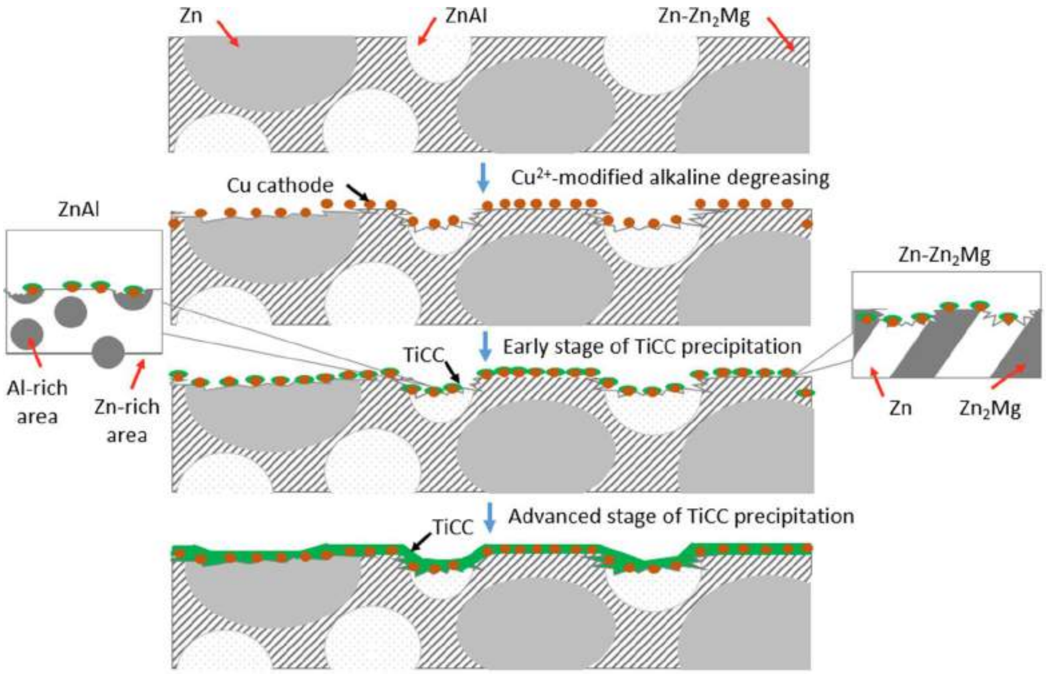

Figure 16: Schéma du mécanisme de précipitation de TiCC sur ZnAlMg après dégraissage alcalin contenant des ions Cu2+

La microstructure de ZnAlMg joue aussi un rôle favorisant l'apparition de cloques. D'un côté, la précipitation hétérogène de TiCC sur les phases de ZnAlMg peut entraîner des manques de CC localement sur la surface et ainsi des zones de moindre résistance à la corrosion. D'un autre côté, en présence d'un défaut à l'acier, la propagation de la corrosion est facilitée par la présence de différentes phases et en particulier de la phase anodique et continue de Zn_2Mg-Zn.

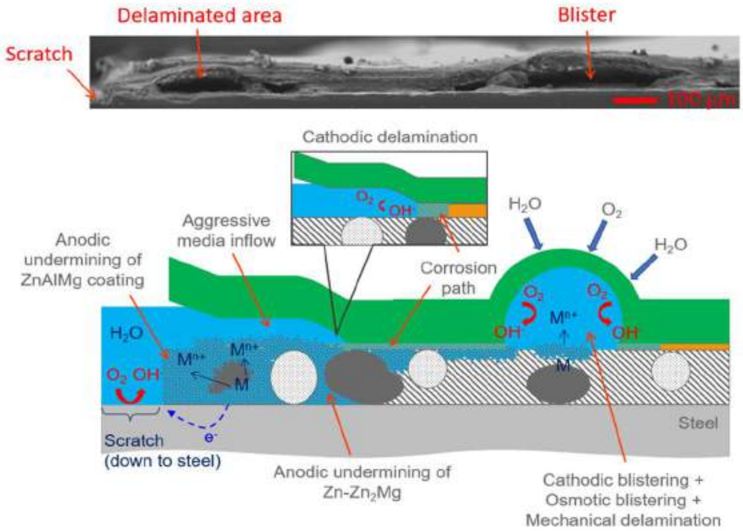

Figure 17: Schéma du mécanisme de dégradation des revêtements ZnAlMg peints en présence d'un défaut à l'acier

RÉSUMÉ

Pour remplacer l'acier galvanisé (HDG) dans les applications peintes, il est nécessaire d'optimiser les couches de conversion (CC) assurant l'adhérence de la peinture et la résistance à la corrosion. Tandis que les CC de phosphates (PCC) et de Ti (TiCC) sont comparables sur acier galvanisé, les tests de corrosion accélérés ont montré une moindre résistance au cloquage du ZnAlMg avec TiCC. Cette thèse vise à comprendre cette différence, en particulier le rôle de la microstructure du ZnAlMg et à proposer une solution améliorant les performances de la TiCC. Grâce au MEB-EDS, XPS et nano Auger, il a été montré, à différentes étapes de la procédure de conversion, que la PCC est homogène sur ZnAlMg et les phases pures, tandis que la TiCC couvre mieux les phases eutectiques que les dendrites de Zn. La distribution de la CC est en accord avec la réactivité des phases attendue pendant le couplage galvanique et variations de pH correspondantes, nécessaire à la précipitation des CC. Pour la PCC, la différence de réactivité est nivelée par la taille des cristaux de PCC non impactés par l'hétérogénéité du ZnAlMg. Pour le TiCC, un prétraitement de Cu a été formulé, offrant un recouvrement complet du ZnAlMg et une meilleure résistance au cloquage après peinture.

MOTS CLÉS

Couches de conversion - Revêtements ZnAlMg – Microstructure - Corrosion

ABSTRACT

To replace Zn coatings for steel by ZnAlMg in painted applications, it is necessary to optimize conversion coatings (CC) ensuring paint adherence and corrosion resistance. While on Zn-coated steels, phosphate CC (PCC) and Ti CC (TiCC) were comparable, accelerated tests demonstrated a lower blistering resistance of ZnAlMg with TiCC. The PhD aimed at understanding this difference, especially the role of the ZnAlMg microstructure and to propose a solution improving TiCC performances. Using SEM-EDS, XPS and nano-AES, it was demonstrated, at different steps of CC procedure, that PCC is homogeneously distributed on ZnAlMg and pure phases, while TiCC better covers eutectic phases than Zn dendrites. CC distribution correlated with the reactivity order expected from galvanic coupling and corresponding variation of local pH, necessary for CC precipitation. The reactivity difference was leveled by the crystal size of PCC, unimpacted by ZnAlMg heterogeneity. For TiCC, a Cu cementation pretreatment was formulated, ensuring a complete coverage of ZnAlMg surface and a higher blistering resistance after painting.

KEYWORDS

Conversion coatings - ZnAlMg coatings – Microstructure - Corrosion